120
6-8-92 JS(2)

DOE/BC/14600-27
(DE92001044)

SUPRI HEAVY OIL RESEARCH PROGRAM

SUPRI TR 85

Annual Report
October 1, 1990 - September 30, 1991

By
William E. Brigham
Henry J. Ramey, Jr.
Louis M. Castanier

May 1992

Performed Under Contract No. FG22-90BC14600

Stanford University
Petroleum Research Institute
Stanford, California

Bartlesville Project Office
U. S. DEPARTMENT OF ENERGY
Bartlesville, Oklahoma

DOE/BC/14600--27

DE92 001044

SUPRI HEAVY OIL RESEARCH PROGRAM

SUPRI TR 85

Annual Report
October 1, 1990 - September 30, 1991

By
William E. Brigham
Henry J. Ramey, Jr.
Louis M. Castanier

May 1992

Work Performed Under Contract No. FG22-90BC14600

Prepared for
U.S. Department of Energy
Assistant Secretary for Fossil Energy

Thomas B. Reid, Project Manager
Bartlesville Project Office
P. O. Box 1398
Bartlesville, OK 74005

Prepared by
Stanford University
Petroleum Research Institute
Stanford, CA 94305

TABLE OF CONTENTS

LIST OF TABLES

LIST OF FIGURES

SUMMARY

This page summarizes the progress made during the 1990-1991 fiscal year. The organization of this report in sections refers to the following projects:

Project 1: Flow Properties

The experimental work on the study of end effects in displacement experiments continued. It was found necessary to provide some shielding to the core to avoid artifacts generated by beam hardening. Software has been developed to calculate the saturations of each voxel in the core. The results are quite repeatable. The runs indicate the presence of a strong saturation gradient both during imbibition and drainage experiments. The effect of flow rate is more pronounced in drainage than in imbibition.

Project 2: In-Situ Combustion

Thirteen combustion tube runs were made using four different crudes. In addition to Hamaca and Huntington and Beach oils, two crude oils, a 12° API and a 34° API Californian oil were also tested. The metallic additives iron, tin and zinc improved the combustion efficiency in all cases. Fluctuations in the produced gas compositions were observed in all control runs, but disappeared with the iron and tin additives. The front velocities were increased by the metallic additives. Changes were also observed in H/C ratio of the fuel, heat of combustion, air requirements and density of the crude produced. The amount of fuel deposited varied between the oils. For Huntington Beach oil, the amount of fuel increased in the order: zinc, control, tin, and iron, while for the Hamaca crude the order was: control, iron and tin. The most interesting result occurred with the light California oil. The control run showed that we were unable to propagate a combustion front while with the iron additive, a good combustion was achieved.

To date we have not been able to find a suitable additive to reduce fuel deposition. Iron and tin salts seem suitable agents to increase fuel when that is needed.

Oxidation kinetics experiments for in-situ combustion with crude oil show two reaction peaks at about 250°C (482°F) and 400°C (725°F). Current oxidation reaction models are based on three oxidation reactions: low, medium, and high temperature oxidation (LTO, MTO and HTO, respectively).

Kinetics experiments with various crude oils leads to the conclusion that the fuel is a hydrocarbon for HTO, and that the sand grain size (i.e., reaction surface area) affects the reaction kinetics. These experiments have led to the development of a new reaction model which includes two partially-overlapping, oxidation reactions: namely, low-temperature oxidation followed by high-temperature fuel oxidation. A new technique for analyzing the LTO reaction has been developed. For the fuel oxidation reaction, the new reaction model includes the effects of sand grain size and the atomic hydrogen-carbon ratio of the fuel. Results based on the new model are in good agreement with the experimental data.

This is an important project and six research assistants are studying different aspects of this project.

Project 3: Steam with Additives

Transient foam flow was described by Liu et al. (1991). Screening of surfactants in the

Liu, D., Brigham, W. E., and Castanier, L. M.: "Transient Foam Flow in Porous Media with Cat Scanner", SUPRI TR 82, DOE Contract No. DE-FG19-87BC14126, October, 1991.

presence of residual oil has continued. It appears that the injection procedure greatly affects the performance of the process. A new micromodel for foam observations is being built using computer technology. This micromodel will be used to study the effect of oil on the flow behavior of foams at the pore level. A three dimensional steam injection model allowing measurement of saturations by CT scan has been built. Runs with steam displacing water showed that the model can be operated as planned and that saturations in gas-liquid systems can be measured. Foam runs are now in progress.

During steam injection experiments, the saturations obtained by CT matched well with the temperature data. That is, the steam override as observed by temperature data was also clearly seen on the CT pictures.

During the runs where foam was present, the saturation distributions obtained from CT pictures showed a piston like displacement. However, the temperature distributions were different depending on the type of steam foam process used. During the experiment which included non-condensible gas (nitrogen) injection, the temperature distributions, contrary to the saturation distributions, still indicated the presence of steam override, although the override was reduced by the foam. When there was no nitrogen, the temperature distributions followed the saturation distributions. This may indicate that the nitrogen foam ahead of steam foam caused the difference between temperature and saturation distributions. These results show that pressure/temperature data alone are not sufficient to study steam foam in the presence of non-condensible gas.

Results of field and laboratory studies indicate that steam injection into fractured reservoirs has economic potential. Though injected water moves rapidly through fractures, the heat front moves uniformly. Oil recovery from heated matrix blocks can be higher than from unheated blocks with recoveries over 60% of the original oil in place. A number of mechanisms operate during steam injection into naturally fractured reservoirs that are largely independent of oil gravity. This makes steam injection into naturally-fractured reservoirs equally attractive for light and heavy oils. This is a new project and initial results are discussed.

Project 4: Formation Evaluation

Much heavy oil exists in low-pressure formations and free surface drainage is an important flow mechanism. There is no information on interpreting well test data for these systems. A finite-difference model is running currently, but is still being tested. This work will continue.

Another new project concerns multivariate optimization of production systems to select the best well completion conditions. Preliminary work is presented.

Project 5: Field Support

A new project was started to study construction of an ultrasonic wellbore flowmeter. The one tool in modern well testing needing improvement is the downhole flowmeter. Currently, testing of an ultrasonic flowmeter is being done in the laboratory. If successful, this device will be installed in to a sonde for downhole field testing.

SUPRI personnel continue to be active in professional society affairs and attend SPE and DOE meetings and conferences.

1.1 A STUDY OF END EFFECTS IN DISPLACEMENT EXPERIMENTS
(S. Qadeer)

The experimental work on the study of end effects in displacement experiments continued. It was found necessary to provide some shielding to the core to avoid artifacts generated by beam hardening. Software has been developed to calculate the saturations of each voxel in the core. The results are quite repeatable. The runs indicate the presence of a strong saturation gradient both during imbibition and drainage experiments. The effect of flow rate is more pronounced in drainage than in imbibition.

1.1.1 EXPERIMENTAL EQUIPMENT

The experiments are conducted using a CT scannable core holder and a conventional two phase liquid-liquid displacement experiment. The details of the experimental equipment and data logging system are given in an earlier report (Aziz, et al. 1990).

As reported in the previous report (Aziz, et al. 1990), there was considerable beam hardening, which resulted in strong concentric artifacts. A plexiglass doughnut filled with distilled water was used to shield the core during scans to avoid these artifacts. Figure 1.1.1 shows the location of the doughnut with respect to the core and X-ray path. The scans obtained with and without shielding are compared in Figure 1.1.2. The difference in the quality of scan data improved.

1.1.2 MATERIALS AND EXPERIMENTAL PROCEDURE

During the previous experiments, sodium iodide was used to prepare the brine causing a change in the x-ray absorption of the brine. It was decided to use sodium bromide to prepare the brine. The concentration was increased to 8% to achieve a high contrast in the CT numbers of the wetting and nonwetting phases.

Consolidated Berea sand stone cores two inches in diameter and about eight inches long are used in the experiments. The cores are heated in a furnace at 600°C for six hours to deactivate the clays. The core and two stainless steel end plugs was placed in a heat shrinkable Teflon sleeve to prevent the contact of fluids with the outside rubber sleeve. The Teflon-encapsulated core is placed inside the core holder.

The core is flushed with carbon dioxide and evacuated. This process is repeated twice. The core is scanned to get the CT number for dry core. The scan locations are shown in Figure 1.1.3. Sodium bromide brine is allowed to imbibe into the core. The brine is injected through the core for one day, and the absolute permeability of the core is measured and scans are done to get the CT numbers of 100% brine-saturated core.

Cyclohexane is injected into the core at 8.0 cc/min to bring the core to irreducible brine saturation. A set of imbibition and drainage experiments were performed at 1.0 cc/min. The core is scanned at preselected locations to measure the saturations. After completion of each experiment at low flow rate, the flow rate is increased to 8.0 cc/min to bring the core back to irreducible saturation. A total of two imbibition and two drainage runs have been made under similar conditions to check the reproducibility of the experiments.

1.1.3 SATURATION CALCULATIONS

The CT numbers from the dry scan, 100% brine-saturated scan and the brine are used to calculate the porosity at any location from:

$$\phi = \frac{CT_{100br} - CT_{dry}}{CT_{br} + 1000} \tag{1.1.1}$$

where CT_{dry} is the CT number of the dry core, CT_{100br} is the CT number of the 100% brine saturated core, and CT_{br} is the CT number for the brine, and ϕ is the porosity. After calculating the porosity, the CT number for 100% oil-saturated core is calculated from:

$$CT_{100oil} = CT_{dry} + \phi CT_{oil} \tag{1.1.2}$$

where CT_{100oil} is the CT number for 100% oil-saturated core and CT_{oil} is the CT number for the oil phase. The water saturations can be calculated from:

$$S_W = \frac{CT - CT_{100oil}}{CT_{100br} - CT_{100oil}} \tag{1.1.3}$$

where S_w is the saturation of water and CT is the CT number at any location.

Water saturation at each scan location was calculated using two different techniques. In the first method, the average CT numbers are measured at each scan location using the CT scanner computer. The average water saturation at that cross section was calculated using these numbers.

In the second method, the CT image files were transferred to the SUN SPARC station and the saturations were calculated using CT numbers for each voxel. The calculated saturation values were then used to generate saturation maps at each cross-section.

1.1.4 RESULTS

The experiments were started with the core at 100% brine saturation. For the primary drainage process, cyclohexane was injected at a rate of 8.0 cc/min for 24 hours. At the end of the primary drainage sodium bromide brine was injected into the core at 1.0 cc /min. After the production of oil from the core had stopped, the flow rate was increased to 8.0 cc/min, to bring the core to irreducible oil saturation. Oil was then injected into the core at 1.0 cc/min for the secondary drainage process. The flow rate was again increased to 8.0 cc/min at the end of low flow rate drainage. The saturations calculated from average scan CT numbers from these runs are shown in Figure 1.1.4.

From Figure 1.1.4, we can see that there is a strong water saturation gradient from the inlet to the outlet of the core during all displacement processes. The water saturation distribution is almost same from primary drainage and secondary drainage at high rate. There is very little change in the water saturations from low-rate imbibition to high-rate imbibition. The wetting phase saturation stays almost at 100% near the outlet end.

The water saturations calculated using the CT numbers for individual voxels for these runs are shown in Figures 1.1.5 to 1.1.7. The saturation map at the end of primary drainage is shown in Figure 1.1.5. The light areas indicate high brine saturation. The presence of a

strong saturation gradient can be seen from this picture. Although the brine saturation calculated from the average scan CT numbers is 100% at the outlet as shown in Figure 1.1.4, Figure 1.1.5 indicates that there are areas near the outlet which have a high saturation of cyclohexane. These areas provide a path for the flow of cyclohexane. The 100% brine saturation may be the result of averaging and statistical variation of the CT numbers.

The brine saturation maps from the low- and high-rate imbibition runs are shown in Figure 1.1.6. The brine saturations calculated from average scan CT numbers for the same runs are shown in Figure 1.1.4. The wetting phase saturation increases from about 0.4 to 0.7 at the inlet. There is little change in the saturations from about 4.0 inches from the inlet to the outlet of the core. The saturation gradient, although smaller than that observed in the drainage process, still exists. There is practically no difference in brine saturations between the low- and high-rate imbibition runs.

The brine saturation pictures obtained at the end of 1.0 cc/min and 8.0 cc/min drainage run are shown in Figure 1.1.7. The pictures indicate that the oil saturation increases throughout the core when the flow rate rate is increased. The saturation gradient still exists at the end of high rate drainage.

Figure 1.1.8 compares the brine saturations obtained at the end of 8.0 cc/min imbibition runs 1 and 2. Corresponding saturation pictures are shown in Figure 1.1.9. The results from drainage runs 1 and 2 are compared in Figures 1.1.10 and 1.1.11. The repeatability of the saturation measurements can be identified.

1.1.5 FUTURE PLAN

We have established a procedure by which we can measure saturations in a core. These runs were made at two extreme flow rates, i.e., 1.0 cc/min and 8.0 cc/min. It is planned to study the effect of flow rate on the saturation gradients. The effect of changing the viscosity ratios and end plug configurations will also be studied. An appropriate model will be developed to simulate the flow behavior observed.

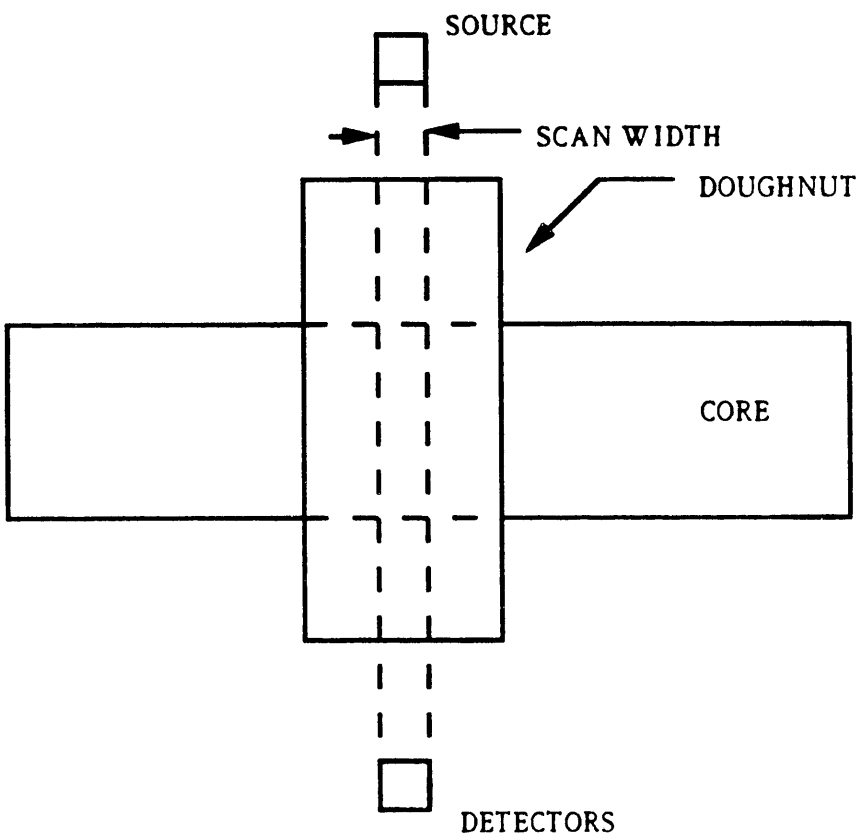

Figure 1.1.1 Location of doughnut with respect to the core and scan location.

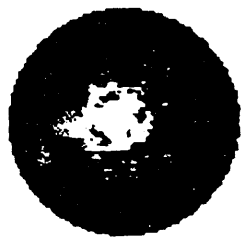

(a) Scan without shielding

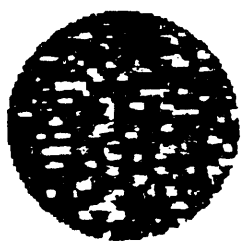

(b) Scan with shielding

Figure 1.1.2 Comparison of scans with and without shielding.

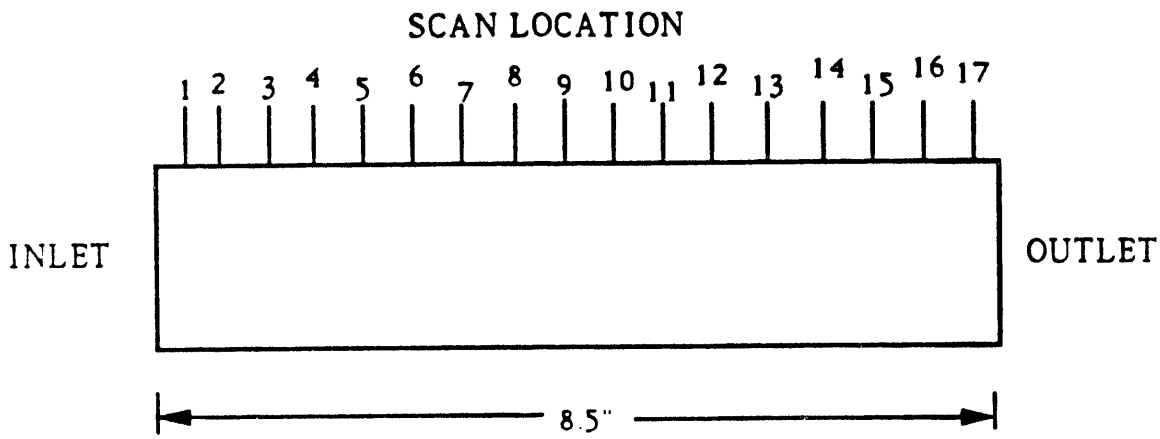

Figure 1.1.3 CT scan locations for Berea sandstone core CIE.

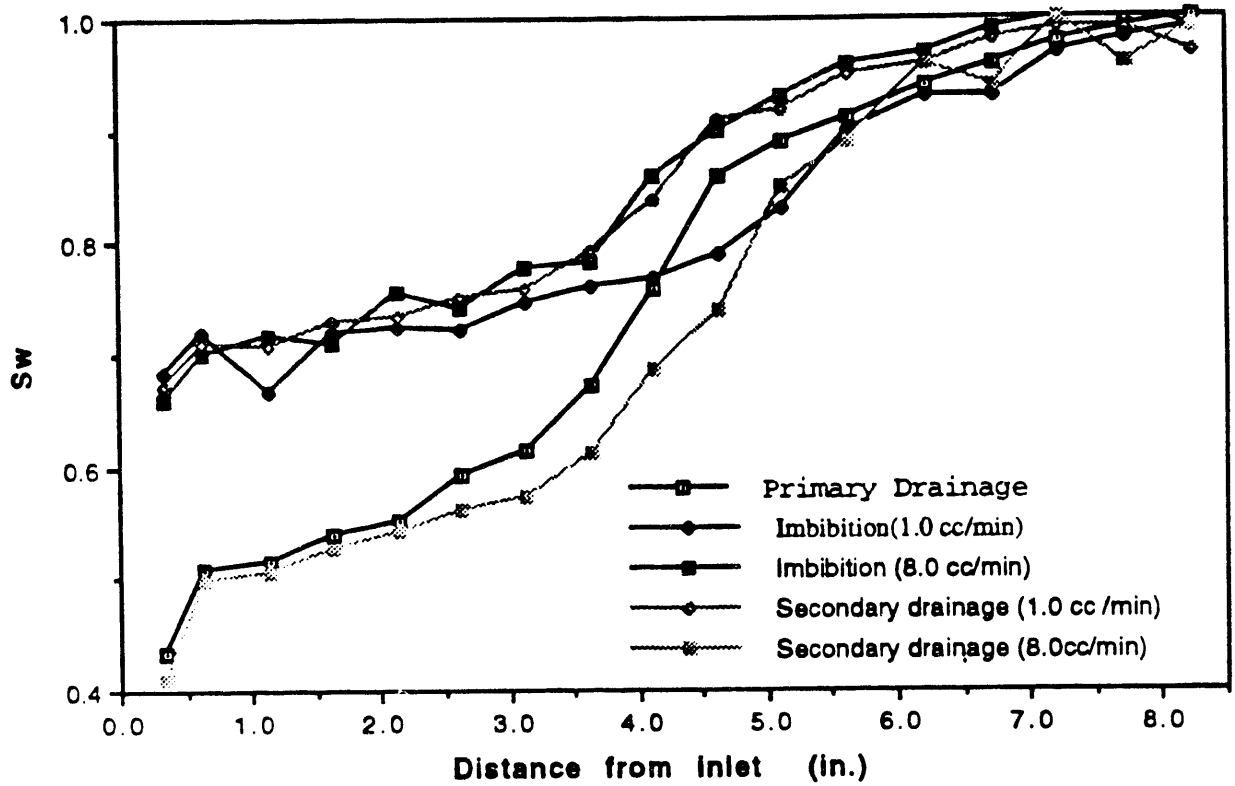

Figure 1.1.4 Water saturation vs distance from inlet calculated from average scan CT numbers.

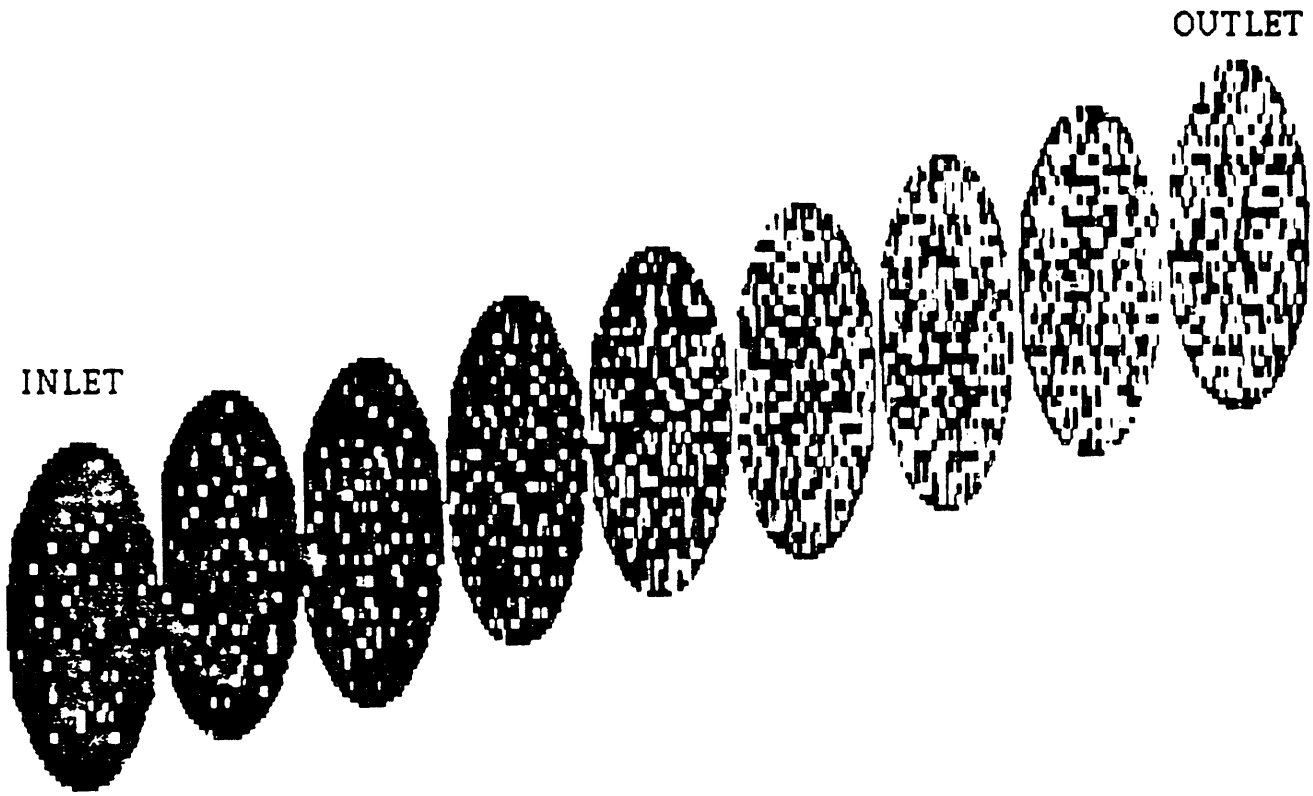

Figure 1.1.5 Saturation picture at the end of primary drainage.

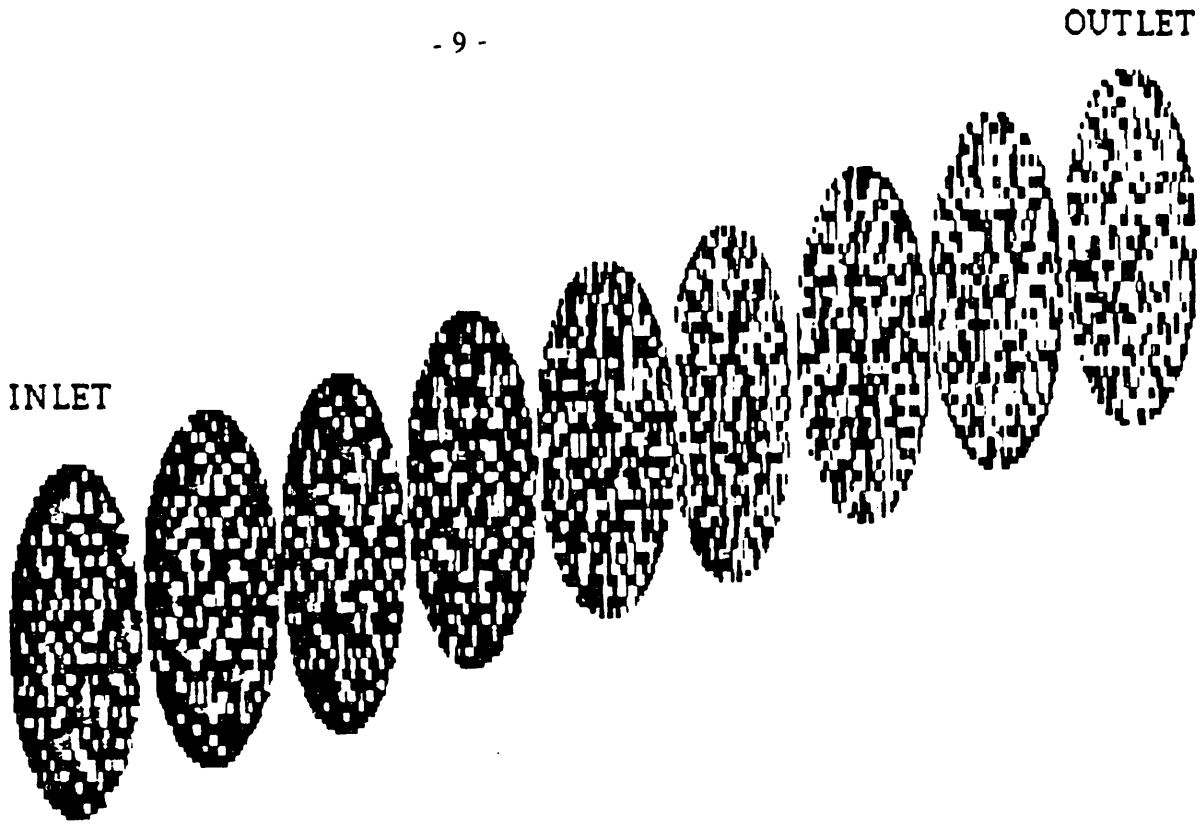

(a) Low-rate imbibition

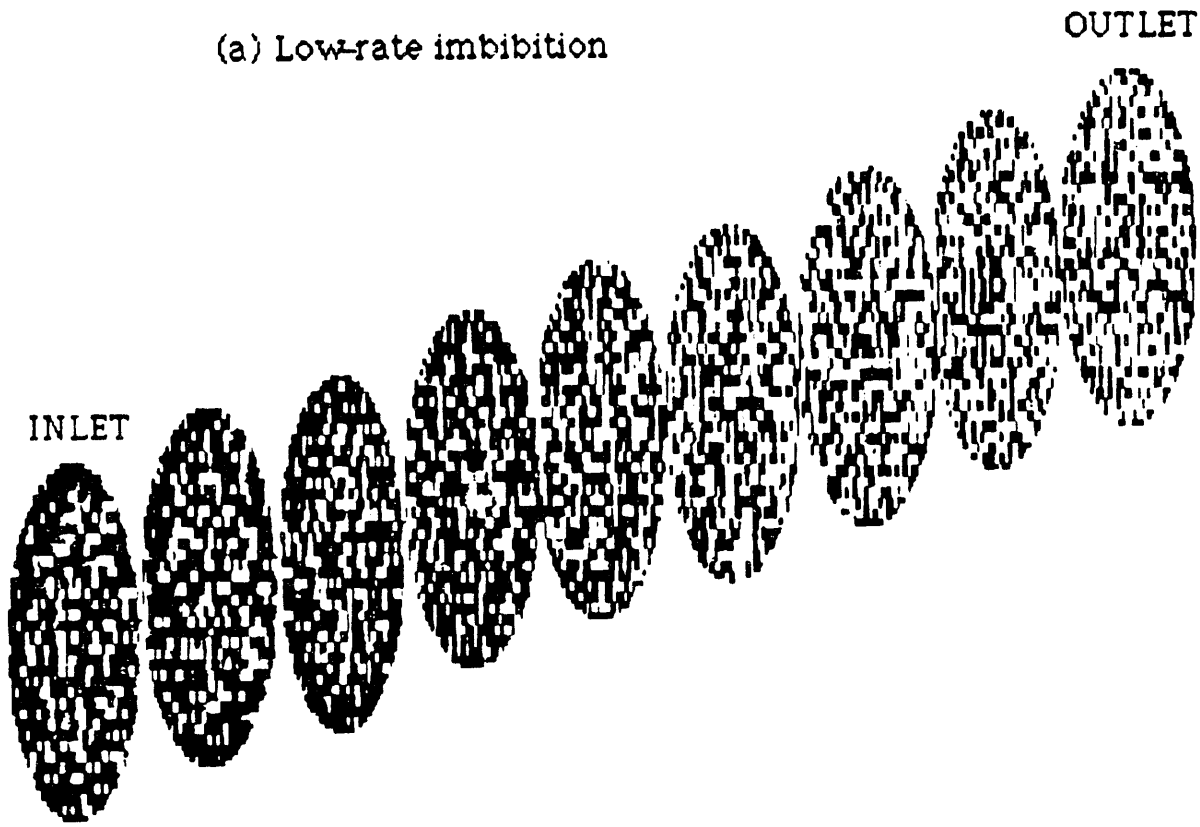

(b) High-rate imbibition

Figure 1.1.6 Water saturation distribution at the end of low- and high-rate imbibition.

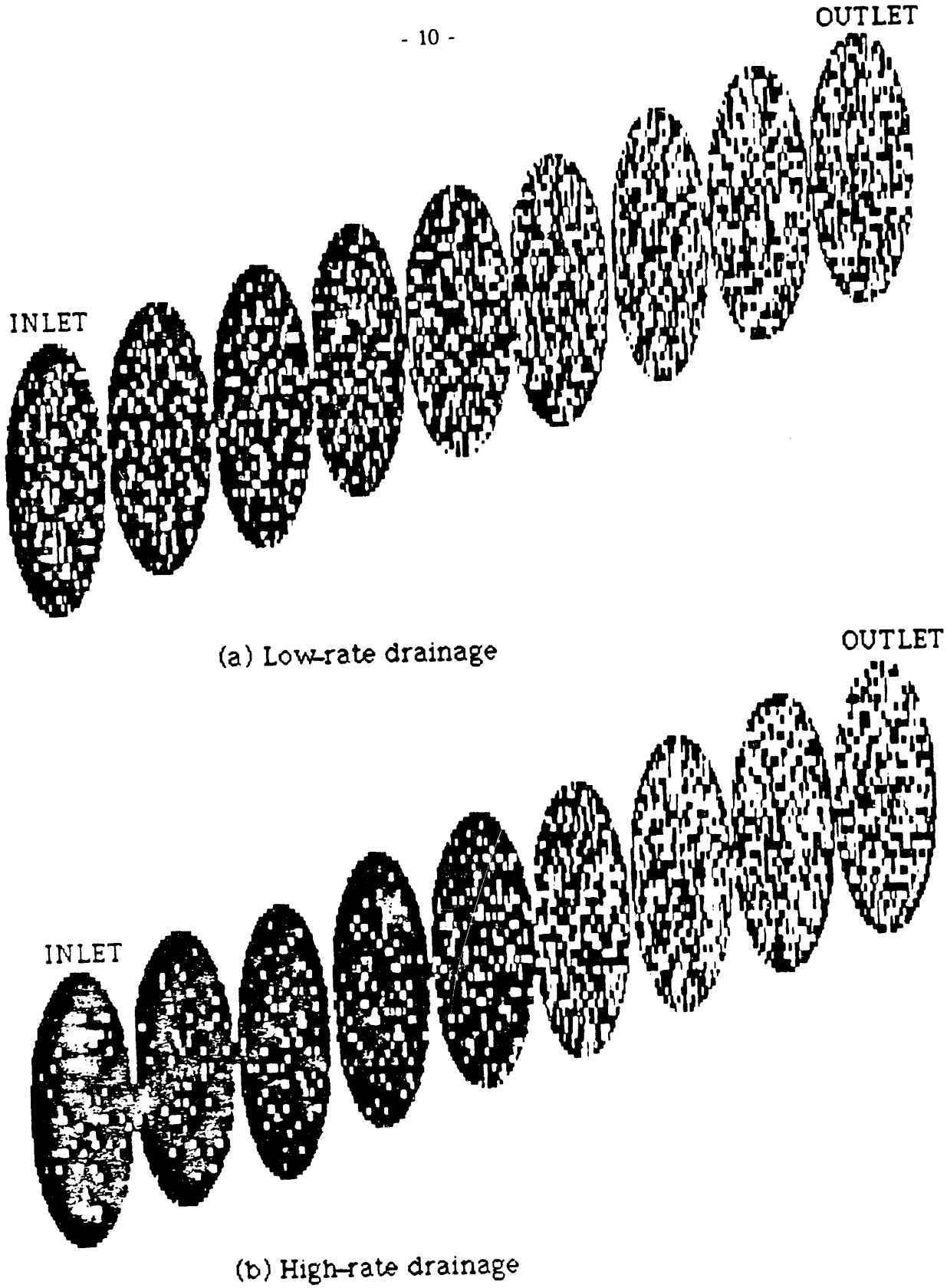

Figure 1.1.7 Saturation distribution at the end of low- and high-rate drainage.

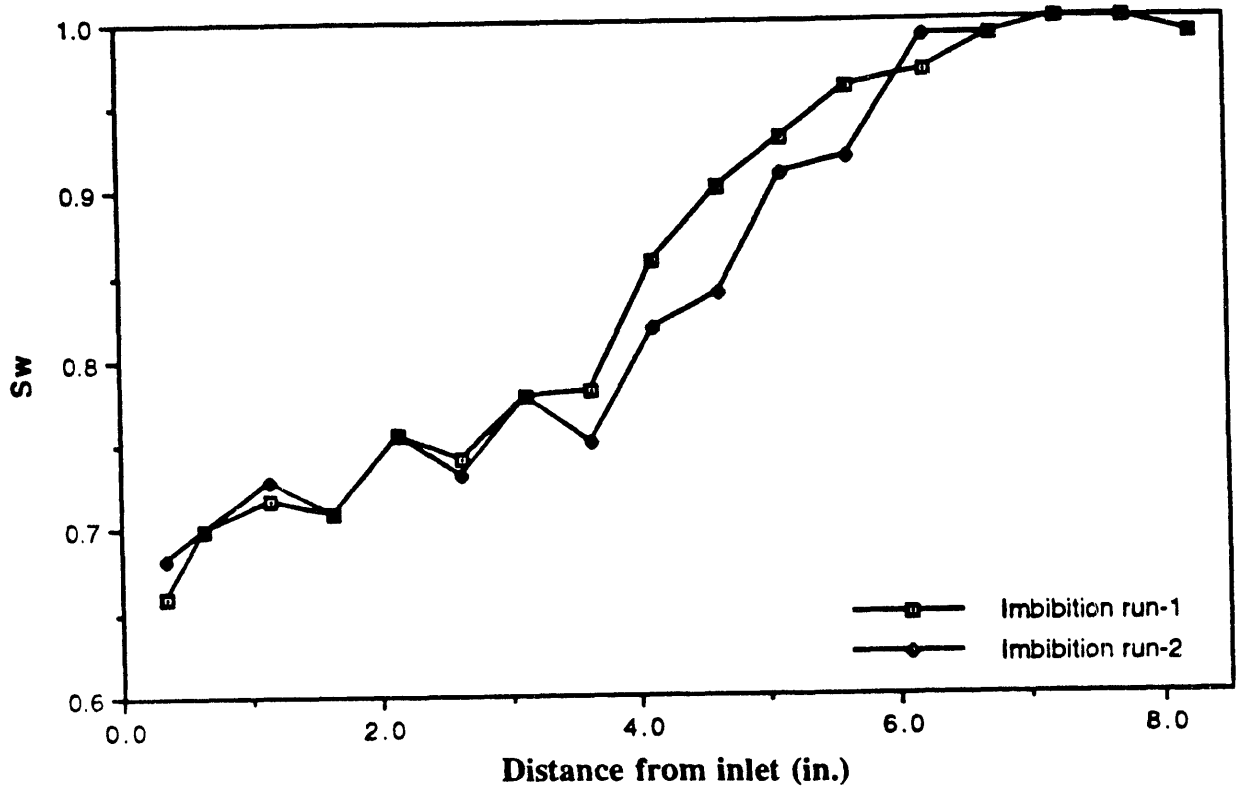

Figure 1.1.8 Comparison between imbibition run-1 and 2.

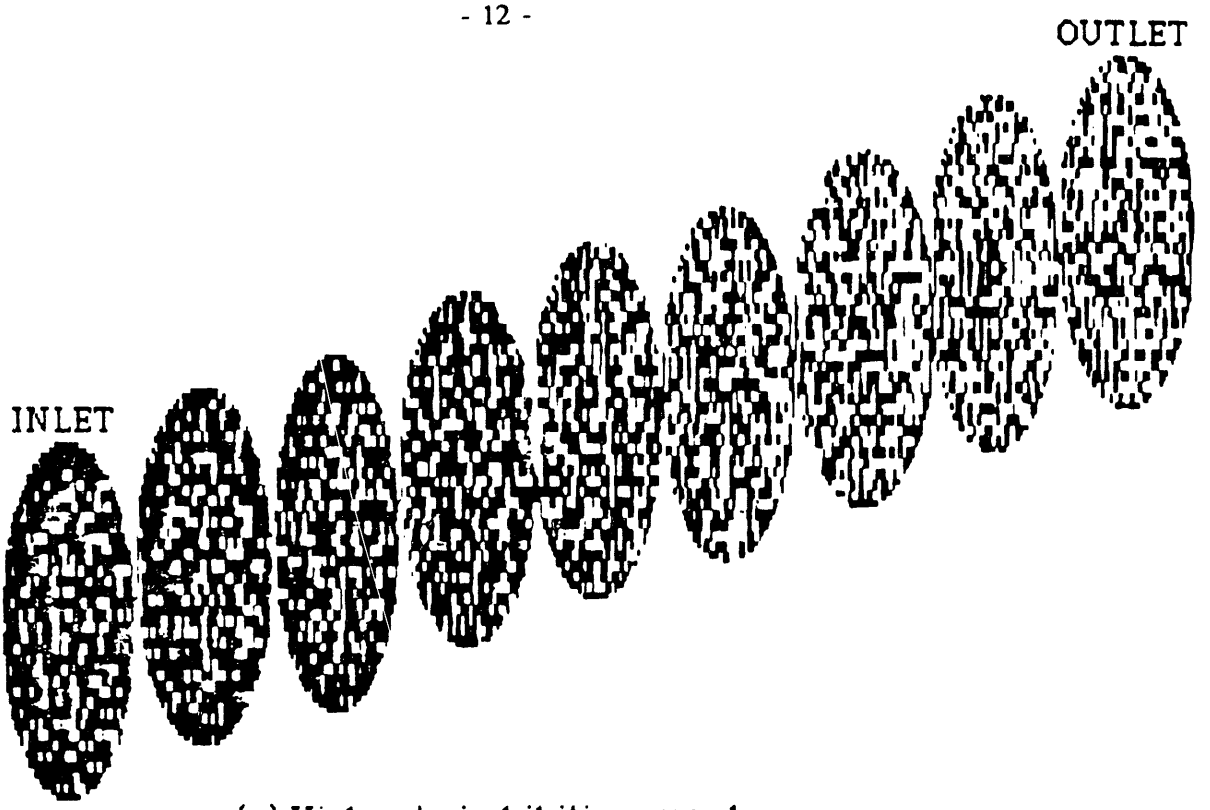

(a) High-rate imbibition run-1.

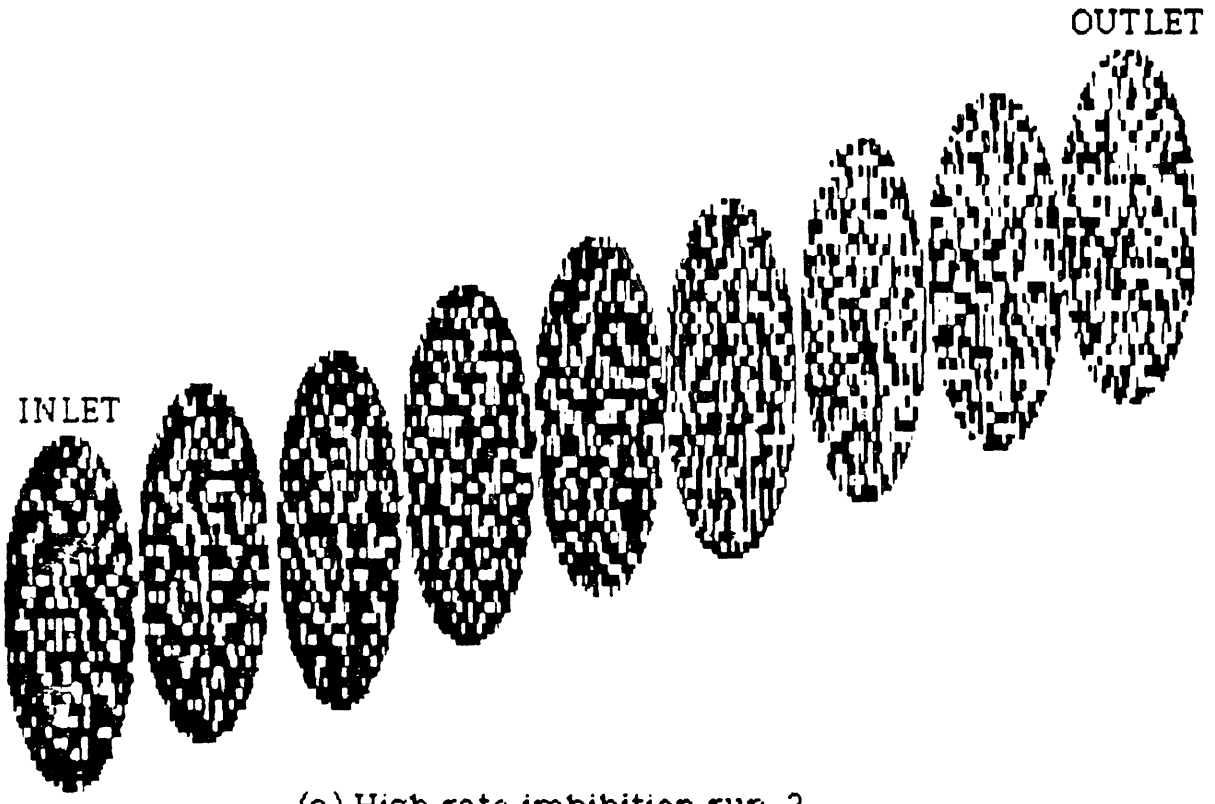

(a) High-rate imbibition run-2

Figure 1.1.9 Comparison of saturation distributions between high-rate imbibition runs 1 and 2.

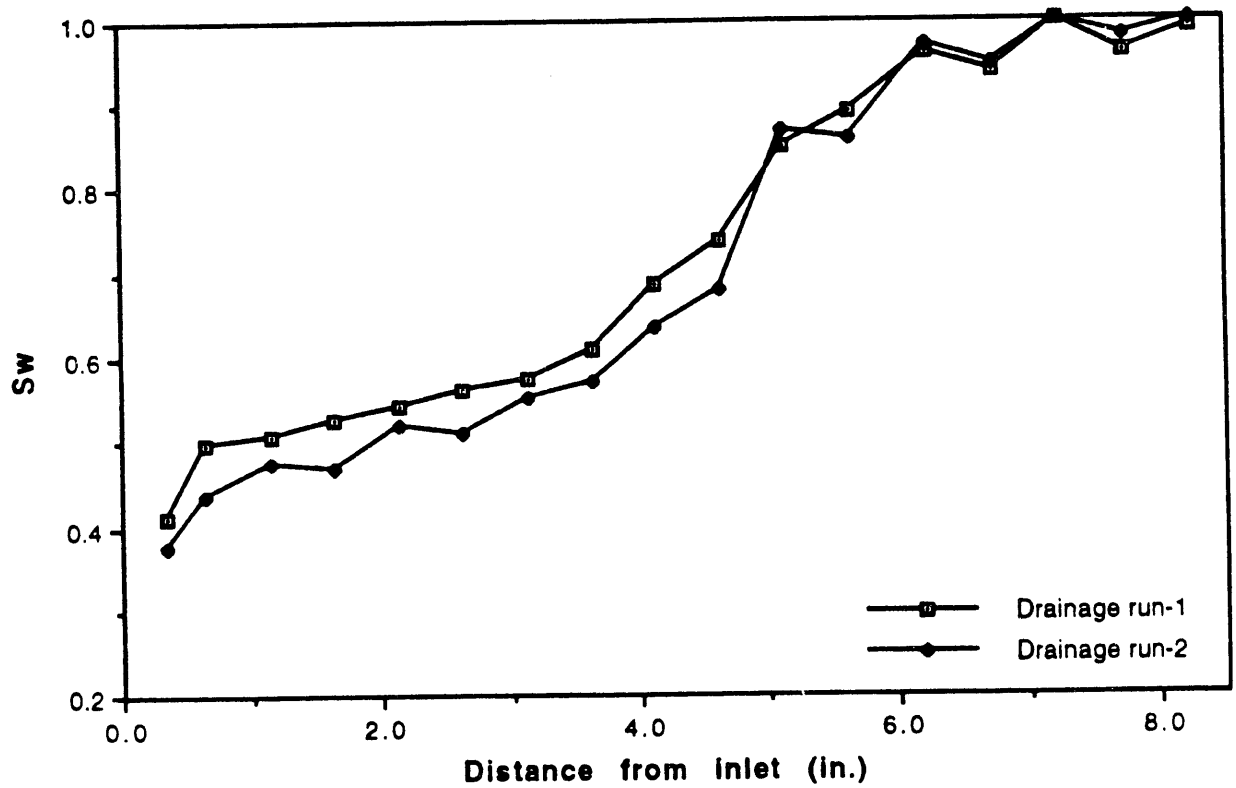

Figure 1.1.10 Comparison between drainage run-1 and 2.

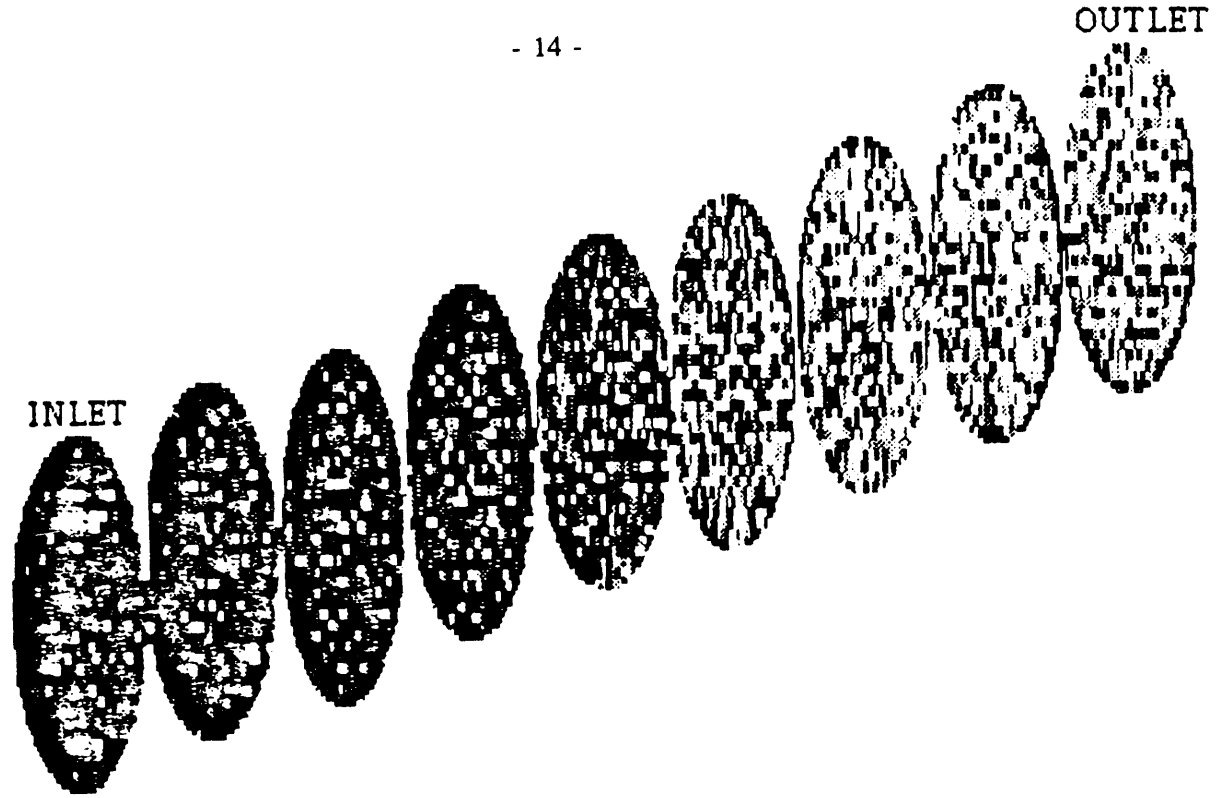

(a) High-rate drainage run-1

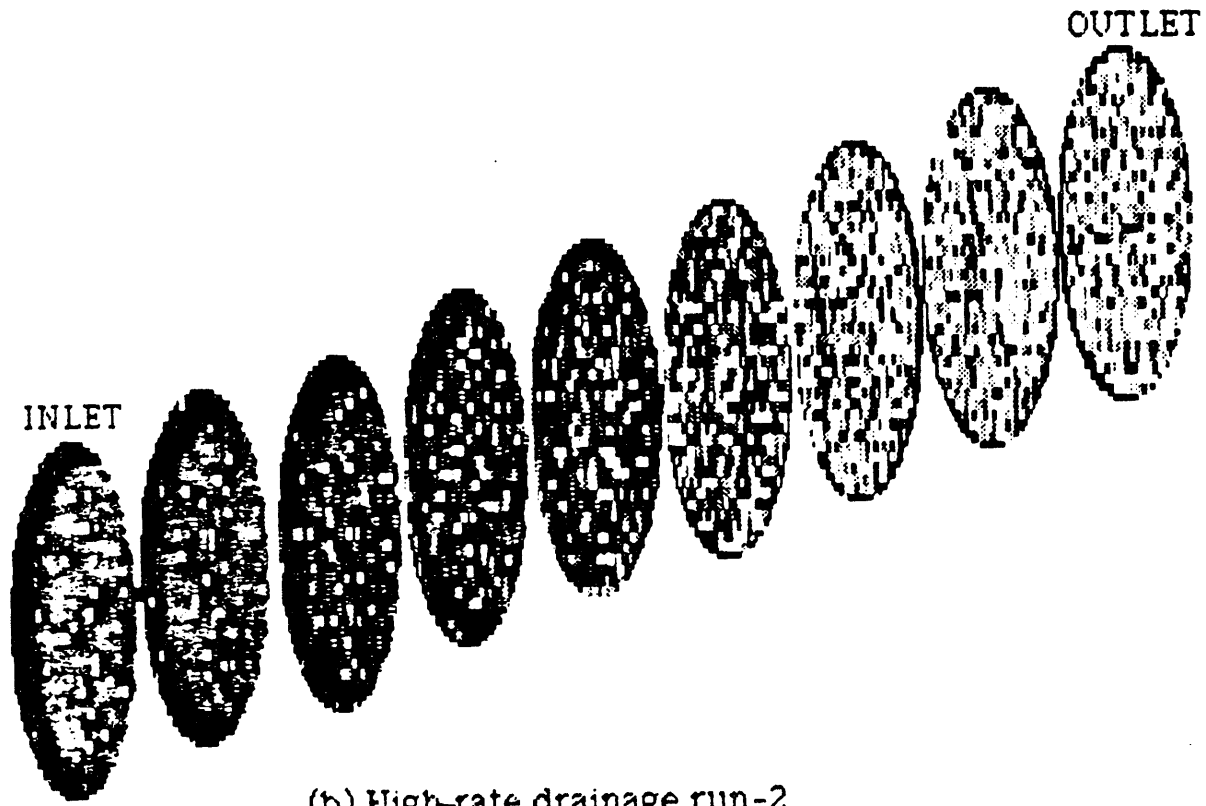

(b) High-rate drainage run-2

Figure 1.1.11 Comparison of saturation distributions between high-rate drainage runs 1 and 2.

2.1 KINETICS OF IN-SITU COMBUSTION
(D. D. Mamora)

2.1.1 ABSTRACT

Oxidation kinetics experiments for in-situ combustion with crude oil show two reaction peaks at about 250 °C (482 °F) and 400 °C (725 °F). Current oxidation reaction models are based on three oxidation reactions: low, medium, and high temperature oxidation (LTO, MTO and HTO, respectively).

Kinetics experiments with various crude oils lead to the conclusion the fuel is a hydrocarbon for HTO, and that the sand grain size (i.e., reaction surface area) affects the reaction kinetics. These experiments have led to the development of a new reaction model which includes two partially-overlapping, oxidation reactions: namely, low-temperature oxidation followed by high-temperature fuel oxidation. A new technique for analyzing the LTO reaction has been developed. For the fuel oxidation reaction, the new reaction model includes the effects of sand grain size and the atomic hydrogen-carbon ratio of the fuel. Results based on the new model are in good agreement with the experimental data.

2.1.2 INTRODUCTION AND PROGRESS TO DATE

A description of the oxidation kinetics experimental apparatus was given in the last annual report (Aziz et al., 1990). A typical experiment is conducted as follows. First, the instruments for measuring the gas rate, pressure, temperature and composition are calibrated. A sand mix of about 50 g sand, 2 g water, and 2 g oil is prepared, sand and water being mixed first. The resulting fractional oil and water saturations are about 0.19. The mix is tamped into the kinetics cell. The cell is placed in the electric furnace whose temperature is increased at about 60 °C/hr. Air is injected at a constant rate of about 1 liter/min. Backpressure is applied to maintain the cell pressure at about 80 psig. At the end of the run, the gas analyzers are recalibrated.

Kinetics experiments were carried out for Huntington Beach oil (18.5 °API) and Cold Lake bitumen (10 °API). In addition, kinetics runs were made for carbon, and a mixture of carbon and crude oil. Two sand packs of 20-30, and 100 mesh Ottawa sands were used to investigate the effect of sand grain size on the oxidation reaction kinetics.

Analysis of the kinetics data using the previous kinetics model was unsuccessful. Review of the current oxidation kinetics model and detailed analysis of the kinetics data were made. This led to the development of a new oxidation kinetics model, as described in Section 2.1.5.

2.1.3 THE PREVIOUS OXIDATION KINETICS MODEL

The previous model was introduced in 1981 (Fassihi, 1981), and has been used by subsequent workers (De los Rios, 1987 and Shallcross, 1989). A brief description of the model together with an example application (Fig. 2.1.1) is given in the following.

In the previous kinetics model, the following assumptions were made.

1. The oxygen consumption curve can be separated into three component curves corresponding to the low, medium and high-temperature oxidation reactions. Each of these reactions is assumed to be the oxidation of a particular fuel.

2. No carbon oxides are produced during LTO.
3. The fuel during HTO is carbon.

For each reaction, the rate (equated to the oxygen consumption rate) is given by:

$$\frac{q\ O_{2c}}{AL} = A_{r_i}\ P_{o_2}^{m_i}\ C_{f_i}^{n_i}\ \exp\ (-E_i/RT\ ) \qquad (2.1.1)$$

where q is the volumetric flowrate, O_{2c} is the concentration of the oxygen consumed, A and L are the cross-sectional area and length of the sand mix in the kinetics cell, A_r is the pre-Arrhenius constant, P_{o_2} is the oxygen partial pressure, C_f is the instantaneous fuel concentration, E is activation energy, R is the universal gas constant, T is the absolute temperature, m and n are the reaction orders in respect to P_{o_2} and C_f, respectively, and i is the index for either LTO, MTO or HTO.

Further, each reaction rate is proportional to the decrease in the fuel concentration:

$$\frac{q\ O_{2c}}{AL} = -\alpha\ \frac{dC_{f_i}}{dt} \qquad (2.1.2)$$

where α is a proportionality constant.

Equations 2.1.1 and 2.1.2 can be solved to yield Eq. 2.1.3, the boundary condition being $C_{f_i} = 0$ at time, $t = \infty$.

$$\frac{O_{2c}}{\left[\int_t^{\infty} O_{2c}\,dt\right]^{n_i}} = \beta_i\ \exp\ (-E_i/RT) \qquad (2.1.3)$$

where:

$$\beta_i = \left[\frac{q}{A}\right]^{n_i-1}\ \frac{A_{r_i}\ P_{O_2}^{m_i}}{\alpha^{n_i}} \qquad (2.1.4)$$

A graph of the natural logarithm of the left hand side of Eq. 2.1.3, the relative reaction rate, versus 1/T should yield a straight line with a slope of $-E_i/R$, and an intercept of ln β_i. The exponent, n_i, may be obtained by trial-and-error, or through non-linear regression. An example of an Arrhenius graph is shown in Fig. 2.1.1b.

Starting with E_H and β_H obtained for HTO, Eq. 2.1.3 may be used to calculate an approximate oxygen consumption curve, Curve I in Fig. 2.1.1c. Curve I may be subtracted from the experimental data to yield Curve II, the curve for MTO and LTO oxygen consumption (Fig. 2.1.1c). Assuming fuel for HTO to be carbon, the oxygen consumption may be represented by the equivalent carbon dioxide and carbon monoxide concentration curve, δ = CO + CO_2. Curve I may be subtracted from the δ curve to yield Curve III, the curve representing LTO and MTO. The assumption that carbon oxides are not produced for LTO implies that Curve III represents the oxygen consumption for MTO only. An Arrhenius graph based on Curve III should yield E_M and β_M for MTO. Subtracting Curve III from Curve II

should yield the oxygen consumption curve for LTO, from which E_L and β_L may be obtained. Superposition of Curve I, Curve II and the LTO curve should yield the total curve for the oxygen consumption for the three reactions (Fig. 2.1.1d).

2.1.4 PROBLEMS WITH THE PREVIOUS KINETICS MODEL

The experimental data were analyzed using the previous kinetics model. However, the following problems were encountered.

1. The Arrhenius graph for the HTO reaction did not yield a satisfactory straight line, even for the single-component fuel, carbon (Fig. 2.1.2). After reaching a maximum value, the slope of the graph becomes positive. Discussions with Shallcross (Shallcross, 1989) revealed that most of the data points after the maximum value in the Arrhenius graph (Fig. 2.1.1b) were considered to be spurious, and ignored. However, these represent a large number of data points corresponding to an oxygen consumption value of up to 20% of the the HTO peak. These data points could represent some kinetics behaviour not considered in the previous model.
2. It was also suspected that the assumption of carbon as the fuel for HTO was a rough approximation of the oxidation reaction. A kinetics run was therefore carried out for a sand mix containing Cold Lake bitumen and carbon. The results (Fig. 2.1.8a) indicate a separate carbon peak at about 450 °C compared to 400 °C for the HTO peak of the crude. The HTO peak for the Huntington Beach crude is about 420 °C (Fig. 2.1.10a). Further, the apparent hydrogen-carbon (H/C) ratios computed from the gas composition data were greater than 0.5 for HTO for the crudes analyzed, and not zero as would be the case if carbon were the fuel. This H/C ratio value is significant and can not be ignored.
3. Results from the graphs of apparent H/C ratio and the fraction of carbon monoxide to carbon oxidized for the crudes (Figs. 2.1.8b, 2.1.9b, 2.1.10b, 2.1.11b) indicate the following.

   (a) A fairly constant H/C ratio is observed after the first oxygen consumption peak. The HTO reaction may be considered to be the oxidation of a fuel consisting of a hydrocarbon with a certain H/C ratio.

   (b) The apparent H/C ratio increases to a fairly high value at low temperatures, indicating that a large amount of oxygen enters reactions which do not produce carbon oxides. Furthermore, the apparent H/C trend does not appear to indicate the existence of two separate postulated reactions, LTO and MTO.

   (c) The apparent H/C trend does support the conclusion that there are two basic oxidation reaction mechanisms: oxygen addition to the hydrocarbon with little carbon oxide generation, followed by high-temperature oxidation. Thus, one LTO reaction plus HTO appears adequate to explain the experimental results.

   (d) Figs. 2.1.8b, 2.1.9b, 2.1.10b and 2.1.11b also present m, the fraction of carbon gasified to carbon monoxide. This ratio ranges from about 0.4 for the LTO temperature range to 0.3 for HTO, and is fairly constant throughout the temperature range covered in these experiments. This observation also indicates that two oxidation reactions appear adequate to explain experimental results.

4. Researchers have found that an increase in the surface area of a porous medium increases LTO reactions (Drici and Vossoughi, 1985) and resulted in the consumption of more fuel (Shahani and Hansel, 1984; Vossoughi, et al., 1985). To investigate the effect of sand grain size on oxidation reactions, a kinetics run was made using Cold Lake bitumen and equal parts by weight of 20-30 and 100 mesh Ottawa sand. The results (Fig. 2.1.9a)

show a significant increase in the LTO reaction, with a marked decrease in the HTO reaction compared to the run made using only 20-30 mesh sand (Fig. 2.1.8a). The results are in qualitative agreement with the observations made by earlier researchers, except for the decrease in the HTO reaction. The salient point is that a proper model should incorporate the effects of sand grain size (i.e., the reaction surface area).

2.1.5 A NEW OXIDATION KINETICS MODEL

Based on the observations mentioned in the preceding section, the basis of a new oxidation kinetics model was formulated.

1. The oxidation of crude oil consists of two main stages: low-temperature oxidation, followed by high-temperature fuel oxidation. Thus the oxygen consumption curve may be separated into two, partially overlapping curves.
2. The fuel is a hydrocarbon which is characterized by a particular H/C ratio.
3. The sand grain size (i.e., the reaction surface area) affects the reaction kinetics. The oxidation sub-models are described in the following.

1. High Temperature Oxidation

Two models were studied, the simplest being the "spherical fuel geometry" model. Each model was tested against the results of a kinetics run (Fig. 2.1.4a) using carbon (60 mesh reagent grade) to minimize uncertainty with regard to fuel composition and activation energy. As expected, Fig. 2.1.4b shows the apparent H/C ratio for carbon to be zero.

1.1. Spherical Fuel Geometry Model

In this model, the fuel is assumed to be deposited evenly around the sand grains, which are assumed to be spheres of radius, r_s, as shown schematically in Fig. 2.1.6. At time, t_e, the fuel is completely oxidized. If r is the outer radius of the fuel at time t, the following expression is obtained (derivation is given in the Appendix).

$$\frac{q_i\, r_s\, O_{2c}}{2(1+\gamma)^{2/3}} = \beta \exp\left(-E/RT\right) \tag{2.1.5}$$

where:

$$\gamma = \frac{\int_t^{t_e} q_o\,(CO+CO_2)(12.011+x)dt}{60 \times 22.4138 AL(1-\phi)\rho_f} \tag{2.1.6}$$

$$\beta = 63.0413\ \alpha\, k_o^*\, P_{o_2}^m\, AL(1-\phi) \tag{2.1.7}$$

where k_o^* is the equilibrium constant, q_o is the effluent gas flowrate at standard conditions, CO and CO_2 are the carbon monoxide and carbon dioxide mol percent in the effluent gas, x is the apparent H/C ratio and ρ_f is the in-situ fuel density. A graph of the natural logarithm of the left hand side of Eq. 5 versus 1/T should yield straight line with a slope of -E/R and an intercept of ln β. However, a straight line relationship could not be found for the carbon data (Fig. 2.1.2). In fact, the data indicate a trend similar to that based on the previous kinetics model (Fig. 2.1.2). This is not surprising since the previous kinetics model in effect assumes a fixed reaction surface area which is encompassed in the fuel concentration exponent, n. The reaction surface area in the spherical fuel geometry model is also approximately constant.

It was concluded therefore that the fuel geometry in this sub-model was too simplified to account for the reaction surface area.

1.2. Varying Fuel Geometry Model

In this model, the fuel is not assumed to be evenly deposited around the sand grains. Instead the fuel surface changes in shape and area as depicted in Fig. 2.1.5.

At the start of fuel oxidation (time = t_o), the fuel at each grain contact region can be divided into two parts.

1. Fuel deposited directly on the grain surface, and
2. Fuel deposited at the grain contact, with its geometry approximated by a toroid of height, h_f.

The first part, being thinner and of larger surface area, would be oxidized quickly, so that from time t_c onwards, only the second part (the toroid) persists to time, t_e, when the fuel is completely oxidized. Graphs of the apparent H/C and m ratios for carbon are shown in Fig. 2.1.4b. The graph for calculated fuel height is shown in Fig. 2.1.4c.

The reaction rate for fuel in a toroid (Appendix) is:

$$\frac{q_i \, r_s \, O_{2c}}{2.7464\gamma^{3/4}} = \beta_o \exp\left(-E_o/RT\right) \tag{2.1.8}$$

where

$$\beta_o = 63.0413 \, \alpha \, k_o^* \, P_{o_2}^m \, AL \, (1-\phi) \tag{2.1.9}$$

A graph of the natural logarithm of the left hand side of Eq. 2.1.8 should yield a straight line with slope of $-E_o/R$ and an intercept of ln β_o in the period, t_c to t_e. Such a graph has been made for carbon data (Fig. 2.1.4d) which indicates that the data points fall on a straight line for 1/T less than/equal to about 0.00135 (i.e. t_c = 298 min.) from which E_o and β_o can be deduced. For 1/T greater than 0.00135, the data points follow a second straight line with a slope of -E/R and an intercept of ln β. The second straight line is due to the change in surface area from that of the toroid to that which includes fuel directly deposited on the sand grain surface. An expression for the second straight line is derived in the Appendix. The data points for 1/T greater than 0.00135 can be normalized so that all the data points fall on a single straight line (Fig. 2.1.4d).

To summarize, the reaction rate in the varying fuel geometry model is given by Eq. 2.1.8 with E_o and β_o for $t_c < t < t_e$ and E and β for $t_o < t < t_c$. The theoretical oxygen consumption curve based on the varying fuel geometry model can be computed (Appendix) and is shown in Fig. 2.1.4e. The results are in good agreement with the experimental data. Further, the activation energy for carbon obtained, 171 KJ/mol, agrees with that obtained by Butt, 1972 and Massoth, 1966 using thermogravimetric analysis, 150 - 170 KJ/mol.

The varying fuel geometry model was used to analyze fuel oxidation reactions for the two crude oils (Figs. 2.1.8a, 2.1.9a, 2.1.10a, 2.1.11a). Calculated apparent H/C and m ratios are shown in Figs. 2.1.8b, 2.1.9b, 2.1.10b, and 2.1.11b from which the average values for fuel oxidation reaction can be obtained. Figs. 2.1.8c, 2.1.9c, 2.1.10c and 2.1.11c show the calculated fuel height as a function of time. The relative reaction rate versus 1/T graphs are shown in Figs. 2.1.8d, 2.1.9d, 2.1.10d and 2.1.11d, indicating a good straight line fit of the data.

Subtracting the computed oxygen consumption curve from the data values yields the oxygen consumption curve for the low temperature reaction (Figs. 2.1.8e, 2.1.9e, 2.1.10e, 2.1.11e).

2. Low Temperature Oxidation

As described in Section 2.1.4 (item 3), the m-ratio remains fairly constant during LTO while the apparent H/C ratio decreases significantly to a value which remains fairly constant throughout HTO. For simplicity, these complex LTO reactions have been reduced to a single oxidation reaction of the hydrocarbons, at the end of which only fuel for HTO remains. Further, it is assumed that the reaction follows the Arrhenius reaction rate law with $C_f = 0$ at $t = 0$. Based on these assumptions, the equation for the LTO reaction rate is (Appendix):

$$\frac{O_{2c}}{\left[\int_o^t O_{2c}\, dt\right]^n} = \beta_f \exp\left(E_f/RT\right) \tag{2.1.10}$$

where

$$\beta_f = \left[\frac{q_i}{AL}\right]^{n-1} \frac{A_r\, P_{o_2}^m}{\alpha^n} \tag{2.1.11}$$

The exponent, n, is obtained by trial-and-error, so that a graph of the natural logarithm of the left hand side of Eq. 10 versus 1/T should yield a slope of E_f/R and intercept of ln β_f for the fitted line. Using the oxygen consumption data for LTO, as described in the previous section, such graphs were made for the crudes studied (Figs. 2.1.8f, 2.1.9f, 2.1.10f, 2.1.11f). These graphs show a linear fit of the data, from which E_f and β_f can be deduced. Using these parameters, the theoretical oxygen consumption curve for LTO reaction can be computed (Appendix). The results are shown in Figs. 2.1.8g, 2.1.9g, 2.1.10g and 2.1.11g, indicating a good fit of the experimental data. Summing, the theoretical curves for LTO and HTO yields the theoretical total oxygen consumption curve as shown in Figs. 2.1.8h, 2.1.9h, 2.1.10h and 2.1.11h, which indicates good agreement between the results of the model and data.

2.1.6 RESULTS AND CONCLUSIONS

1. The main differences between the previous and new oxidation kinetics models are summarized below.

Previous model	New model
a. Three reactions: LTO, MTO, HTO	a. Two reaction mechanisms: LTO and HTO.
b. Fuel at HTO is carbon	b. Fuel is a hydrocarbon of a particular H/C ratio
c. Reaction surface area not considered	c. Reaction surface area incorporated in HTO

2. Kinetics parameters obtained for the crudes studied, based on the new oxidation kinetics model, are given in Table 2.1.1.

   Except for Cold Lake Run No. 2, oxygen consumed was calculated using Eq. A.1, in which it was assumed that only carbon oxides and water are reaction products. The resulting apparent H/C ratios tend to be lower than expected values. This approximate method was also used by past researchers. For Cold Lake Run No. 2, the oxygen consumed was based on Eq. A.5, which utilizes the produced nitrogen content and is more accurate.

   For Cold Lake Run No. 3, equal parts by weight of 20-30 and 100 mesh sand were used. Porosity and r_s values for 20-30 mesh sand were used, so that E and β obtained are incorrect. This run was meant to illustrate the effect of reaction surface area on reaction kinetics.

3. Additional data are required as input in the new kinetics model, namely the porosity and dimensions of the sand mix, the fuel density, average H/C and m ratios. Estimated porosity and fuel density values have been used so far, and measured values of these parameters will be used in the future.

4. The new oxidation kinetics model describes the physics of the reaction reasonably and enables a better insight into the reaction kinetics than was previously possible.

2.1.7 FUTURE WORK

1. Additional kinetics experiments will be run which will cover a wide range of crude oil gravities. Some of the experiments to date will be repeated to test and refine the new model. In future kinetics runs, a slower temperature schedule of about 40 °C/hr (instead of 60°) will be used to minimize temperature humps which tend to complicate the results. Oxygen consumption calculations will be based on Eq. A-5.

2. Kinetics experiments will be carried out using various oxygen concentrations and pressures.

3. Kinetics experiments using a recently constructed titanium cell will be run to determine the change in mass of the crude with temperature. The titanium cell will enable determination of the porosity of the sand mix using the CAT scanner. The change in H/C

ratio with temperature will be evaluated by subjecting samples of the sand mix to analysis using an elemental analyzer. The crude density change with temperature will also be measured. HPLC analysis will be made to determine the change in crude composition with temperature.

4. To understand the physical changes that occur to crude oil during in-situ combustion, combustion tube runs will be made which will be quenched. The sand mix will be cored and analyzed for the hydrocarbon H/C ratio and density along the combustion tube.

5. The new oxidation kinetics model has confirmed the importance of the H/C ratio in kinetics reactions. Research will be carried out aimed at obtaining a correlation between crude oil gravity, H/C ratio and heat of combustion using the Universal-Oil-Product constant or UOP K-factor (Hougen, et al. 1954) as the correlating parameter. Results of the kinetics and combustion tube experiments will be compared, where possible.

Table 2.1.1: Results of Kinetics Experiments

			HTO		LTO		
	H/C	m	E_o (KJ/mol)	β_o (1/sec)	E_f (KJ/mol)	β_f (1/sec)	n
Carbon	0	0.3	171×10^3	5.1×10^9	-	-	-
Cold Lake No. 1	0.5	0.3	187×10^3	9.8×10^{11}	82×10^3	2.9×10^{-12}	1.2
Cold Lake No. 2	0.9	0.3	146×10^3	6.0×10^8	94×10^3	6.8×10^{-15}	2.0
Cold Lake No. 3	0	0.3	255×10^3	3.4×10^{17}	94×10^3	5.2×10^{-14}	1.6
Huntington	0.45	0.29	142×10^3	3.0×10^8	83×10^3	9.6×10^{-13}	1.5

Cold Lake No. 1: 20-30 mesh sand
Cold Lake No. 2: 20-30 mesh sand
Cold Lake No. 3: 20-30 and 100 mesh sand

Table 2.1.2: Sieve Analysis of 20-30 Ottawa Sand

U.S. Std. sieve no.	wt. %	Sieve size (cm)	Grain size (cm)
16	0.002	0.1180	-
20	3.381	0.0850	0.1015
25	68.897	0.0710	0.0780
30	25.207	0.0600	0.0655
35	1.791	0.0495	0.0548
40	0.278	0.0425	0.0460
45	0.186	0.0355	0.0390
50	0.122	0.0295	0.0325
60	0.051	0.0250	0.0273
>60	0.085	-	-

Mean grain size = 0.0750 cm
Av.grain radius, r_s = 0.0375 cm

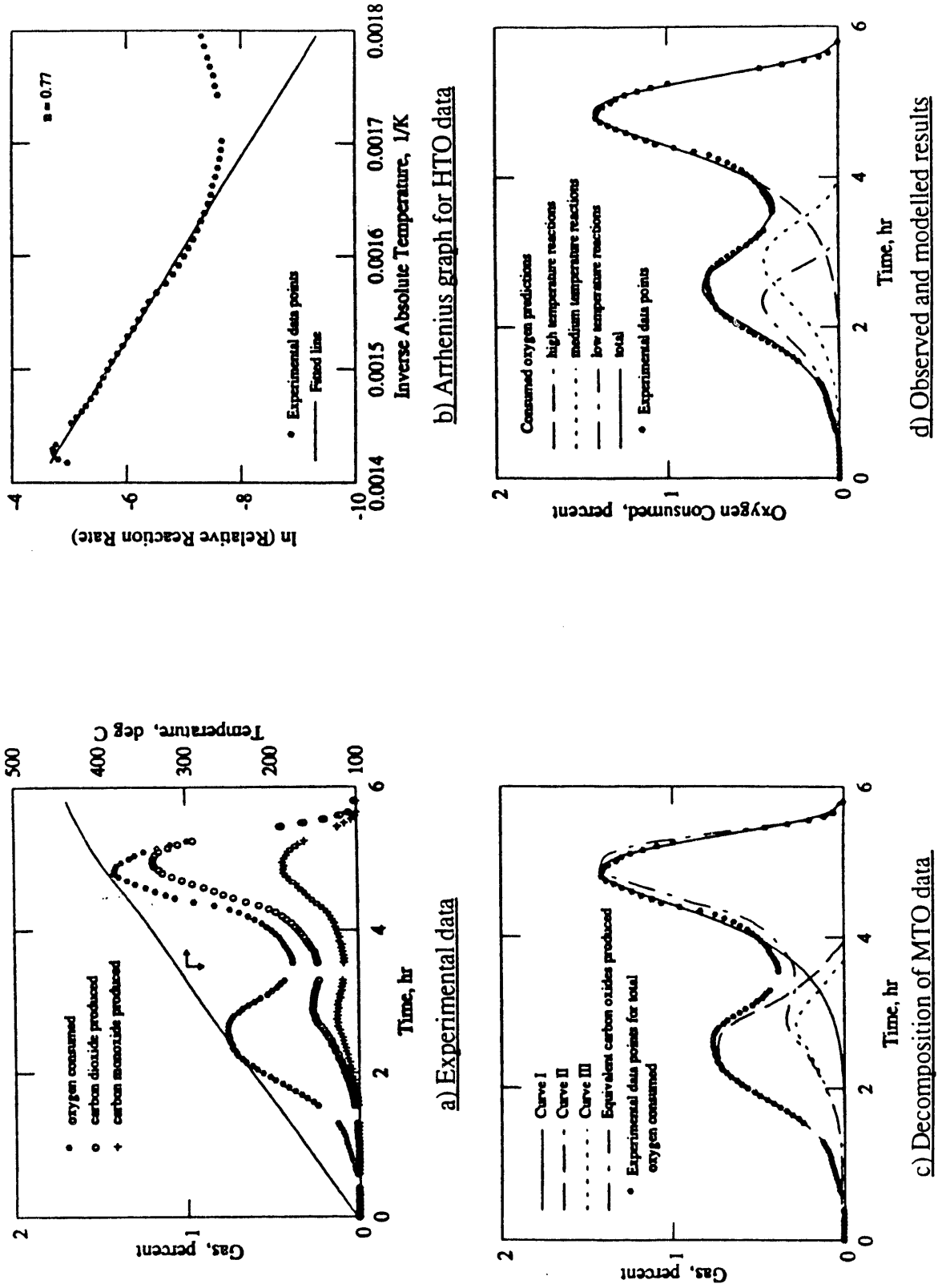

Figure 2.1.1a-d Huntington beach oil-analysis using previous kinetics model (Shallcross, 1989).

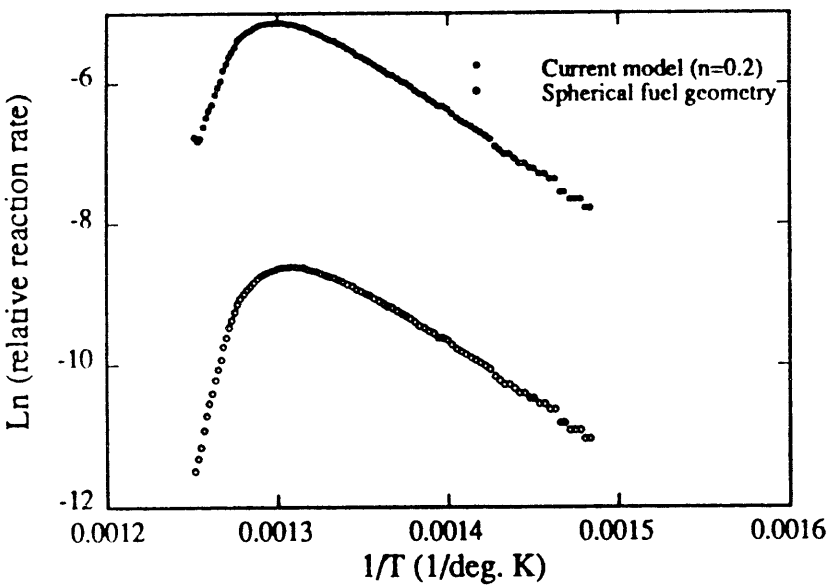

Figure 2.1.2 Carbon-Arrhenius graphs for HTO.

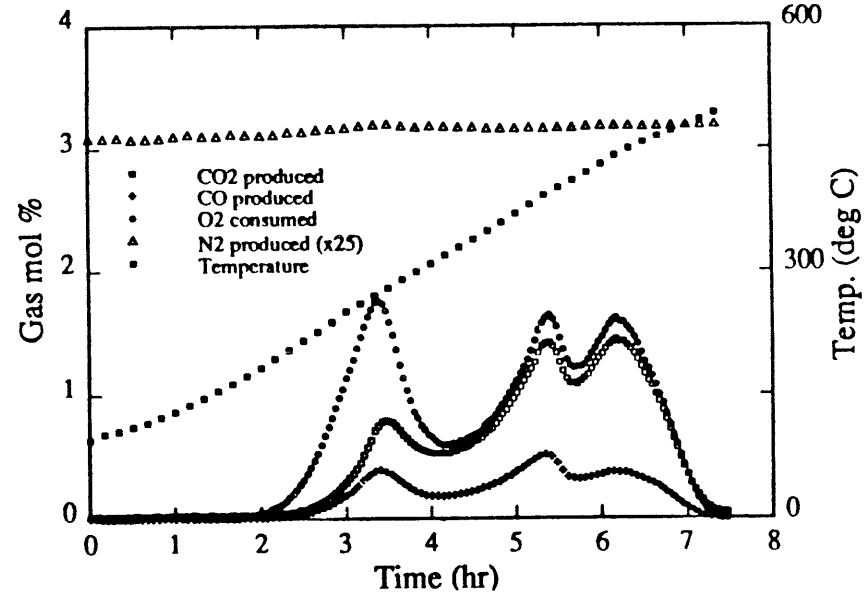

Figure 2.1.3 Cold Lake bitumen and carbon-experimental data.

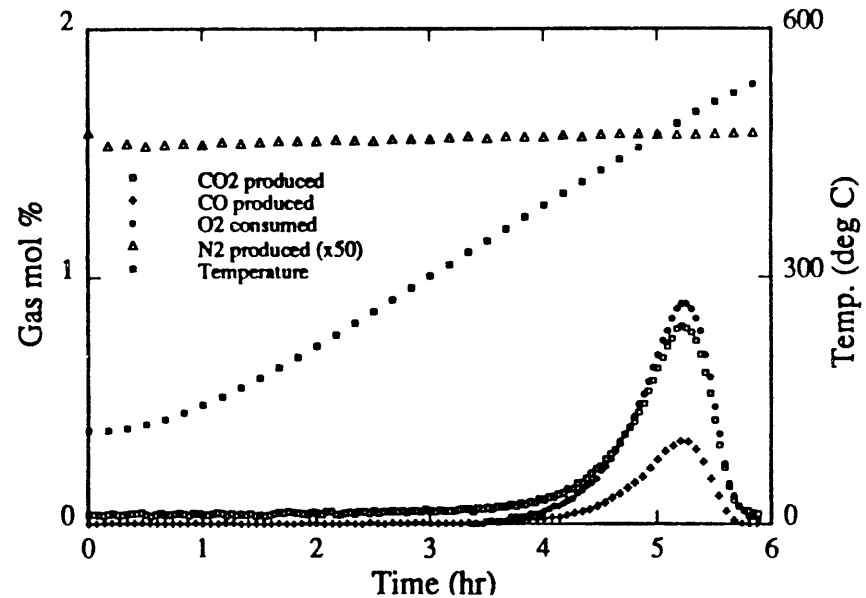

Figure 2.1.4a Carbon-analysis using new model.

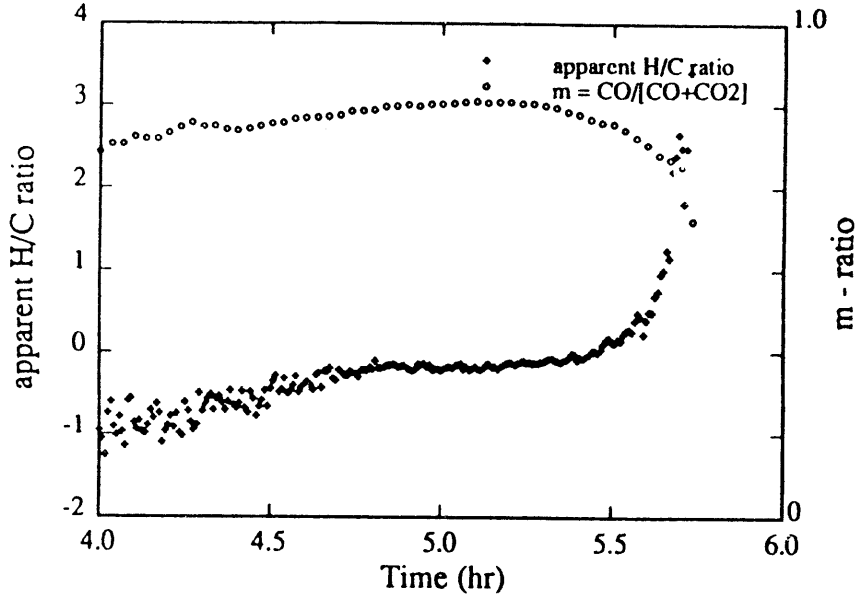

b) H/C and m-ratios versus time

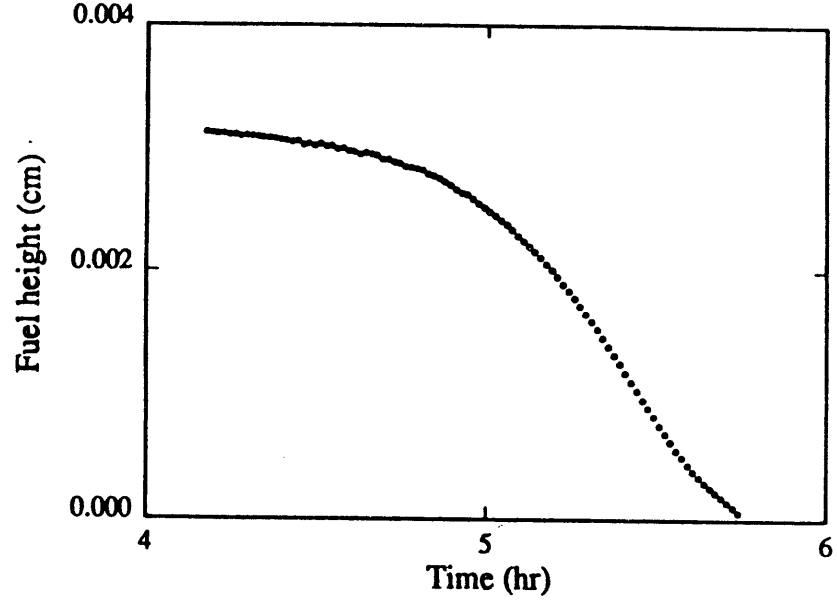

c) Fuel height versus time

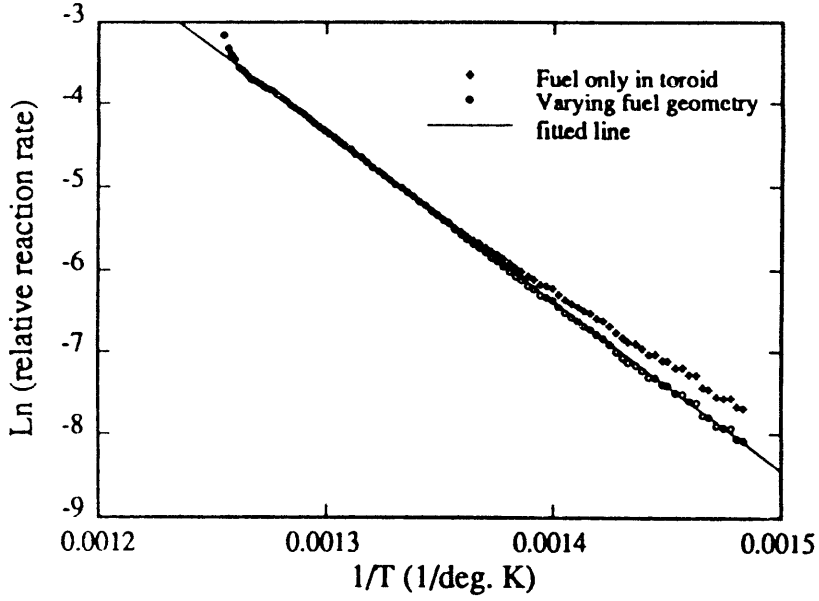

d) Arrhenius graph for HTO data

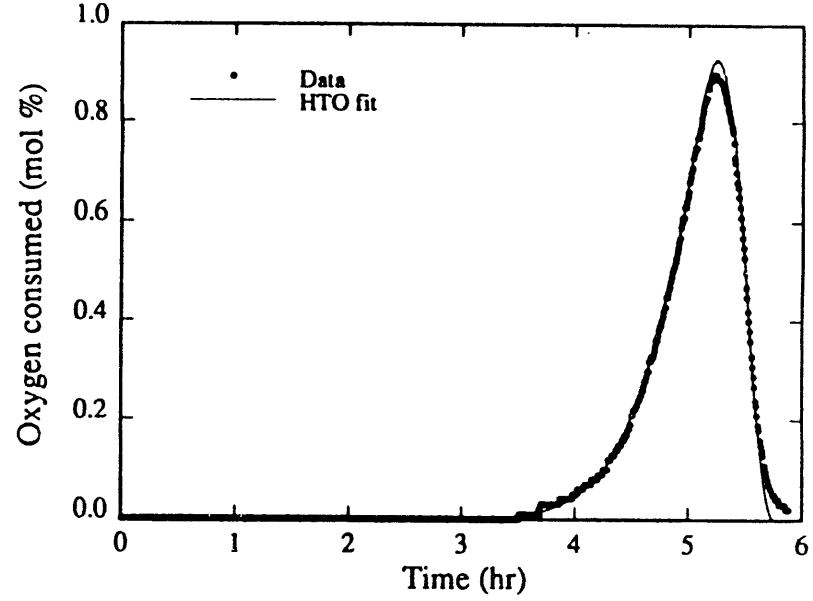

e) Observed and modelled results

Figure 2.1.4b-e Carbon-analysis using new model.

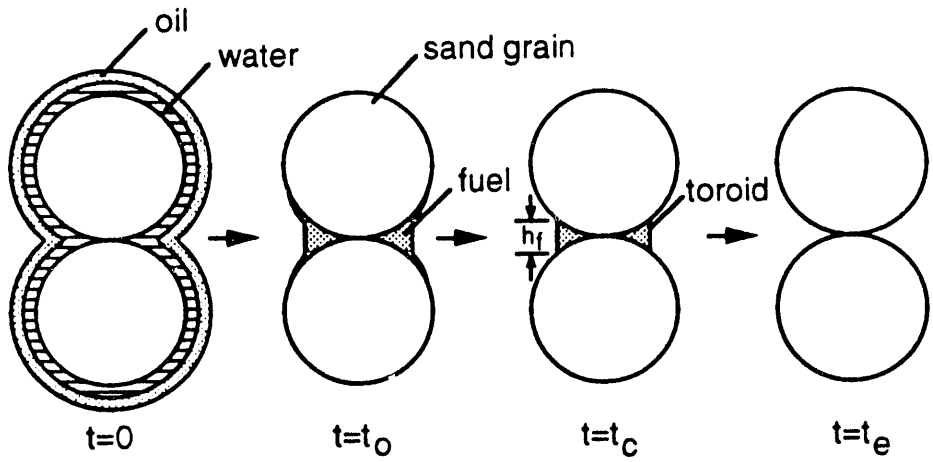

Figure 2.1.5 Schematic of varying fuel geometry model.

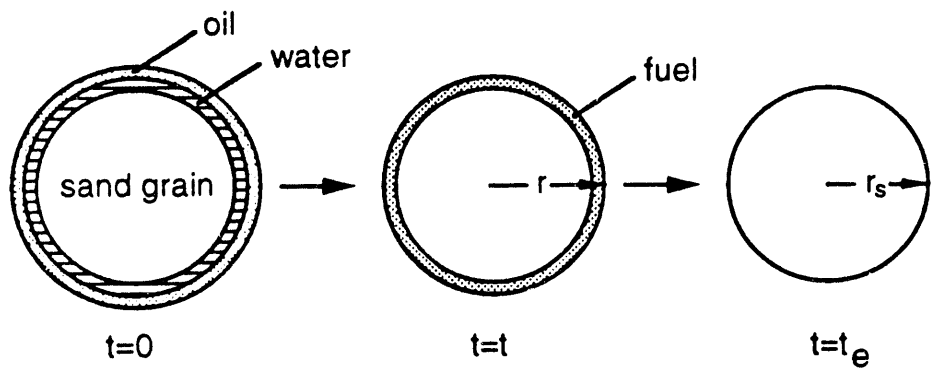

Figure 2.1.6 Schematic of spherical fuel geometry model.

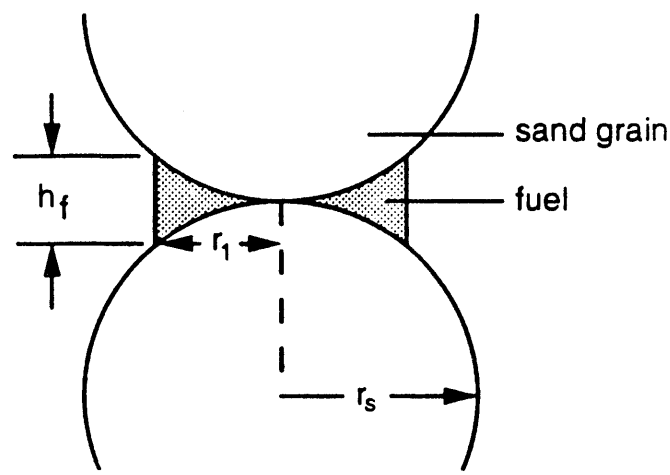

Figure 2.1.7 Toroid geometry of fuel.

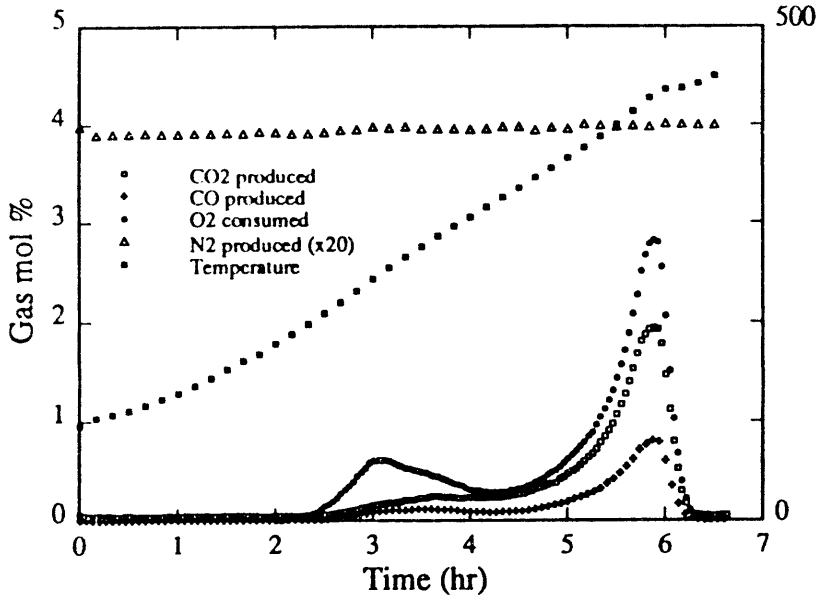

a) Experimental data

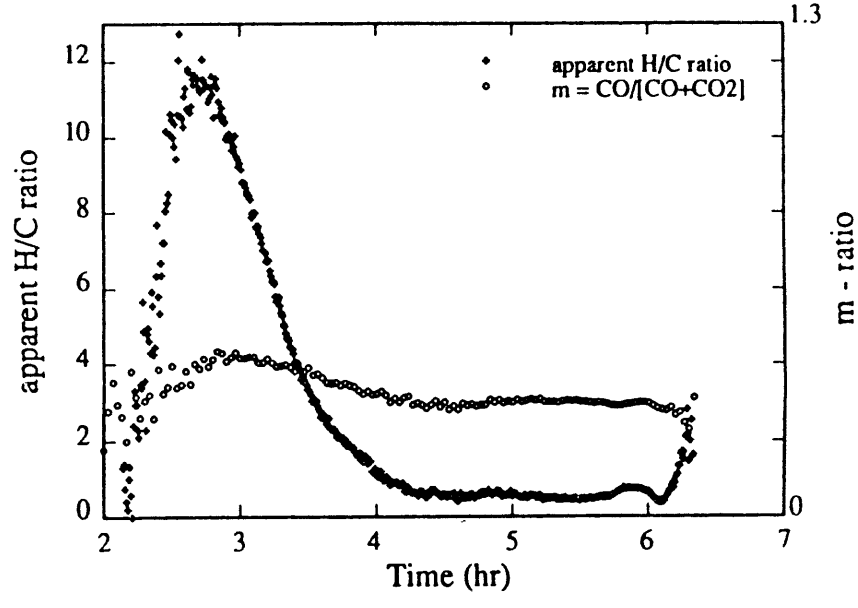

b) H/C and m-ratios versus time

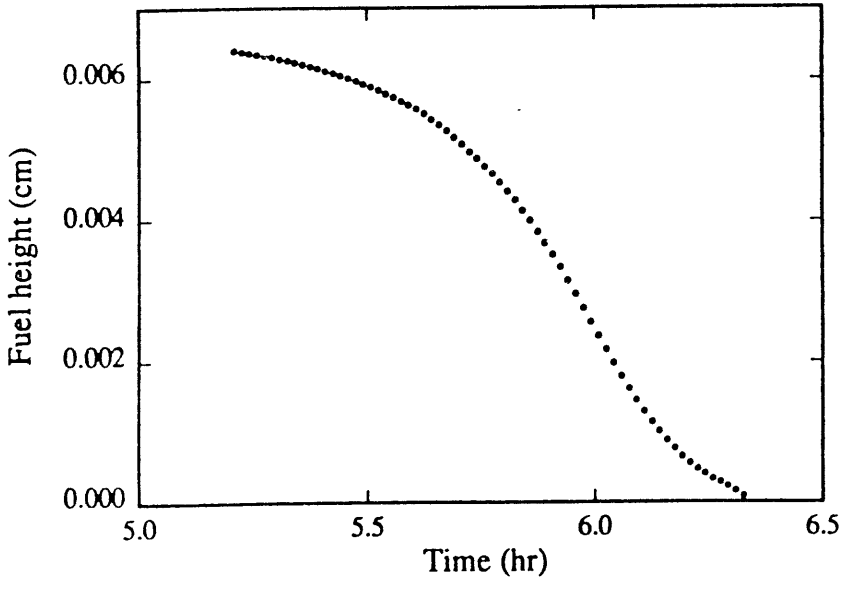

c) Fuel height versus time

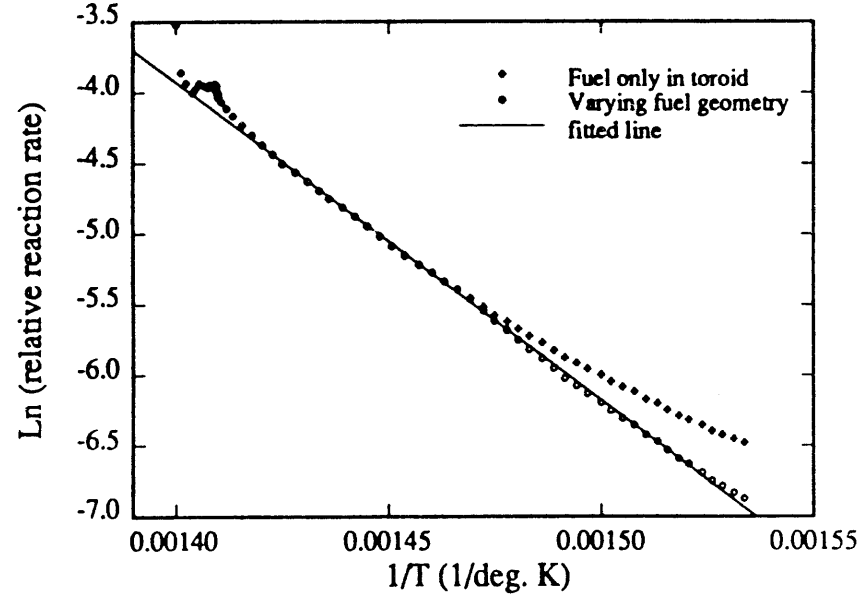

d) Arrhenius graph for HTO data

Figure 2.1.8a-d Cold Lake bitumen No. 1 - analysis using new model.

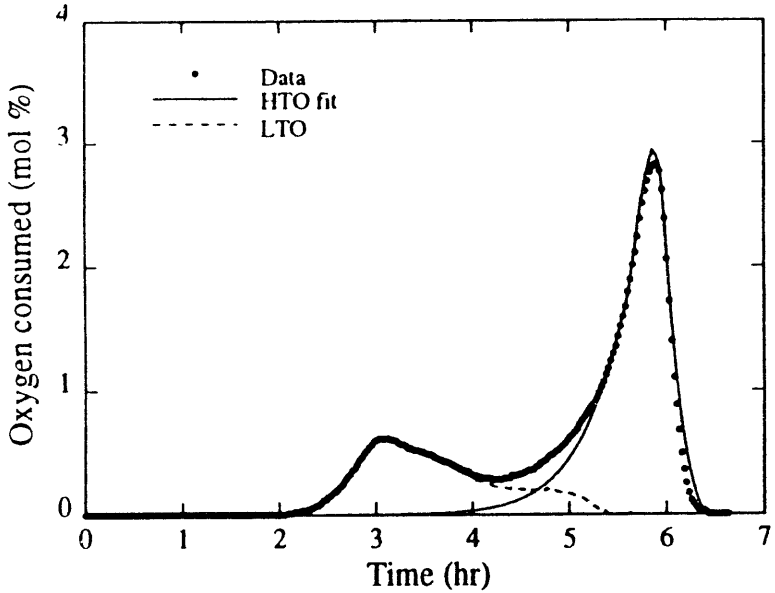

e) HTO modelled results

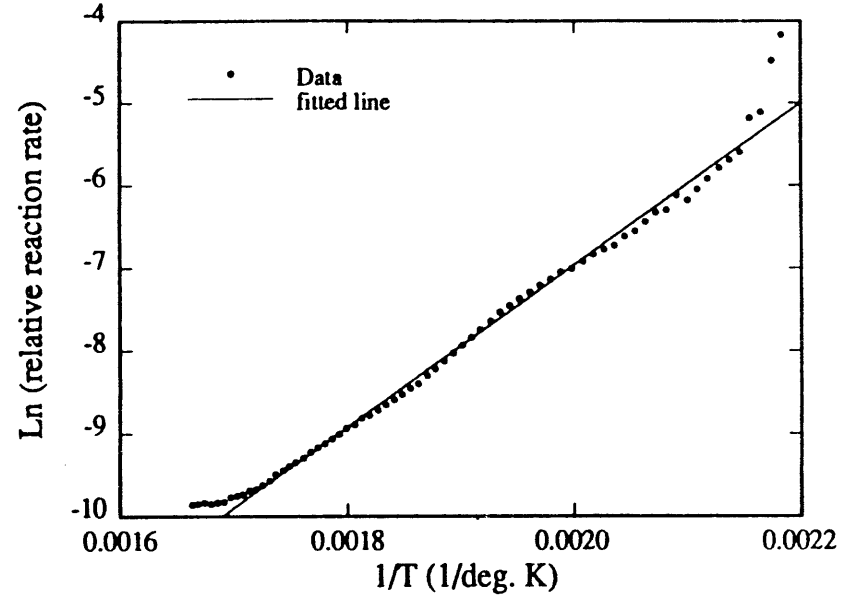

f) Arrhenius graph for LTO data

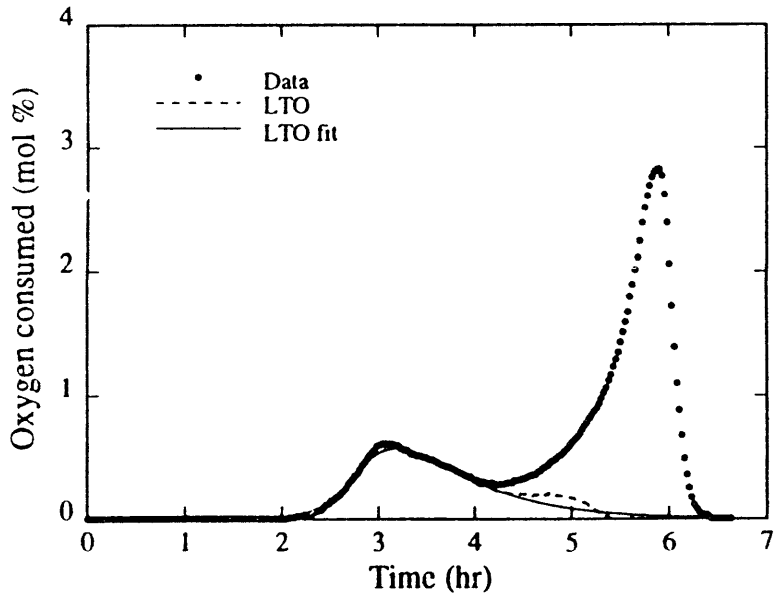

g) LTO modelled results

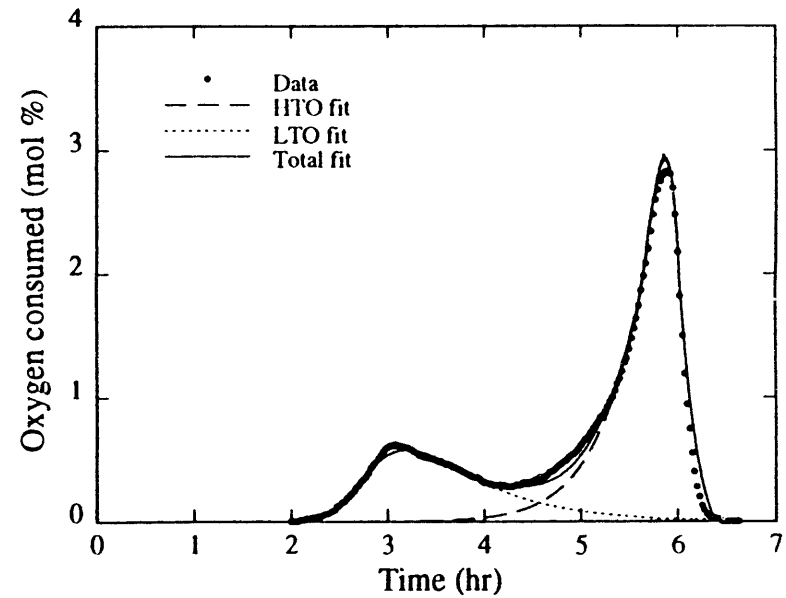

h) Observed and modelled results

Figure 2.1.8e-h Cold Lake bitumen No. 1 - analysis using new model.

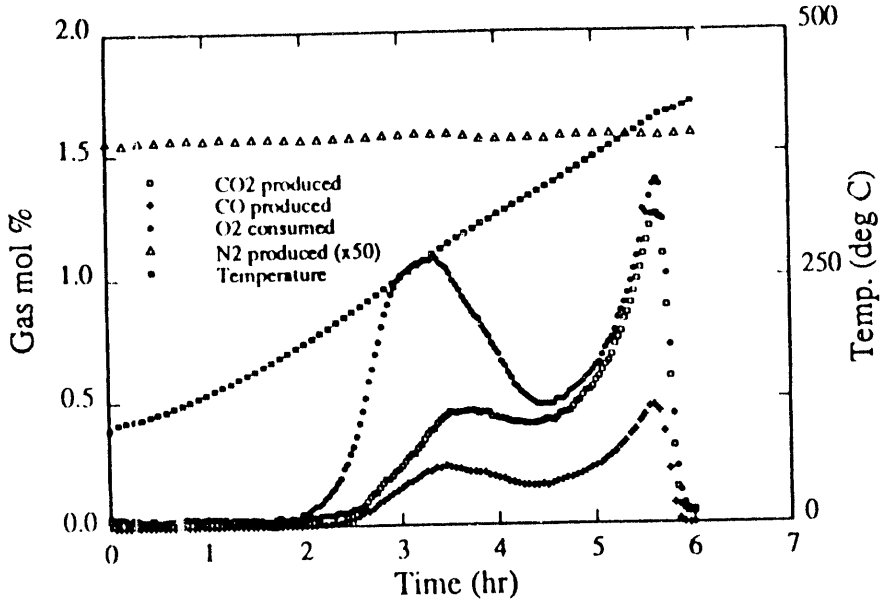

a) Experimental data

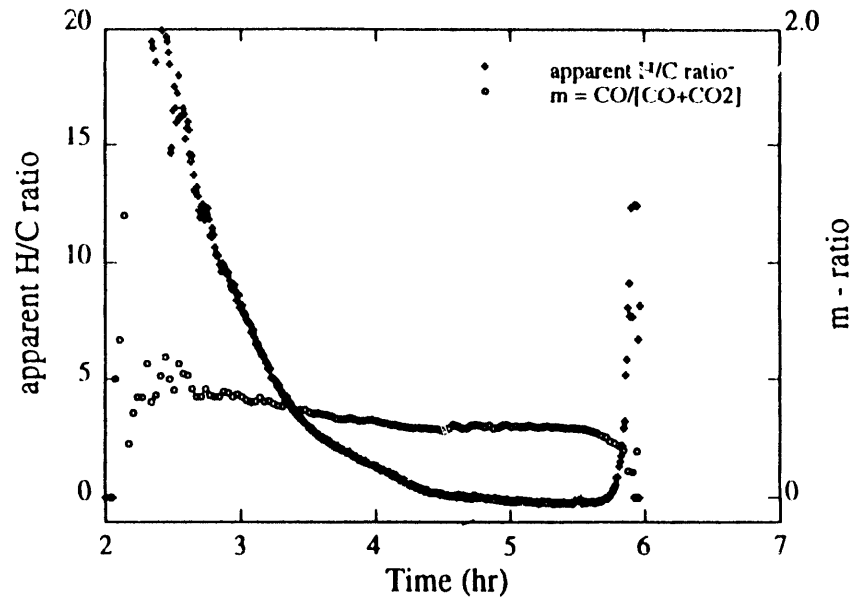

b) H/C and m-ratios versus time

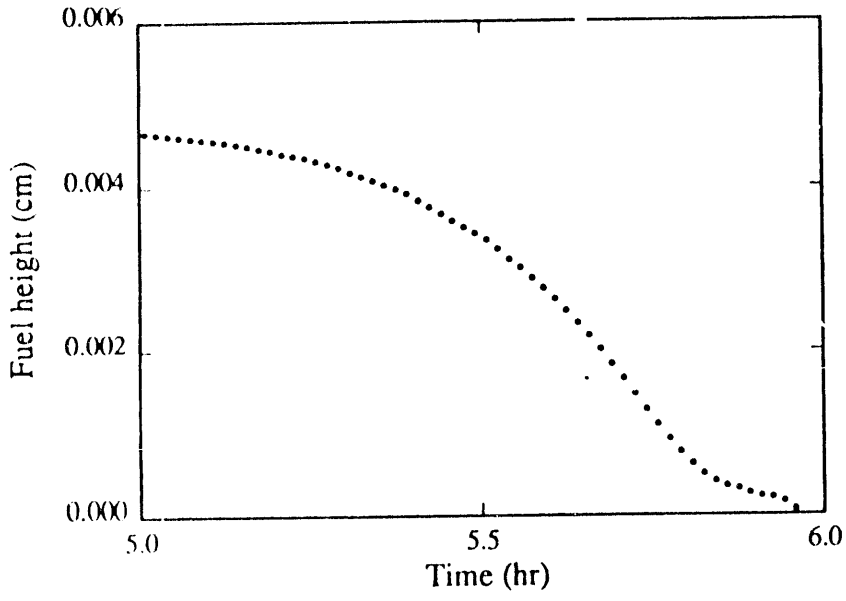

c) Fuel height versus time

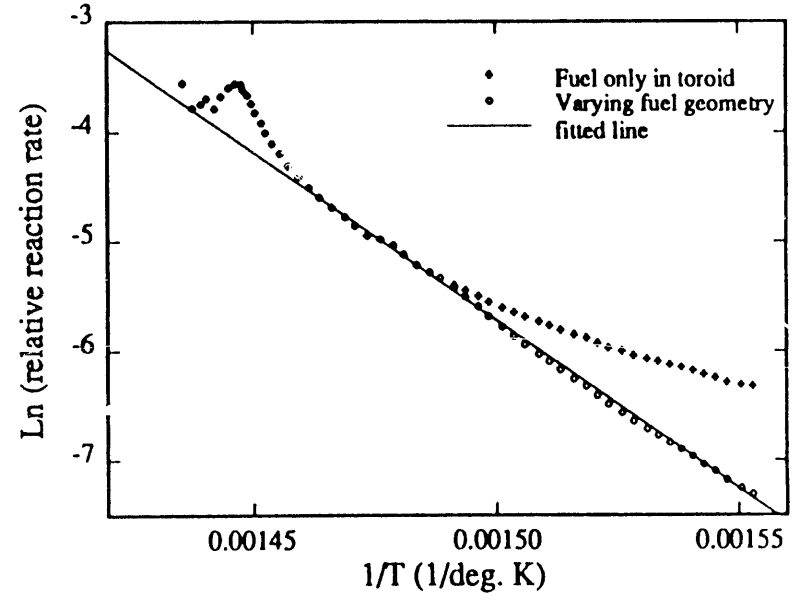

d) Arrhenius graph for HTO data

Figure 2.1.9a-d Cold Lake bitumen No. 3 (mixed sand) - analysis using new model.

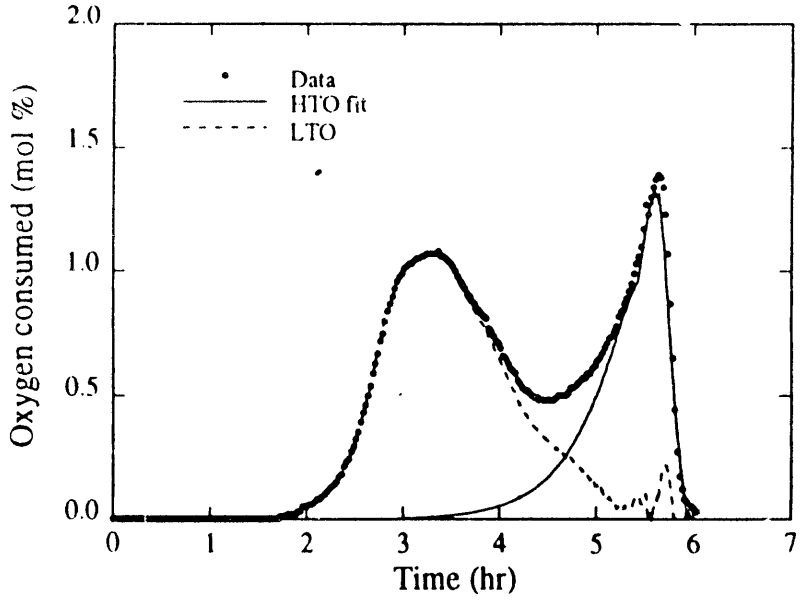

e) HTO modelled results

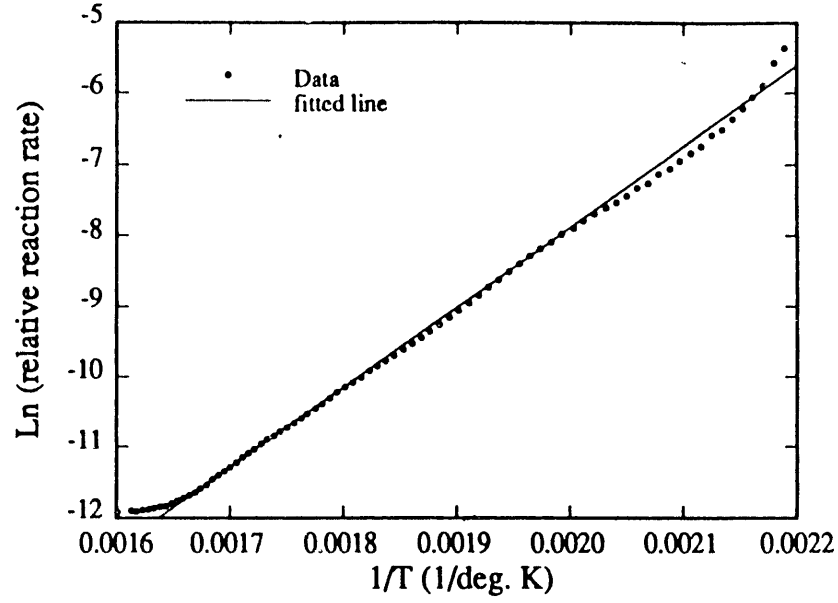

f) Arrhenius graph for LTO data

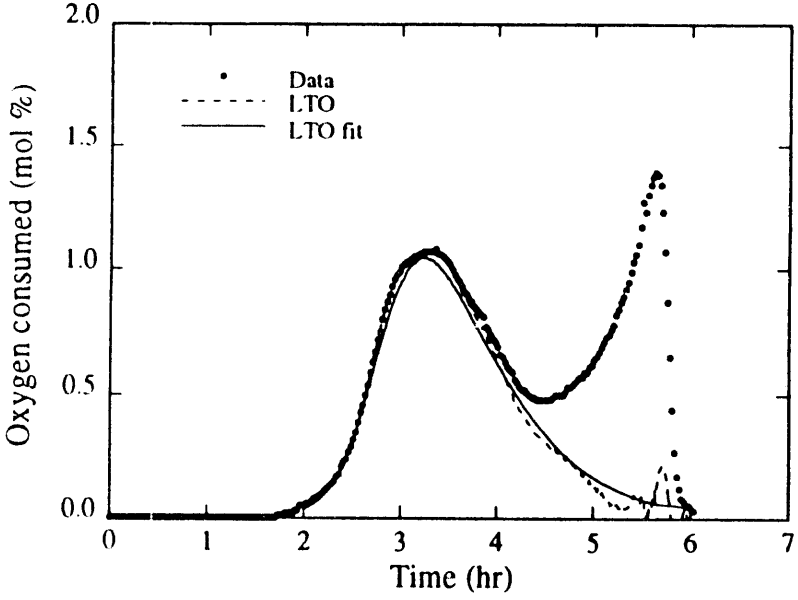

g) LTO modelled results

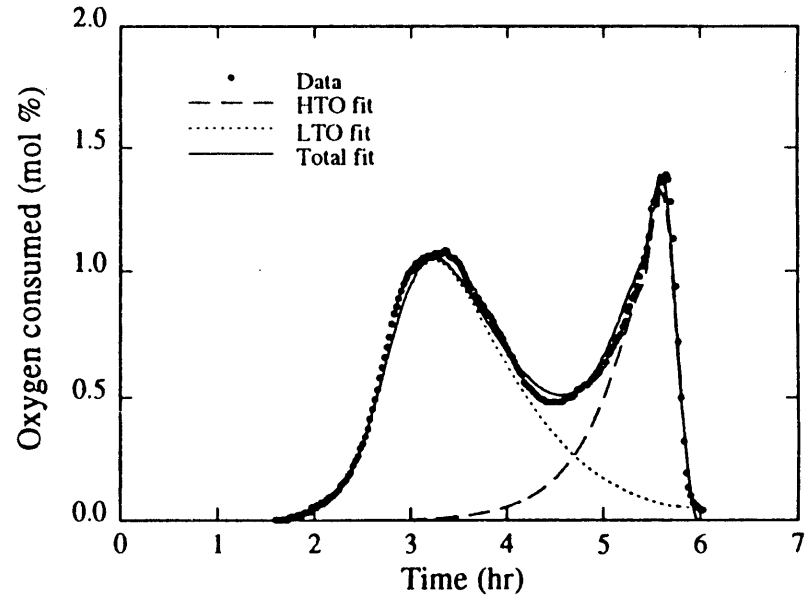

h) Observed and modelled results)

Figure 2.1.9e-h Cold Lake bitumen No. 3 (mixed sand) - analysis using new model.

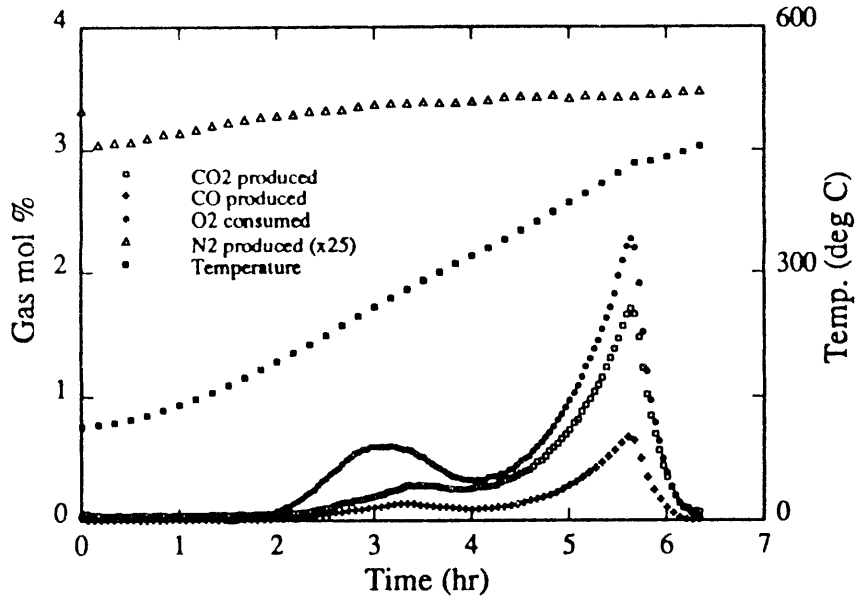

a) Experimental data

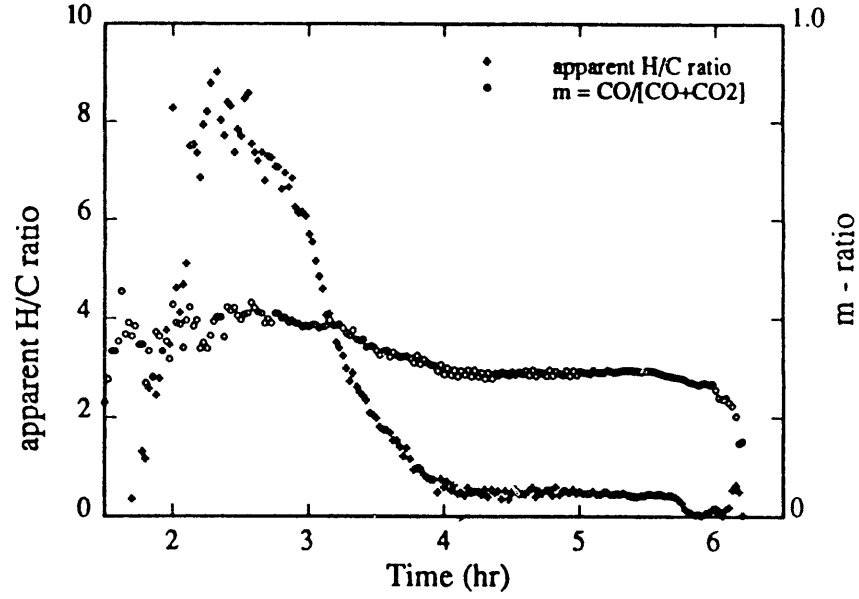

b) H/C and m-ratios versus time

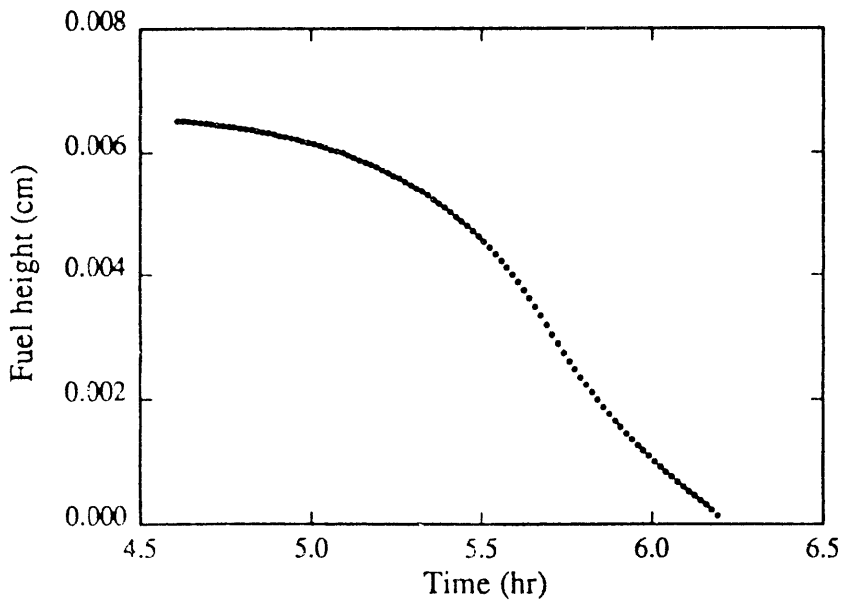

c) Fuel height versus time

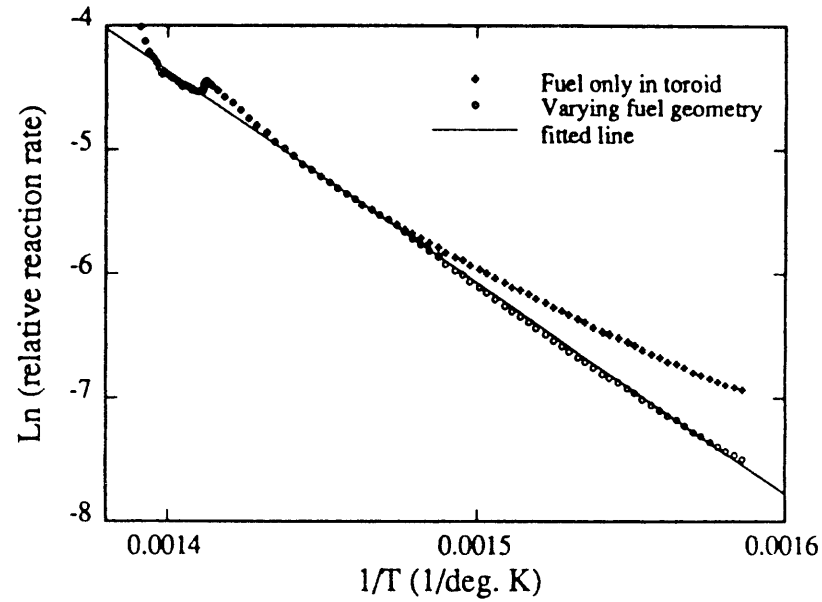

d) Arrhenius graph for HTO data

Figure 2.1.10a-d Huntington Beach oil - analysis using new model.

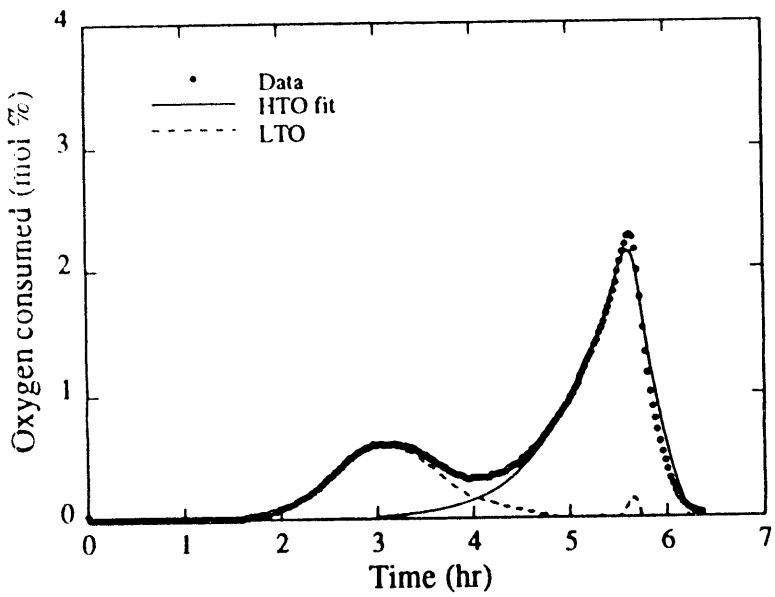

e) HTO modelled results

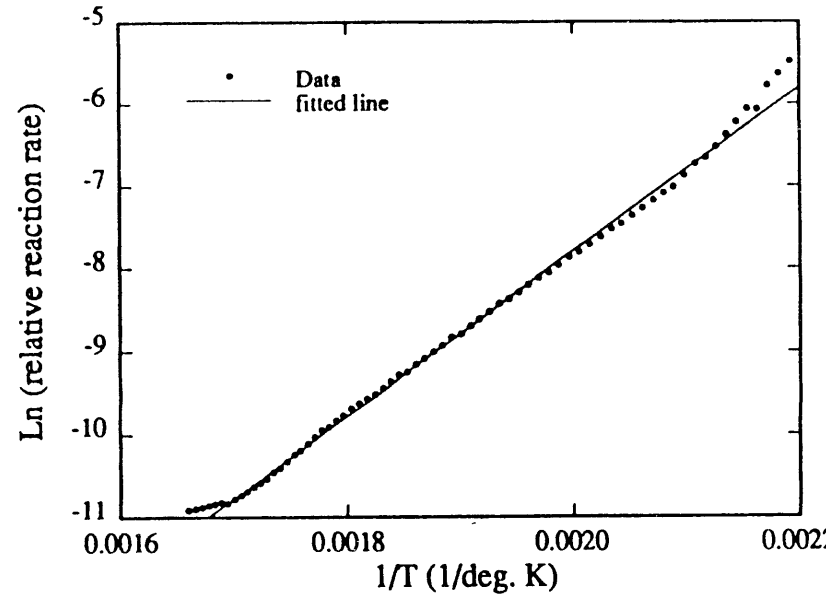

f) Arrhenius graph for LTO data

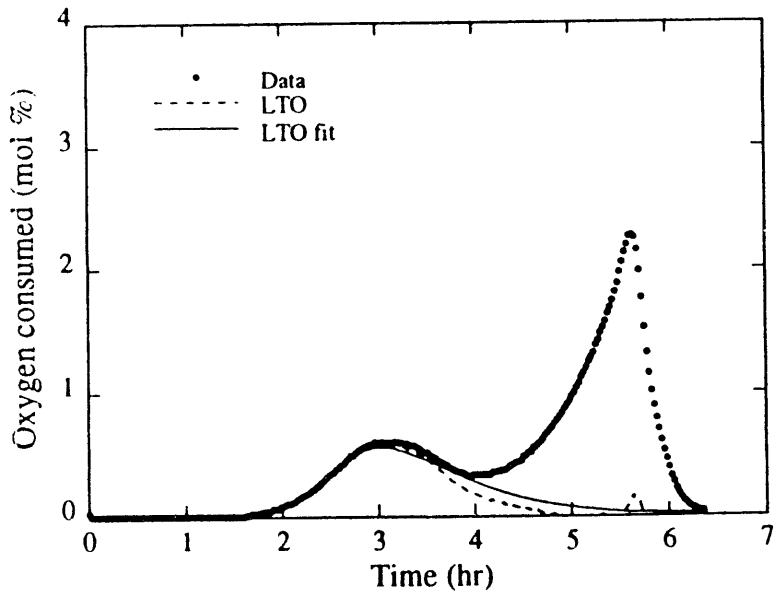

g) LTO modelled results

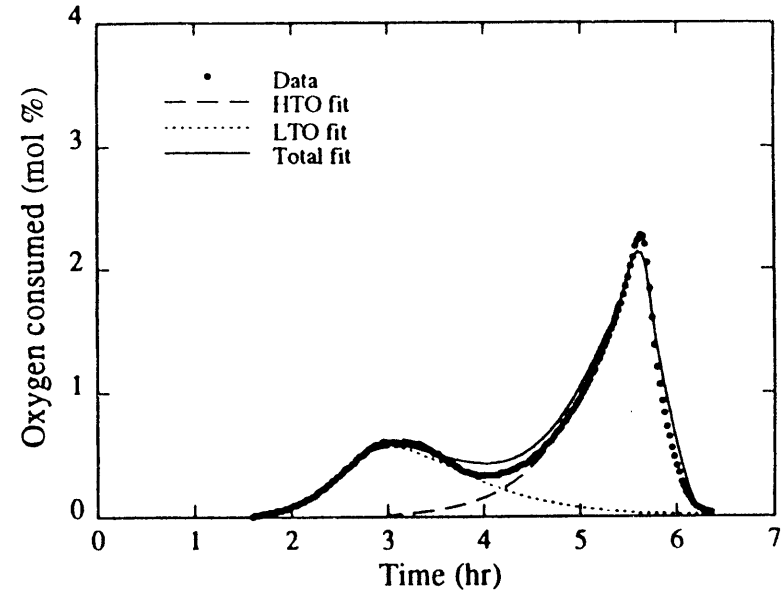

h) Observed and modelled results)

Figure 2.1.10e-h Huntington Beach oil - analysis using new model.

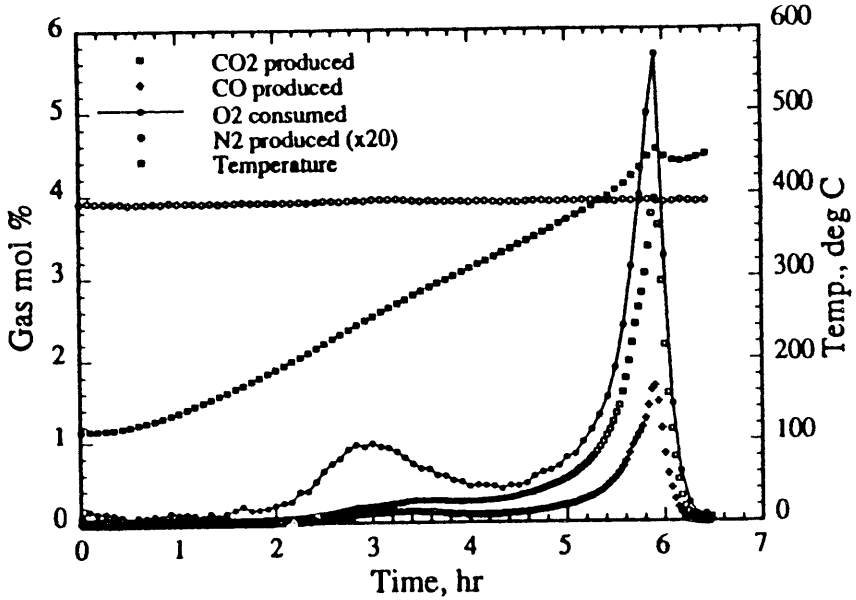

a) Experimental data

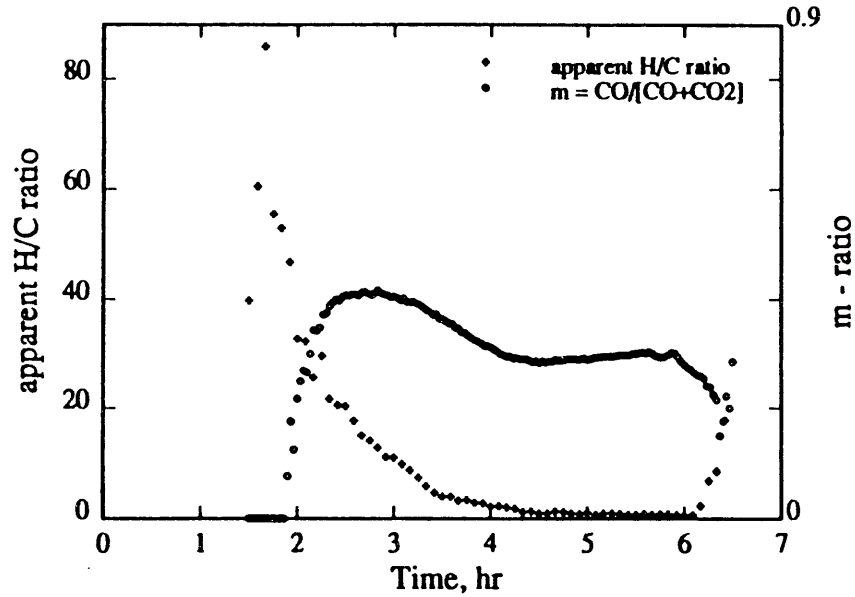

b) H/C and m-ratios versus time

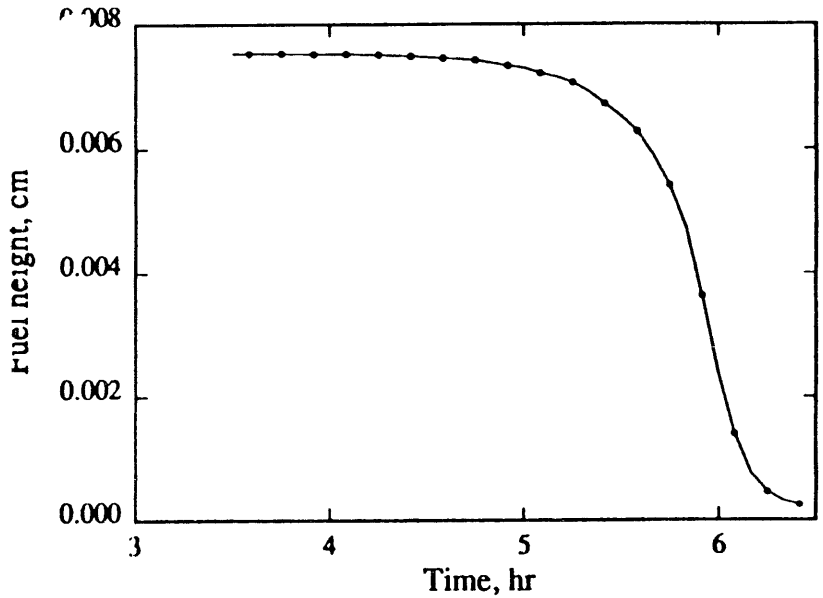

c) Fuel height versus time

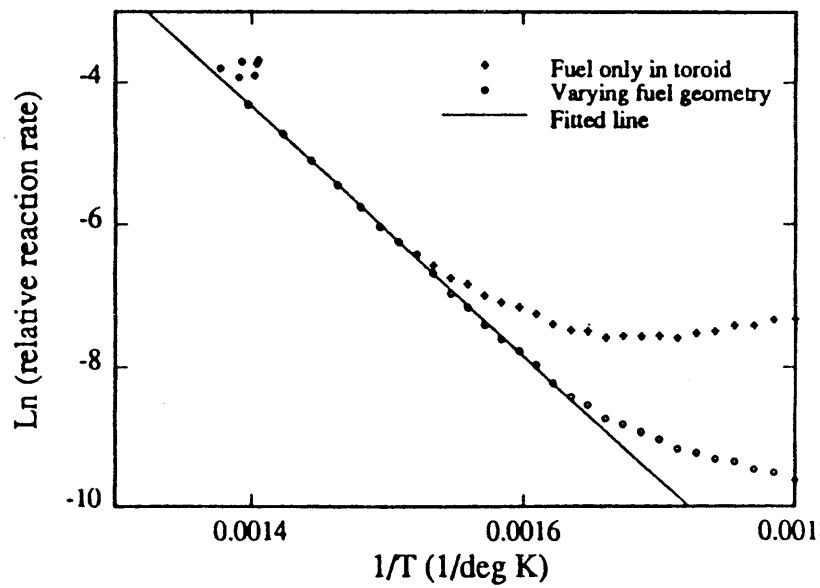

d) Arrhenius graph for HTO data

Figure 2.1.11a-d Cold Lake bitumen No. 2 - analysis using new model.

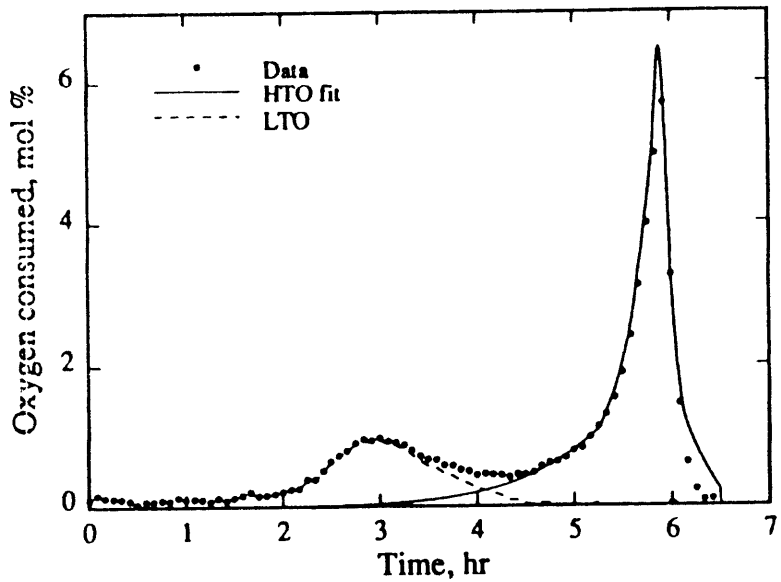

e) HTO modelled results

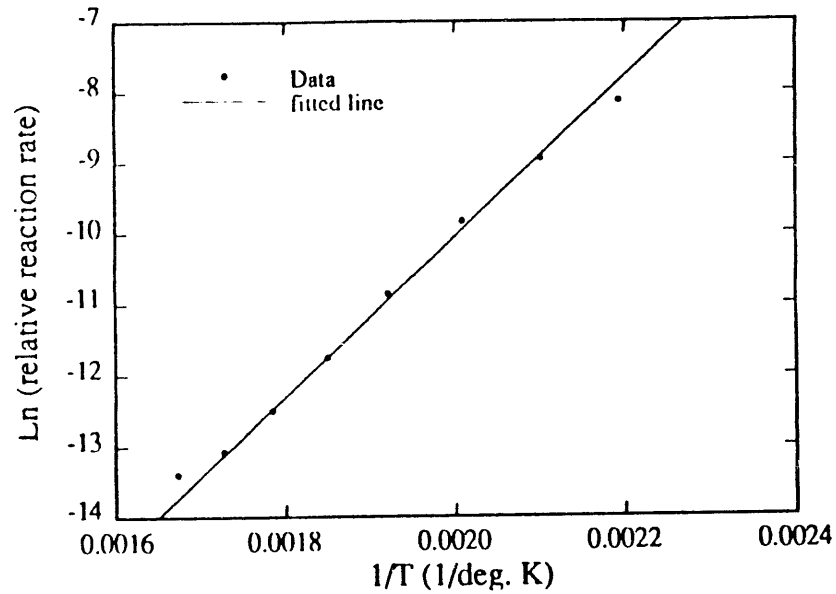

f) Arrhenius graph for LTO data

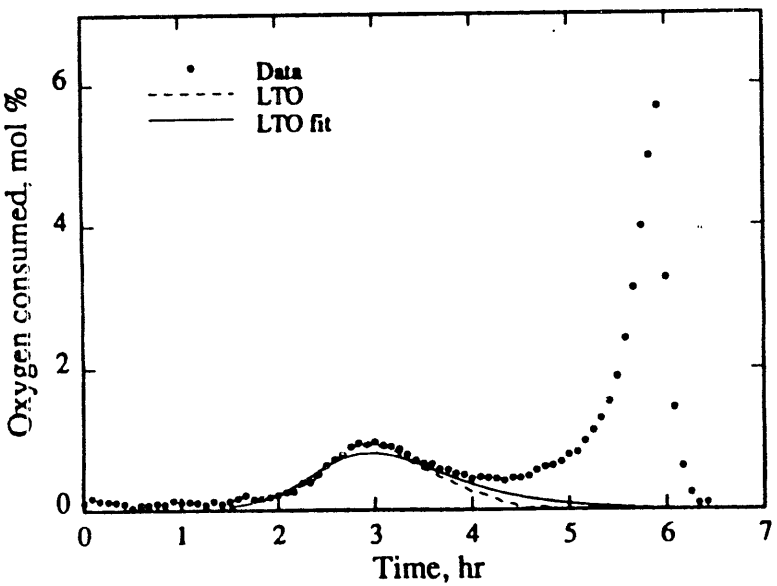

g) LTO modelled results

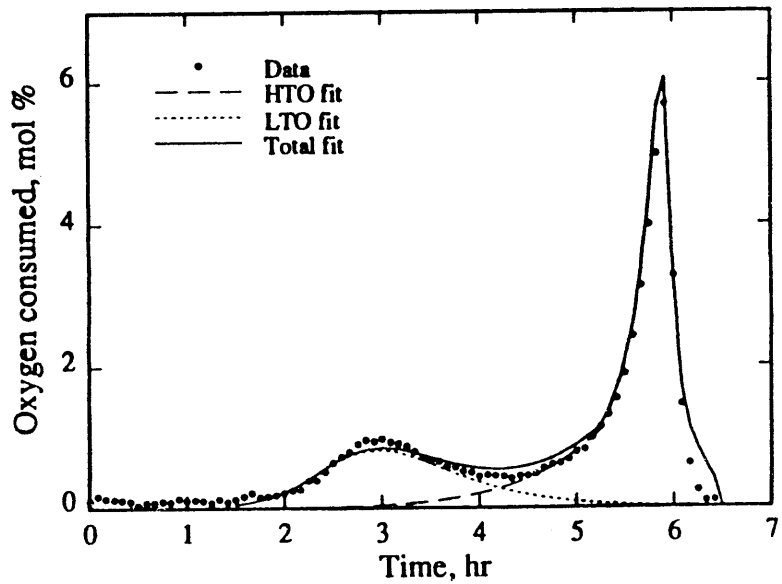

h) Observed and modelled results

Figure 2.1.11e-h Cold Lake bitumen No. 2 - analysis using new model.

2.2 INSITU COMBUSTION WITH METALLIC ADDITIVES
(R.J. Holt)

2.2.1 ABSTRACT

In-situ combustion is the most energy efficient of the thermal recovery methods. In light oil reservoirs, too little fuel may be deposited thus making combustion impossible while in heavy oil reservoirs too much fuel may be deposited thus ruining the economics of the process. A research program has been initiated to attack these problems. Water-soluble metallic additives were tested to modify fuel deposition.

In a previous paper (Shallcross, et al. 1991), results were reported from kinetics experiments run on Huntington Beach, California and Hamaca, Venezuela crude oils in the presence of aqueous solutions of metallic salts. While the presence of copper, nickel and cadmium had little or no effect; iron, tin, zinc and aluminum increased fuel concentration for Huntington Beach oil. The results were similar for the heavier Hamaca oil.

This chapter describes thirteen combustion tube runs using four different crudes. In addition to the two crude oils, a 12° API and a 34° API Californian oil were tested. The metallic additives iron, tin and zinc improved the combustion efficiency in all cases. Fluctuations in the produced gas were observed in all control runs, but disappeared with the iron and tin additives. The front velocities were increased by the metallic additives. Changes were also observed in H/C ratio of the fuel, heat of combustion, air requirements and density of the crude produced. The amount of fuel deposited varied between the oils. For Huntington Beach oil, the amount of fuel increased in the order: zinc, control, tin and iron, while for the Hamaca crude the order was: control, iron and tin. The most interesting result occurred with the light California oil. The control run showed that we were unable to propagate a combustion front while with the iron additive, a good combustion was achieved.

To date we have not been able to find a suitable additive to reduce fuel deposition. Iron and tin salts seem suitable agents to increase fuel when that is needed.

2.2.2 INTRODUCTION

In-situ combustion is a thermal oil recovery technique. In this process, air or oxygen is injected and burns part of the oil which is used to generate a burning front which propagates in the reservoir. Oil production is improved by a host of mechanisms (frontal displacement, gravity drainage, etc.). Although the main application of thermal recovery is to recover viscous, heavy oils, a broad range of oils and reservoirs are potential targets for these recovery methods. The major constraint limiting the applicability of in-situ combustion is the amount of fuel deposited on the reservoir matrix ahead of the combustion zone. If insufficient fuel is deposited, as can be the case for light oils, the combustion front will not be self sustaining and will die from lack of fuel. Conversely, if excess fuel is deposited, the front advance will be slowed and the quantity of oxidizing gases required to sustain combustion will be high. The amount of fuel deposited and the velocity of the combustion front are affected by the kinetics of oxidation and pyrolysis reactions of the crude oil in the porous matrix. Catalytic compounds affect the kinetics of the reactions and so can influence the fuel concentration. If the proper catalyst can be introduced in the reservoir to modify the fuel deposit, in-situ combustion could be feasible for a broad range of crude oils and reservoirs. Such an application was first presented in 1985 by Racz. Recent work at Stanford University (Shallcross et al., 1991 and Baena et al., 1990) showed that water soluble metallic additives can change the kinetics of the combustion reactions. Kinetics studies, although useful in a qualitative sense (Burger and Sahuquet, 1972), are unable to provide an engineer with field related parameters such as the fuel

concentration or the amount of air needed to burn a given volume of reservoir. The existing literature has so far not addressed the quantitative determination of the influence of metallic additives on the nature of the fuel and its impact on the combustion parameters. The objective of this paper is to describe combustion tube runs performed with metallic additives and to interpret the results of these experiments in terms of possible field applications.

2.2.3 EXPERIMENTAL EQUIPMENT AND PROCEDURE

The equipment is similar to that used by a number of researchers at Stanford University. The following outlines the main features of the apparatus. Further detail is given in Baena et al., 1990. A schematic of the equipment is shown on Figure 2.2.1.

The combustion tube is 1 m long and 7.6 cm O.D. made of 316 stainless steel with 0.041 cm wall thickness. A thermowell is placed along the axis, allowing temperature measurements anywhere along the axis of the tube. Two electrical heaters located at 10 cm from the top of the tube are used as igniters. The tube is placed vertically in a thermally insulated pressure shell. Air injection is controlled by a mass flowmeter. The produced fluids are collected via a separator and condenser. The gases are continuously monitored for oxygen, carbon monoxide and carbon dioxide. A gas chromatograph is used to spot check for other gases. All the measurement sensors are connected to a microcomputer.

A mix of 20-30 mesh Ottawa sand, fire clay, oil and water containing the desired additive is packed into the tube. The clay content is 5% by weight of the sand. Porosity of the pack is about 35%, oil saturation around 35% and water saturation about 25%. The tube is preheated to a reservoir temperature of 60° C by the external heaters, nitrogen is injected and the igniter is turned on. When the temperature at the igniter reaches 315° C, air at a rate of 3.0 slpm is injected and nitrogen shut off. The start of combustion is indicated by the gas composition at the outlet. The igniter is shut off when the combustion is stable and the front begins to propagate downwards. At the end of the run, the combustion is quenched by replacing the air injected by nitrogen. This is typically done at 90 cm from the top to avoid damage to the bottom flange.

Four runs were performed using Huntington Beach oil (22° API gravity) from California. The first run had no additive, while the next three had ferrous chloride, stannic chloride and zinc chloride at 1.0% by weight dissolved in the connate water.

Four runs were done using Hamaca oil (10° API gravity) from Venezuela. Two control runs with no additive were followed by runs with iron chloride and with stannic chloride at 1.0% by weight in the connate water.

Three runs were performed on the Cymric heavy crude (12° API gravity) from California. One was a control run while the two others included iron and zinc at 1.0% weight concentration. All runs were performed at air fluxes of 3 slpm and 100 psi (7 bars) back pressure. The last two runs used the Cymric light crude (34° API gravity) from California. The first run was a control, while the second run included iron as the additive.

2.2.4 RESULTS AND DISCUSSION

The results will first be analyzed in a qualitative manner via examination of the effluent gas behavior, then by a method similar to the method described by Alexander et al. (1962) and Dew and Martin, (1965).

The main feature of the behaviour of the produced gases during the control runs is poor oxygen utilization with average oxygen produced ranging from 2 to 5 mole %. In addition, fluctuations were observed in the oxygen and carbon dioxide produced. Figure 2.2.2 is an example of a typical control run.

When iron was introduced as an additive, a marked change was observed. The oxygen produced almost vanished and the gas production curves were essentially constant with time, showing a uniform and efficient combustion. Figure 2.2.3 is an example of this kind of result. The carbon dioxide shows a low level in the control runs, with fluctuations reversed as compared to the oxygen fluctuations.

The tin salts had a similar effect on the gas produced, while the zinc salts exhibited a behavior intermediate between the iron and the control runs. The front velocities measured from the temperature profiles show a slight increase caused by the additives.

The fluctuations could have been caused by improper packing of the combustion tube, however, repeat control runs using different packing methods showed the same variations. An examination of the cores by Cat scanning showed no packing defect or porosity fluctuations.

The gas composition variations in the control runs made a detailed analysis using the raw data impossible. In order to obtain quantitative numbers for the relevant economic parameters, it was decided to analyze the average data over the time of the runs when the combustion was stable, neglecting the period during which the igniter influences the start of combustion and the time at the end during which the combustion is quenched with nitrogen.

Table 2.2.1 gives the values obtained for the Huntington Beach crude, while Tables 2.2.2 and 2.2.3 provide the data for the Hamaca and the Cymric heavy crude. The Cymric light results will be discussed separately later. The same information is presented in Figures 2.2.4 to 2.2.8.

In Figure 2.2.4, one can see that the oxygen produced during the control runs is in all cases higher than the oxygen produced when iron and tin additives are present. The zinc additive does not seem to have affected the Cymric heavy crude behavior in this respect. The carbon dioxide produced (Figure 2.2.5) shows a different trend with the control run being the lowest, followed by the zinc, and the tin with the iron runs showing the highest carbon dioxide content in all runs.

The carbon monoxide concentration went from 6% for the control run to 5% with the additives in the Huntington Beach crude runs, from 4.4% for the control to 4.3% with iron and to 3.9% with zinc in the Cymric heavy crude runs, and from 4% for the control to 3.5% with iron in the Hamaca runs. An exception to this general decrease of carbon monoxide with the additives is the run with tin and Hamaca crude which shows an increase from 4% for the control run to 4.4% with tin.

The apparent H/C ratio is presented in Figure 2.2.6. The differences in the H/C ratio indicate that the nature of the fuel burned during the control runs was changed from the fuel deposited during the runs with additives. We are at this stage unable to find a clear trend of evolution of the apparent H/C ratio with different additives. The nature of the fuel deposited is dependent on the composition of each crude, and each crude oil was affected differently by the different metallic additives. The average values of the air/fuel ratios which can be calculated from the gas composition data (Figure 2.2.7) also show some differences with the presence of additives but no definite trend or ranking of the various metals seems possible. The values of air-fuel ratio obtained during this study are in the range of values shown in the literature, but more analysis of the chemistry of each crude used in this study is needed.

The original goal of this study was to investigate whether the additives can modify the amount of fuel deposited on the rock matrix. Figure 2.2.8 shows the evolution of the amount of fuel with and without the additives. This was calculated using the material balance procedure outlined in Baena et al. (1990). The changes observed are small but significant. For all crudes, iron gave higher fuel concentration than the control runs. This is consistent with the results of Racz et al., (1985). Tin seems to exhibit the same behavior as iron, but zinc gives results in between the control and the iron runs.

Only two runs were made with the Cymric light (34° API gravity) crude. The operating parameters were the same as for the other crudes, with the exception of the air flux which was reduced from 3 to 2 slpm. The gases produced during the control run are shown on Figure 2.2.10. After the igniter was turned off, sustained combustion was not achieved. The oxygen produced went back to the injected level and the carbon oxides production stopped in less than two hours. The run performed with iron as an additive showed sustained combustion for over eight hours. Figure 2.2.10 can be compared with the control run results and show a distinctly different behavior. Oxygen is almost fully used, and carbon oxides are produced in a steady manner. Equipment failure caused the loss of the temperature data, hence we could not calculate the amount of fuel deposited. Repeat experiments are in progress.

2.2.5 CONCLUSIONS

Water soluble metallic salts have been tested as combustion additives for four different crude oils. Modifications in the nature and in the amount of fuel formed were observed whenever additives were introduced.

Iron consistently increased the fuel deposition. The most interesting result was obtained with a light crude, for the additive allowed sustained combustion under conditions where a run failed without an additive.

Iron and tin increased the efficiency of combustion, reducing the amount of oxygen produced as well as eliminating the fluctuations in gas compositions observed during the control runs. Zinc does not seem as effective as iron or tin.

Changes in the nature of the fuel can be deduced from the gas analysis. It is impossible at this stage to find a trend, or an order in the way the additives affect the nature of the fuel. This is probably crude and porous medium specific.

Table 2.2.1 22.9° API HBO Crude

Averages For Each Run			
	Control	Iron	Tin
CO_2%	14.0	16.2	14.9
CO%	6.0	5.0	5.0
O_2%	3.95	1.40	0.45
Y_d	0.82	0.94	0.99
N	0.07	0.13	0.79
FaF (scf/lb fuel)	135.6	135.7	150.4
H_c (btu/lb fuel)	11942	12490	14972
MR (lbs/ft^3)	2.46	2.55	2.51
AR (scf/ft^3)	274.6	241.4	240.5
WR (lb fuel/100 lb rock)	1.50	1.55	1.52
VEL (cm/hr)	14.8	17.0	16.6
T_{peak} (°C)	503.2	503.0	533.3

Table 2.2.2 10° API Hamaca Crude

Averages For Each Run			
	Control	Iron	Tin
CO_2%	8.78	13.66	13.44
CO%	4.00	3.49	4.38
O_2%	5.03	0.20	0.07
Y_d	0.77	0.99	0.99
N	1.92	1.48	1.37
FaF (scf/lb fuel)	171.0	169.3	164.1
H_c (btu/lb fuel)	18222	17814	17066
MR (lbs/ft^3)	1.32	1.41	1.60
AR (scf/ft^3)	293.1	241.7	264.5
WR (lb fuel/100 lb rock)	0.80	0.85	0.97

* Velocity of front temperature could not be obtained because of thermocouple failure.

Table 2.2.3 12° API Cymric Crude

Averages For Each Run			
	Control	Iron	Tin
CO_2%	9.22	15.49	11.91
CO%	4.40	4.30	3.92
O_2%	2.14	0.74	2.37
Y_d	0.90	0.96	0.89
N	2.65	0.56	1.40
FaF (scf/lb fuel)	184.4	148.1	165.1
Hc (btu/lb fuel)	20244	14476	17158
MR (lbs/ft^3)	2.95	3.39	3.20
AR (scf/ft^3)	373.7	325.4	370.8
WR (lb fuel/100 lb rock)	1.79	2.06	1.94
VEL (cm/hr)	12.3	13.9	12.13
T_{peak} (°C)	501.7	539.3	517.8

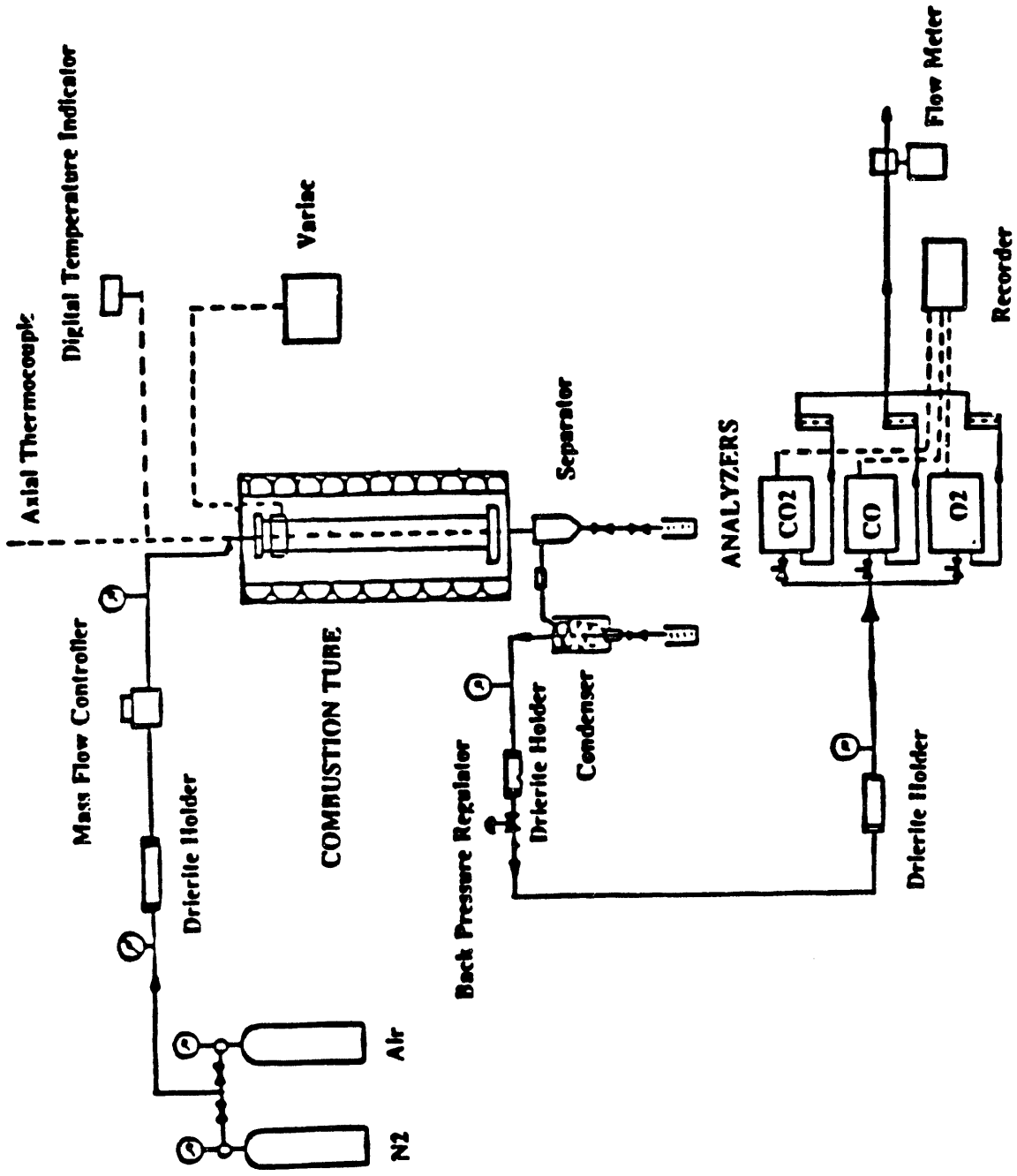

Figure 2.2.1 Schematic of the experimental apparatus.

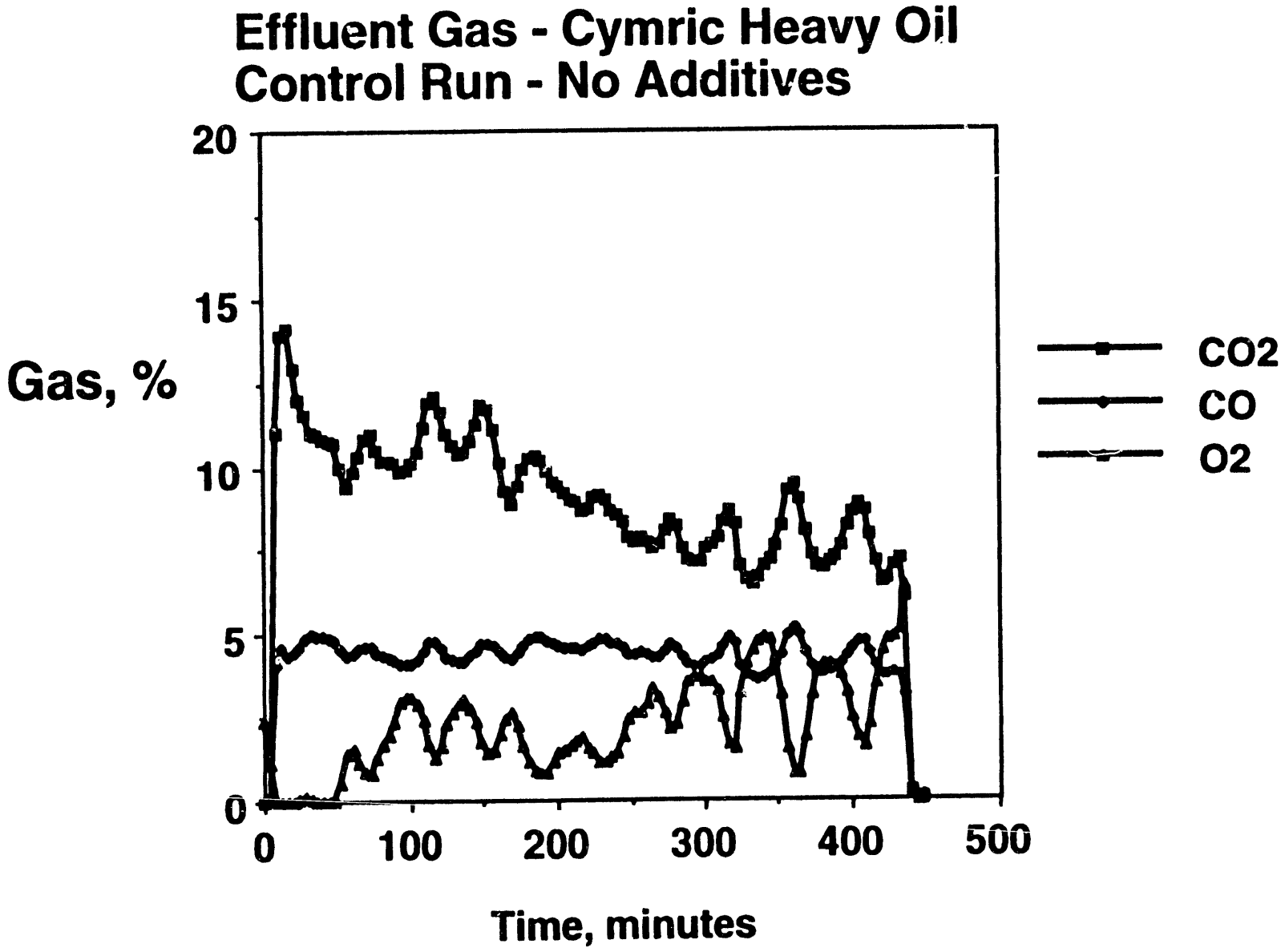

Figure 2.2.2 Produced gases control run cymric heavy.

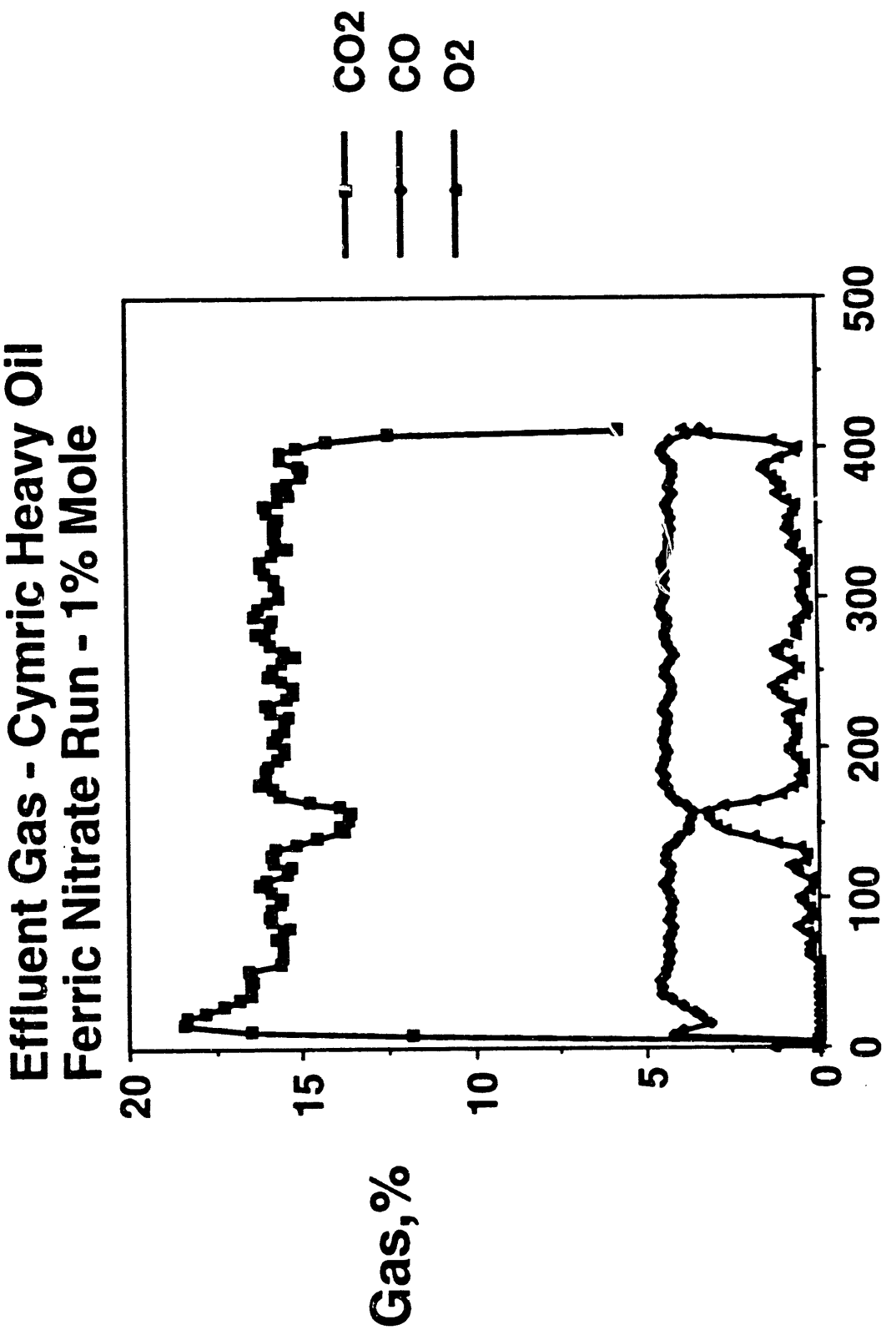

Figure 2.2.3 Produced gases iron run cymric heavy.

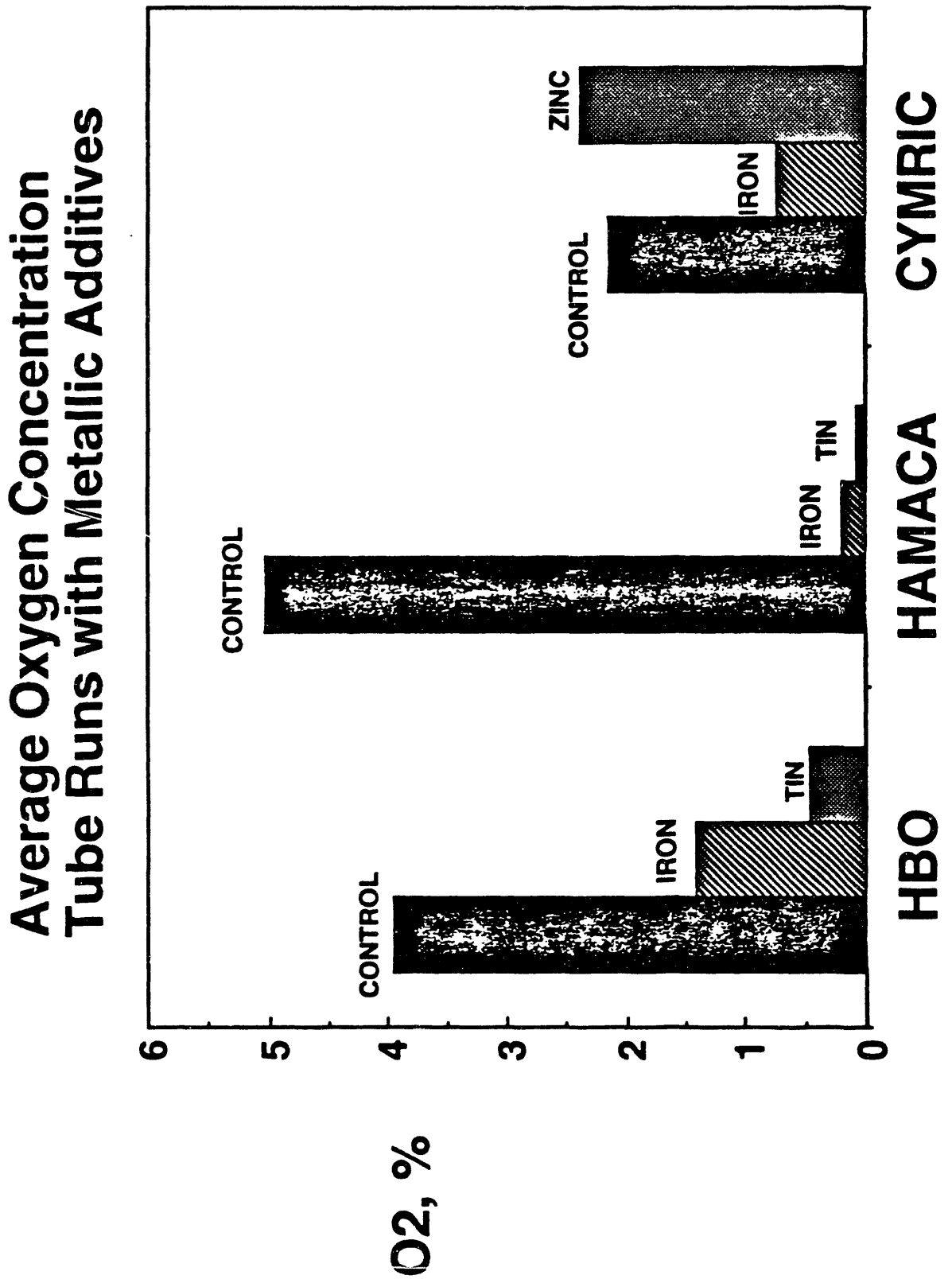

Figure 2.2.4 Oxygen produced: summary for all runs.

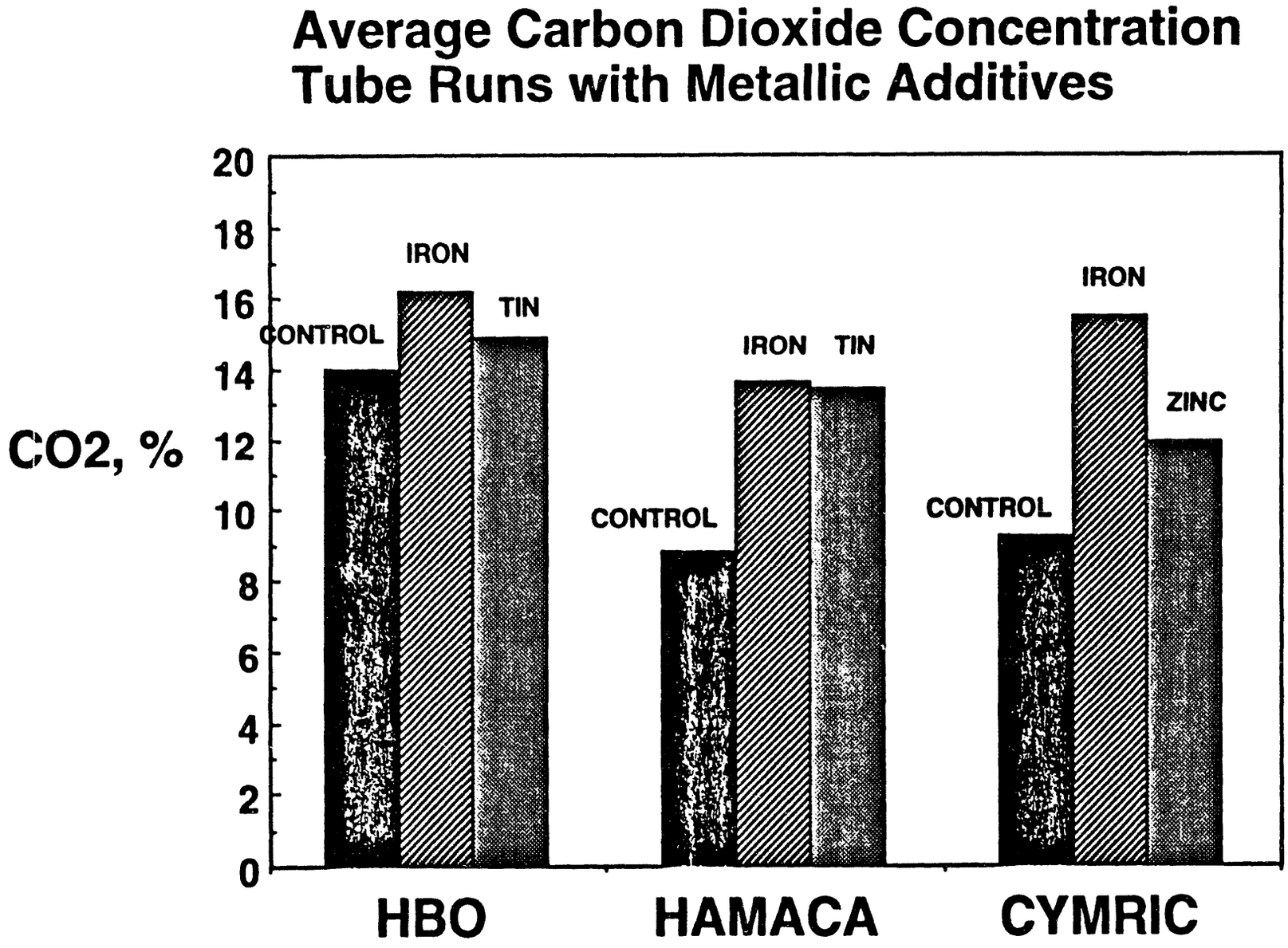

Figure 2.2.5 Carbon dioxide produced: summary for all runs.

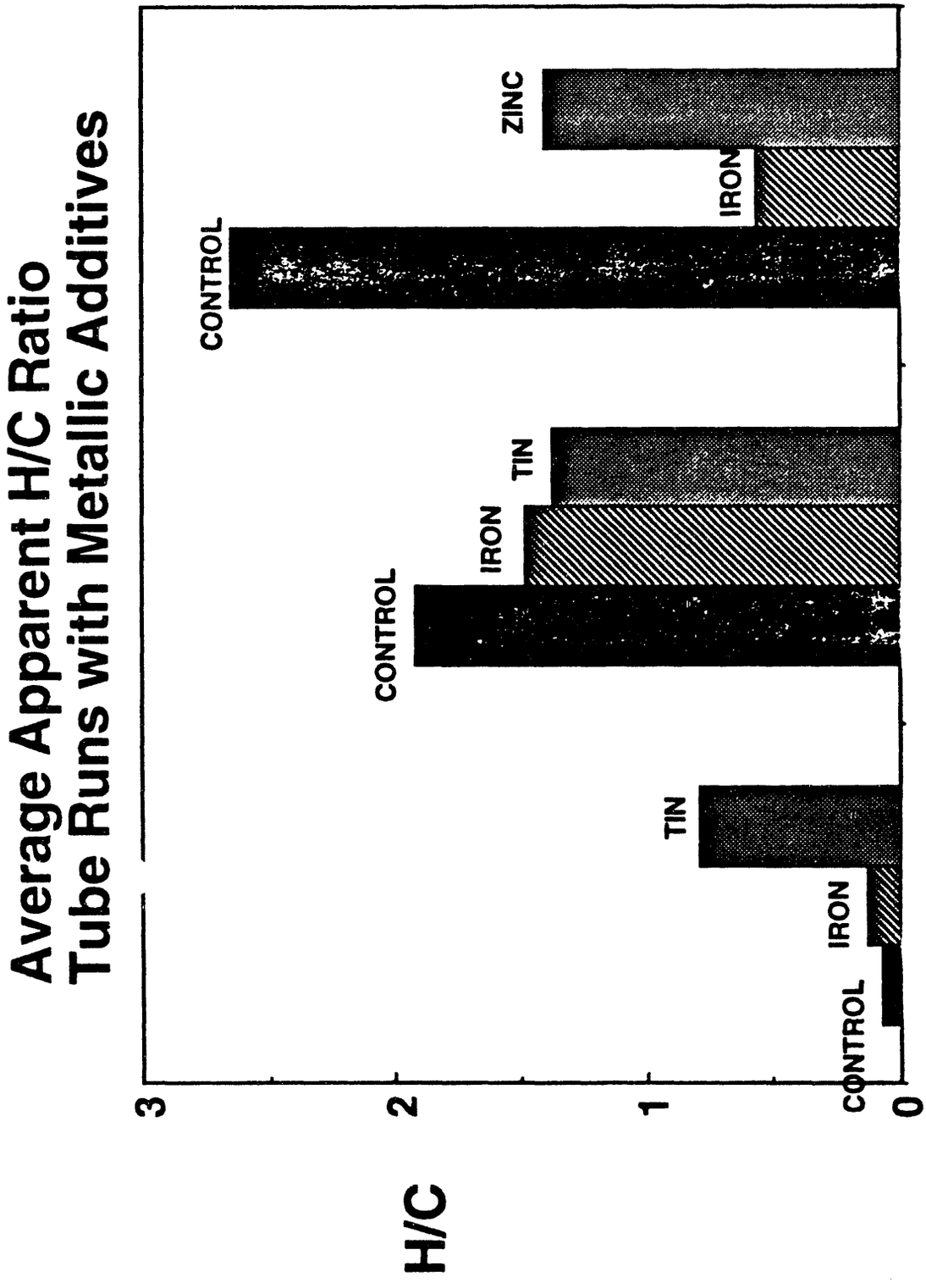

Figure 2.2.6 Apparent H/C ratio.

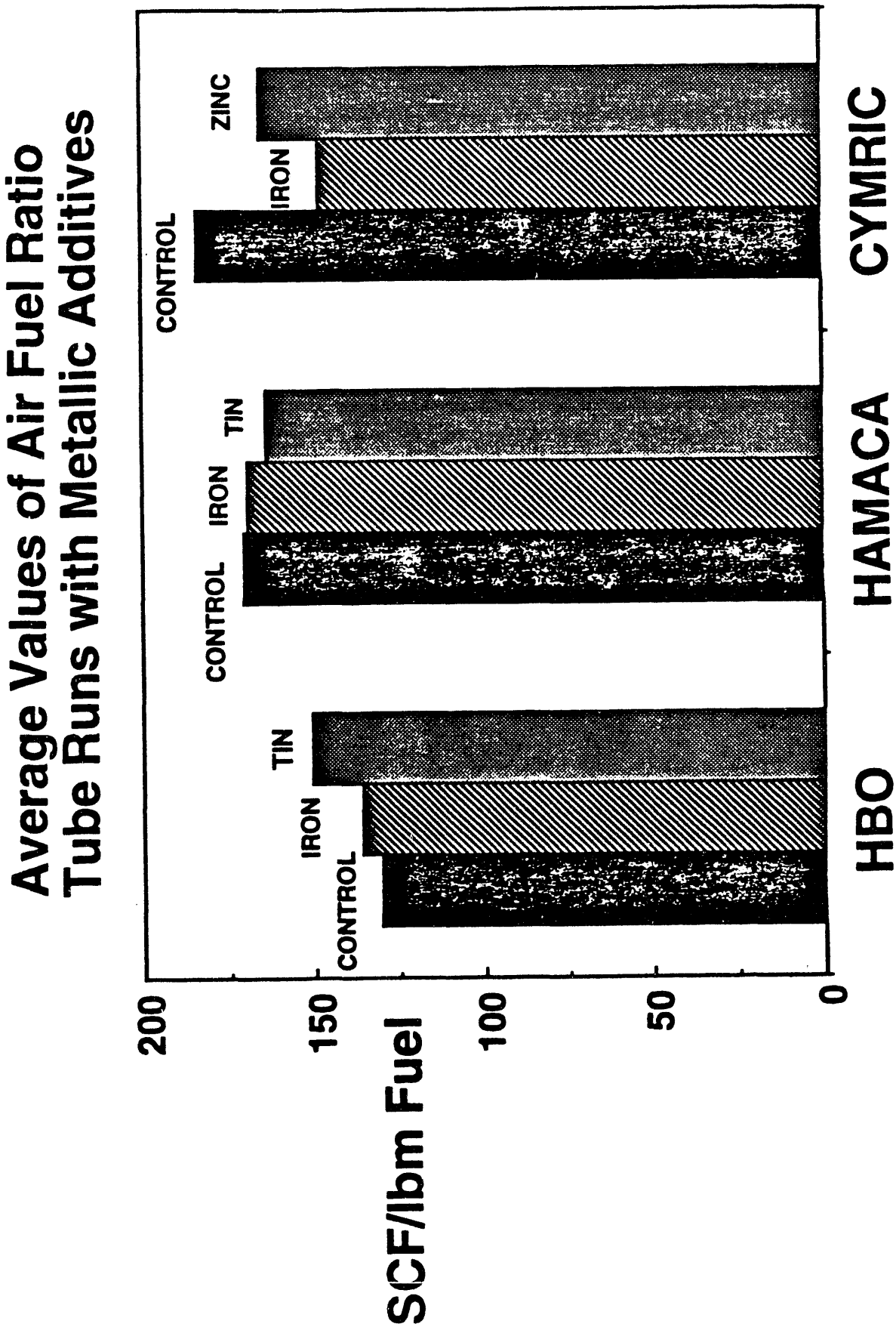

Figure 2.2.7 Average air/fuel ratios.

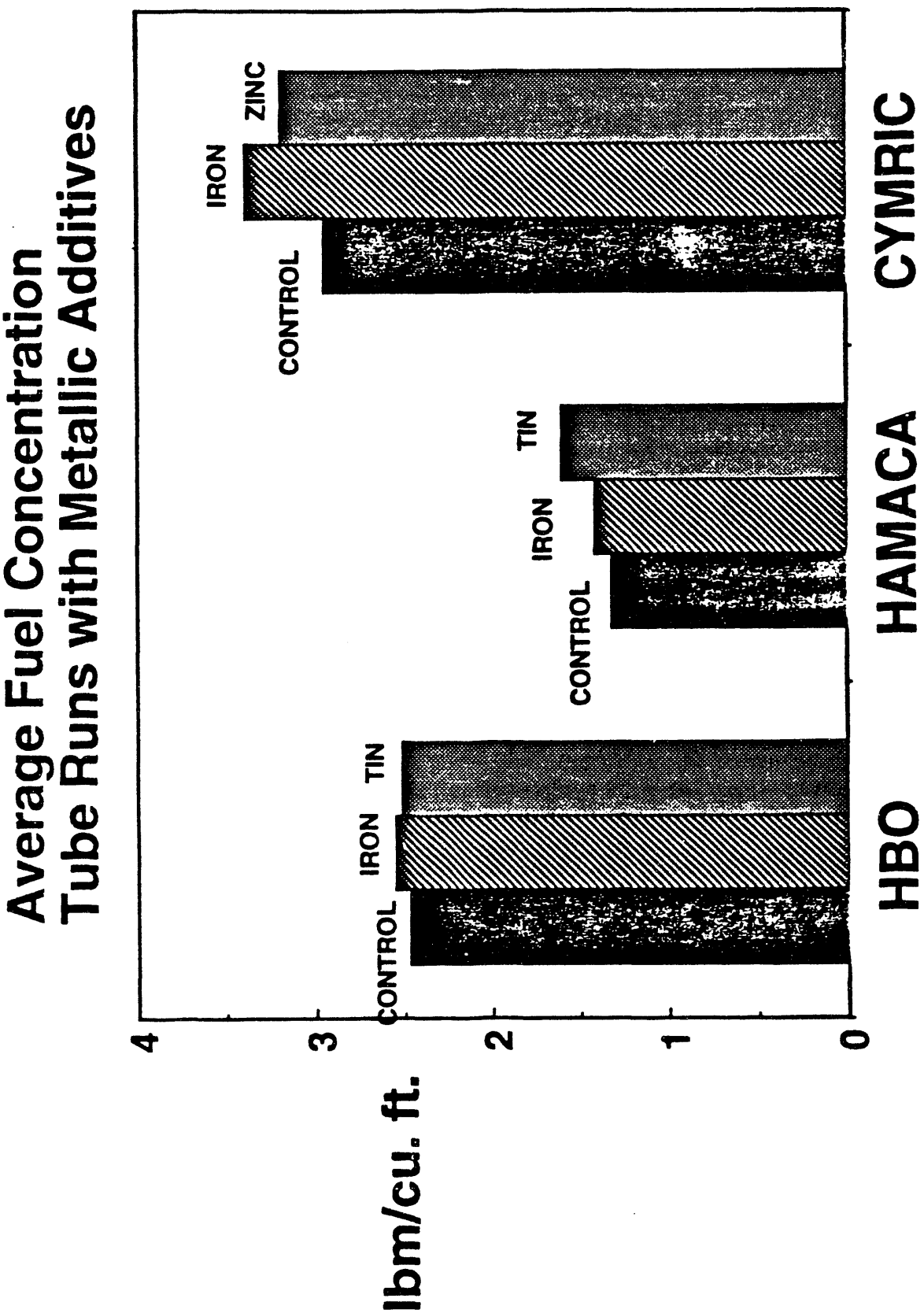

Figure 2.2.8 Amount of fuel deposited.

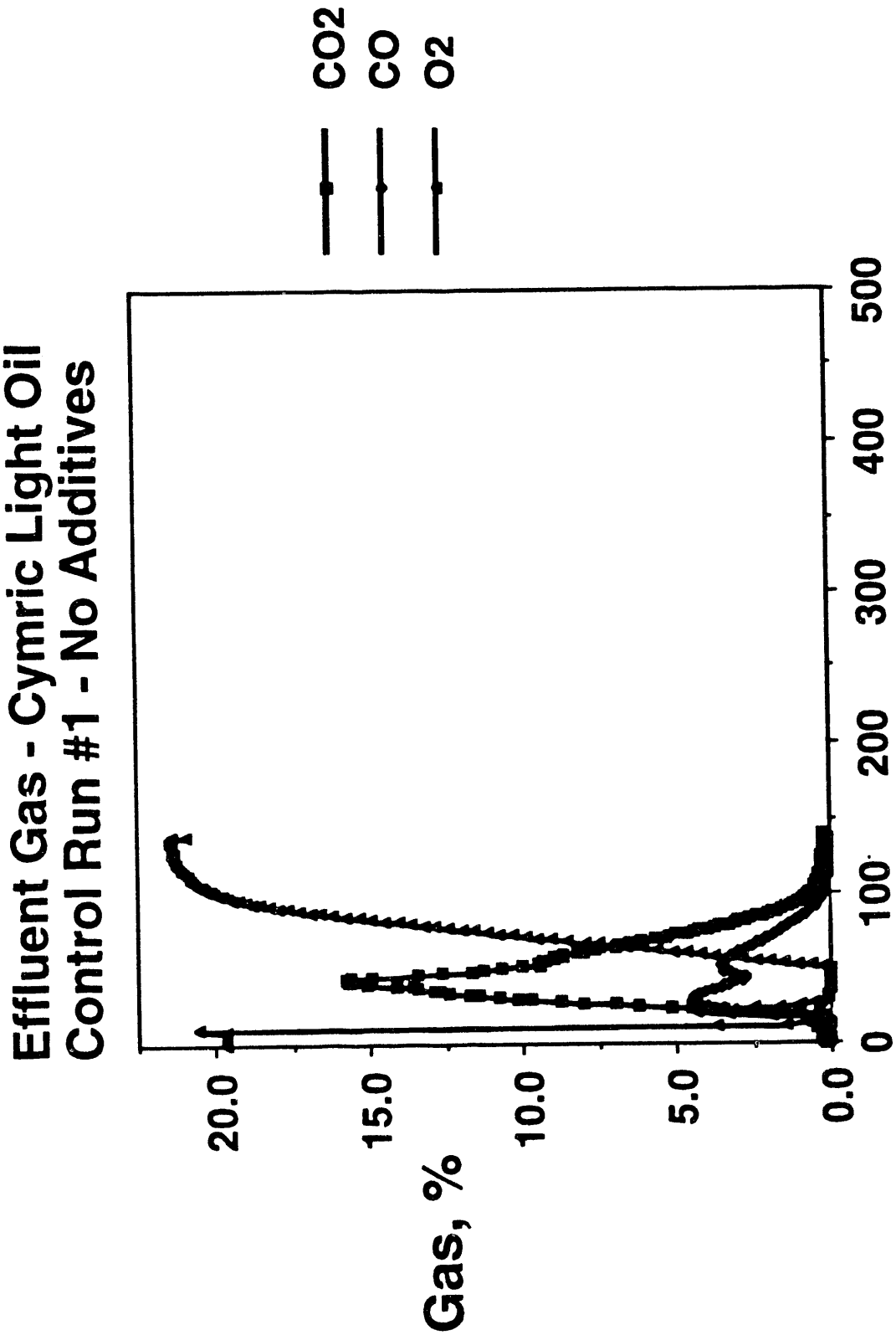

Figure 2.2.9 Cymric light: gas prodced during the control runs.

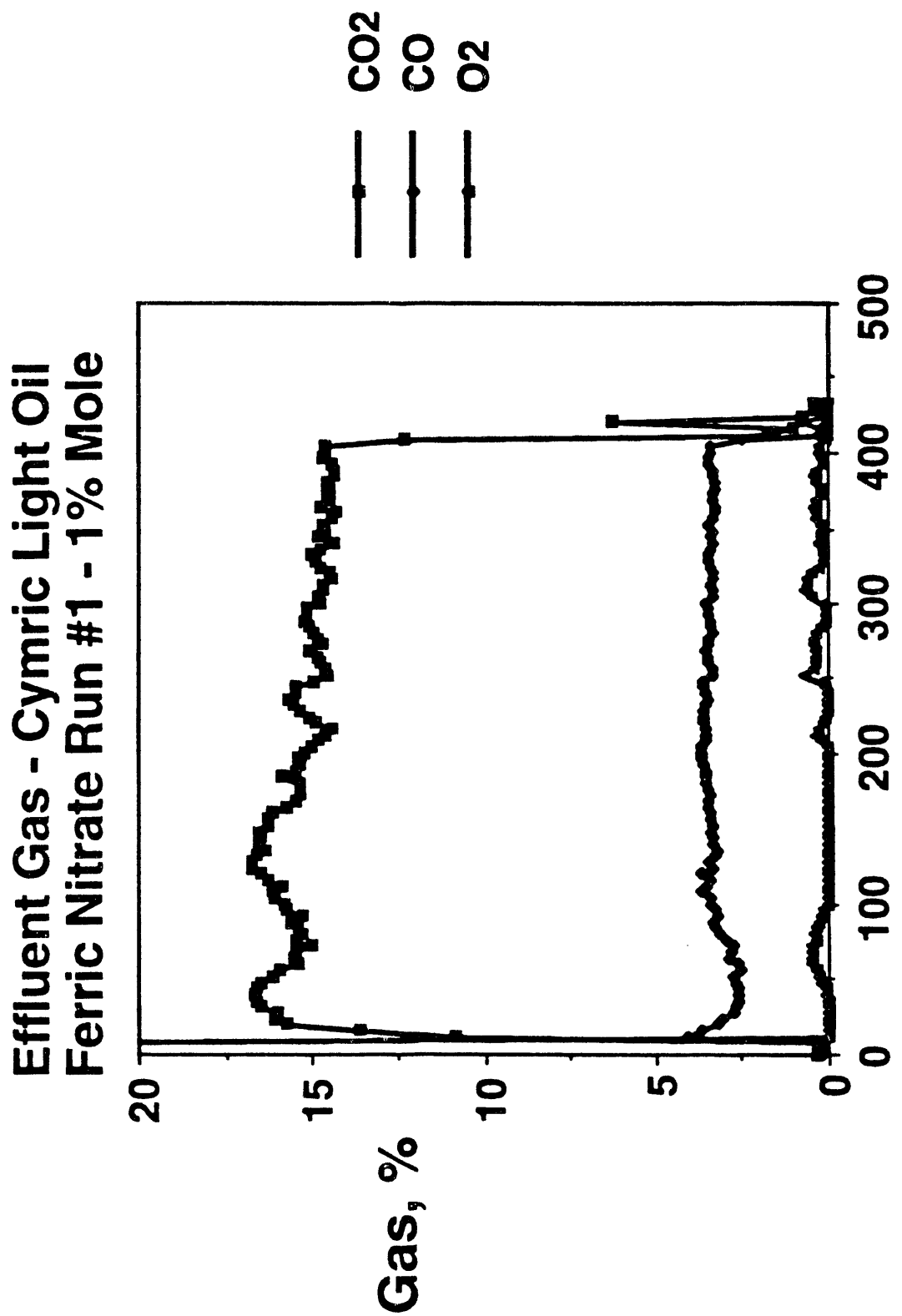

Figure 2.2.10 Cymric light: gas produced during the run with iron.

3.1 STEAM-FOAM STUDIES IN THE PRESENCE OF RESIDUAL OIL
(D. A. Hutchinson)

3.1.1 ABSTRACT

This study reports continuing work concerning understanding of steam-foam flow behavior with oil present. Steam foam systems were studied in a one dimensional sandpack at residual oil saturation (about 12%). The strength of the in-situ generated foam, indicated by pressure gradients, is affected significantly by injection procedure, slug size, steam quality and non condensible gas (nitrogen). In the range studied, surfactant concentration had a minor effect.

In the presence of residual oil, simultaneous injection of steam and surfactant failed to generates foam in the model, while the same procedure generates a strong foam without oil. When surfactant was injected as a liquid slug ahead of the steam, foam was generated, although at a lower strength than when no oil was present. The minimum slug size required to generate foam by this procedure was about 5% of the pore volume at 1.0% weight concentration. Above this minimum, increases in slug size or in concentration had little effect. Increased quality of steam improved the foam strength. One implication of these results is that savings in the amount of surfactant needed for a steam-foam project may be possible by using a large slug of dilute solution. That is, if the slug volume is above some minimum, a dilute concentration may give acceptable foam generation. The reverse procedure, a small slug of high concentration surfactant gives poor foam generation and should probably be avoided in field operations. Steam quality effects are consistent with observations in the existing literature.

3.1.2 INTRODUCTION

Foaming additives have been used extensively in field operations to improve steam injection efficiency (Castanier and Brigham, 1989). The purpose of foaming additives is to reduce gravity override and channeling of injected gases and reduce gas/oil ratios and improve sweep efficiency. Despite numerous studies dating back to the 1950's, the mechanisms involved during the flow of steam/surfactant/noncondensible gases in an oil reservoir are not fully understood. Modelling of steam foam processes in order to compute production of oil is not yet possible. Optimization of the injection method, amount, concentration and type of surface-active agent, relative amounts of steam and noncondensible gas, and steam quality is needed for improved application of this enhanced oil recovery technique.

Previous studies have focussed on selecting thermally stable surfactants suitable for use as foaming agents at steam injection conditions. Most of this work was performed without oil or under static conditions. Recent work by Hamida et al. (1990) showed that at experimental conditions it was not possible to generate foam as indicated by increased pressure gradients when residual oil saturation to steamflood was present. The procedure used was coinjection of steam, nitrogen and surfactant solution. Other authors (Demiral and Okandan, 1987) reported success with the slug injection method although at different conditions. This study of steam foam mechanisms was made at residual oil saturation under dynamic conditions by using an alternating injection technique at the same experimental conditions previously reported by Hamida et al. (1990).

3.1.3 EXPERIMENTAL EQUIPMENT

The equipment schematic is presented in Figure 3.1.1. The main components are injection and production equipment and a cylindrical tube of 2m length and 5cm diameter. The tube is instrumented with 21 thermocouples and divided in 4 sections for pressure gradient measurements. The first section (near the inlet) was later subdivided into 4 subsections for detailed pressure gradient measurements. Details of the equipment can be found in Wang et al. (1986), Shallcross et al. (1990), and Hamida et al., 1990). The tube is packed with clean Ottawa sand of 35% porosity and 95 Darcies permeability. Seven heat flux sensors provide heat loss information from which steam quality inside the pack can be calculated. A complete description of the use of heat flux sensors can be found in Shallcross and Wood (1990).

The pack is saturated with 17° API crude oil, from Newport Beach Field California, at residual water saturation. Steam at 100% quality is injected at a back pressure of 70 psi until breakthrough. Then steam injection is continued under the same experimental condition until no oil production is observed. The residual oil saturation is usually about 12% at this stage. Steam is injected at the conditions of rate and quality desired for the specific run, nitrogen is coinjected with the steam for about one hour prior to the start of the run. Two main surfactant injection methods were studied:

- Coinjection of steam, nitrogen and surfactant solution. As previously discussed by Hamida et al. (1990), this method never generated a significant increase in pressure gradient in the presence of residual oil at our experimental conditions.
- Slug injection during which nitrogen and steam injection are stopped and a slug of surfactant solution is injected, and steam and nitrogen injection is resumed. Most of the results described in this paper pertains to this injection method.

3.1.4 RESULTS AND DISCUSSION

Six runs were conducted whose experimental conditions are given in Table 3.1.1.

During Run 1, two 10% PV slugs of surfactant solution at 1.0% weight concentration were injected. The aim was to observe if the alternate slug injection technique could generate foam in the presence of oil. The result was encouraging as shown in Figure 3.1.2, although the pressure gradient observed was weaker than when no oil was present by a factor of five to six. The response to the second slug of surfactant was larger than the response for the first slug. Apparently the first slug reduced surfactant losses for the second slug. This effect was seen in all runs with the first slug always being weaker than the others. Details of the pressure data show that the last section (S4) had the lowest pressure gradient while the last section had the highest when no oil was in the model. Perhaps the residual oil saturation in the last section was higher than for the previous sections.

Run 2 was a control experiment to see whether the pressure response in the slug injection procedure was caused by the injection of a liquid slug ahead of steam. In this case, instead of injection of a slug of surfactant solution, the same amount of distilled water was injected. No pressure response was observed. Relative permeability effects caused by slug injection are minor.

Runs 3 and 4 were attempts to optimize slug size. Pressure drop response during Run 3 (Figure 3.1.3) shows that reducing the slug size from 10% to 5% of the pore volume did not affect the magnitude or duration of the pressure drop. The splitting of large slugs into several small ones can give improved oil recovery (Gopalakhrishan et al., 1978) and increased gas resistance (Raza, 1970). A surfactant savings can be realized through proper slug size.

Run 4 shows that a limit exists below which further reduction in slug size is detrimental. In our case, this limit seems to be about 5% of the pore volume (Figure 3.1.4). Such a minimum confirms the need for both sufficient wetting phase and surfactant, although in this

case there seems to be a greater need for more aqueous phase. The gases and the liquid surfactant need a large volume for mixing to generate foam. In field operations, with a radial geometry, the amount of liquid to be injected will probably be considerably less than in this linear model. The exact optimization of the slug size should be done in field operations.

The effect of large slugs at reduced surfactant concentration was investigated in Run 5. The benefits of this approach are apparent in Figure 3.1.5. A reduction by a factor of 10 in surfactant use caused only a 25% decline in pressure gradient increase. Runs 4 and 5 results lead to the speculation that the minimum slug size found in Run 4 was more the result of insufficient liquid phase than a lack of surfactant. The effect of stopping the nitrogen confirmed the previous results; that the pressure gradients decreased when no nitrogen was injected. A surprising result was obtained when nitrogen rate was doubled from 3% of the mole fraction of steam to 6%. Injection of nitrogen at this rate proved to be detrimental with pressure gradients even lower than when no nitrogen was injected. At this stage, we can not explain the reason. Verification runs are in progress and further research will be done on this topic.

During Run 6, the effect of steam quality was examined. The desired steam quality was obtained through addition of liquid water at ambient temperature to the steam. In order to keep the total injected energy constant, the steam injection rate was not varied. Since latent heat was used to raise the water temperature, steam condensation occurred with the result that the steam reaching the sandface was reduced by 5% at 80% quality, by 12% at 60% quality, and by 25% at 40% quality. This reduction in injected steam reaching the sandface also explains why the nitrogen mole % of the steam phase increased from 2.9 mole % at 100 % quality to 3.9 mole % at 40 % quality, even though the nitrogen rate was kept constant. The total injected steam plus water consequently increased with decreasing quality. Figure 3.1.6 shows that at 40% quality five slugs were needed to obtain a minor pressure response. In that case, the detrimental effect of reduced steam quality was probably caused by dilution and washing away of the surfactant by the liquid phase of the steam. This detrimental effect of reduced steam quality on foam generation and stability is contradictory to some laboratory studies (Khatip et al., 1988) which found that a lower quality was beneficial. Those studies kept the surfactant concentration constant in the injected liquid phase. Since the injected liquid phase increased when quality decreased, the amount of surfactant injected also was increased when quality decreased. This provided a dual benefit of increased wetting phase and increased surfactant mass.

In our case, the surfactant slug had a fixed mass and the injected liquid phase of low quality steam did not have surfactant. The principal role of the liquid phase was to dilute the slug and wash away surfactant previously lost through partioning and adsorption. For such cases, the subsequent slugs also experience losses since the sites have been washed clean by the water of low quality steam. This conclusion is confirmed by further increasing the steam quality. Increasing the quality to 60%, then to 80% gave increasing pressure gradients. The maximum pressure gradients were achieved at 100% steam quality. The quality was varied in ascending(from 40% to 100% by 20% increments) and descending (from 100% to 40% by 20% increments) order with essentially the same results for the same quality.

3.1.5 CONCLUSIONS

Under the subject experimental conditions, we can make the following observations:

1. The injection technique for a steam/foam flood is important. Coinjection of surfactant with steam gave poorer results than slug injection of liquid surfactant solution followed by steam. This is probably caused by increased mixing between phases because the steam must pass through each surfactant slug after each slug injection.
2. The slug size must be above a minimum. Above this minimum, dilute slugs can prove almost as effective as concentrated slugs. This can lead to possible optimization of surfactant use.
3. The first few slugs give a lower pressure increase response than subsequent slugs. Surfactant losses from the first few slugs can reduce such losses from the following slugs and hence improve the pressure response.
4. High quality steam improves the performance of the system when the slug injection procedure is used.
5. Even as low a residual oil saturation as 12% greatly destabilizes the foam with pressure gradients in the best cases being reduced by an order of magnitude over the case when no oil is present.

Table 3.1.1 Experimental Program

RUN	Surfactant Concentration % by Weight	Slug Size % PV	Steam Quality %
1	1.0%	10	100
2	0	10	100
3	1.0	5	100
4	1.0	1-5	100
5	0.1	10	100
6	0.1 same same	10 same same	40 to 100 100 100 to 40
7	0.1	10	40 to 100

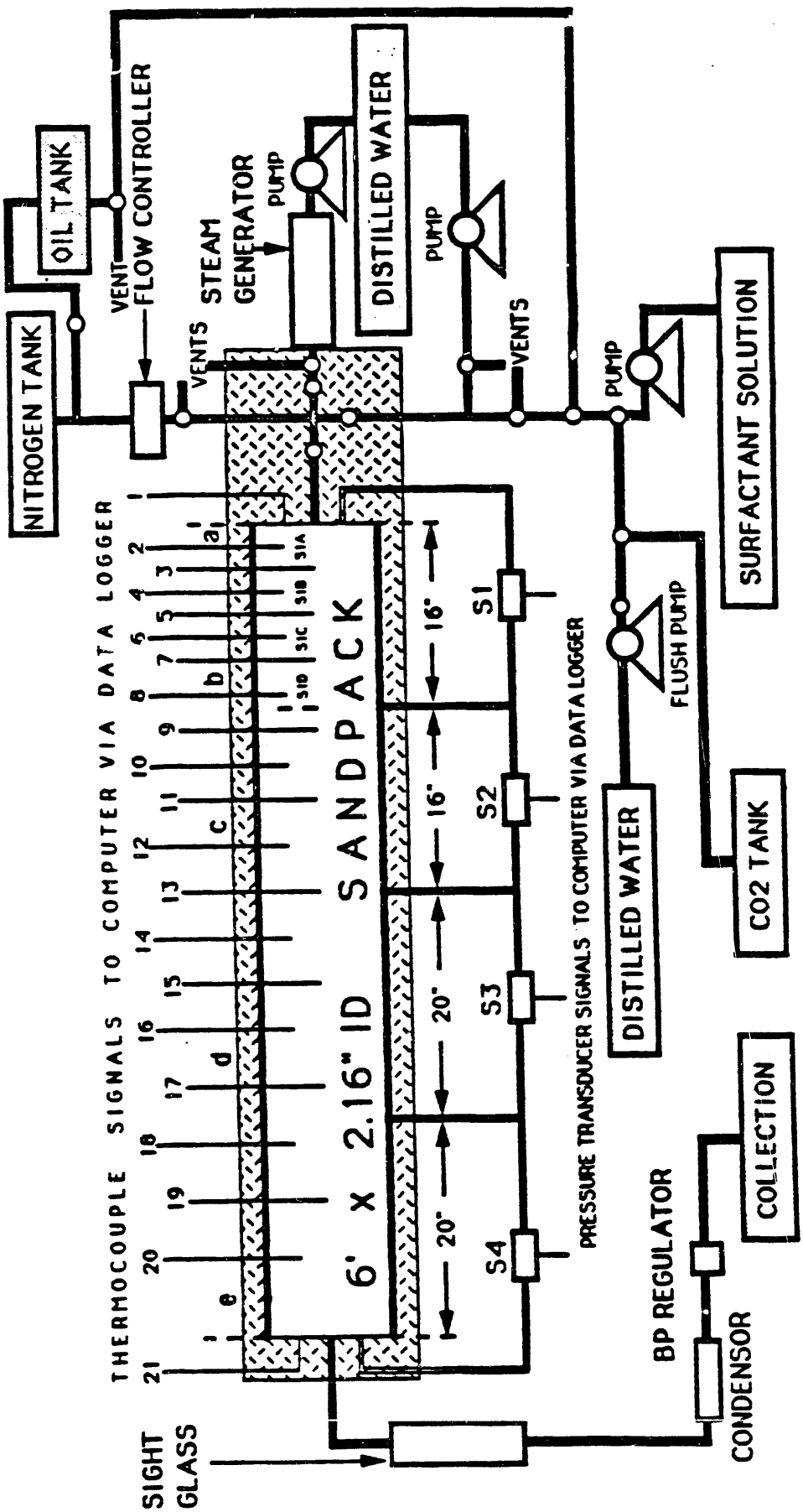

Figure 3.1.1 Schematic of the experimental equipment.

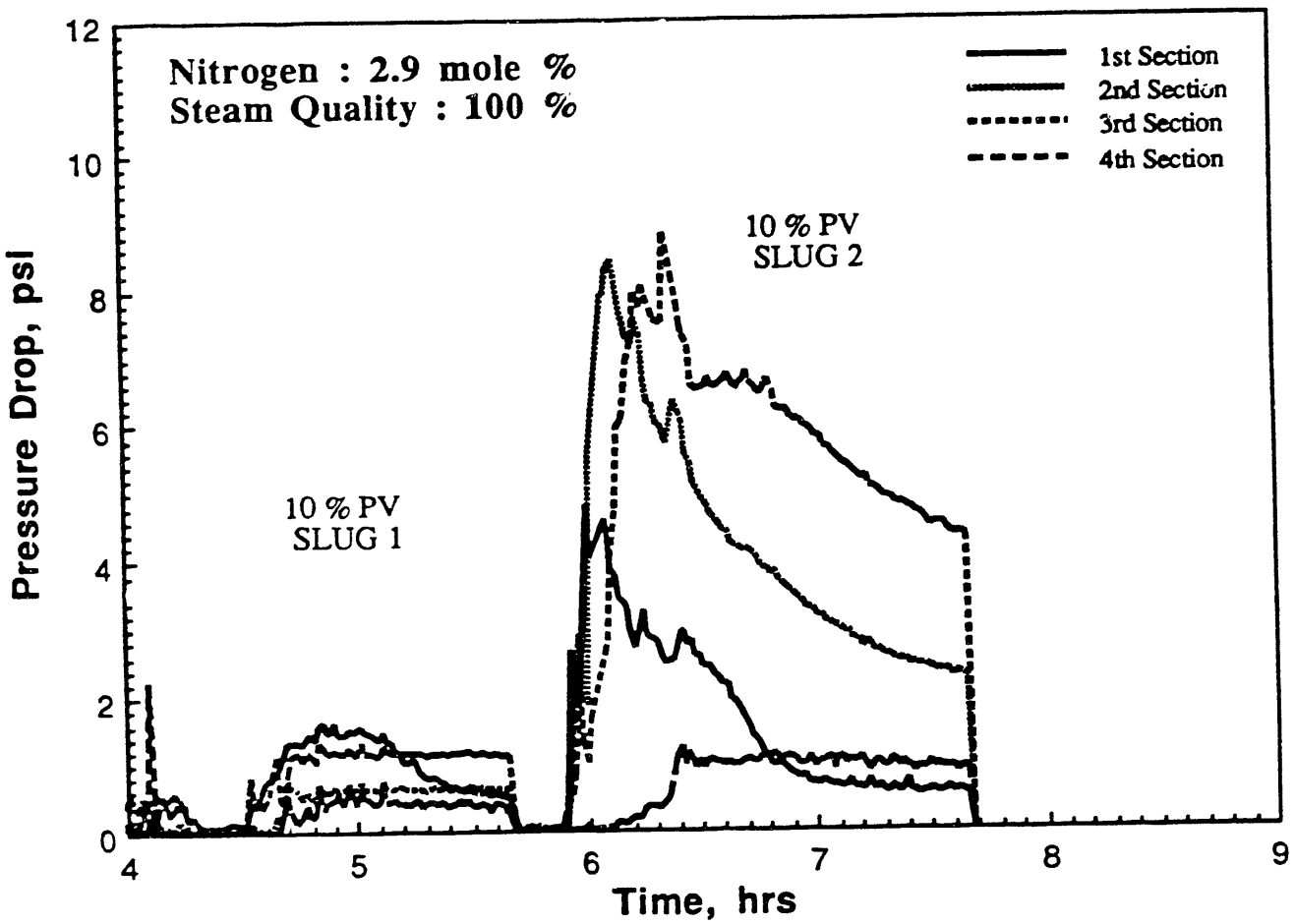

Figure 3.1.2 Pressure drop across the sandpack during Run 1.

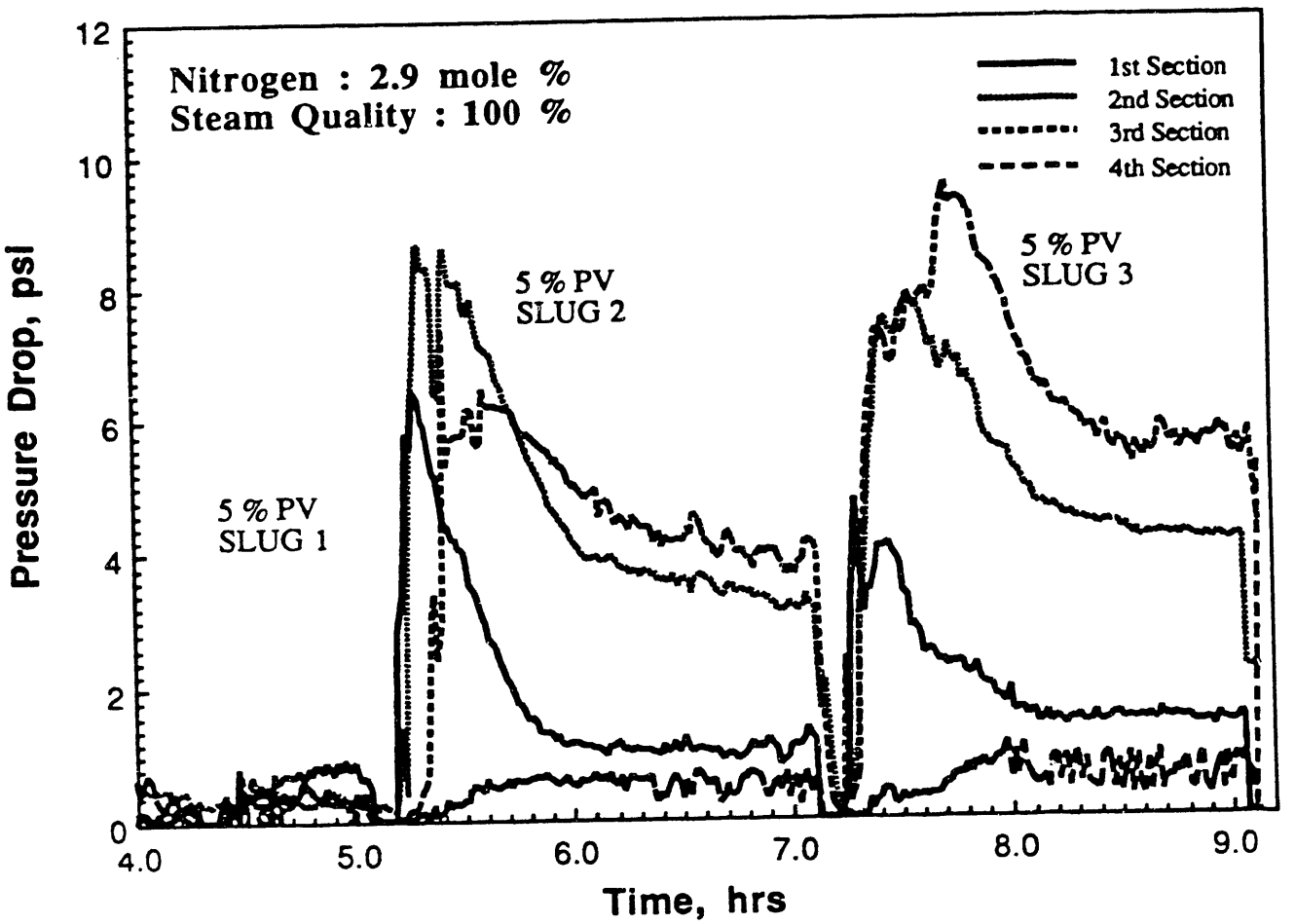

Figure 3.1.3 Effect of slug size on pressure drop during Run 3.

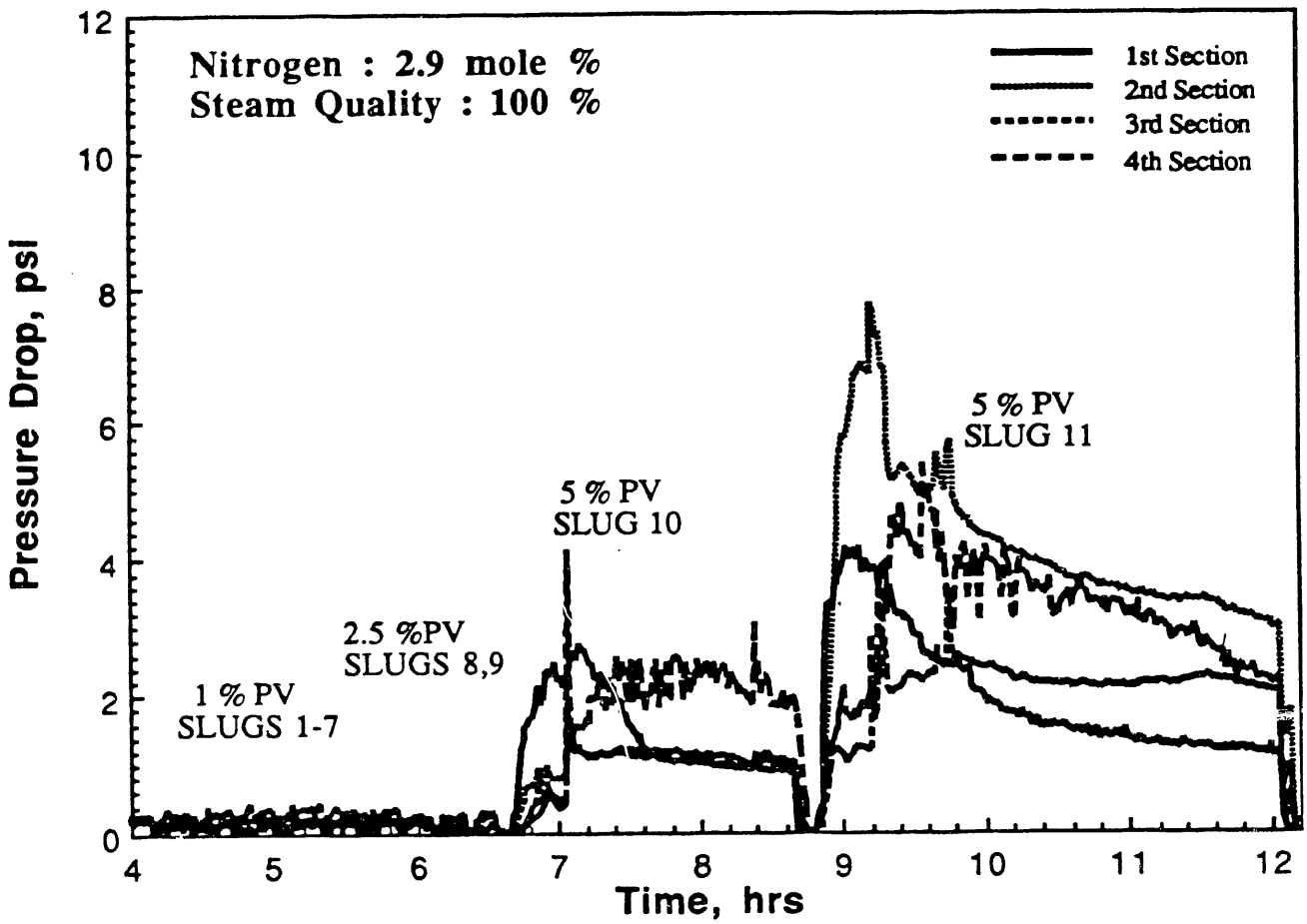

Figure 3.1.4 Effect of slug size on pressure drop during Run 4.

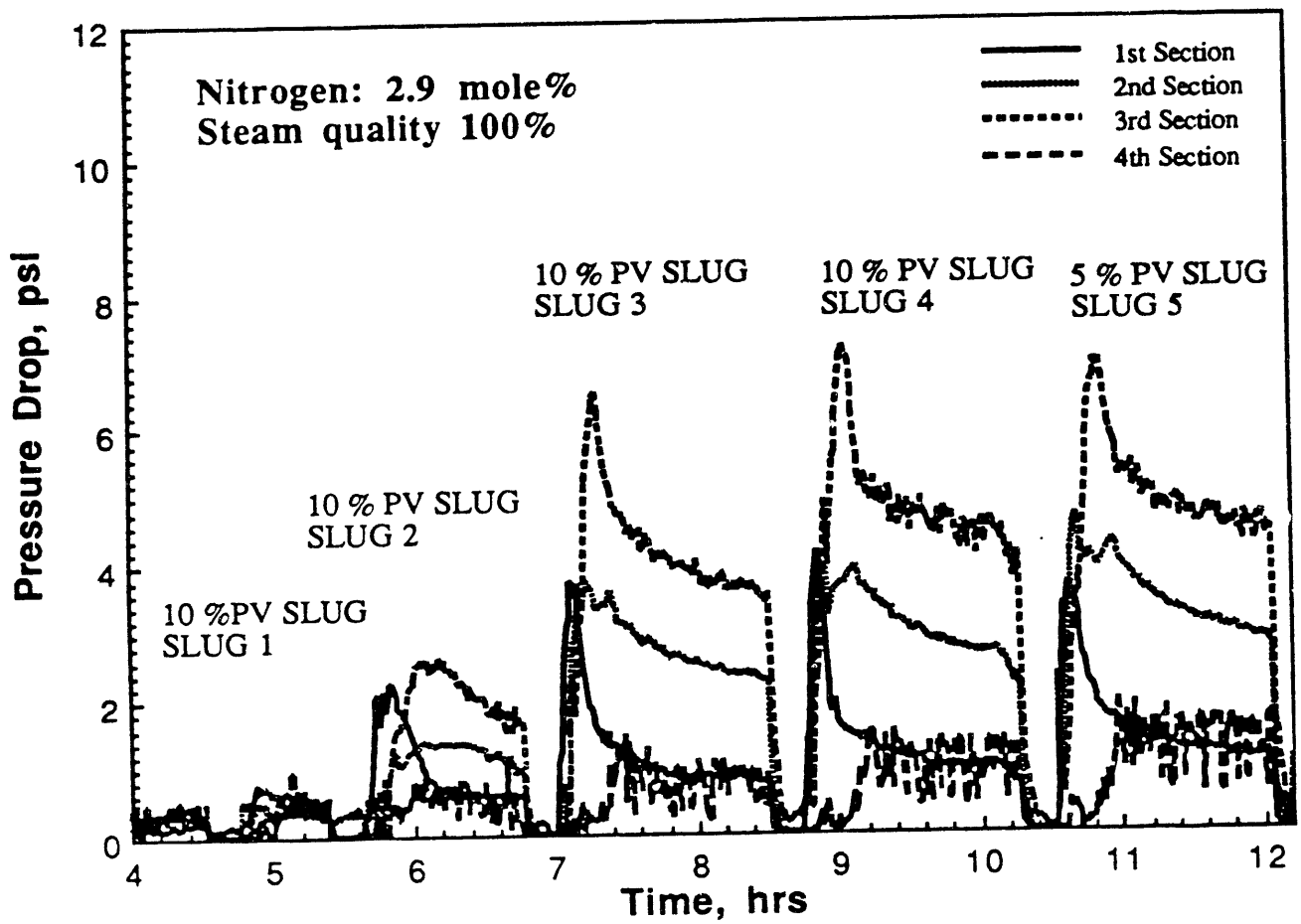

Figure 3.1.5 Effect of dilute slugs on pressure drop during Run 5.

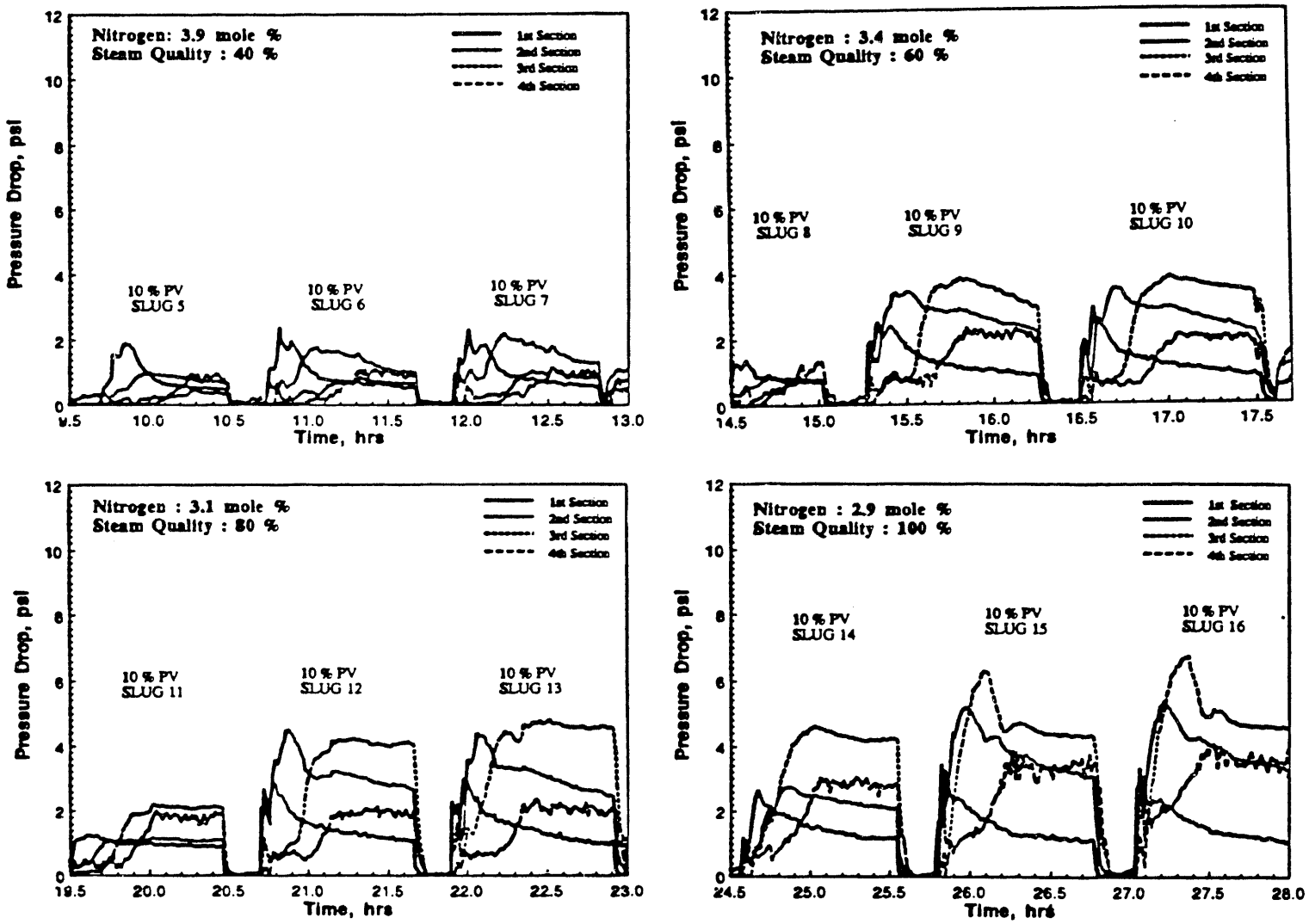

Figure 3.1.6 Effect of steam quality on pressure drop during Run 6.

3.2 CHARACTERIZATION OF SURFACTANTS IN THE PRESENCE OF OIL FOR STEAM-FOAM APPLICATIONS
(A. Razzaq)

3.2.1 INTRODUCTION

This report describes an experimental program designed for testing the foam-forming ability of selected surfactants at moderate temperature conditions (150°C) typical of California operations. The scope of the work, however, is limited to surfactant variation and pressure drop caused by the foams. For comparison with the performance of the surfactants without oil, the results of an earlier study by Shallcross et al. (1990) are used. This work has the following objectives:

- To study the behavior of in-situ produced foam from selected surfactants.
- To establish a link between the foamability and chemical structure of a surfactant.
- To rank surfactants according to the strength of produced foam and sensitivity to oil at typical California steam injection conditions (low temperature and pressure).
- To investigate the generality of surfactant alternating gas (SAG) injection mode.
- To compare the foamability of surfactants with and without oil.

For our purpose, all experiments are carried out under the same operating conditions. The pressure drops observed across the sandpack as well as in different sections are investigated.

3.2.2 EXPERIMENTAL EQUIPMENT AND PROCEDURE

A one-dimensional laboratory model was used to investigate the foam forming characteristics of surfactants under the same set of conditions in the presence of a crude oil. The surfactants studied included an alpha olefin sulfonate, AOS2024, a linear toluene sulfonate, LTS18, a CHEVRON disulfonate, SD1020 and an alpha olefin sulfonate, AOS1618. A description of the apparatus and experimental methodology used, and the experiments performed follows. The experimental conditions are summarized in Table 3.2.1.

1. Experimental Conditions

The equipment used in this study was a one-dimensional sandpack model and was first built by Wang et al. (1986). Similar equipment was also used by Maneffa (1987), Shallcross (1989-1990), Hamida (1990), and Hutchinson (1991).

1.1. Surfactant Selection

Four anionic surfactants, AOS2024, LTS18, SD1020 and AOS1618 were used. The surfactants used represent three broad categories of sulfonates, two alpha olefin sulfonates, a linear toluene sulfonate and, a disulfonate. All four surfactants were commercial products. The numbers attributed to their names indicate the alkyl chain length, or the range of alkyl chain length, e.g., the chain length of molecules in AOS2024 varies from 20 to 24 carbon atoms. SD1020 is a disulfonated alpha olefin sulfonate of unknown chain length. The selection of three surfactants, AOS1618, AOS2024 and LTS18, was based on the highest ranking of these surfactants out of the seventeen surfactants tested by Shallcross et al. (1990). The ranking of the surfactants was based on the magnitude and duration of response at minimum (0.1%) concentration level in the sandpack in absence of oil. The higher pressure drops created by the foam generated by these

surfactants was also reported by Hamida (1990). The selection represents the variations in length AOS2024 vs AOS1618, variation in structure AOS2024 vs LTS18, and includes disulfonated surfactant. The experiments were carried out for a two-phase system, gas(steam and nitrogen)/water. The fourth selected surfactant was, however, at the lowest level in the ranking of Shallcross as there was no response (without oil) at the highest tested concentration (1.0%).

1.2. Run Sequence

Four experiments were performed using the selected surfactants in the following sequence: AOS2024 was used in Run 11, LTS18 in Run 12, SD1020 in Run 13 and AOS1618 in Run 14. In all the experiments the concentration of surfactant solution was 1.0% by weight of active surfactant, and 1.0% by weight of sodium chloride. All experiments were performed at residual oil saturation which was estimated to be 12.0% on the average. Each run is described in the following.

1. Run 11: AOS2024

The surfactant used in this run is an alpha olefin sulfonate AOS2024. The objectives of this run were to:

Check the equipment performance after reassembling the apparatus in a new location.

Check the effect of a third slug injection of the surfactant at 1% weight concentration.

Serve as the base case for later surfactant studies.

Prior to the run, the equipment was pressure tested at 300 psi. Carbon dioxide was injected to remove the air in the system. The equipment was flushed with 10 PV of water. The pressure transducers were calibrated. The oil was injected and steam flooding was performed.

2. Run 12: LTS18

The surfactant used in this run is a linear toluene sulfonate, LTS18. During the preparation of the surfactant solution, a slight heating (60°C) was needed. The solution was kept at 40-45°C during the experiment. Three slugs of surfactant solutions were injected during this run. The back pressure was set at 70 psig. After the second injection, a strong foam was produced. Big foam bubbles were observed through the sight glass at the outlet. The back pressure control valve was working but a lot of fluctuations in the pressure were observed. To some extent, these were reduced by manually operating a valve provided for this purpose.

3. Run 13: SD1020

This run followed the LTS18. The run was a normal run. Three slugs of surfactants were injected.

4. Run 14: AOS1618

The run of AOS1618 was a normal run. No significant pressure drop increase was observed during this run and the run was extended to five slug injections. The run was stopped. The results of this run were not stored due to a computer malfunction during shutdown. The results presented are produced from the log charts from backup recorders.

3.2.3 RESULTS AND DISCUSSION

1. Results

The pressure drop across a sand pack is usually the main criterion used to compare the effectiveness of surfactants. The results are analyzed on this basis. This is in line with similar studies carried out using the same type of systems (e.g. Dilgren et al. (1978), Huang et al. (1985), Muijs (1987)). The results of the experiments performed in this study, are shown in Figures 3.2.1 to 3.2.11 and summarized in Table 3.2.2.

1.1 Run 11: AOS2024

The surfactant used was an alpha olefin sulfonate, AOS2024. The total peak pressure drops observed along the sandpack were 2.0, 12.0, 16.0 and 17.0 psig for the four slug injections respectively. The behavior of the pressure drop during the run is shown in Figure 3.2.1.

An increase in the pressure drop was only observed in section 1 when the first slug injection was performed (Figure 3.2.2). For subsequent slugs, responses were observed in every section except section 4. Figure 3.2.2 also shows that the pressure drop across section 3 of the pack was high as compared to section 2. The trend continued with similar pressure differential for the two sections. This was due to the difference in the lengths of these two sections which are 20 inches and 16 inches respectively. Corresponding pressure gradient per foot observed in these two sections were 6.0 psi/ft and 5.04 psi/ft. The actual pressure gradient is, therefore, lower in section 3 than in section 2.

The pressure drop responses from the experiment in sections 1A to 1D are shown in Figure 3.2.3. No response was observed in section 1A and 1B during the experiment. The pressure drop was higher in section 1D than section 1C. This trend was observed in all experiments.

1.2 Run 12: LTS18

The surfactant used in this run is a linear toluene sulfonate, LTS18. The highest total pressure drop was observed in this run. Figure 3.2.4 shows that the total pressure drops were 5, 20 and 25 psi for the three slug injections respectively. The large fluctuations observed in this run are due to back pressure control problem as stated earlier in section 3.2. The increase in the pressure drop is significant from the first to the second slug injection as in case of run 11.

Section-wise results which are shown in Figure 3.2.5 indicate that the pressure drop in both sections 1 and 2 increased after the first slug injection. The important observation of this run is the clear response from section 4 after the second slug injection. The response of section 4 is comparable with section 3. As explained in AOS2024 run, the corrected pressure gradients for sections 1, 2, 3 and 4 are 5.2, 7.0, 4.9 and 3.6 psi/ft respectively.

Figure 3.2.6 shows the response of sections 1A-1D which are similar to the AOS2024 case.

1.3 Run 13: SD1020

The surfactant used in this run is a CHEVRON disulfonate, SD1020. The increasing trend of total pressure drop with successive slug injections followed a different trajectory then run 11 and run 12. As shown in Figure 3.2.7, the response to the first slug was low (5.0 psi). The figure shows that the maximum pressure drop across the pack did not increase much with the second slug injection (6.0 psi). However, the response from the third slug was significant with a value of 15.0 psi.

The highest pressure drop for any section in this run was recorded across section 1 (Figure 3.2.8). This is in contrast to Runs 11 and 12 where section 2 produced the largest drop. Figure 3.2.8 shows that sections 3 and 4 had no response to the first two slug injections. For the third slug injection, an increase in pressure drop was observed. Pressure drop from section 3 after the third slug injection was comparable with section 2. (5.5 psi vs 5.0 psi). Section 4 of the pack showed a response of 2.0 psi to this slug injection. Near the inlet, the response was similar to other runs with no response from section 1A and 1B. This is shown in Figure 3.2.9. The responses for section 1C and 1D are similar (2.6 psi vs 2.9 psi).

1.4 Run 14: AOS1618

The surfactant used in this run is an alpha olefin sulfonate, AOS1618. The maximum pressure drop produced was 3.5 psi after the fourth slug injection. Accordingly the pressure drops observed in each section were also low.

2. Maximum Pressure Drop

The total pressure drop observed at steady state conditions prior to the surfactant slug injection was in the range of 0.5 to 1.0 psi. Among the tested surfactants, the pressure drop increased to the highest level of all the experiments (23 psi) in the case of LTS18. This was followed by AOS2024 (16.0 psi) and SD1020(15.0 psi). The lowest response was observed in the case of AOS1618 (3.5 psi) (Table 3.2.2).

3. Inlet Zone

A consistent behavior was observed near the inlet of the sandpack in sections 1A and 1B. In these sections, a negligible increase in pressure drop was observed for all surfactants and numbers of slug injections. A maximum increase of 0.2 psi was observed in section 1B in the case of LTS18 and AOS 2024. Consequently, a zone of about 8 inches exists at the pack inlet with little pressure gradient. Away from the inlet zone (section 1C and 1D), the pressure drop increased with varying degrees for different surfactants. A higher increase was observed in section 1D relative to 1C.

The lack of pressure drop increase in the inlet zone in all cases, irrespective of the number of slug injections was due to complete dryness/ low aqueous phase concentration because 100% quality steam was injected in the sand pack. Another reason may be wettability alteration.

Given the fact that a maximum volume of steam had passed through these sections, the first explanation is more plausible. This explains the reason for a similar response under similar conditions when no oil was in the pack as reported by Hamida (1990).

4. Slug Sequence Response

The pressure response for the first slug was lowest in each case. Response to the subsequent slug injections did not follow a particular pattern. In the case of LTS18, a 300% increase in pressure drop was observed after the second slug compared to the response after the first slug (20 vs 6.0 psi), while an increase of only 15% was observed for the third slug (23 vs 20 psi). The increases for AOS2024 were 500%, and 25%; and in the case of SD1020 the respective increases were 20% and 200%.

Three factors contributed to the difference of the responses and are discussed in the following sections.

4.1. Possible Adsorption Problems

Oil and rock may scavenge surfactant from the gas water interface or from the surfactant solution. This mechanism will occur to the point that oil and rock are not saturated with the surfactant. Once enough surfactant has been injected into the system and has contacted the oil and rock, this effect should diminish. In laboratory experiments this is achieved by equilibrating oil and rock with the surfactant. In this study, this phenomenon would affect the surfactant performance only in the first few slugs injected. After saturation of oil and rock with surfactant, the mechanism should not hinder the creation or stabilization of foam as no more surfactant should be adsorbed by rock or scavenged by the oil.

Adsorption losses should be different for different surfactants, brine concentration and oil saturation. In this study, adsorption losses were not estimated. For SD1020, where the response was delayed to the third slug injection, adsorption losses should be determined for proper evaluation of the behavior of the surfactant.

4.2. Macroemulsion Formation

The formation of macroemulsion has been avoided by injecting the surfactant solutions at high concentration. The critical micellar concentration (CMC) is, fortunately, usually low and in the range of 0.1-0.2 percent surfactant concentration (Al-Khafaji et al., 1982). One percent surfactant solutions used in this study are higher than the CMC.

This is specially true at the injection end. Downstream concentration of surfactant should depend on surfactant propagation; foam propagation, surfactant solution propagation, and propagation of surfactant with aqueous phase. Thus at the downstream end, formation of macroemulsion cannot be totally rejected in the first few slug injections.

4.3. Wettability Changes

Oil may cause a wettability change from water-wet to oil-wet, and destabilize the foam.

Ottawa sand was used in the sand pack which was strongly water wet. The oil was at residual oil saturation (12%). In a recent micromodel study, Hornbrook et al. (1991) observed that when a surfactant solution comes in contact with an oil interface, the surface is converted to water-wet even at 100% oil saturation. The change in wettability (except in dry zones as discussed earlier) was not expected, even at the down stream end. The generation/propagation of foam in the sandpack also negates the the wettability alteration.

4.4. Foam Propagation Rate

The foam propagation rates were compared by the delay in response from the sections after the slug injection. For AOS 2024, no pressure drop increase was recorded in section 2 and 3 after the first slug injection. The section 2 response was immediate and a delay of 10 minutes was noted for section 3 after the second slug injection. The same trend continued for subsequent injections. However a slight improvement in the response time for the section 3 was observed (Figure 3.2.2). The response for LTS 18 was as follows; the second section responded after 10 minutes of the first slug injection. Sections 3 and 4 did not respond to the first injection. The response from the sections 2 and 3 was immediate and the pressure drop increase in section 4 was observed after three to five minutes for the subsequent two slugs. (Figure 3.2.5) It was deduced that the foam propagation rate was slower in the case of AOS2024 than in the Run with LTS 18.

The results of Run 13 with SD1020 indicated an immediate response for section 2 from the injection of the first slug. For sections 3 and 4, the response was observed

with a delay of 10 and 15 mins, respectively, after the third slug injection. (Figure 3.2.8) The foam propagation rate in the case of SD1020 was higher than for AOS2024, and lower than for LTS18.

The propagation rate cannot be measured for the case of AOS1618 as the response was low.

4.5 Foam Generation at High Oil Saturations

The estimated residual average oil saturation in the pack is about 12%. However section 4 of the pack would be at a higher oil saturation as less pore volumes of steam have swept this area. Observations of section 4, therefore, are presented separately. The highest pressure drop increase was observed in section 4 for LTS18 (5,6 psi) for the second and third slug injections. A nominal increase of 1.0 psi happened for the AOS2024 case after the third slug injection. A 2.0 psi response in the case of SD1020 was observed in section 4 after the third slug injection.

This complements the results of Jensen and Friedmann (1987), who observed that the foam of less sensitive surfactants propagates at a rapid rate.

4.6. Injection Method

The surfactants tested produced foam in the presence of oil under the slug injection technique (SAG mode). Foam was not produced when steam and surfactants were injected simultaneously (SIS mode), (Hamida 1990). The results for the surfactant AOS2024 compare well with the results reported by Hutchison (1991).

The different results for the two injection modes may be attributed to better in-situ contact of the gas phase with the surfactant-laden aqueous phase. The generation of foam requires adequate aqueous phase saturation in the pores to create a liquid film which forms bubbles by capillary action at a constriction neck by flow of liquid through the annulus (snap-off action). Surfactant molecules at this liquid film, called lamella, stabilize the film. The injection by the SAG method ensures both contact and required pore level saturation because the steam and nitrogen which is present as a noncondensible gas, must pass through the injected slug.

In other words, the gas must make a new path through the aqueous phase. The presence of a sufficient quantity of the aqueous phase, the necessary ingredient required for snap-off action, is the main cause of success for this mode.

In case of SIS injection with continuous steam injection, the concentration of surfactant at any given point will be so low that the lamella produced are not stabilized. In addition, the low saturation of aqueous phase where steam flows may not be able to produce lamella. If lamella are not produced at the first stage, no foam will be generated. This occurs for the SIS injection mode near the injection end. Away from the injection end, the surfactant will be in the aqueous phase while steam and nitrogen may follow a preferential path caused by gravity override or other factors. The low aqueous phase concentration in this particular path will not create foam generation phenomena.

Another possible cause of little foam generation is the continuous flushing action of gas. If the rate of surfactant injection is just equal to this quantity, all or most of the injected surfactant will end up in the produced gas. The lamella produced in this case will not have the required amount of surfactant to be stable, and thus there will be no foam generation.

4.7. Oil-Free Case

The sandpack used in this study was used to observe the behavior of surfactants in the two phase system, steam/water only, by Shallcross et al. (1990) and Hamida (1990).

The performance of the surfactants reported by Shallcross et al. were used for comparison with the oil-free case. These results are reported at a surfactant concentration of 0.1% by wt. as against 1.0% by wt. for this study.

The major observation was that SD1020 did not produce foam. AOS2024 produced a maximum pressure drop with a single injection (234 psi). AOS1618 followed with a response of (132, 247 psi), and this was followed by LTS18 (58 psi, 237 psi for 2 slugs). The durations of the pressure response, defined as the time when the pressure drop increased at a rate less than 1 psi/min., were 85, 68 and more than 120 minutes for AOS2024, AOS1618 and LTS18, respectively.

Foam propagation rate, as indicated by section responses of the surfactants, was highest for LTS18. AOS2024 was next best followed by AOS1618. The respective time lag in response to the first slug injections were 10, 20, and 30 minutes respectively. The results, taken from Shallcross et al. (1990), are shown in Figures 3.2.12 through 3.2.17.

4.8. Comparison With Oil-Free Case

In the absence of oil, AOS2024 created the maximum pressure drop, while in the presence of oil, LTS18 created the maximum pressure drop. The high propagation rate of LTS18 in both cases improved the performance in the presence of oil. The surfactant, SD1020, did not create foam in the absence of oil. However, in the presence of oil, its performance was comparable with AOS2024. This implies that dimerized surfactants perform better in the presence of oil.

The increase in alkyl chain length of a particular structure increased the performance irrespective of the presence of oil as the results of AOS2024 and AOS1618 indicate.

4.9. Theoretical Explanations

In this section we will analyze the causes for the observed behavior for various surfactants in the presence of oil. In three phase flow, it is not known how oil affects foam stability. However, the performance of a surfactant with a fast foam propagation rate is little affected by the presence of oil. The process can be understood by two existing postulates regarding the effect of oil on foams.

One of the mechanism observed is the interaction between aqueous foam films and emulsified oil droplets. The foam bubble ruptures due to destabilization of the psuedoemulsion films with the emulsified oil (Manlowe and Radke, 1988). The rupture times are much faster than the drainage time, which is the main cause of coalescence. If the oil/water contact time is less then the rupture time, the gas bubble persists. A fast propagation rate decreases the contact time, decreases the number of coalescences due to breakage of pseudoemulsion and, thus, increases the foam performance.

The second postulate links the spreading of oil on a gas bubble surface as a main cause of coalescence. In this case, the imbibition of oil particles occurs before spreading. While imbibition depends upon surface forces, the amount of oil deposited on a particular gas bubble will depend upon the oil/bubble contact time. Insufficient spreading of oil on a gas bubble will not affect the lamella, and the gas bubble will collapse due to other factors like drainage or film thinning. Obviously, the amount of oil deposition depends upon the contact time, and will be less in case of a rapidly moving bubble. The foam propagation rate affects the life of individual bubbles. A rapid foam propagation rate will lessen oil effects.

The observation that high-oil saturation decreases the foam strength can also be explained by these postulates. Increase in oil saturation increases the average pore size where oil is present, and increases the pore throat size. The increase in the contact time

is due to an increase in the pore throat size where the oil/lamella interaction occurs. The bubble rupture rate should increase, decreasing the foam strength. On analogy, an increase in the area of contact results in increasing the oil deposition on the bubble surface and, increasing the number of coalesces. How the foam propagation rate changes due to the structural change of the surfactant remains unanswered.

3.2.4 CONCLUSIONS

The following conclusions may be drawn from the study.

1. For the experimental conditions studied, a linear toluene sulfonate surfactant generated the strongest foam in the presence of oil.
2. The propagation rate of the foam generated by a surfactant measures the resistance of foam to oil. The faster the propagation of a foam, the more oil resistant it is.
3. Only disulfonate surfactants created strong foams in the presence of oil as compared to the absence of oil.
4. Generally foam strength decreases with an increase in oil saturation.
5. Under the experimental conditions, the linear toluene sulfonate LTS18 generated a strong and fast propagating foam, and was superior to the foams generated by any of the other surfactants tested in this study.
6. Under the experimental conditions, the strength of foam produced by an alpha olefin surfactant increases with the increase in alkyl chain length.
7. Adsorption/partitioning losses seem larger for disulfonates than for monosulfonates.

Table 3.2.1 Experimental Conditions

EXPERIMENTAL CONDITIONS	
SANDPACK PROPERTIES	
LENGTH	1.83m (6.0 ft)
DIAMETER	54.8mm (2.16 in)
POROSITY	33 %
ABSOLUTE PERMEABILITY	89.8 μm^2 (89.8 D)
PORE VOLUME	1500 ml (0.0502 ft^3)
CRUDE OIL:	MOBIL'S NEWPORT BEACH CRUDE OIL
INJECTION RATES	
BACK PRESSURE	580 kPa (70 psig)
STEAM INJECTION RATE	4.0 ml/min
NITROGEN INJECTION RATE	0.081 l/min
SURFACTANT INJECTION RATE	9.0 -10.0 ml/min
SURFACTANT CONCENTRATION	1.0 wt % (Active)
SLUG VOLUME	150 ml
SODIUM CHLORIDE CONCENTRATION	1.0 wt %
SURFACTANTS USED	
RUN 11	ALPHA OLEFIN SULFONATE AOS2024
RUN 12	LINEAR TOLUENE SULFONATE LTS18
RUN 13	SD-1020 (CHEVRON TRADE NAME)
Run 14	ALPHA OLEFIN SULFONATE AOS1618

Table 3.2.2 Surfactant Performance in Presence of Oil

Run	SLUG NO	SEC-TION 1	SEC-TION 2	SEC-TION 3	SEC-TION 4	TOTAL PRESSURE DROP
11 AOS-2024	1	1.4	0.4	0.4	0.0	2.0
	2	2.0	6.0	6.2	0.4	12.0
	3	3.0	8.0	8.4	0.5	16.0
	4	3.4	7.8	8.4	0.5	17.0
12 LTS-18	1	2.6	2.2	0.6	0.5	6.0
	2	5.6	9.0	7.5	5.0	20.0
	3	7.0	9.4	8.2	6.0	23.0
13 SD-1020	1	3.8	1.4	0.0	0.0	5.0
	2	4.6	2.8	0.0	0.0	6.0
	3	5.6	5.4	5.0	2.0	15.0
14 AOS-1618	1	0.7	0.8	0.3	0.0	1.5
	2	0.9	0.9	0.6	0.0	2.5
	3	1.0	1.8	0.6	0.0	3.4
	4	1.0	2.5	0.8	0.0	3.6

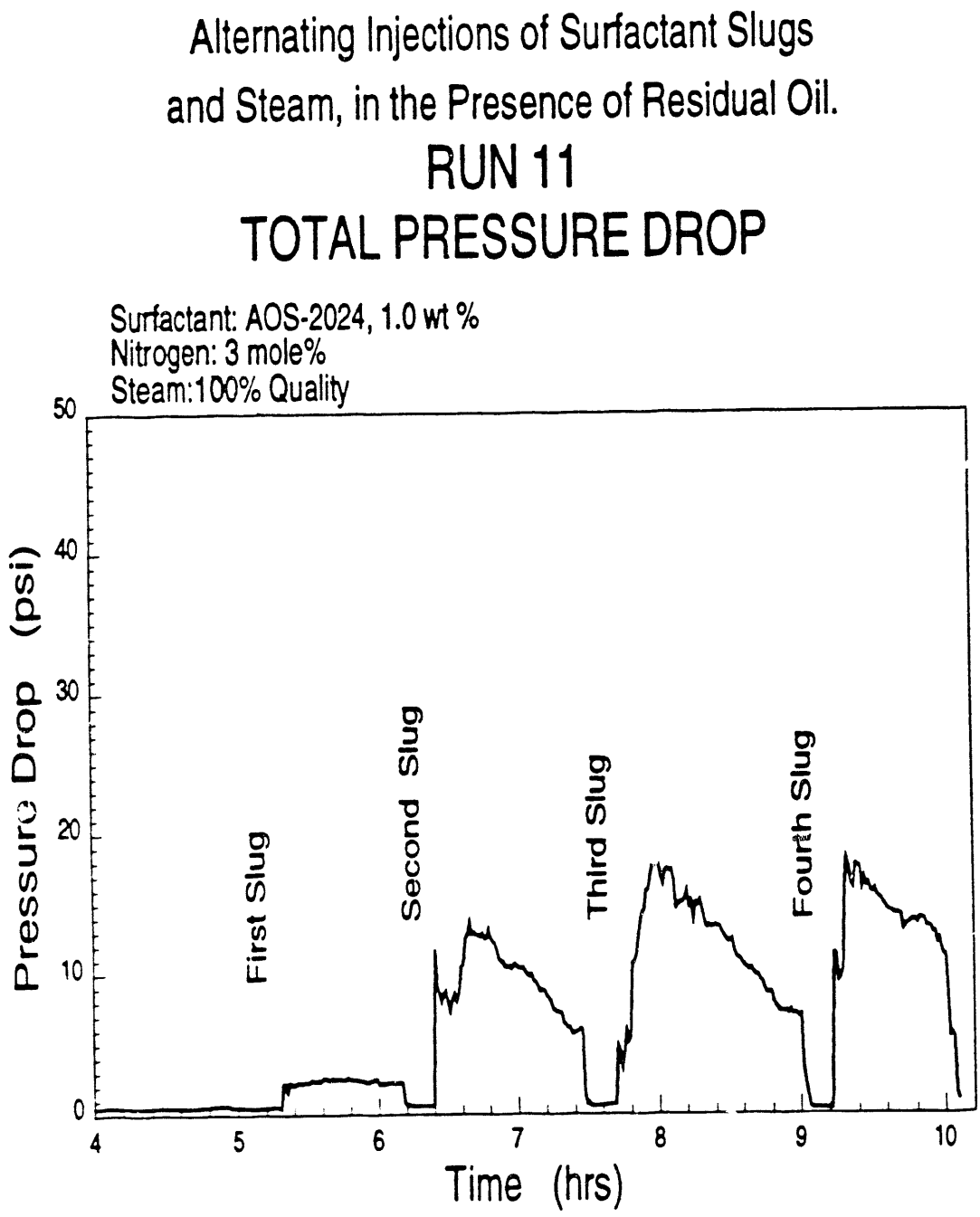

Figure 3.2.1 RUN 11, AOS 2024: Pressure-drop across the sandpack.

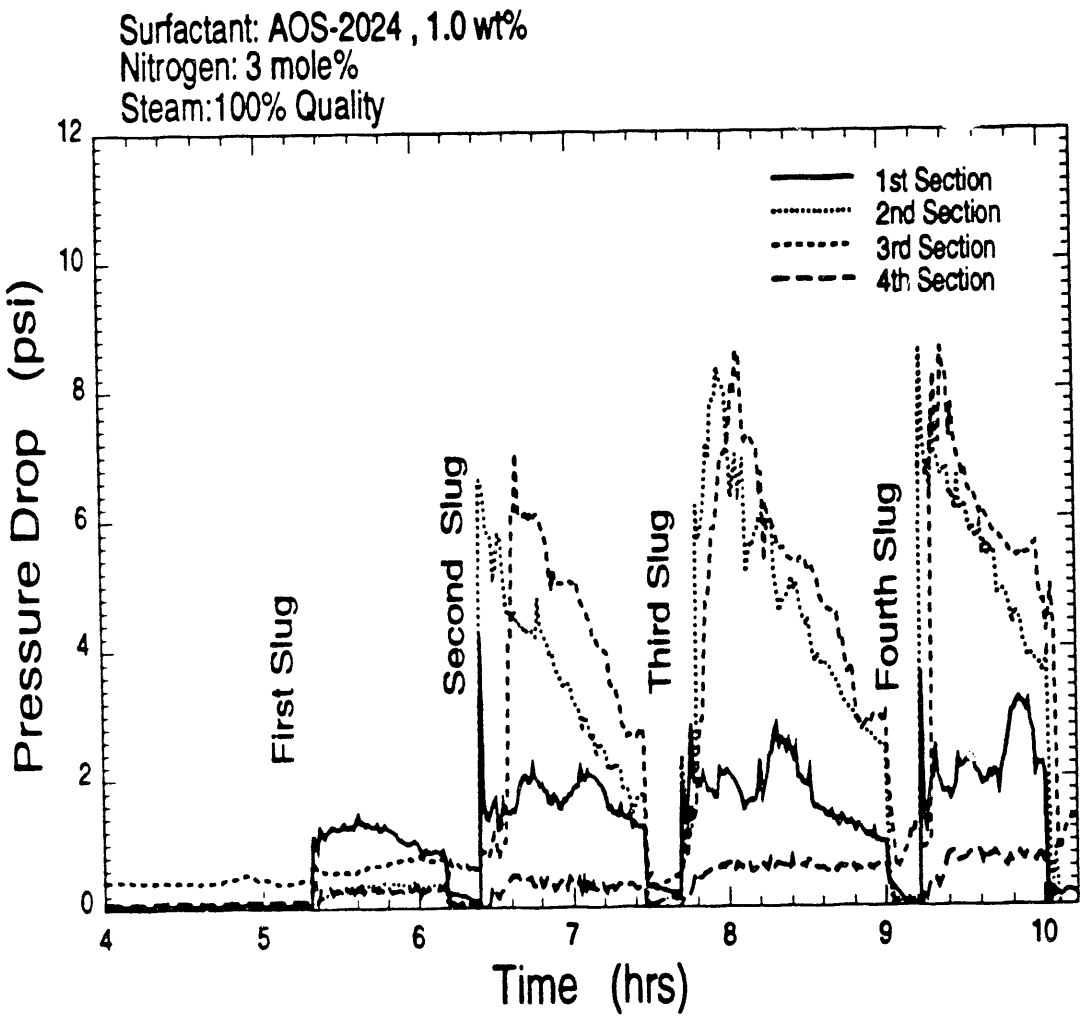

Figure 3.2.2 RUN 11, AOS 2024: Section-wise pressure drop across the sandpack.

Alternating Injections of Surfactant Slugs and Steam, in the Presence of Residual Oil.
RUN 11

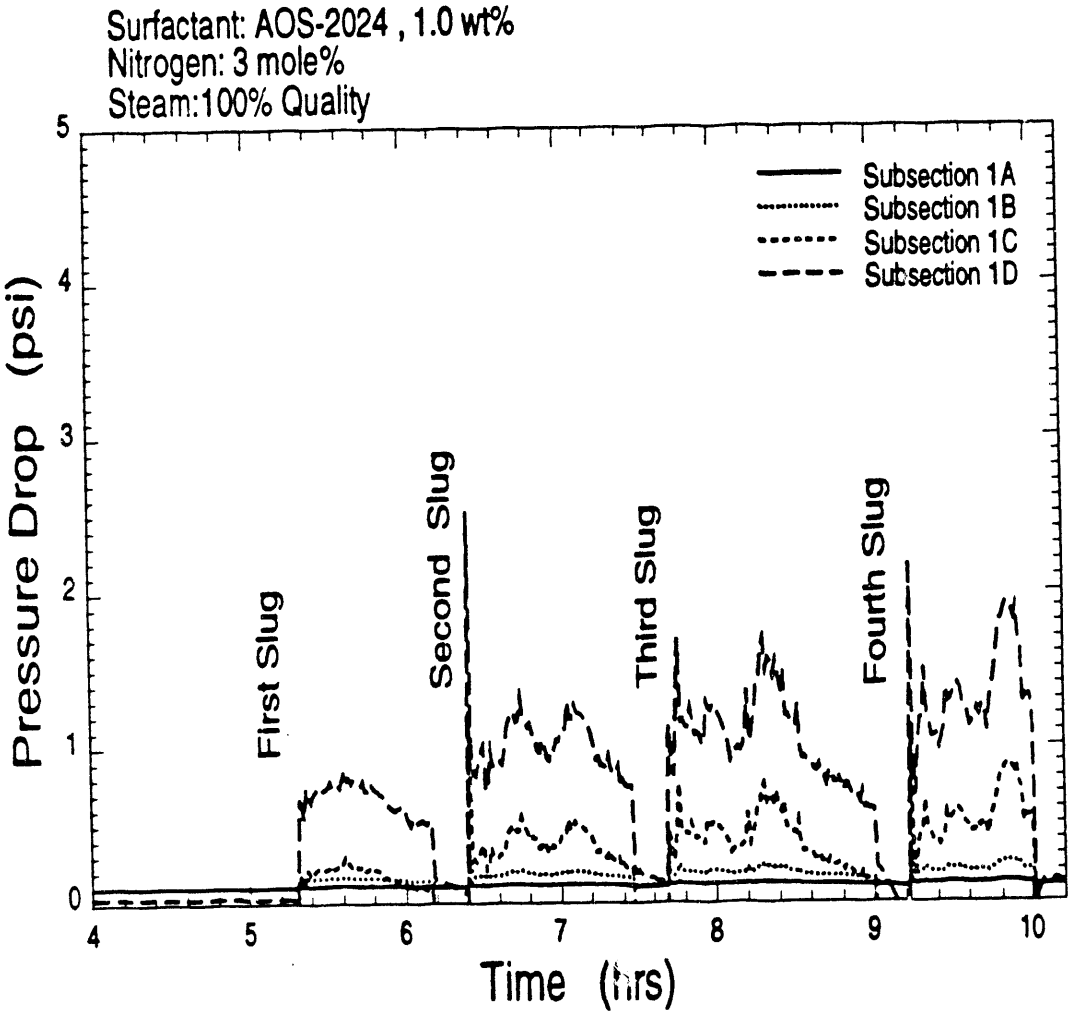

Figure 3.2.3 RUN 11, AOS 2024: Pressure-drop across the sandpack of inlet sections.

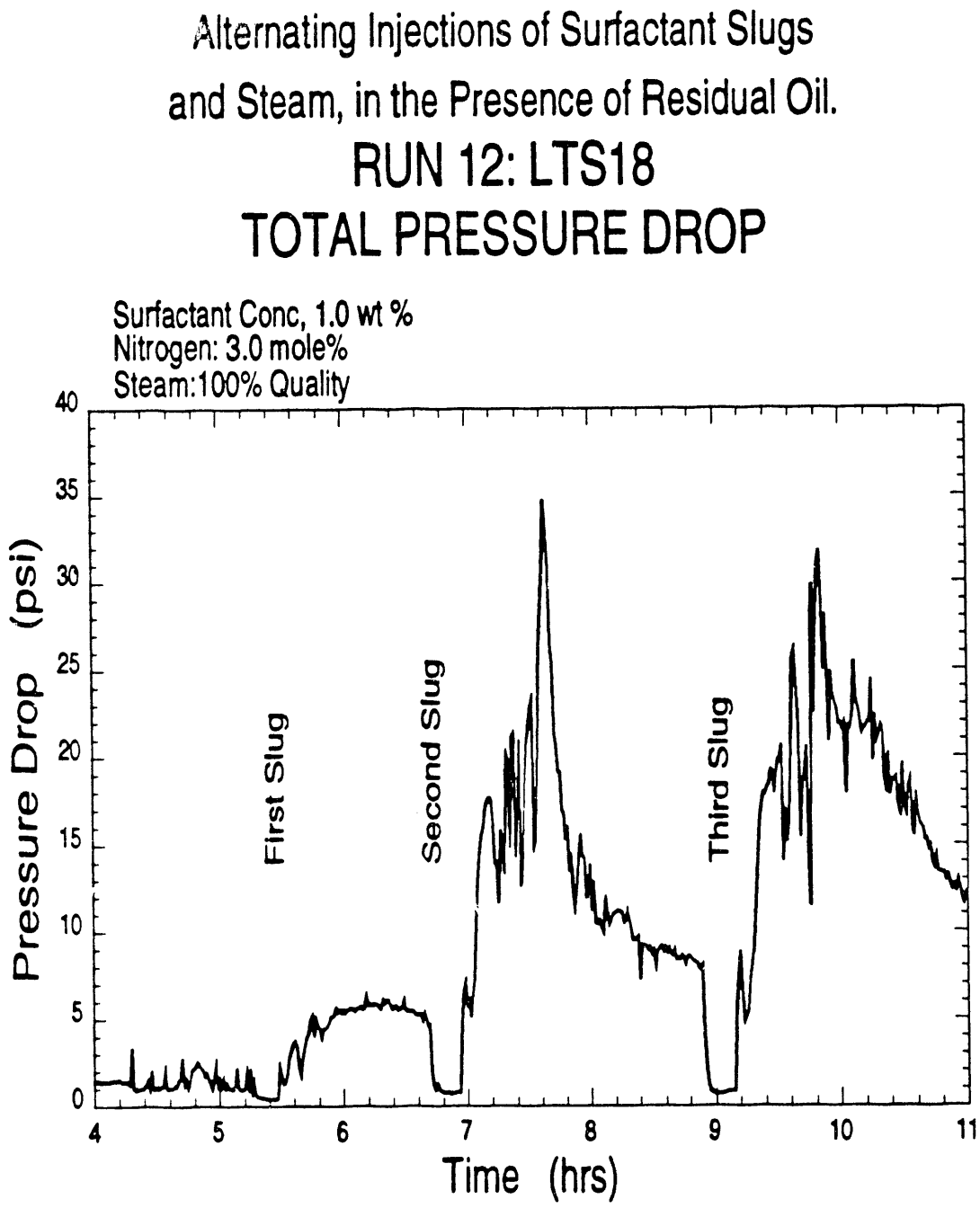

Figure 3.2.4 RUN 12, LTS 18: Pressure-drop across the sandpack.

Alternating Injections of Surfactant Slugs
and Steam, in the Presence of Residual Oil.
RUN 12 : LTS18

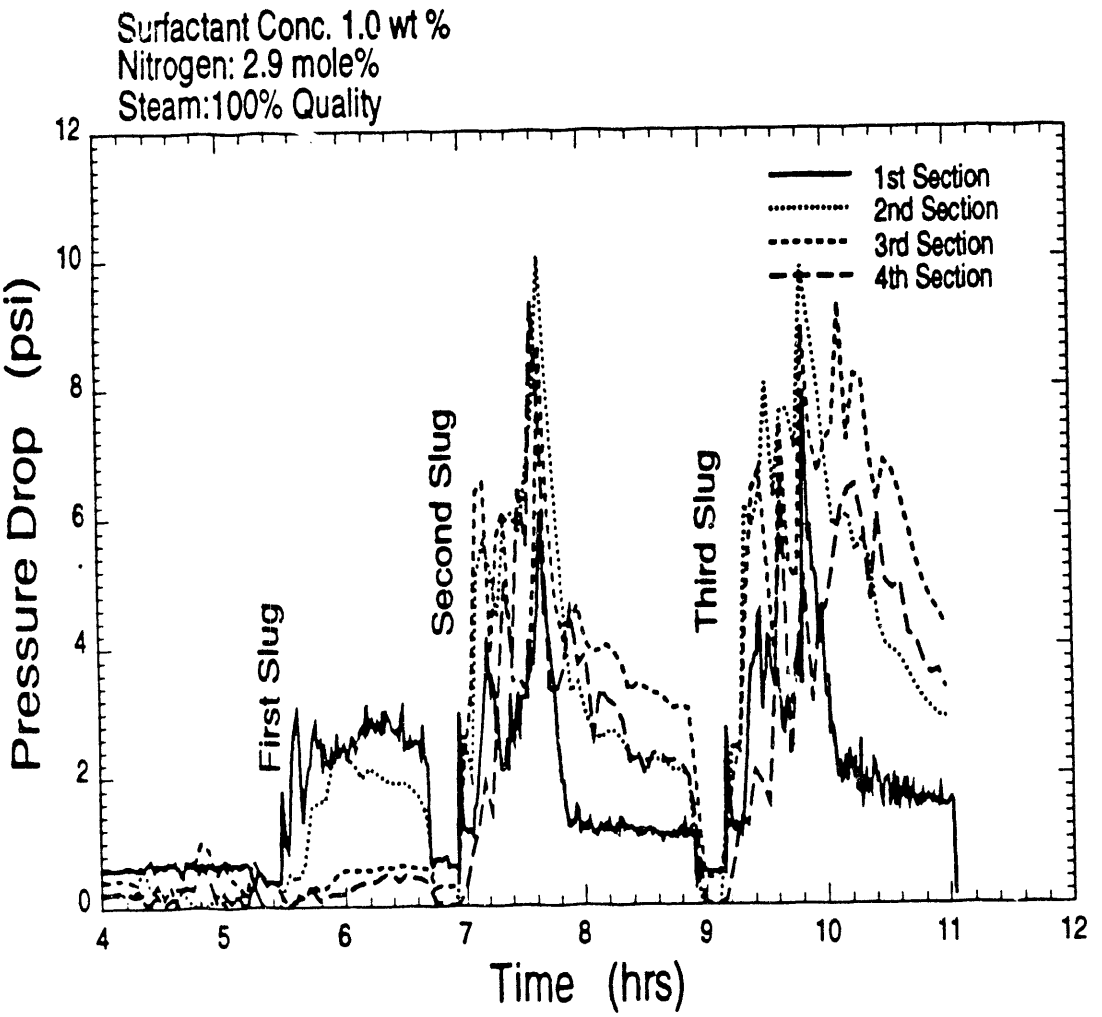

Figure 3.2.5 RUN 12, LTS 18: Section-wise pressure-drop across the sandpack.

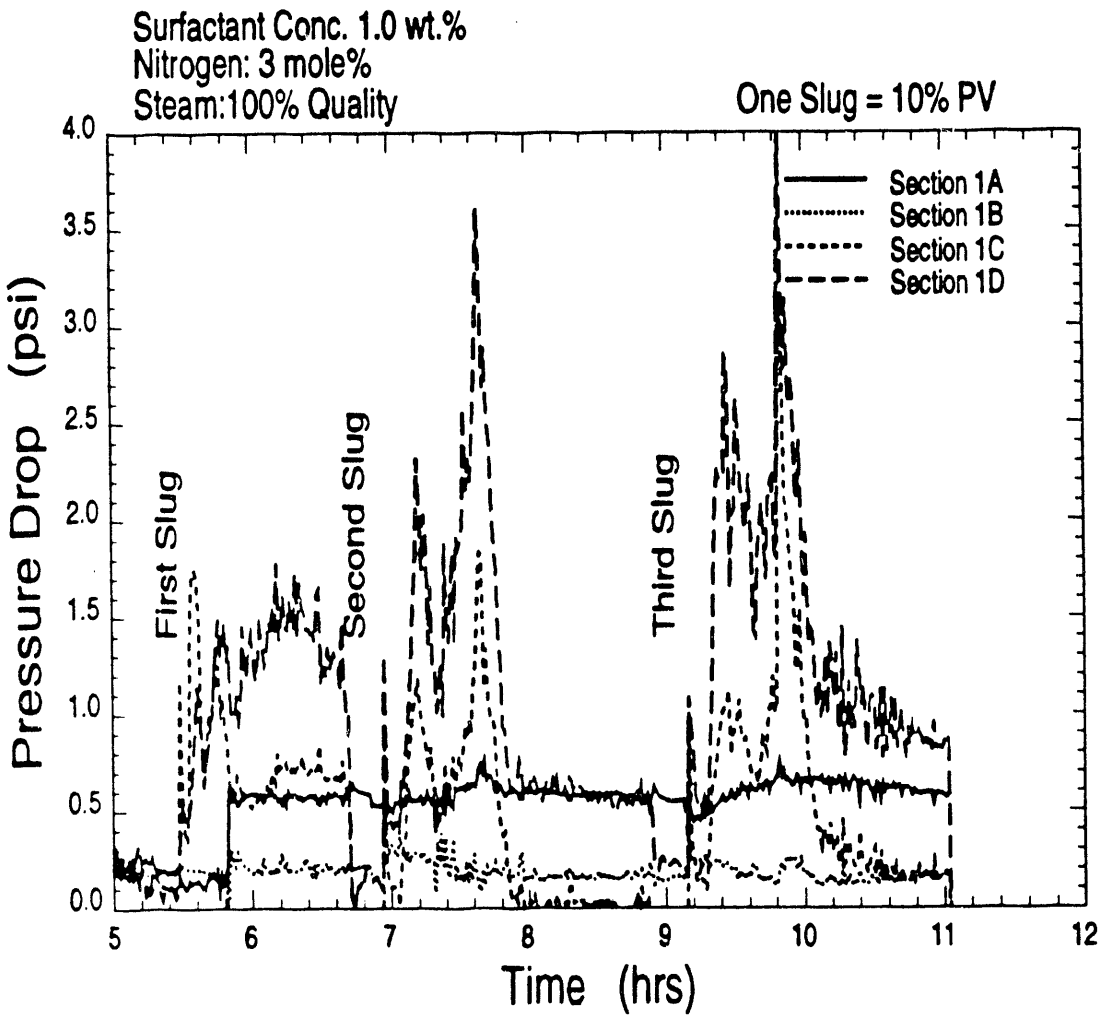

Figure 3.2.6 RUN 12, LTS 18: Pressure-drop across the sandpack of inlet sections.

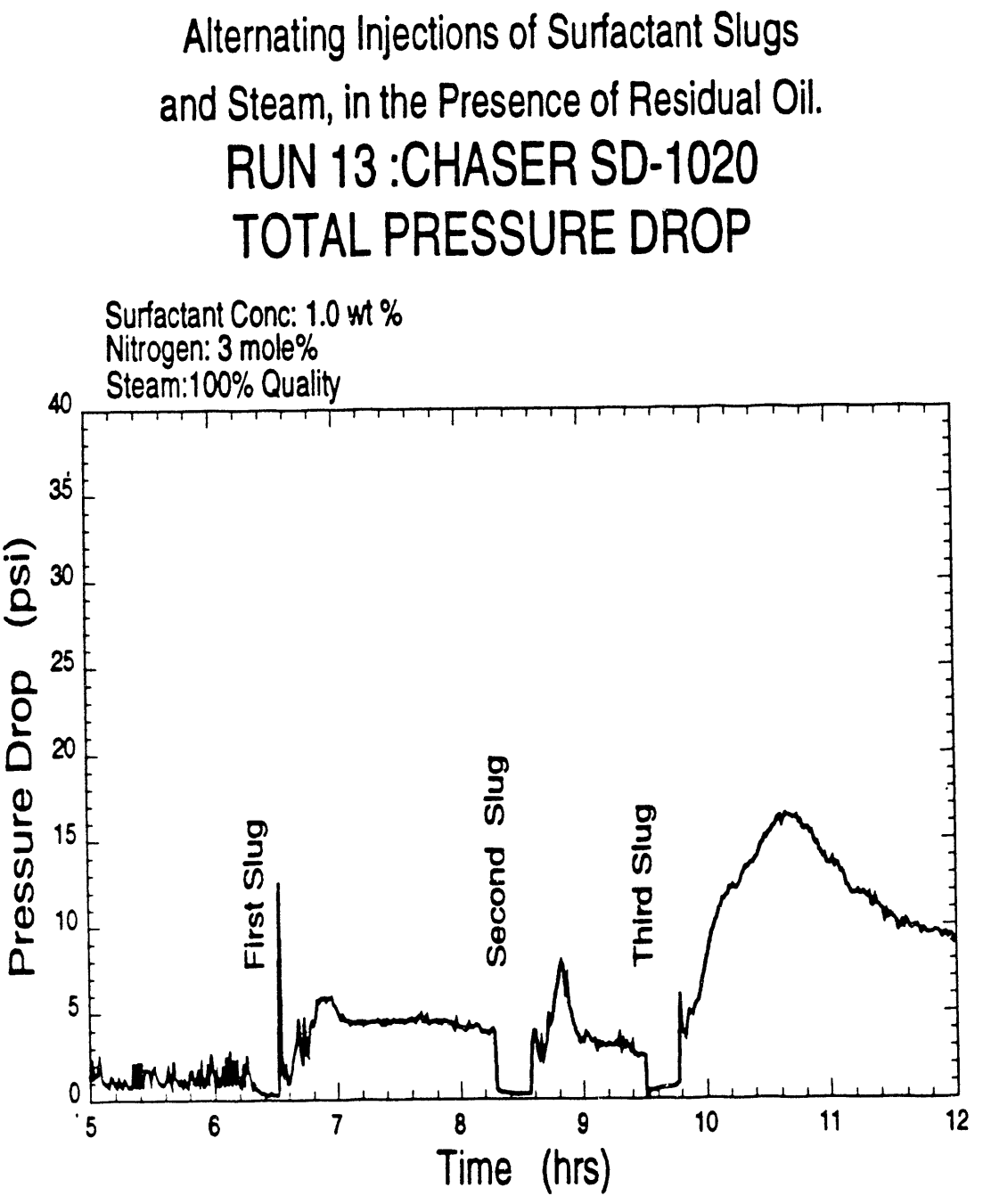

Figure 3.2.7 RUN 13, SD 1020: Pressure-drop across the sandpack.

Alternating Injections of Surfactant Slugs and Steam, in the Presence of Residual Oil.

RUN 13: CHASER SD1020

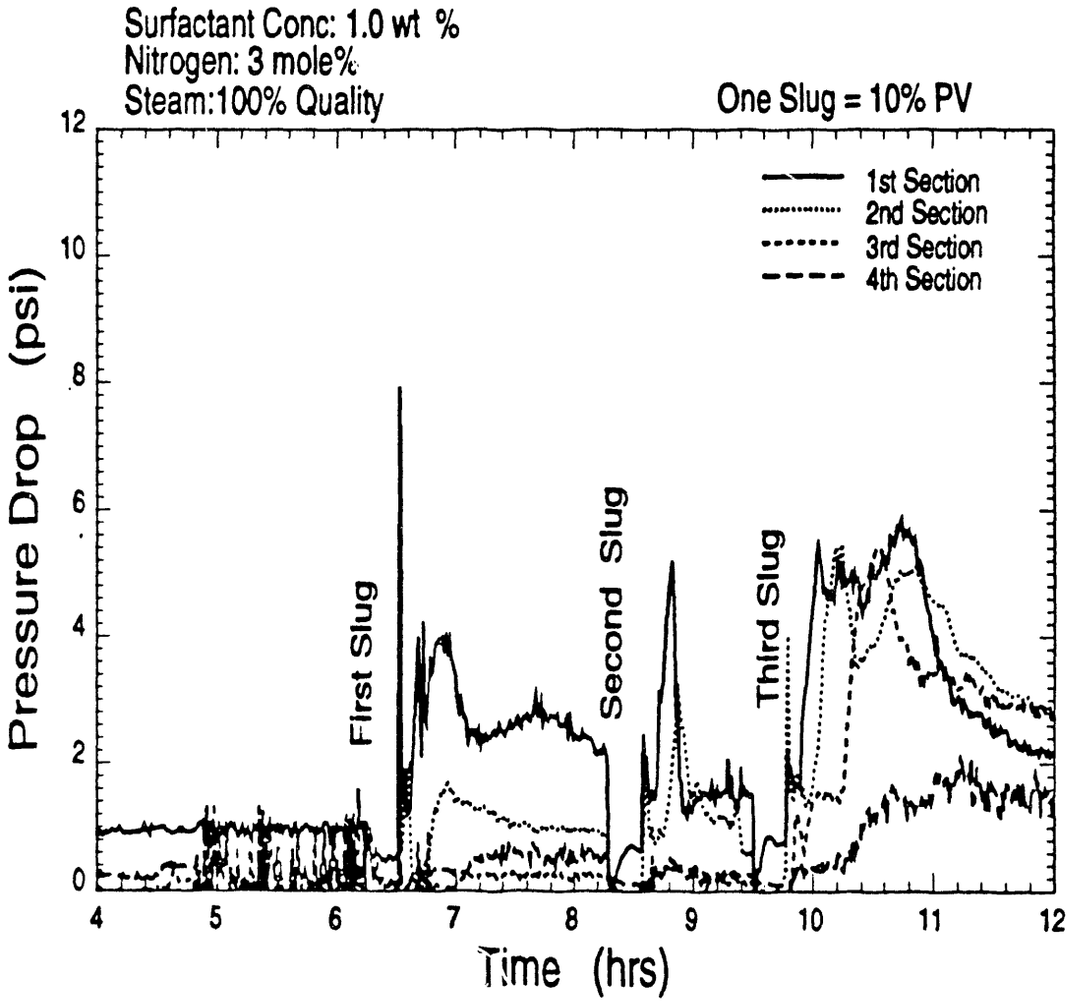

Figure 3.2.8 RUN 13, SD 1020: Section-wise pressure-drop across the sandpack.

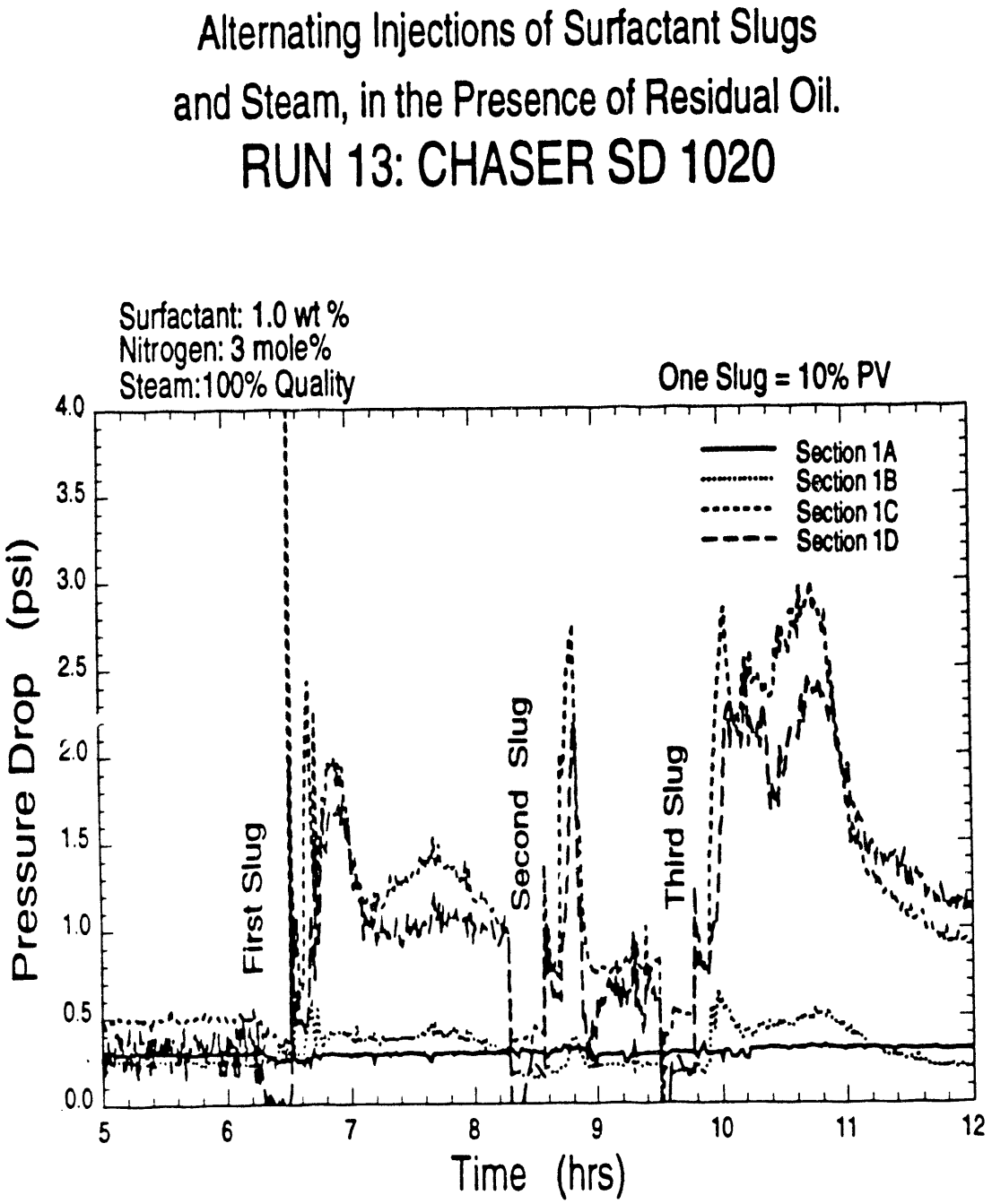

Figure 3.2.9 RUN 13, SD 1020: Pressure-drop across the sandpack of inlet sections.

Alternating Injections of Surfactant Slugs
and Steam, in the Presence of Residual Oil.

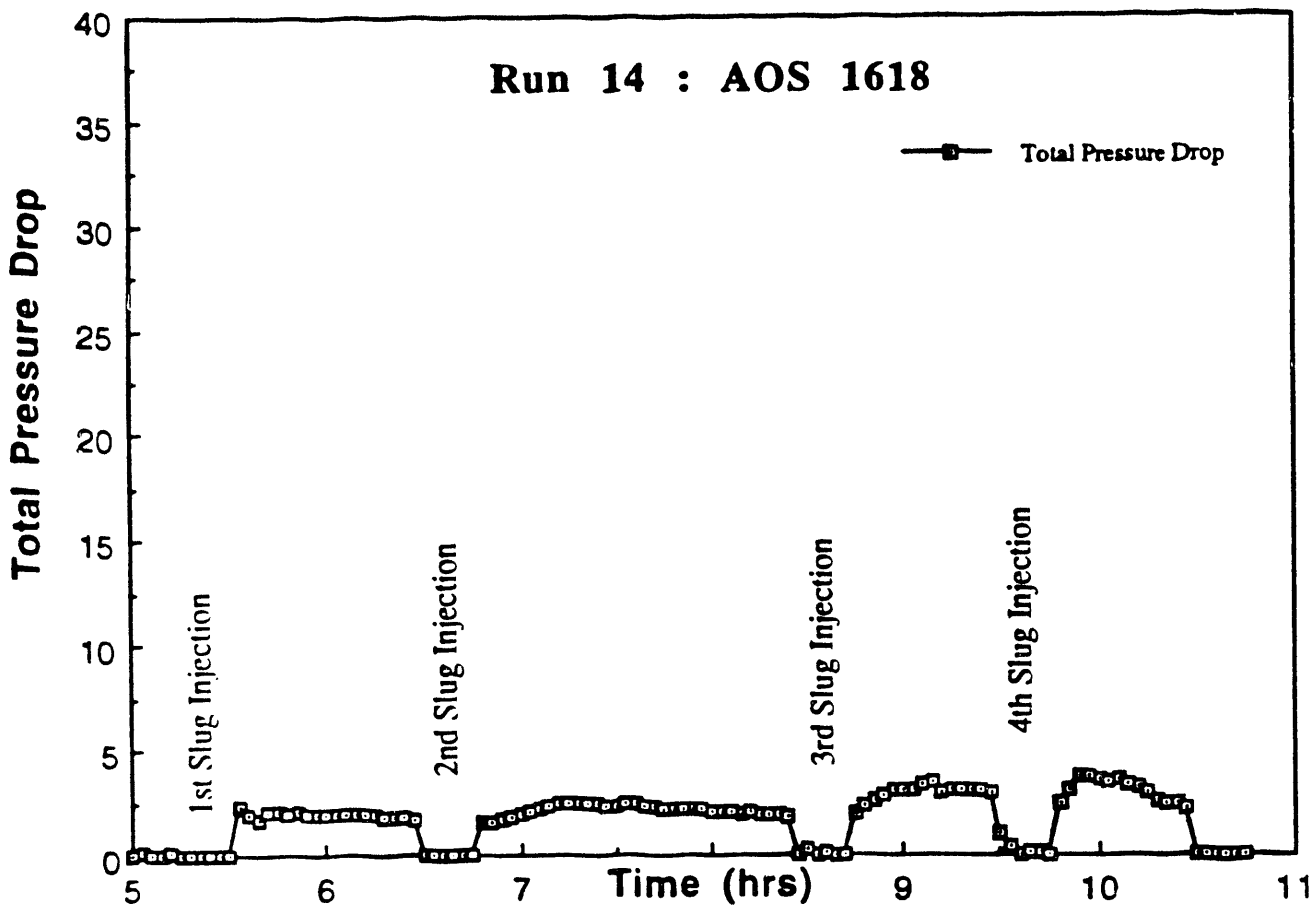

Figure 3.2.10 RUN 14, AOS 1618: Pressure-drop across the sandpack.

Alternating Injections of Surfactant Slugs
and Steam, in the Presence of Residual Oil.

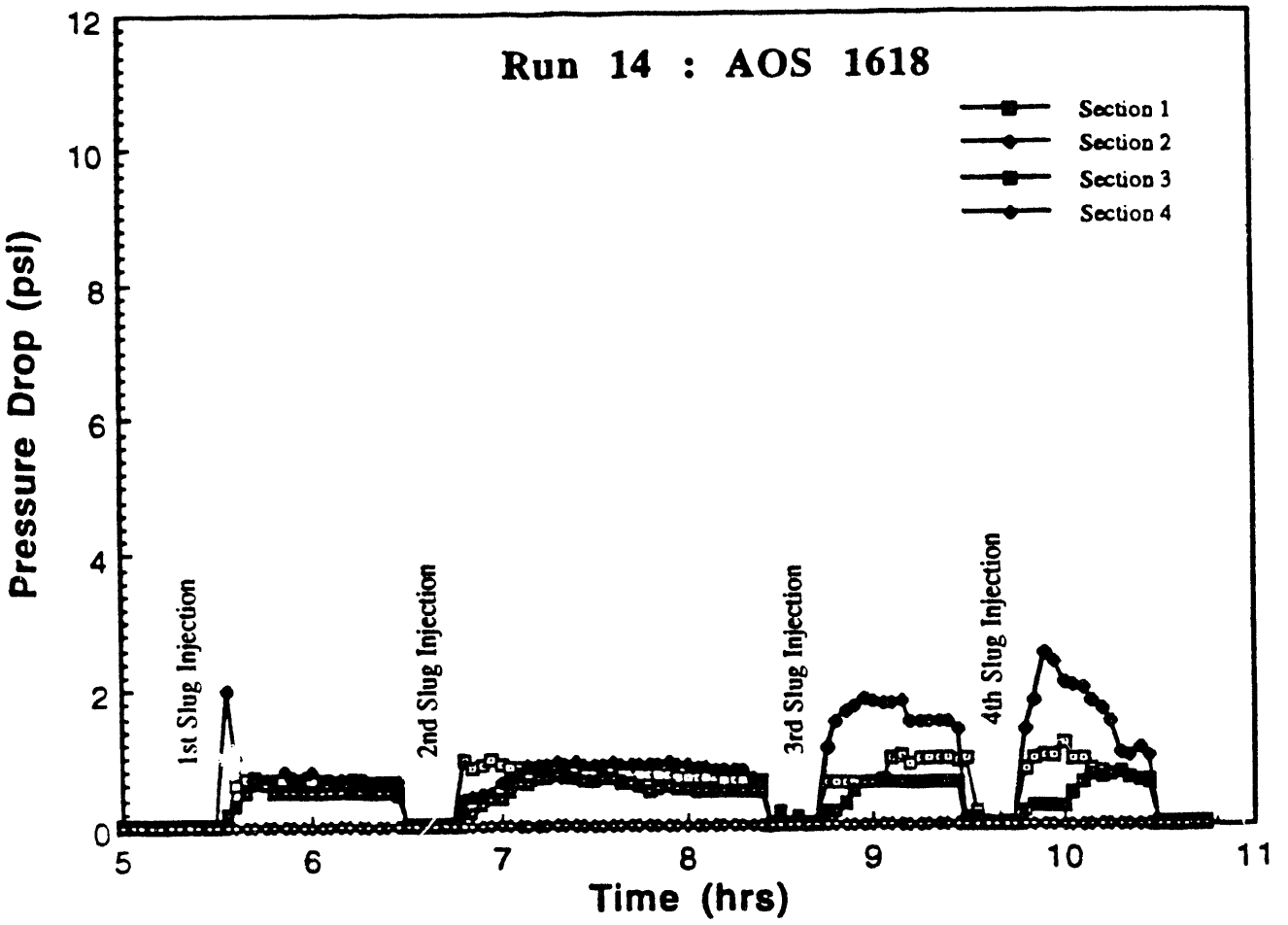

Figure 3.2.11 RUN 14, AOS 1618: Section-wise pressure-drop across the sandpack.

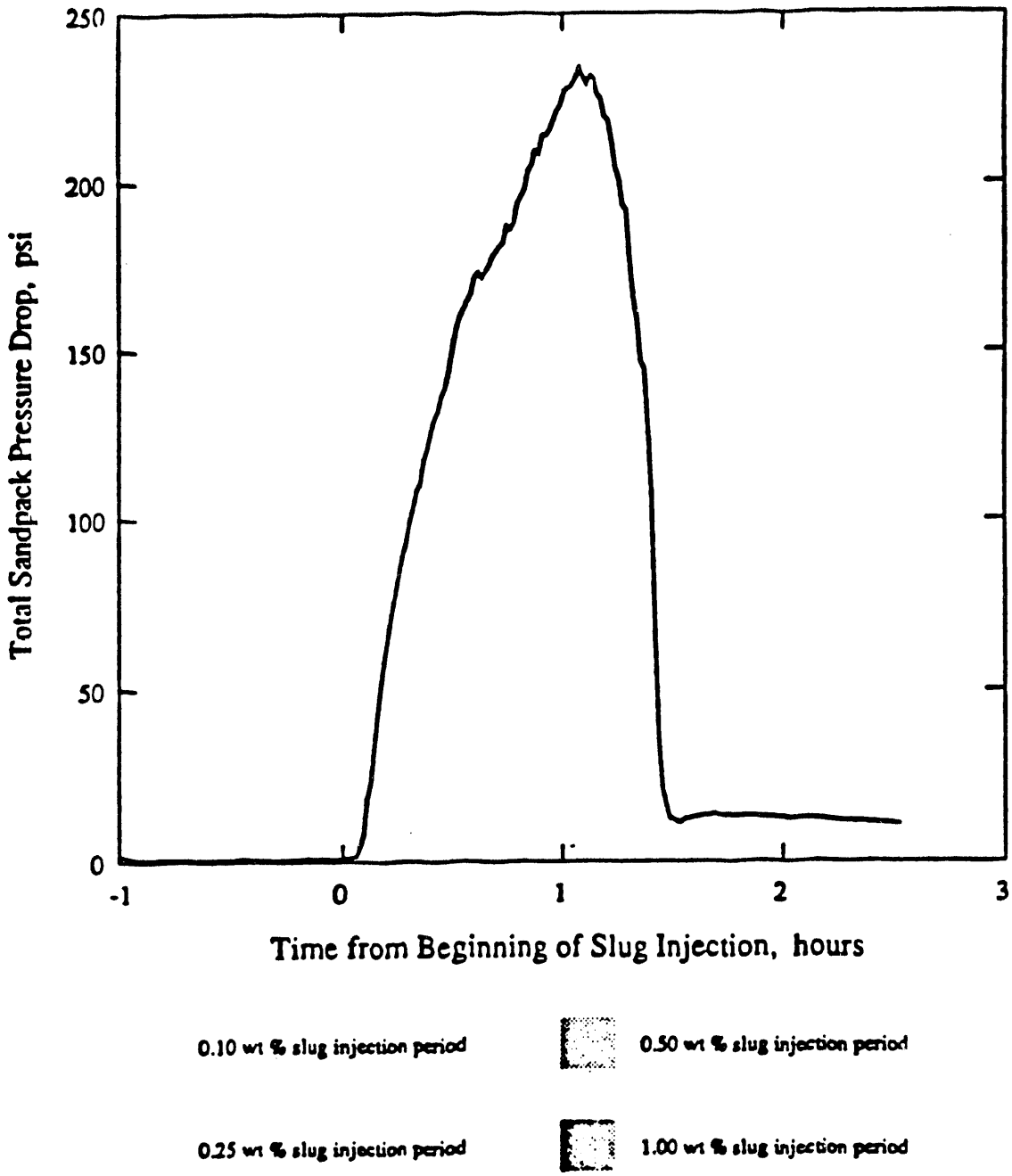

Figure 3.2.12 Pressure-drop across the sandpack in the absence of oil for AOS 2024 (after Shallcross, 1990, Fig. 5.36).

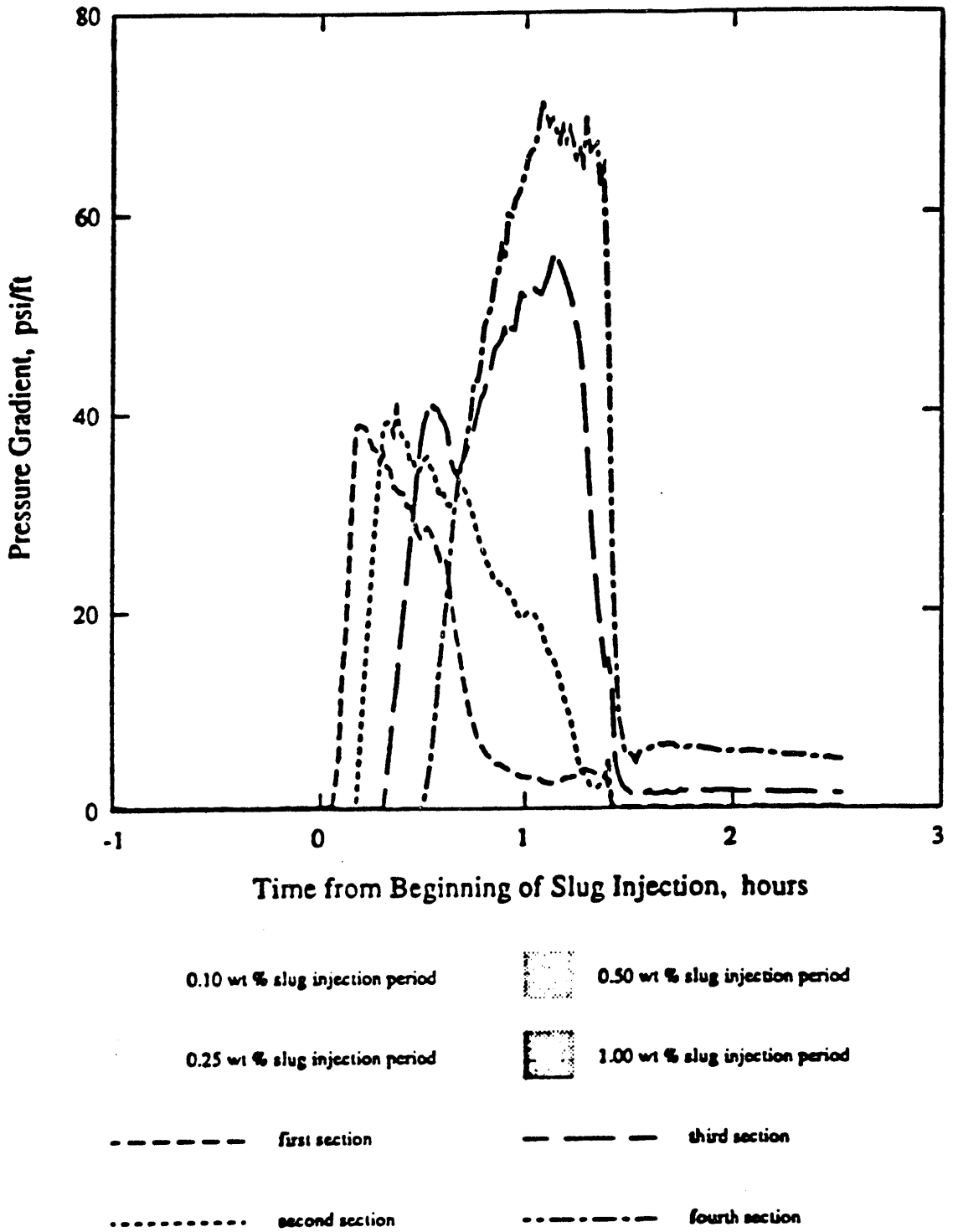

Figure 3.2.13 Section-wise pressure-drop across the sandpack in the absence of oil for AOS 2024 (after Shallcross, 1990, Fig. 5.37).

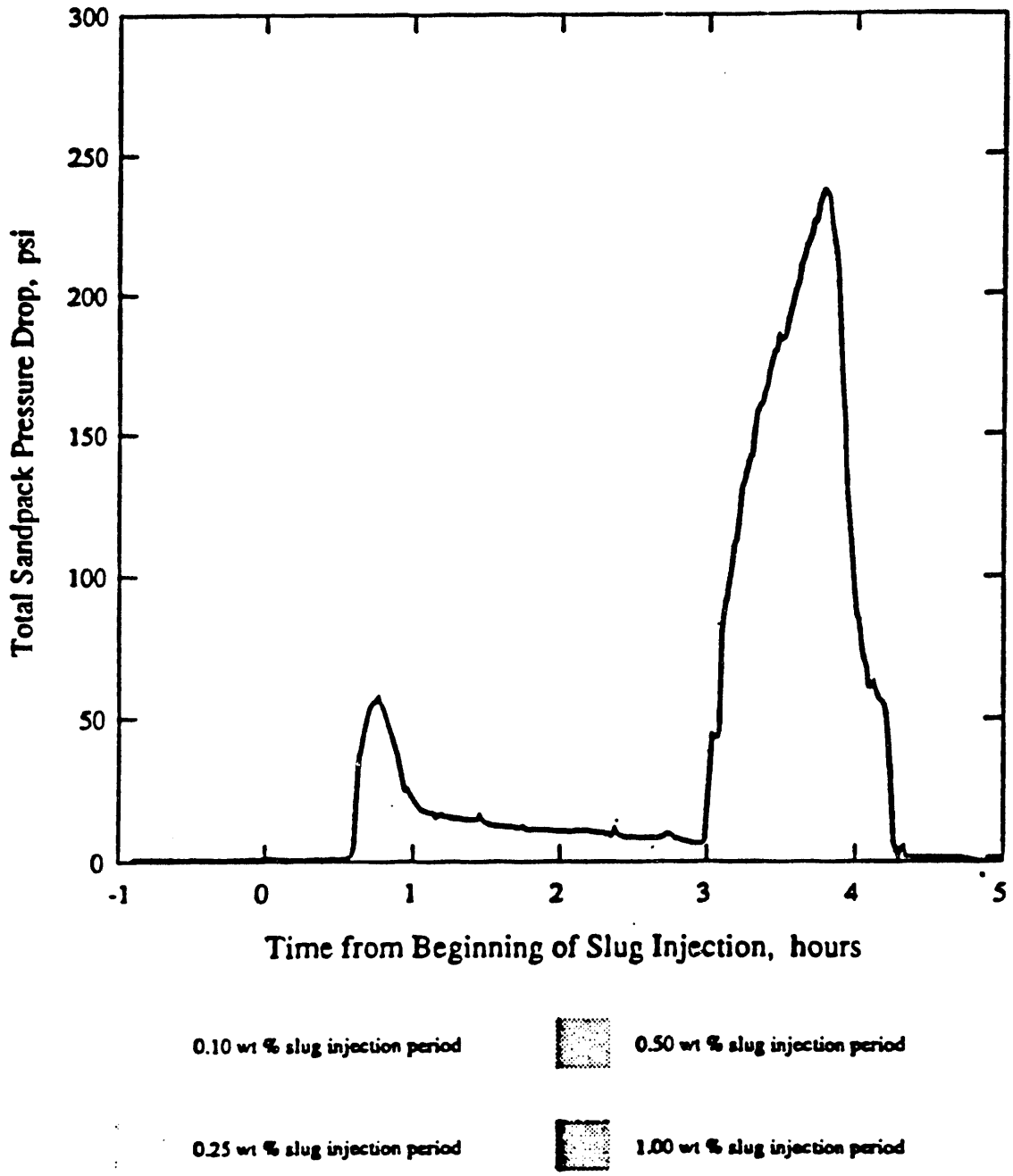

Figure 3.2.14 Pressure-drop across the sandpack in the absence of oil for LTS 18, (after Shallcross, 1990, Fig. 5.57).

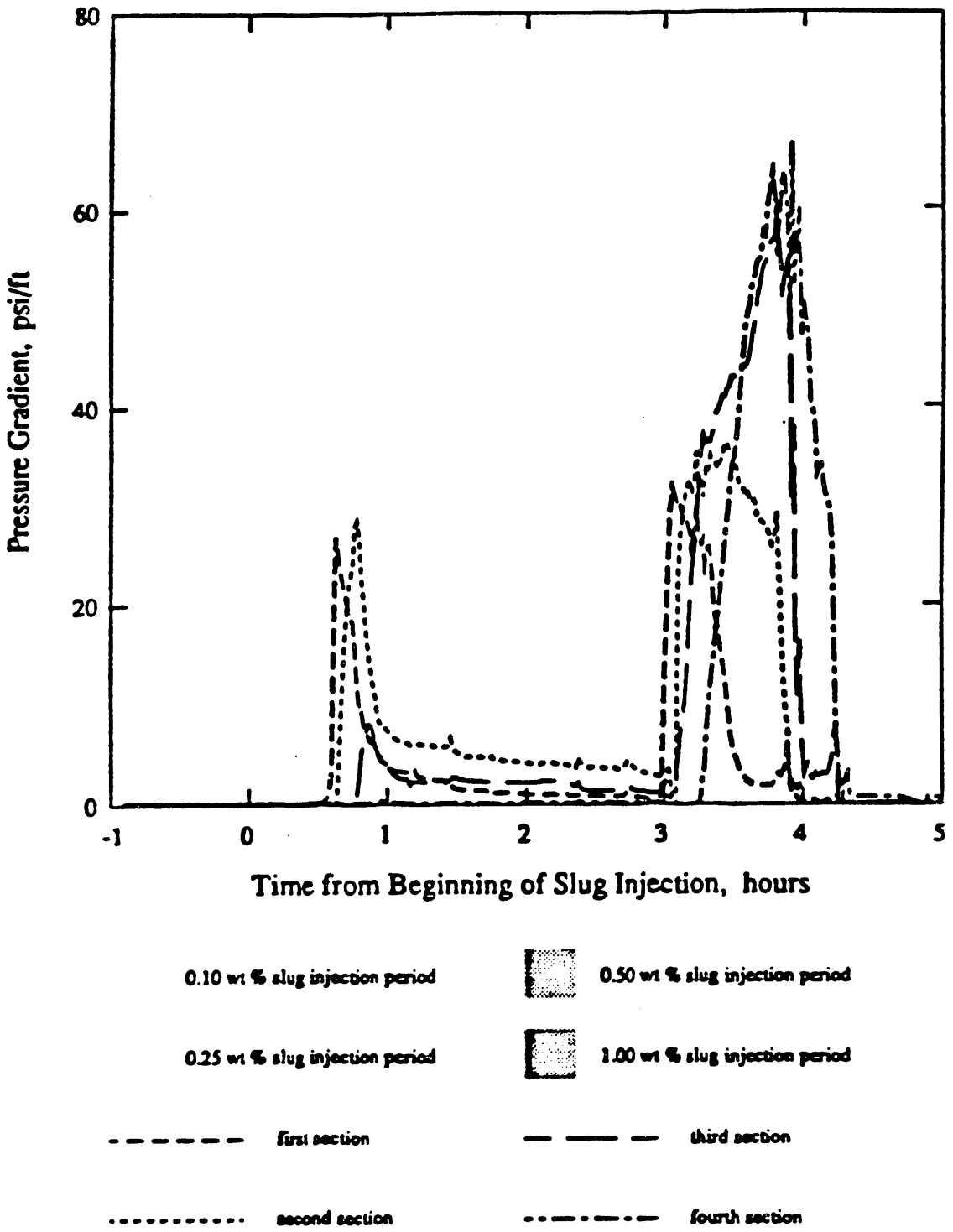

Figure 3.2.15 Section-wise pressure-drop across the sandpack in the absence of oil for LTS 18 (after Shallcross, 1990, Fig. 5.58).

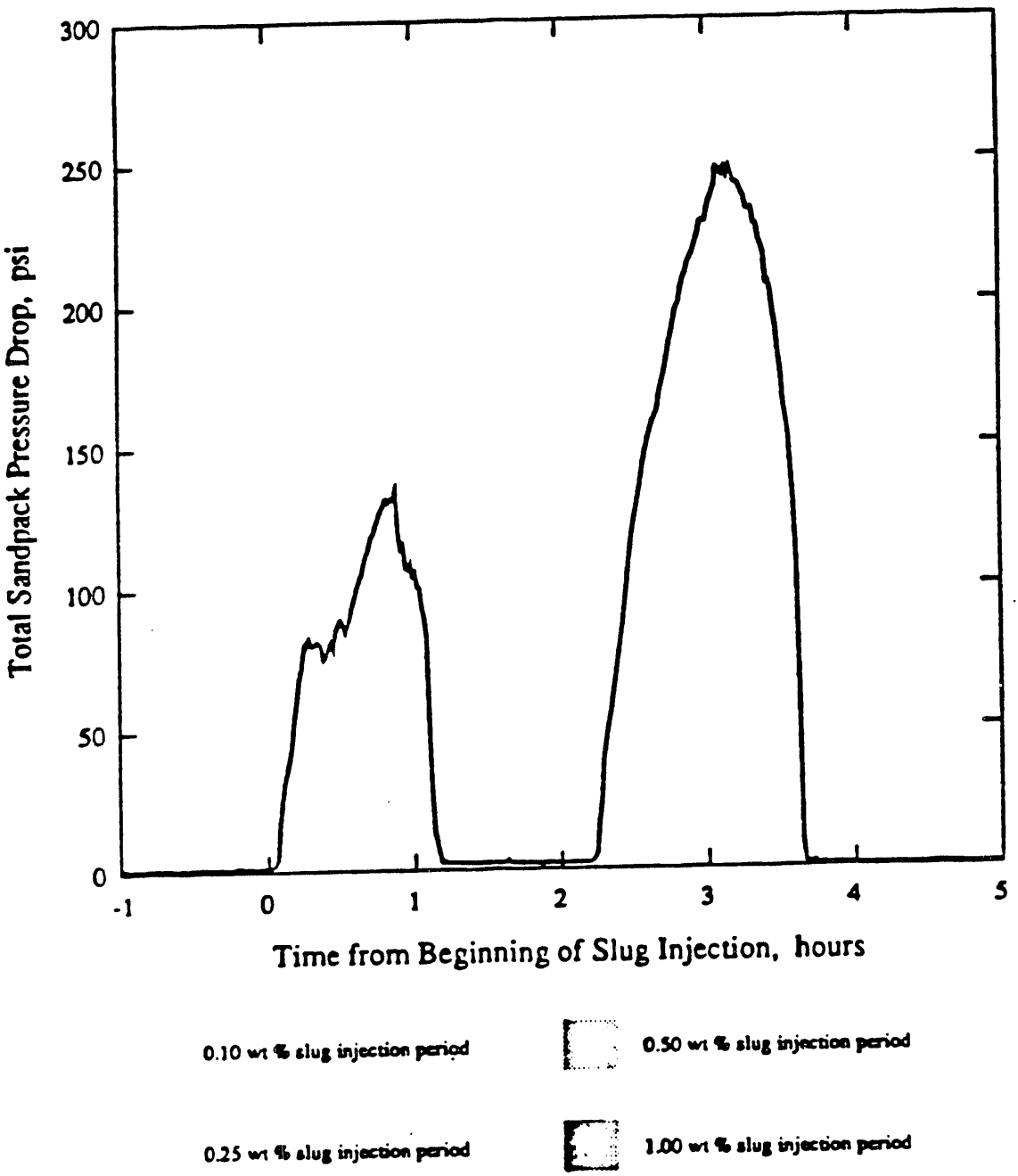

Figure 3.2.16 Pressure-drop across the sandpack in the absence of oil for AOS 1618 (after Shallcross, 1990, Fig. 5.32).

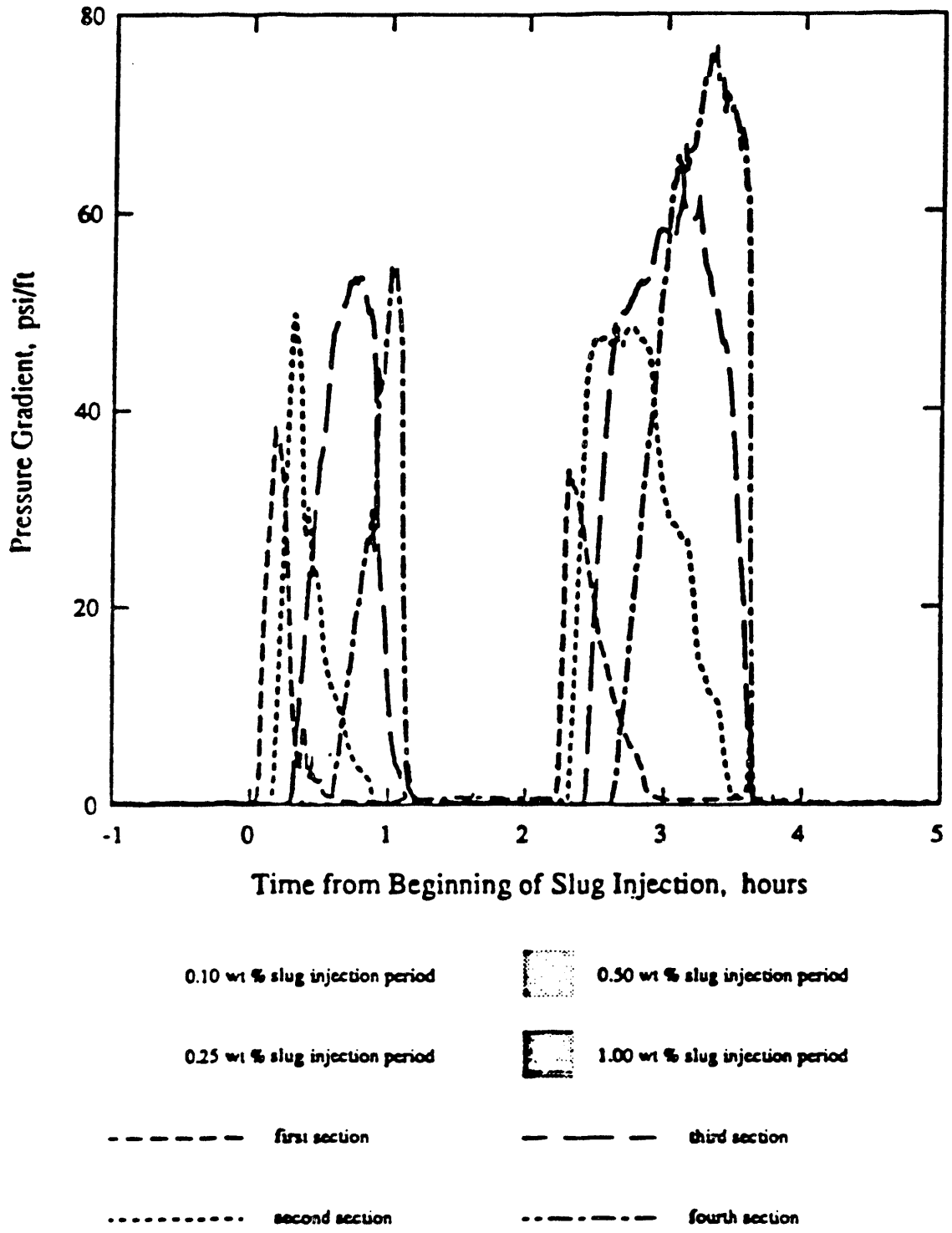

Figure 3.2.17 Section-wise pressure-drop across the sandpack in the absence of oil for AOS 1618 (after Shallcross, 1990, Fig. 5.33).

3.3 CT IMAGING OF STEAM AND STEAM FOAM LABORATORY EXPERIMENTS (B. M. R. Demiral)

3.3.1 ABSTRACT

The CT imaging technique together with temperature and pressure measurements were used to follow steam propagation during steam and steam foam injection experiments in a three-dimensional laboratory steam injection model. During the design period, the advantages and disadvantages of different geometries were examined to find out which could best represent radial and gravity override flows and also fit the dimensions of the scanning field of the CT scanner. As a result of this analysis, a 3D rectangular box with dimensions 20x20x7.5 cm was constructed. This box simulates one quarter of a five spot pattern. Aluminum, Teflon^{TM} and Fiberfrax^{TM} were chosen as supporting and insulating materials. Teflon^{TM} was placed between the porous medium and the aluminum shell so that the rate of heat transfer in the porous medium would be much faster than that in the aluminum during a steam injection run. During experiments, steam was injected continuously at a constant rate into the water-saturated model, and CT scans were taken at six different cross sections of the model. Pressure and temperature data were collected with time at three different levels in the model. CT pictures and three-dimensional temperature distributions were compared and analyzed in terms of the observed steam zone at each section. To do that, CT numbers within the scan section were used to determine the steam and water zones, and with the aid of x-ray pictures, the position and propagation of the steam zone were determined. In addition, using the three-dimensional temperature distribution measurements at the same times, steam displacement fronts could be drawn at the scan-section locations. These pictures and drawings were used to compare the results obtained from classical temperature-pressure monitoring and from CT scans.

During steam injection experiments, the saturations obtained by CT matched well with the temperature data. That is, the steam override as observed by temperature data was also clearly seen on the CT pictures.

During the runs where foam was present, the saturation distributions obtained from CT pictures showed a piston like displacement. However, the temperature distributions were different depending on the type of steam foam process used. During the experiment which included non-condensible gas (nitrogen) injection, the temperature distributions, contrary to the saturation distributions, still indicated the presence of steam override, although the override was reduced by the foam. When there was no nitrogen, the temperature distributions followed the saturation distributions. This may indicate that the nitrogen foam ahead of steam foam caused the difference between temperature and saturation distributions. These results show that pressure/temperature data alone are not sufficient to study steam foam in the presence of non-condensible gas.

3.3.2 INTRODUCTION

Although invented for medical purposes in 1972 (Haunsfield, 1972), CT scanners have been heavily used in petroleum engineering applications. A CT scanner can be a useful tool for insitu saturation and porosity determinations and investigations of coreflood experiments (Wellington and Vinegar, 1987; Withjack, 1988; Wang et al., 1984; Hove et al., 1987; Vinegar and Wellington, 1987) comparison of simulation results with coreflood experiments (Wellington and Vinegar, 1987) and EOR applications (Wellington and Vinegar, 1987; Withjack, 1988; Franshan and Jaroslaw, 1986; Chatzis et al., 1988; Withjack, 1988). Although CT scanners have been used to investigate the mechanisms of some EOR processes, these experiments were mainly carried out in linear models, with only a few in 3D models. This leads to poor

representation of phenomena such as gravity override and channeling. On the other hand, CT scanners aren't used for applications where high temperature and pressure play an important role, as in the case of thermal recovery processes. The high pressure and temperatures involved in laboratory simulation of thermal EOR methods require metallic coreholders making it difficult to use x-ray absorption techniques. The mechanisms of these processes, specifically steam and steam foam injection, have been investigated by using material balance techniques together with temperature and pressure data. Nevertheless, the displacement mechanisms during steam or steam foam processes could be examined in a better way if the insitu fluid saturations were known. Since CT Scanning has been proven to be a useful tool in determination of insitu fluid saturations, a laboratory model with x-ray scanning capability would be helpful in understanding displacement mechanisms during steam and steam foam injection experiments.

In this study a three-dimensional laboratory model was designed and constructed such that it could be used to measure temperature, pressure and heat loss data. The model was also designed such that construction material was not a limiting factor during scanning. The main advantage of this comprehensive data gathering approach is to offer new insight into the mechanisms of oil displacement by steam and steam foam.

3.3.3 EXPERIMENTAL EQUIPMENT AND PROCEDURE

One objective of a 3-D laboratory model is to represent field applications reasonably realistically. The design considerations included shape, radial flow pattern, dimensions of the scanning field of the SUPRI-A CT Scanner, minimizing heat loss from the model, and the possibility of cleaning the model between experiments without repacking it. The details of design and operation principles of this model are given by Demiral et. al. (1992). A 3D box with dimensions of 20x20x7.5 cm was constructed. This box simulates a quarter of a five spot pattern. It is not scaled to a specific field because we are interested in studying the flow mechanisms in a generic sense. Aluminum, Teflon^{TM} and Fiberfrax^{TM} were chosen as supporting and insulating materials. As can be seen from the injector/producer diagonal cross-section of the model, (Figure 3.3.1) the inner heat insulation (Teflon^{TM}) is in direct contact with the porous medium. We felt it was necessary to use Teflon^{TM} in contact with the porous medium because of chemical and temperature stability. Because of its low thermal conductivity (0.1333 BTU/hr °F ft), the rate of heat transport in the porous medium (by means of conduction and convection) is much faster than that of conductive heat transport in the aluminum construction material. Some type of metal was necessary to support the Teflon^{TM} for strength under the proposed pressure and temperature conditions. Aluminum was chosen as the construction material since it absorbs less x-ray energy than other possible materials. The Teflon^{TM} box was sealed against gas or liquid leaks by using Chemgrip^{TM}, a special epoxy which bonds Teflon^{TM} to Teflon^{TM} or Teflon^{TM} to metal. Fiberfrax^{TM}, a ceramic fiber insulating material which is inexpensive and can be applied as a wet putty which air dries to a semi-permanent cast, was used as a secondary insulation material around the aluminum. A top cover was introduced to compress the porous medium to assure there is no gas space above the pack. The injection well system was designed to allow injection of steam with a quality of 0 to 100% through the total depth of the well. This was done by placing a heater cartridge within an aluminum tube through which the steam flows (Figure 3.3.2).

The 3D model has heat flux sensors at four sides and on the top. The general working principles of these heat flux sensors were discussed by Shallcross and Wood (1990). These sensors were used to study the heat loss during the steam injection experiments. But the results obtained from these measurements will not be given in this report. The calculations made during the preliminary analytic heat transfer design were matched well by the experimental results.

The thermocouple and pressure tap locations were chosen as seen in Figure 3.3.3 to provide a clear area of 1.5 cm width between these locations for scanning. The model can be scanned at for scanning for scanning for scanninggggg six different locations. Two positioning tables, as seen on Figure 3.3.4, were used to position the 3D model precisely at these scanning locations to an accuracy of ± 0.005 cm during every scan. Laser pointers were used to align the model within the gantry.

The general experimental equipment, as seen on Figure 3.3.5, consists of three parts: injection system, 3D steam model and production equipment.

Injection System: Two liquid chromatography pumps were used to inject water or surfactant solution and to feed the steam generator with distilled water. There was also a gas mass flow controller which could be used to inject nitrogen at a constant rate into the model during the experiments.

3D Steam Model: The 3D steam model had a total of 34 J-type thermocouples located at three-different levels in the model (Figure 3.3.1). Sixteen of them, center thermocouples, were placed at a level of 3.810 cm from the bottom of the model. Nine top and nine bottom thermocouples were placed at 6.985 cm and 0.635 cm from the bottom. Sixteen pressure taps were located at the same locations as the center thermocouples.

The model was packed with unconsolidated +25-30 mesh Ottawa sand. The average porosity was 39% and the absolute permeability was 25 Darcies.

Production End: A back pressure regulator maintained a constant pressure at the producing corner of the model. A cooler was used to condense the produced steam, as shown in Figure 3.3.5.

The CT scanner used in this study is an EMI 5005 x-ray scanner. This is a second generation machine allowing energy levels from 80 keV to 140 keV and a 320x320 pixels imaging capability.

Five Experiments were carried out in the model. The experimental conditions are given on Table 3.3.1.

During the experiments, the model was first saturated with distilled water, then either steam or nitrogen was injected depending on the type of experiment. In the case of continuous steam injection runs, steam was injected at a constant rate of 6 cc/min as cold water equivalent. During the steam foam injection experiments, steam was injected continuously until a gravity override was observed from both temperature data and CT pictures. Then, the steam injection was stopped and 5% PV slug of 0.25 weight % AOS2024 solution was injected. The steam injection was restarted together with nitrogen when the slug injection was completed. The pressure and temperature data were collected by means of a data-logging device every 30 seconds.

The model was scanned at six different locations during the experiments. These scans were taken through the 1.5 cm. clearance between the thermocouples. Figure 3.3.6 shows how six scan slices were used to present 3D saturations. These sections were arranged as shown from the injector to the producer as they appear in the model. The view of the model has been slanted for better 3D presentation. The same approach was followed to image the three dimensional temperature distribution at the same times. They are presented in the figures of the next section as two slanted boxes on top of each other, the top one being the saturation distribution and the bottom one being the temperature distribution.

There are diagonal strikes in all of the saturation distribution pictures. These strikes are the artifacts created by our CT, and they were not taken into account in the analysis and discussion of the CT pictures. These artifacts were inevitable since the 3D model had a rectangular shape in the gantry in which CT assumed a circular geometry, and more x-ray was absorbed through the diagonal cross-section of the model.

3.3.4 RESULTS AND DISCUSSION

For calibration purposes, the first run consisted of steam injection at different rates. CT scans were taken that allowed us to study the growth of the steam zone as a function of time, thus verifying the design calculations on heat losses. The heat loss calculations were based on steady state heat transfer and on material thermal conductivity data given by the manufacturers. The rate of growth of the steam zone at different rates showed these assumptions and data to be valid. Rates of 4, 6 and 8 cc/min of cold water equivalent, 100% quality steam were used. It was decided to use 6 cc/min rate for all further experiments. This was the optimum design rate to obtain a growing steam zone in a reasonable time.

The second experiment was a continuous steam injection experiment. It will be used as a reference test to analyze the other steam/nitrogen, and steam-foam experiments. As can be seen from Figures 3.3.7-3.3.9, the saturation distributions and the temperature distributions match well, and both show gravity override. At the end of the experiment, although 1.31 PV of steam (as cold water equivalent) had been injected, a large part of the bottom of the model was still unswept.

The next run was a steam foam injection experiment in the presence of nitrogen. The first part of the run was similar to the previous experiment and the saturations and the temperature distributions were very close to the previous run at the same steam injection times, at 0.30 PV steam injected (Figure 3.3.10). Steam was injected continuously at the same rate until steam override was obvious. At this time, (0.41 PV of steam injected), steam injection was stopped and a 5% PV slug of 0.25% (by weight) ENORDET surfactant AOS2024 solution was injected. The injection rate of surfactant solution was kept the same as the steam injection rate (cold water equivalent). After the surfactant slug injection, steam injection resumed together with the nitrogen at a rate of 160 cc/min (2 mol % of the injected steam).

The three-dimensional saturation distributions within the model suddenly changed, showing almost a piston-like displacement front, as seen in Figure 3.3.11. The interesting point here is that the three-dimensional temperature distributions, which theoretically are the indicator of steam zone propagation during steam injection experiments, were not changed as much as the saturation distributions. Instead they almost followed the same pattern as that for the continuous steam injection experiment as if there were not a steam foam process going on in the system. In addition to that effect, there was a minor change in pressure gradient after foam was created in-situ. The saturation and temperature distributions at a later time (Figure 3.3.12) indicate a complete sweep after 0.58 PV of steam injection. This stage was never achieved during the continuous steam injection experiment, although almost 3 times more steam was injected.

The changes in saturation and temperature distributions seen in the previous experiments led us to make a control run which might help us to understand and analyze steam foam injection experiments in the presence of non-condensible gas. To do this, a steam foam injection experiment was conducted without a non-condensible gas under the same experimental conditions. Temperature and saturation distributions before surfactant injection were similar to those in the control run (Figure 3.3.13). However, after injection of 5% PV of 0.25% (by weight) AOS2024 solution, the steam front was satisfactorily corrected by in-situ foaming, as seen in Figure 3.3.14, although there was no non-condensible gas phase in the system. We didn't see a major pressure drop increase during this run either. Although the pressure drop along the injector-producer diagonal of the model indicated an increase of 1.0 to 1.5 psi after each slug injection as seen in Figure 3.3.15, this was not persistent and dropped back to the original value after a short time. Another interesting point was that the three-dimensional saturation distributions closely matched the temperature distributions. This indicates that the nitrogen foam ahead of the steam foam in the previous experiment had caused the difference between temperature and saturation distributions in that previous run.

The low temperature, low saturation zone ahead of the steam front is probably filled by "nitrogen foam", a high-quality bank of foam with a large amount of non-condensible gas. It would have been impossible to detect this bank without the in-situ saturation measurements.

During this experiment another 5% PV slug of surfactant solution with the same concentration was injected after seeing that steam foam propagation had slowed down at 0.77 PV of steam injection as seen on Figure 3.3.16. The saturation and temperature distributions looked much like those after the first slug, as can be seen in Figure 3.3.17. However, after an additional 0.50 PV of steam injection, the system was almost swept by steam (Figure 3.3.18).

The last experiment was a run to investigate the behavior of nitrogen foam alone, with no steam. Nitrogen was continuously injected at the same rate it would be during a steam foam run until nitrogen started to override as seen Figure 3.3.19. Gas injection was stopped and a 5% PV slug of 0.25% (by weight) AOS2024 solution was injected. Gas injection was resumed. The saturation distributions showed little effect of foaming (Figure 3.3.20). Subsequently, we injected a bigger slug of surfactant solution (10% PV). The saturation distributions showed that the gas was moving downward in the model at a very slow rate (Figure 3.3.21). The foam, if any, was not very effective as blocking agent in that run.

The raw CT numbers, the processed and digitized CT number images, and the digitized temperature images of the first slice of the model at the same times during each experiment are used as a basis for comparisons. Figure 3.3.22 shows these images at 5% PV steam injected. The images show similar patterns indicating the reproducibilities of steam injection experiments in the 3D model. Figure 3.3.23, which is just before surfactant solution injection in foam runs, shows the extent of gravity override during steam injection applications. On Figure 3.3.24, which is after surfactant solution injection, the behavior changed depending on the type of steam foam injection process. During the steam-foam injection run in the presence of non-condensible gas, the saturation distributions, both from real x-ray images and from digitized CT number images differ considerably from the temperature distributions. The saturation and temperature distributions of the steam foam injection experiment without a non-condensible gas behave similarly. This indicates that the temperature distributions in the previous run were following the steam foam saturation distributions only. These results showed the effect of nitrogen on the steam foam processes.

3.3.5 CONCLUSIONS

A new experimental apparatus was designed, built and tested. It allows steam injection in a three-dimensional pack and measurements of temperatures, pressures, heat losses and fluid saturation distributions. The model can be CT scanned while performing experiments.

Steam injection runs are reproducible both in terms of temperature distributions and saturation distributions as function of time (or steam injected).

Steam-foam with a non-condensible gas added shows the presence of a "gas-foam" zone ahead of the steam where both the temperature and the liquid saturations are low.

In-situ saturation measurements are useful to help identify the flow mechanisms in the steam-foam process. Thus CT scanning has proven to be a useful tool for thermal recovery laboratory research.

Table 3.3.1 Experimental Conditions

Experiment Type	Steam Injection Rate cc/min (cold water eq.)	Amount of N_2 mol %	First Slug Injected at (PV of Steam or PV of N_2)	Second Slug Injected at (PV of Steam or PV of N_2)
Steam	4.00, 6.00, 8.00	0.00		
Steam	6.00	0.00		
Steam-Foam	6.00	2.00	0.41	
Steam-Foam	6.00	0.00	0.42	0.77
N_2 Foam	0.00	100.00	10.80	23.10

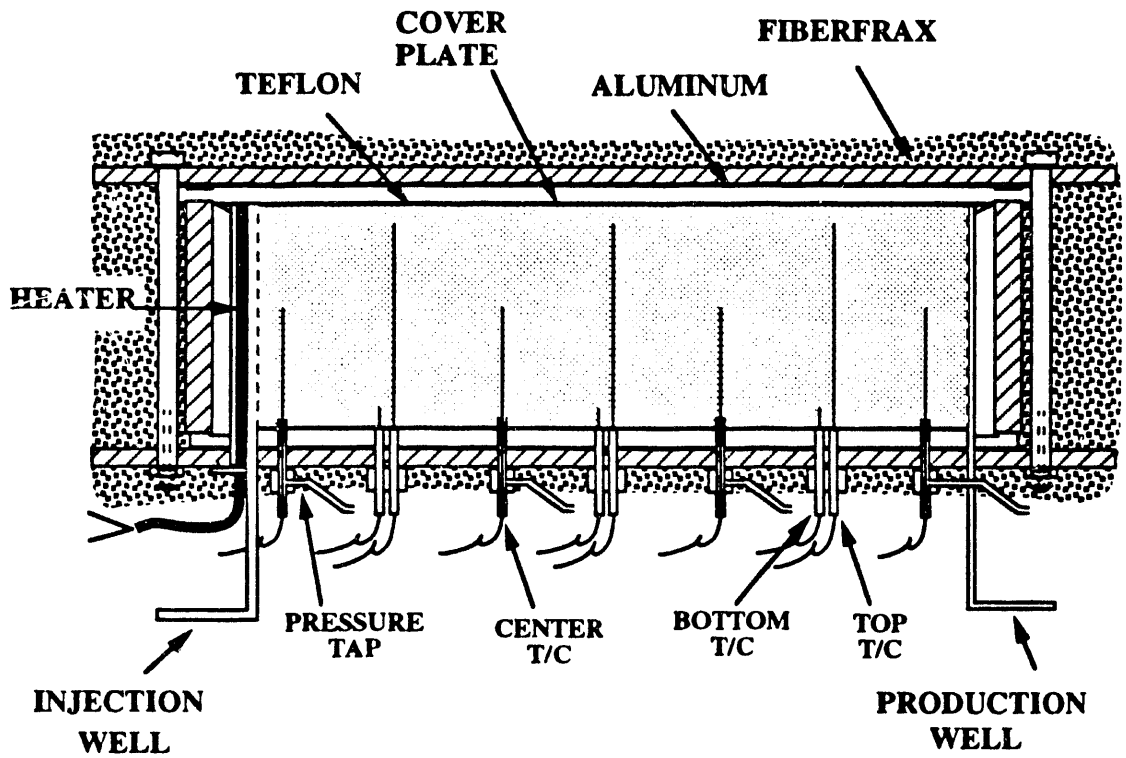

Figure 3.3.1 Injector producer diagonal cross section of the 3D model.

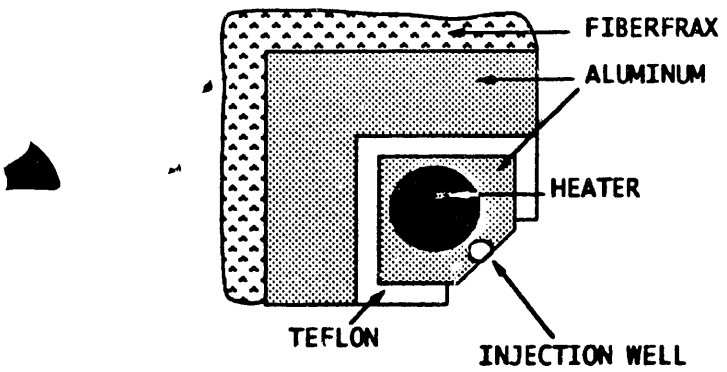

Figure 3.3.2 The cross section of the injector.

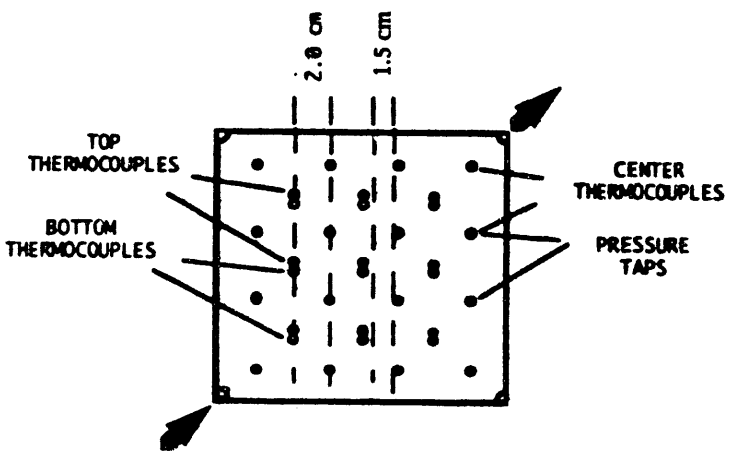

Figure 3.3.3 The thermocouple and pressure tap locations.

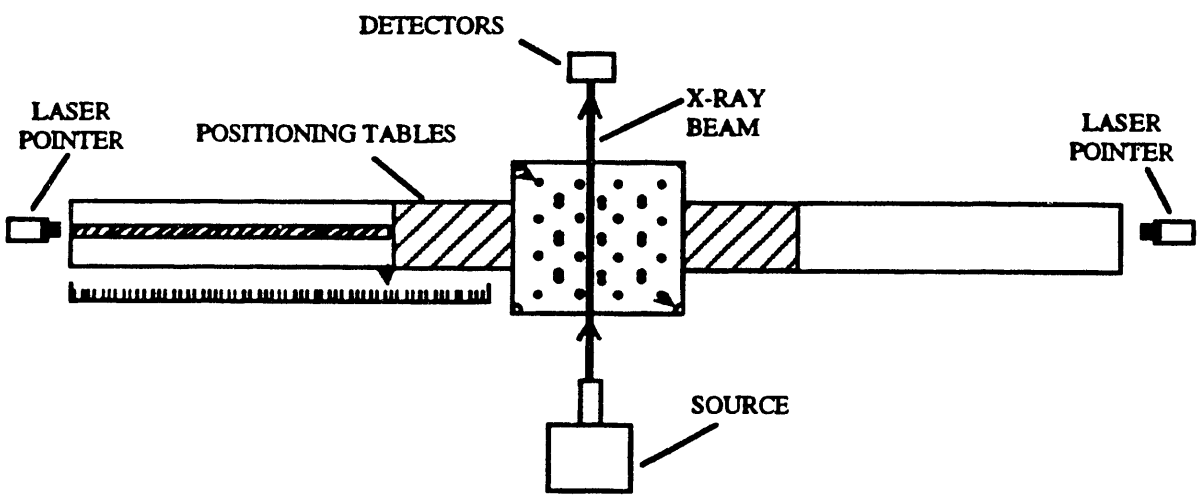

Figure 3.3.4 The positioning tables.

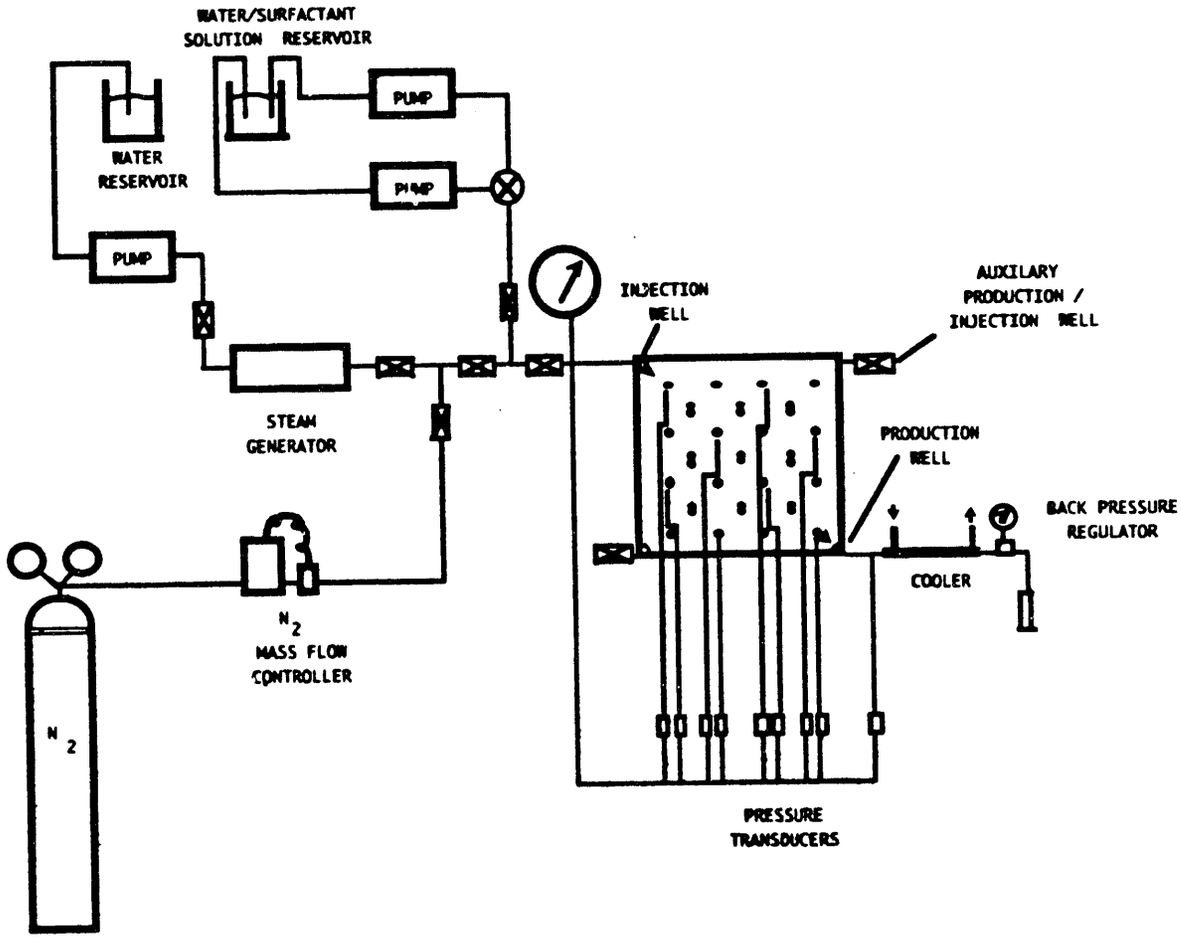

Figure 3.3.5 The schematic of the experimental setup.

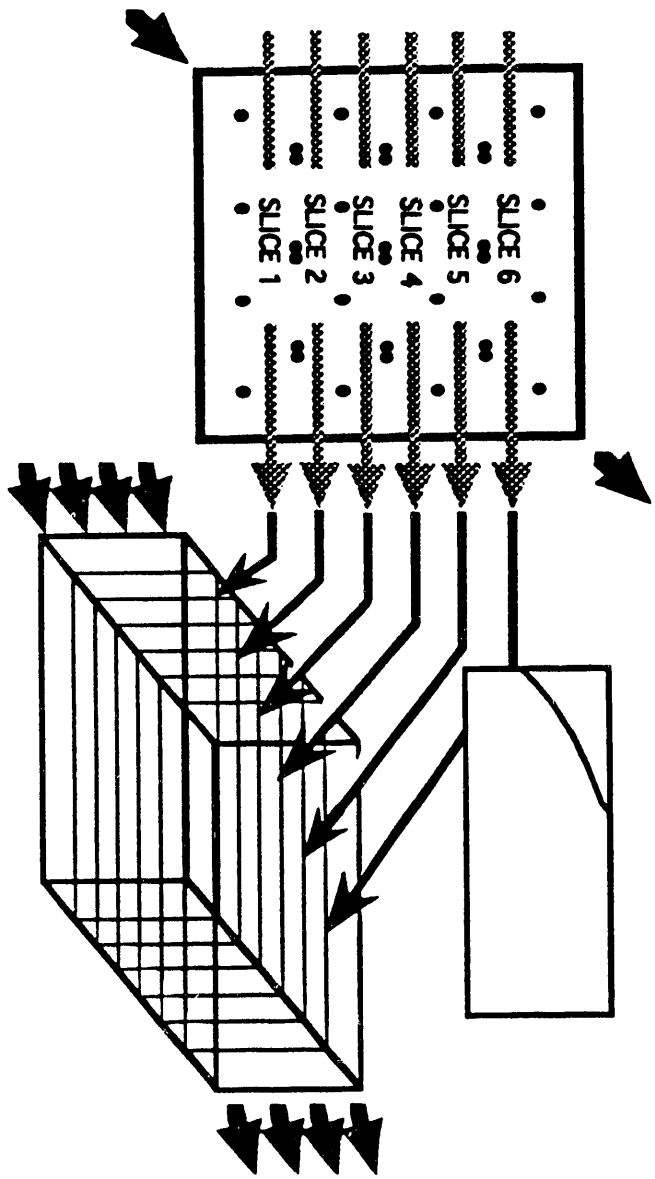

Figure 3.3.6 Positioning scan slices in the 3D model.

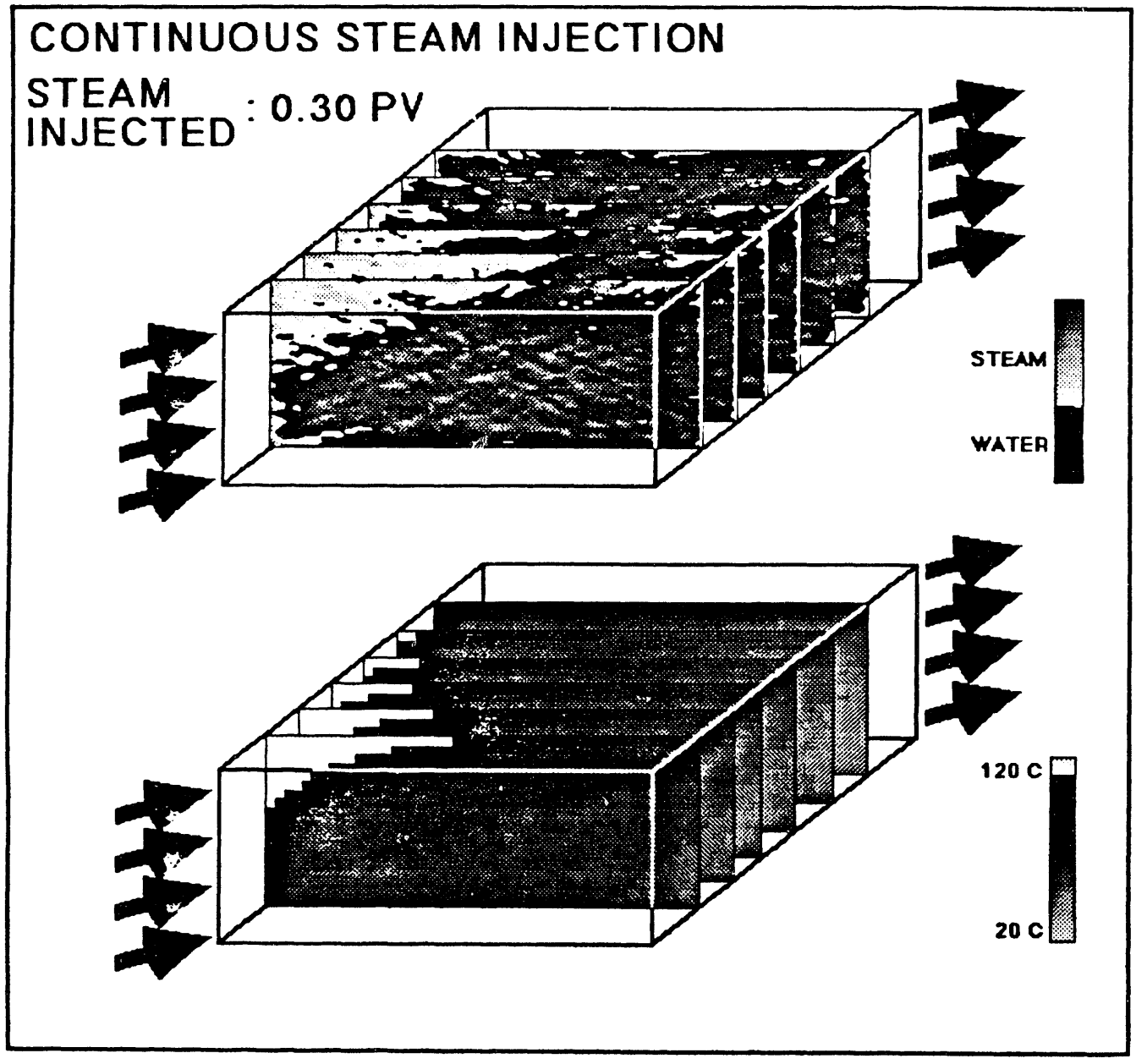

Figure 3.3.7 The saturation and temperature distributions during continuous steam injection at 0.30 PV steam injected.

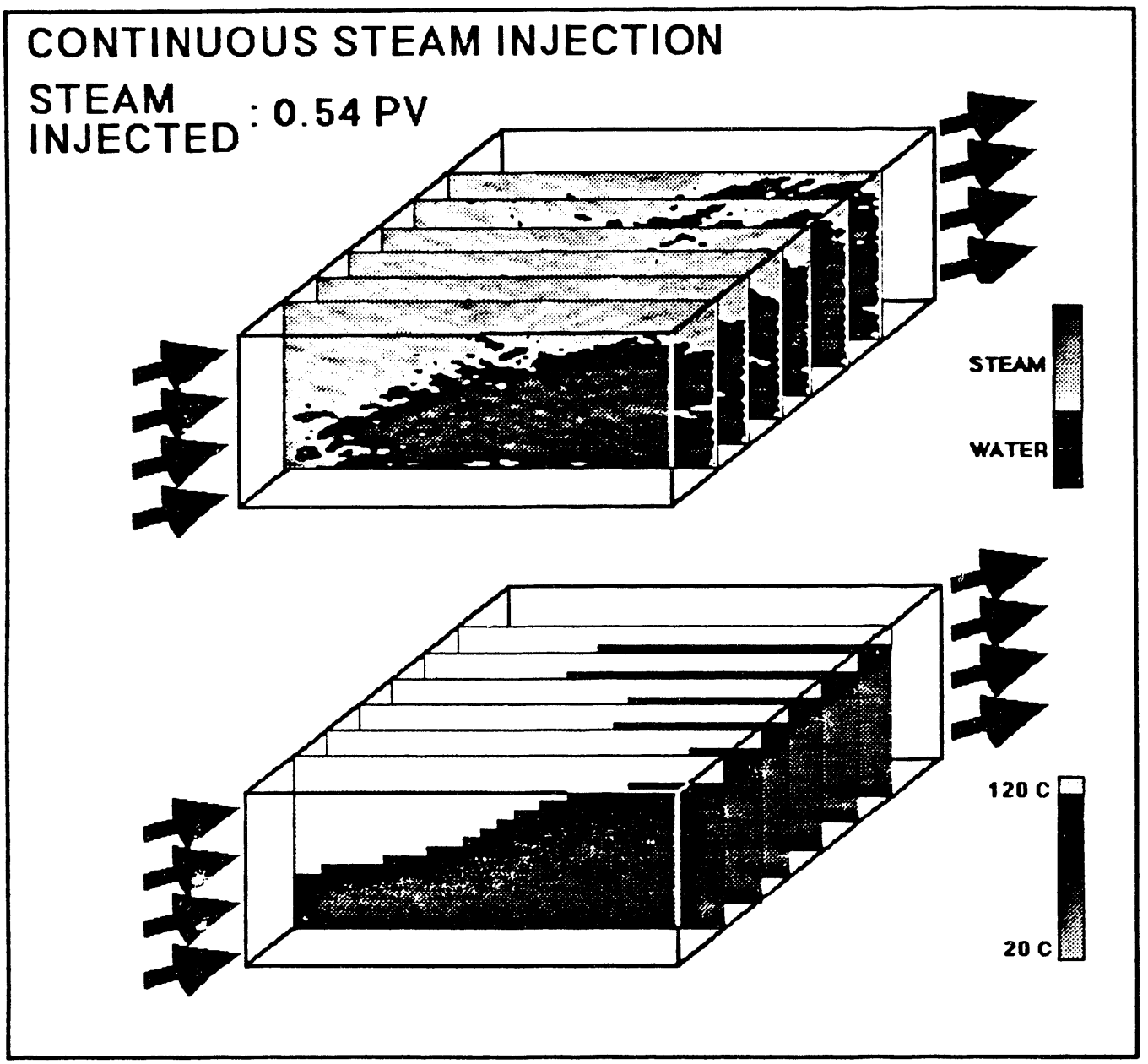

Figure 3.3.8 The saturation and temperature distributions during continuous steam injection at 0.54 PV steam injected.

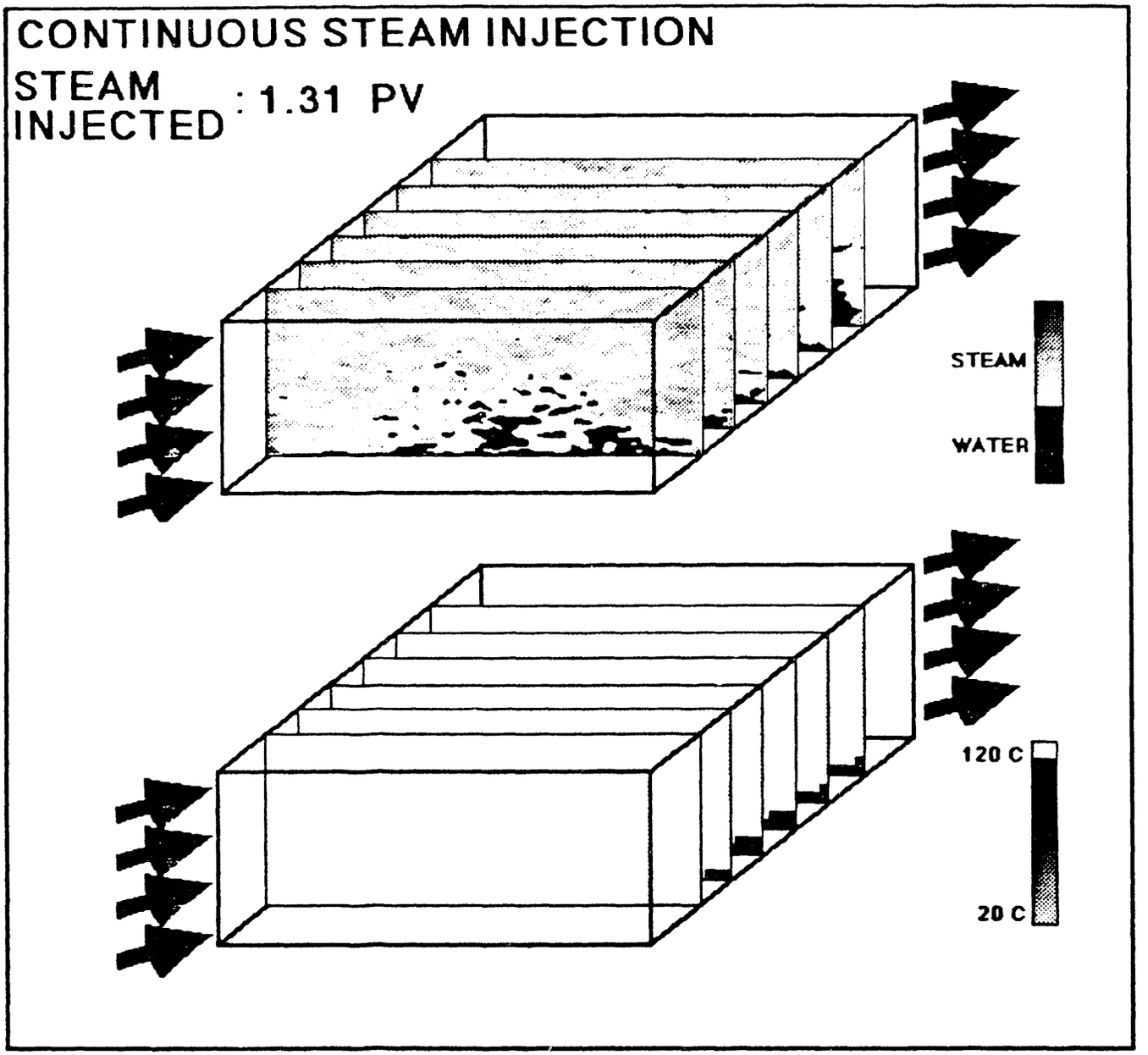

Figure 3.3.9 The saturation and temperature distributions during continuous steam injection at 1.31 PV steam injected.

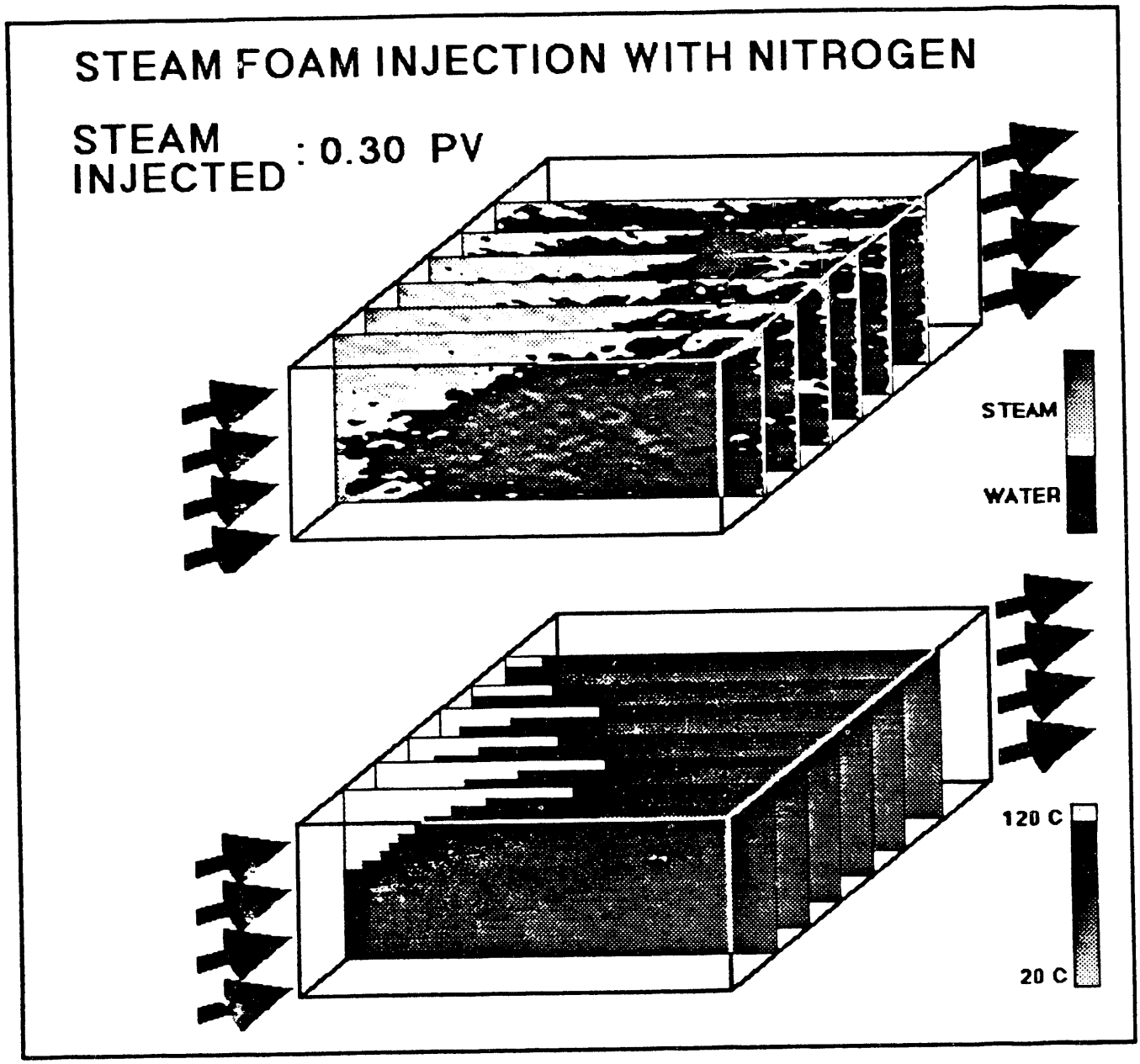

Figure 3.3.10 The saturation and temperature distributions during steam foam injection with nitrogen at 0.30 PV steam injected.

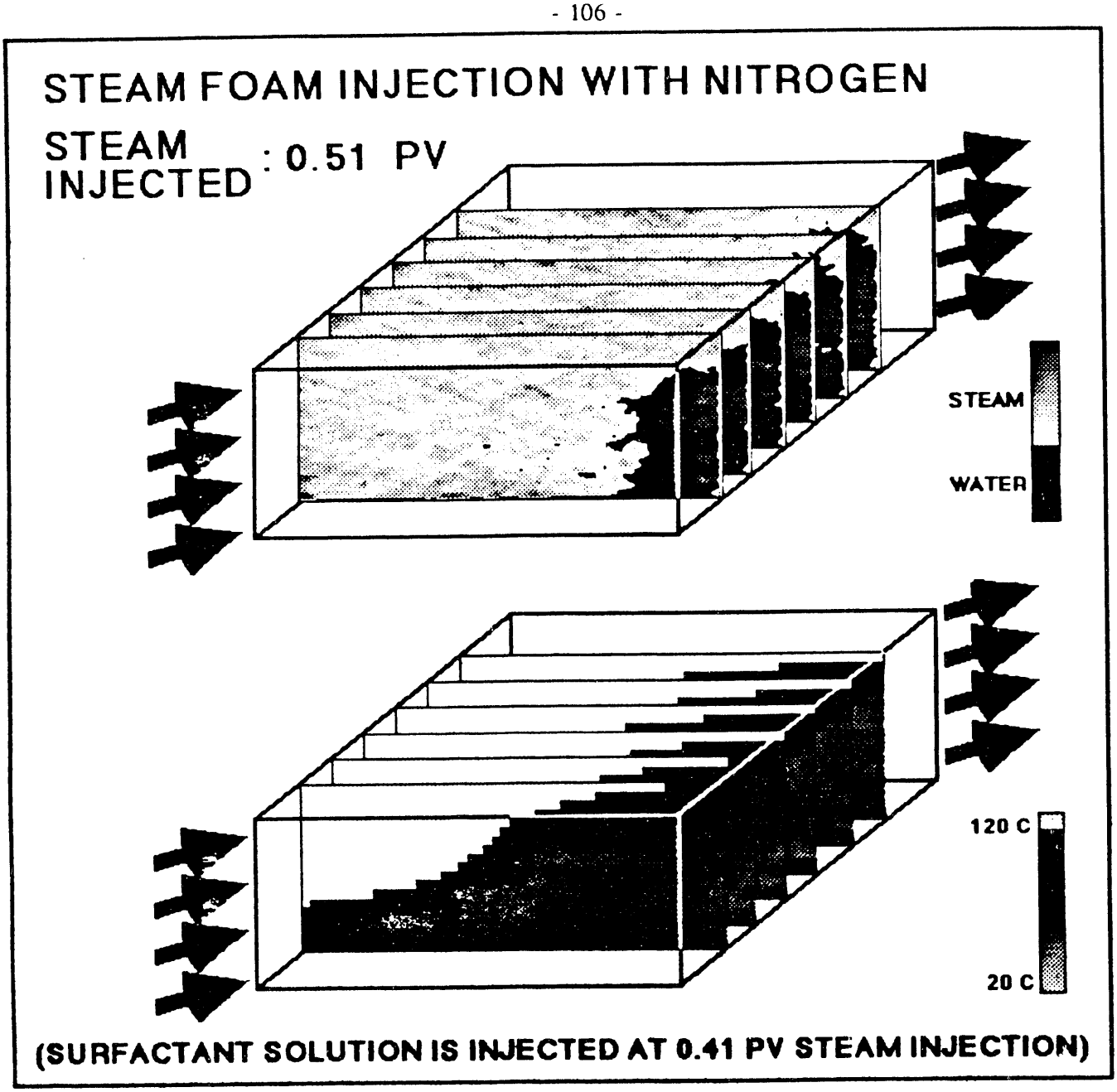

Figure 3.3.11 The saturation and temperature distributions during steam foam injection with nitrogen at 0.51 PV steam injected.

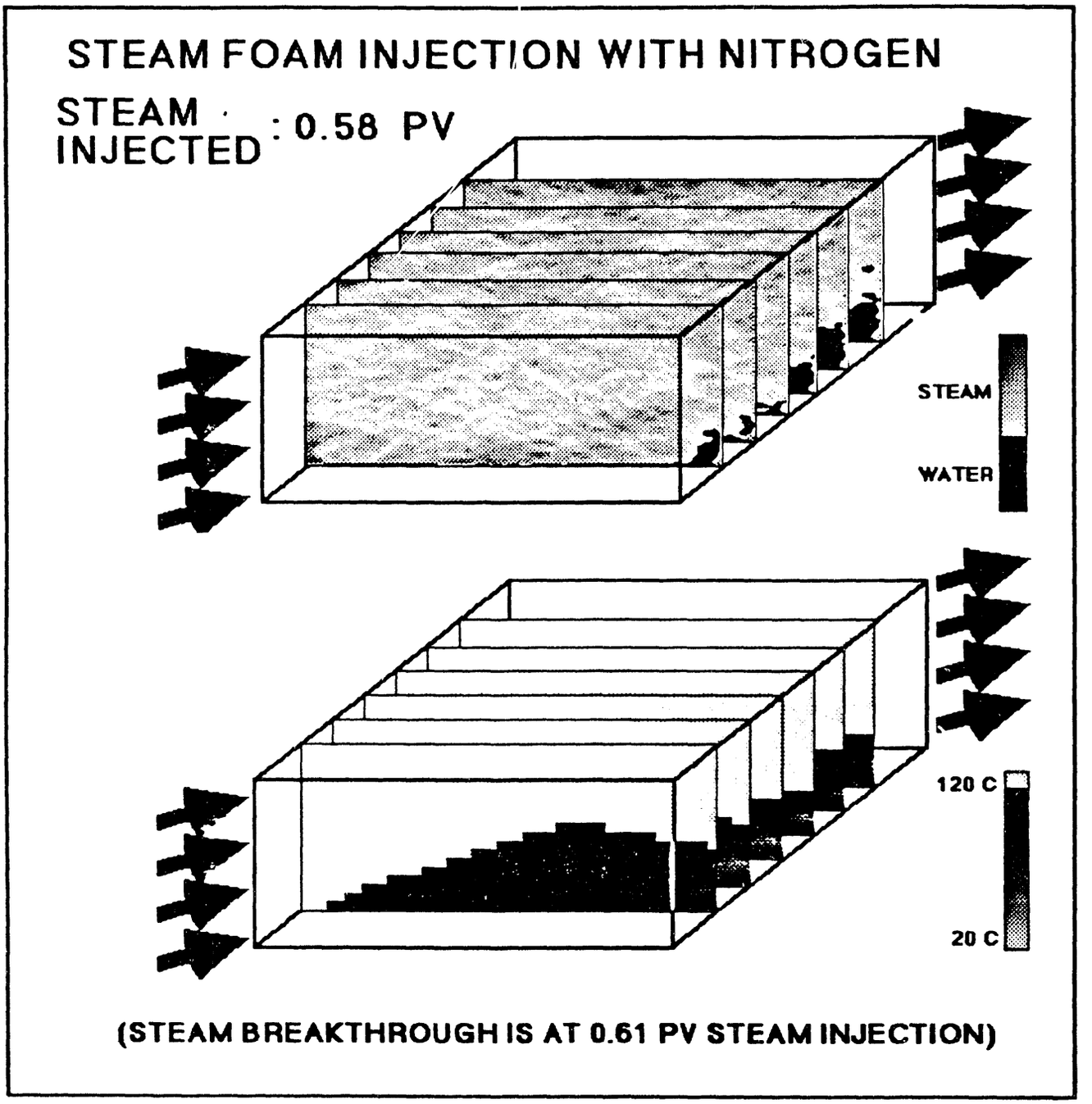

Figure 3.3.12 The saturation and temperature distributions during steam foam injection with nitrogen at 0.58 PV steam injected.

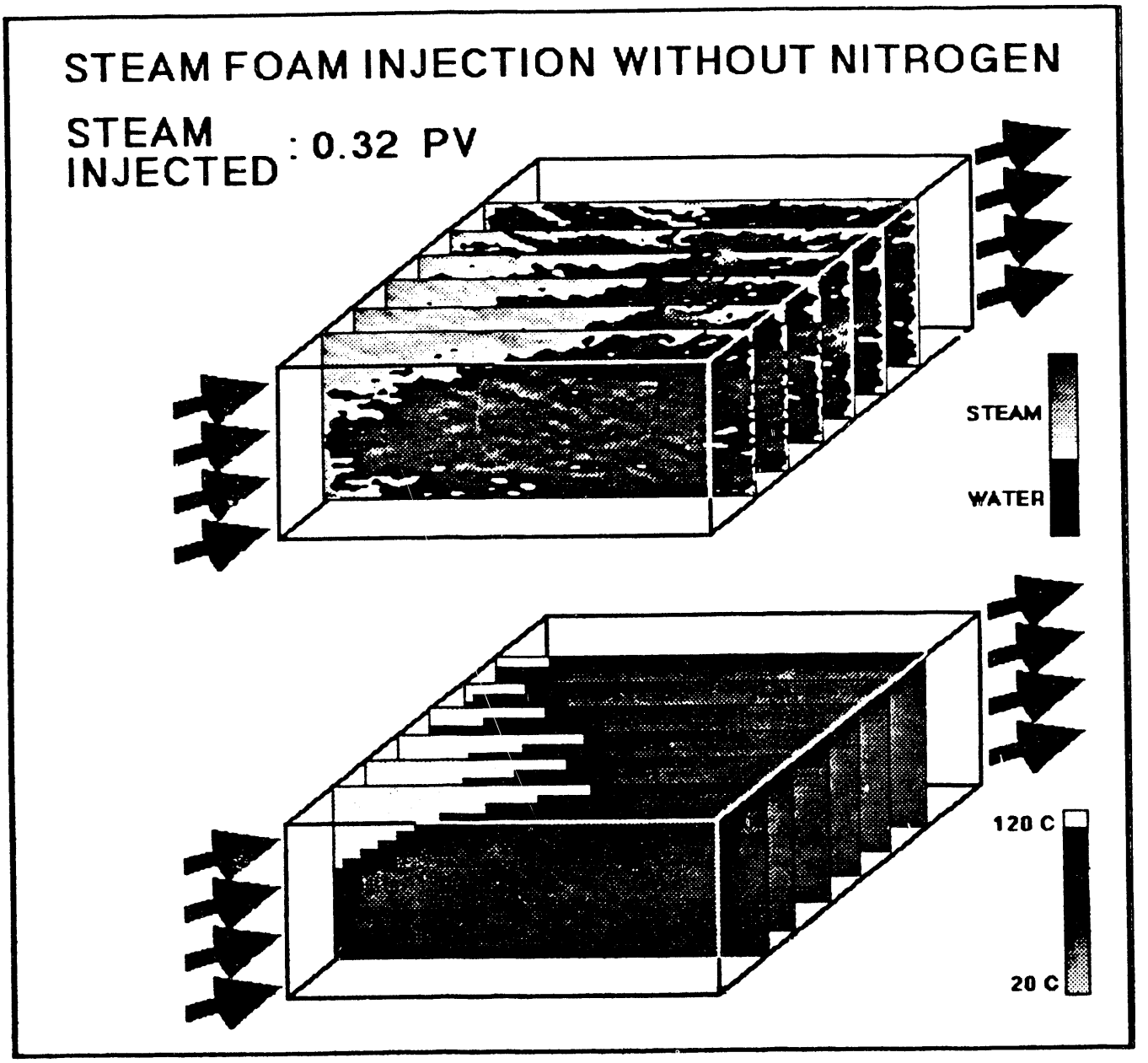

Figure 3.3.13 The saturation and temperature distributions during steam foam injection without nitrogen at 0.32 PV steam injected.

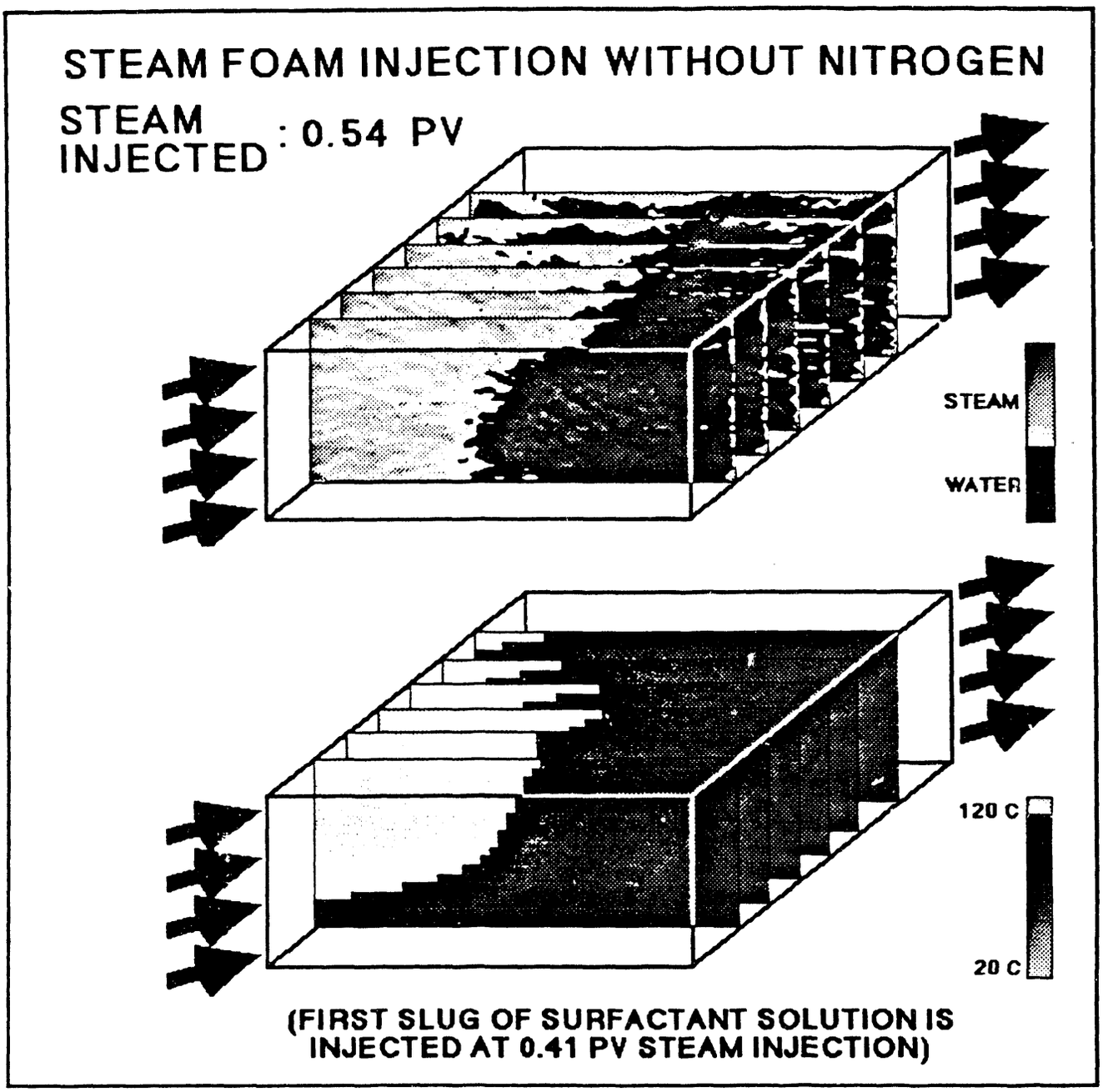

Figure 3.3.14 The saturation and temperature distributions during steam foam injection without nitrogen at 0.54 PV steam injected.

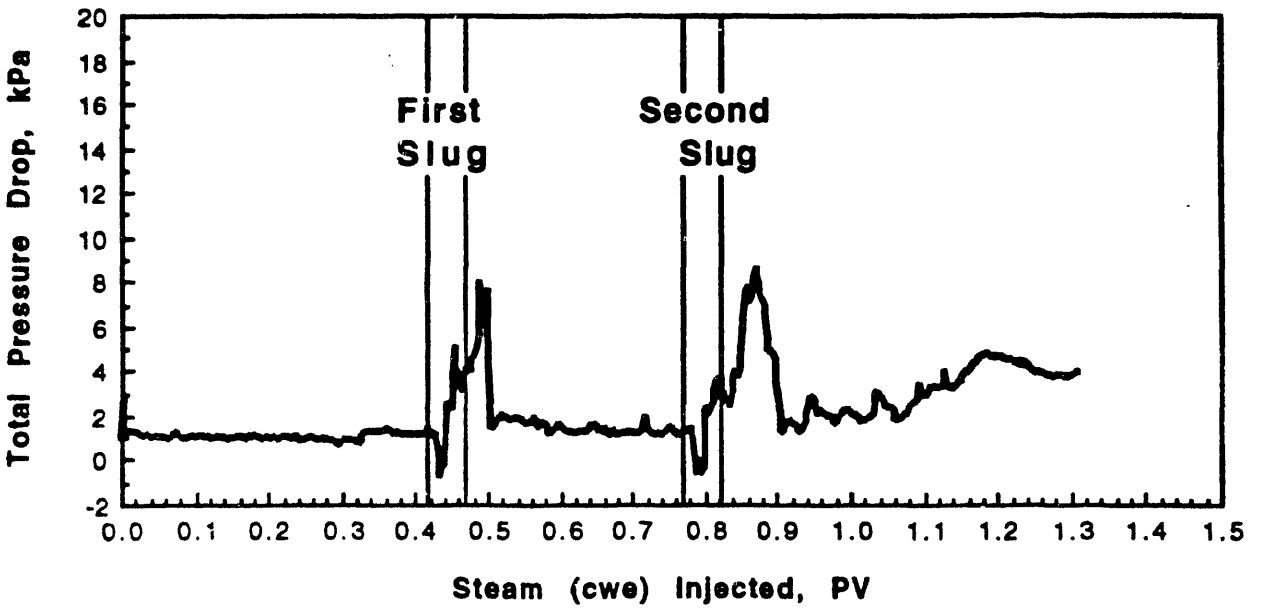

Figure 3.3.15 The total pressure drop along injector producer diagonal during steam foam injection without nitrogen.

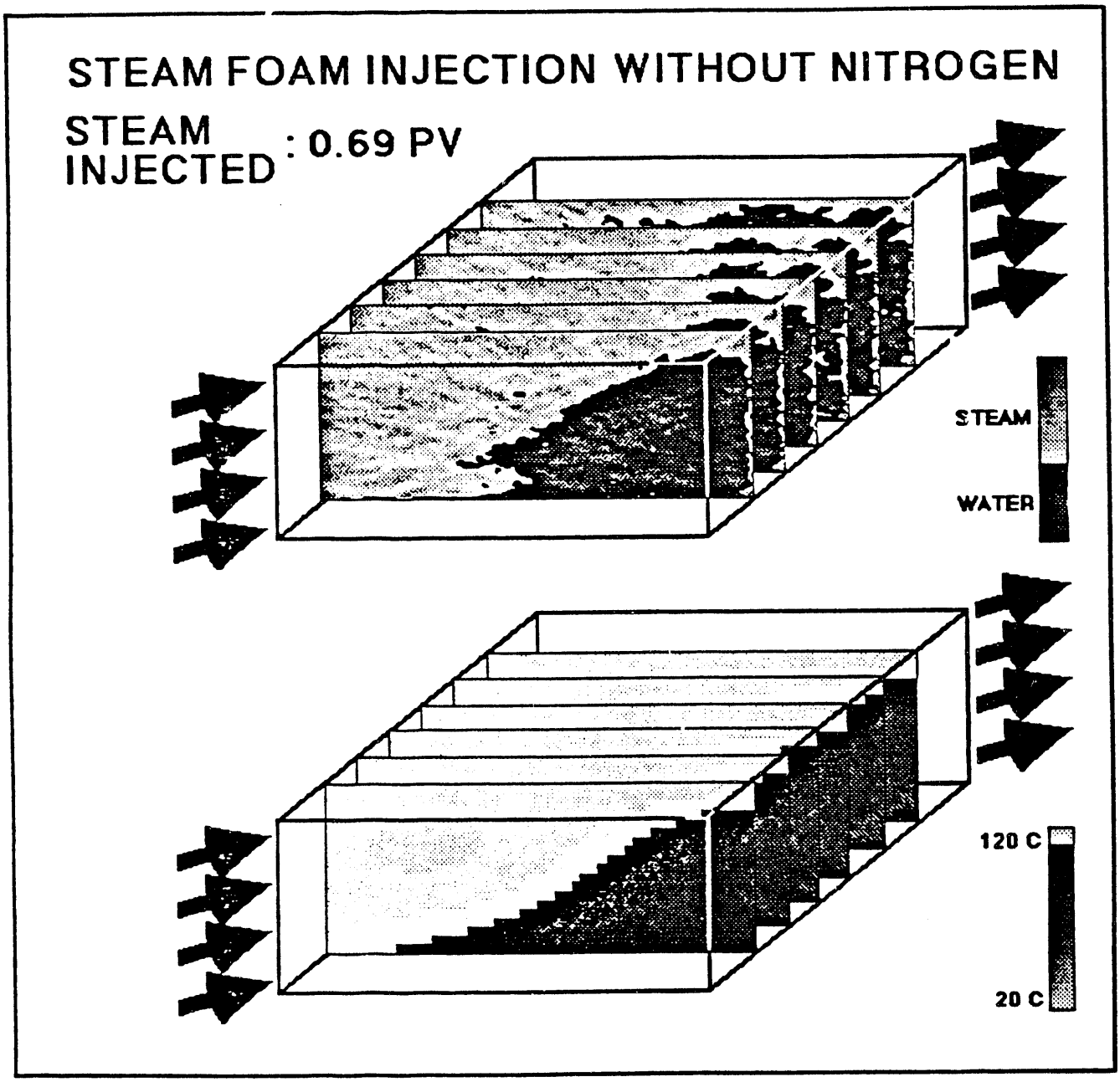

Figure 3.3.16 The saturation and temperature distributions during steam foam injection without nitrogen at 0.69 PV steam injected.

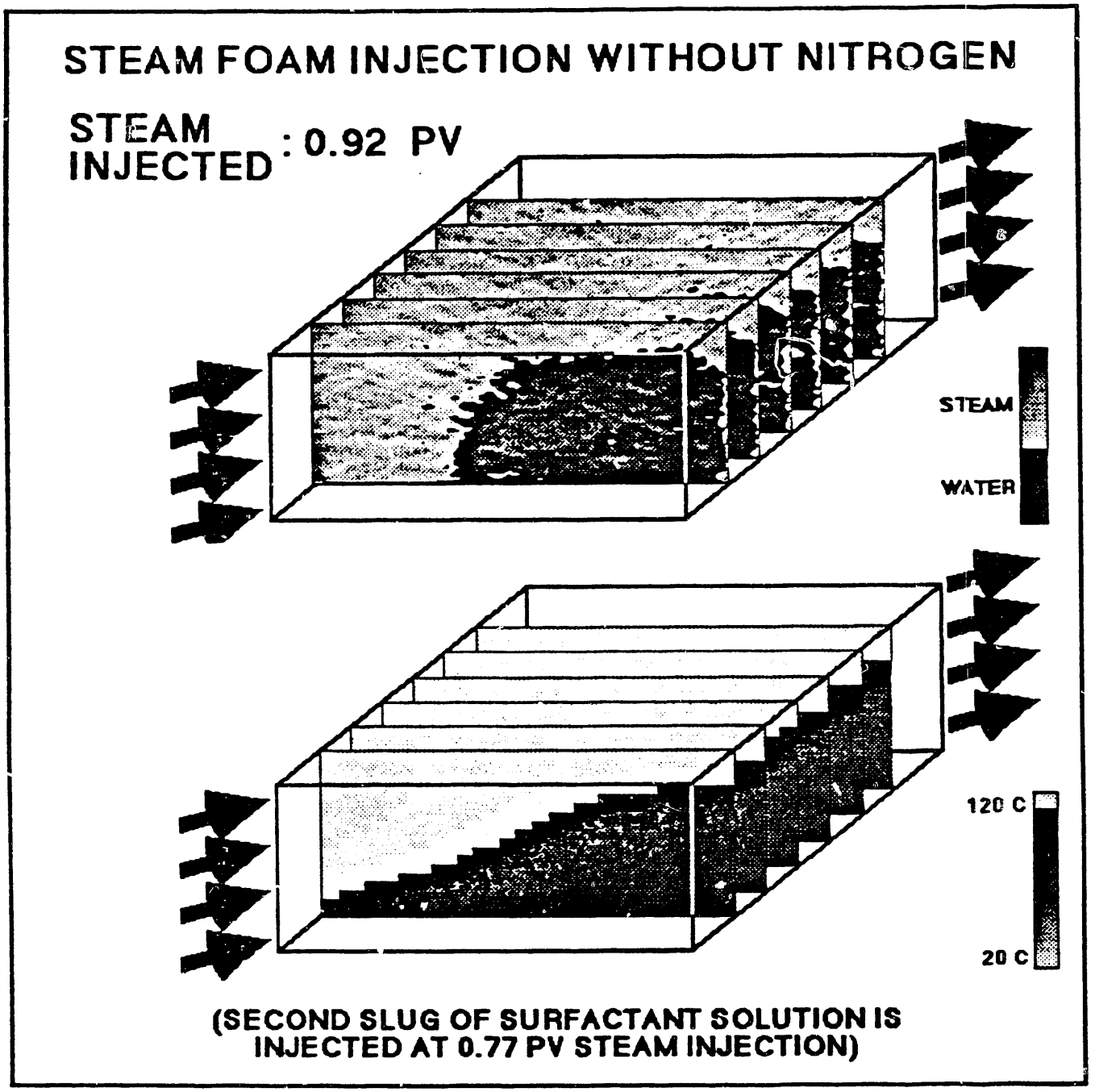

Figure 3.3.17 The saturation and temperature distributions during steam foam injection without nitrogen at 0.92 PV steam injected.

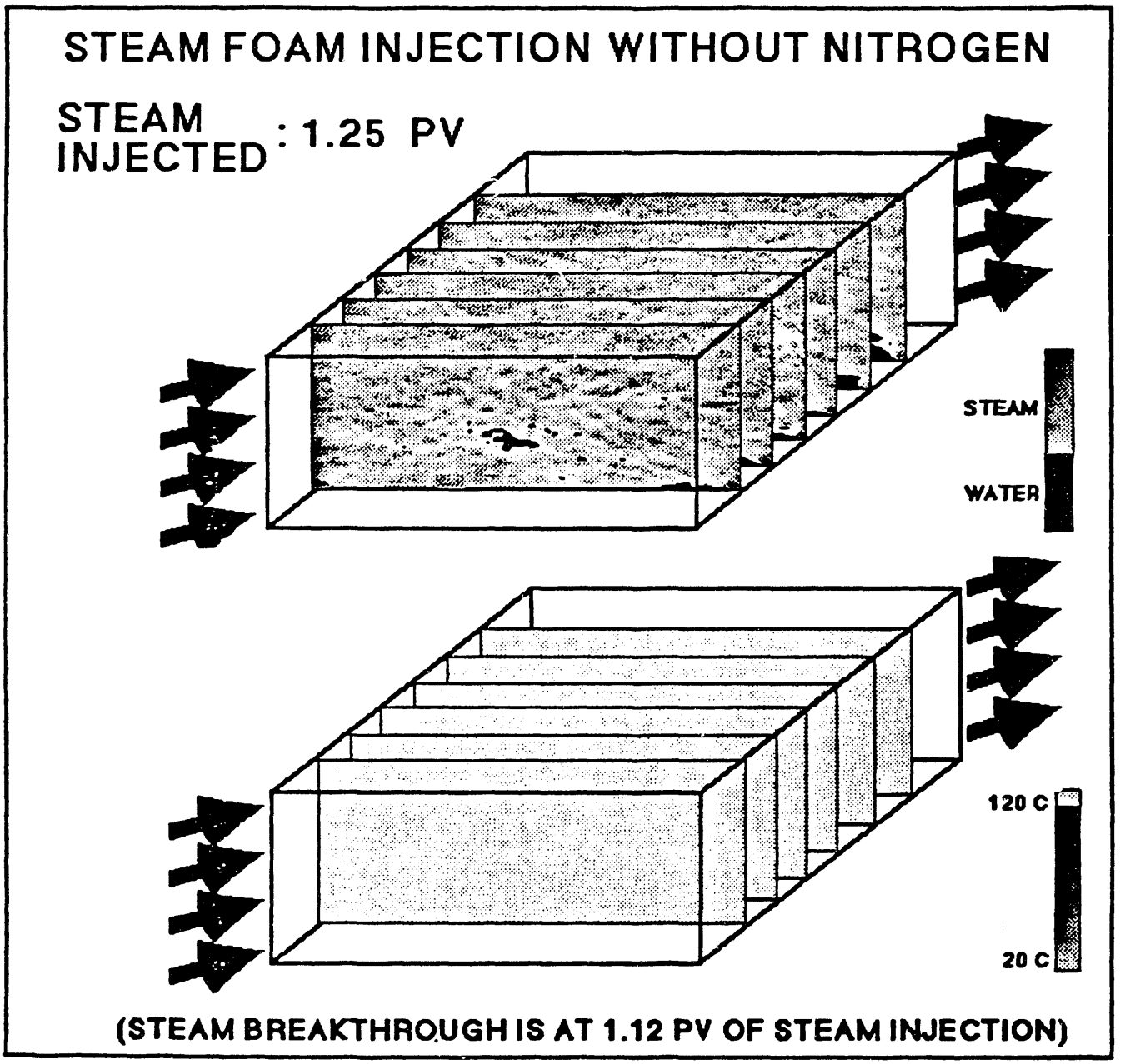

Figure 3.3.18 The saturation and temperature distributions during steam foam injection without nitrogen at 1.25 PV steam injected.

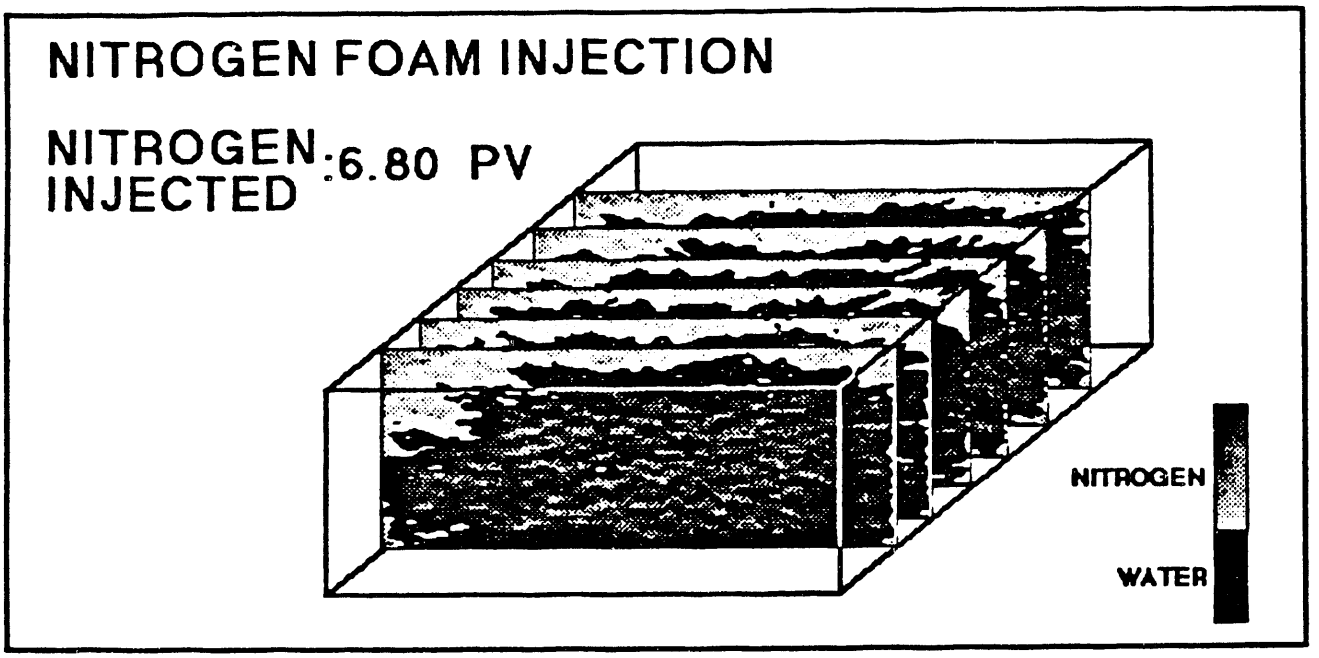

Figure 3.3.19 The saturation distribution during nitrogen injection at 6.80 PV nitrogen injected.

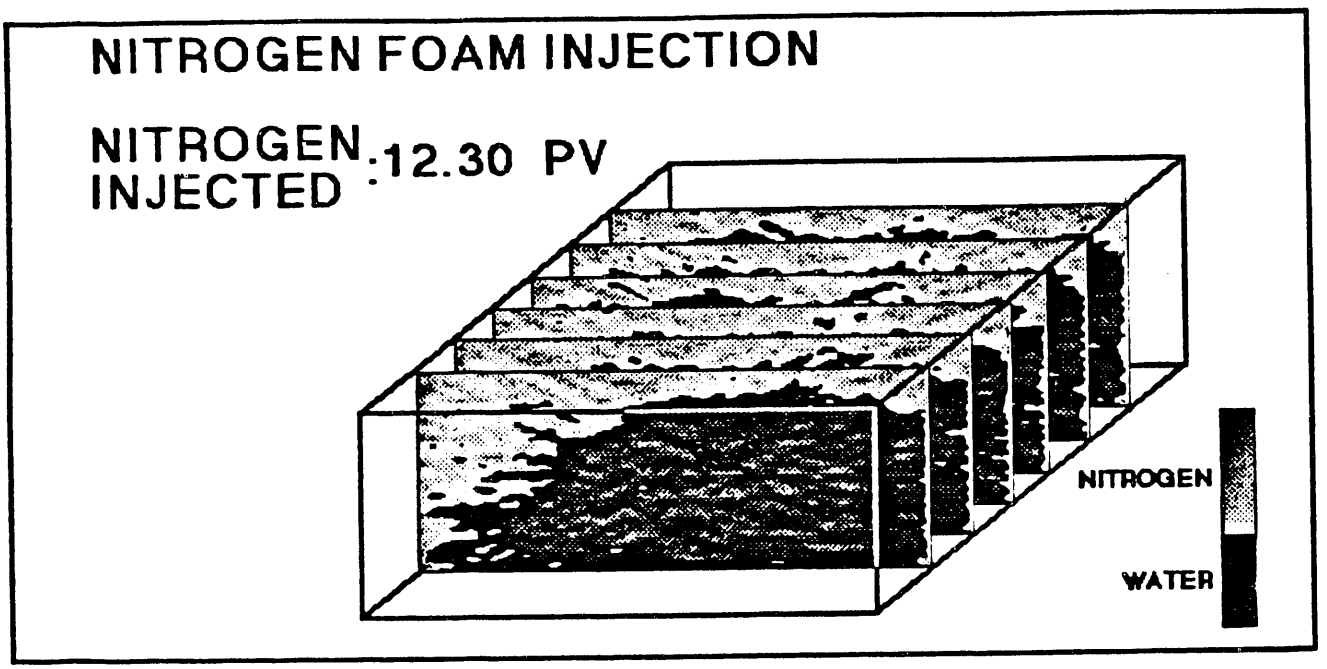

Figure 3.3.20 The saturation distribution during nitrogen injection at 12.30 PV nitrogen injected.

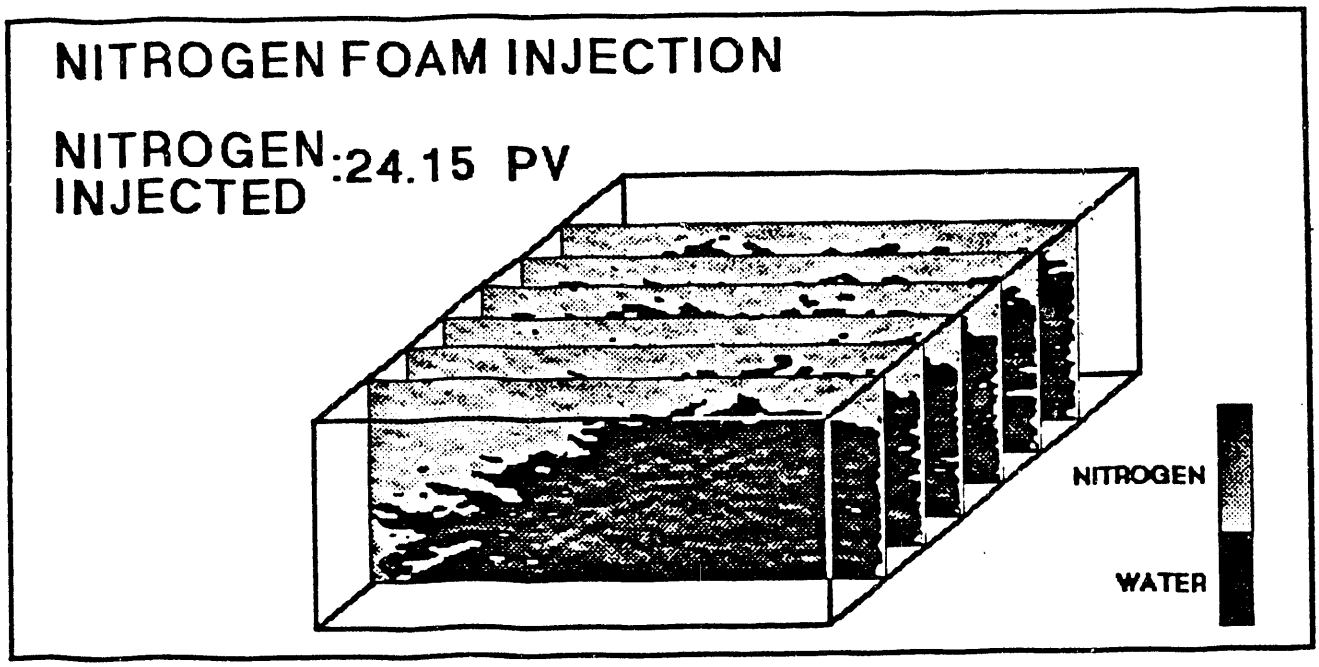

Figure 3.3.21 The saturation distribution during nitrogen injection at 24.15 PV nitrogen injected.

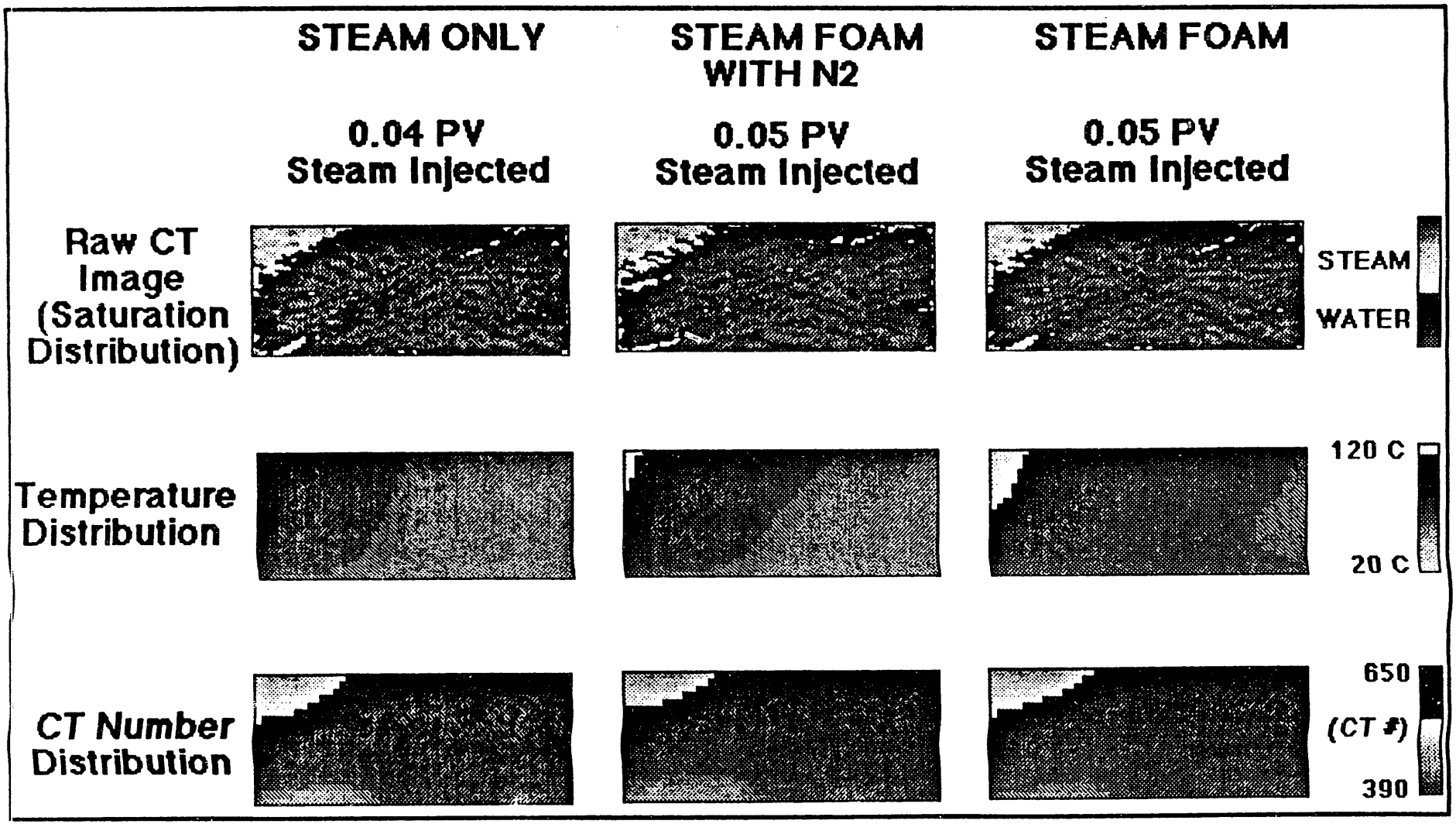

Figure 3.3.22 Comparison of steam injection experiments at 0.05 PV steam injected.

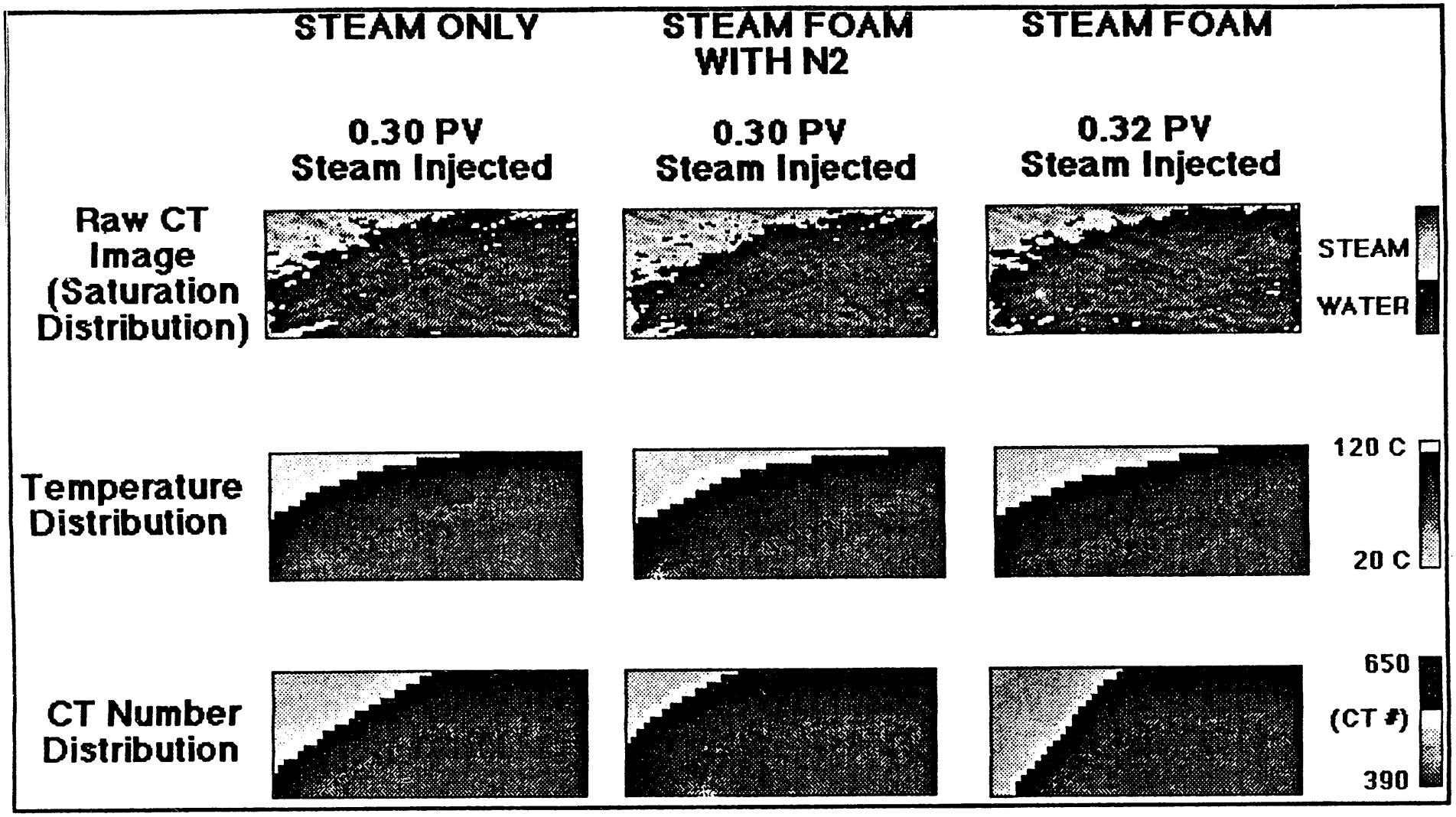

Figure 3.3.23 Comparison of steam injection experiments at 0.30 PV steam injected.

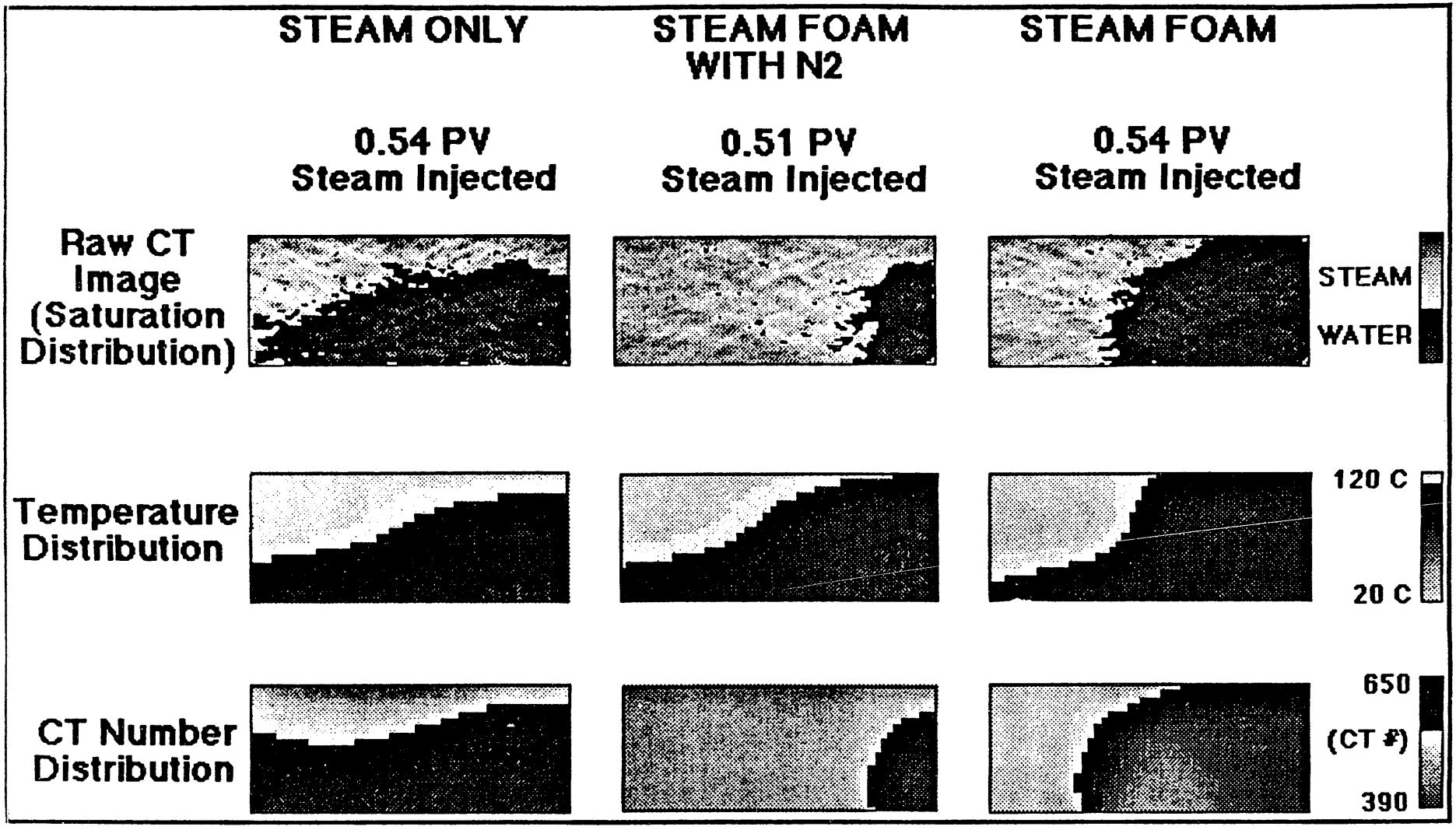

Figure 3.3.24 Comparison of steam injection experiments at 0.54 PV steam injected.

3.4 MICROVISUALIZATION OF FOAM FLOW IN A POROUS MEDIUM
(J. Hornbrook)

3.4.1 INTRODUCTION AND OBJECTIVES

Since the late 1950's foam has been recognized as a fluid possessing oil production enhancement capability. Foam may be used to decrease the mobility ratio of an oil displacement process, or foam may be used as a selective blocking agent to reduce the effects of fingering induced by permeability streaks in a formation. The surfactants used to produce foams may aid in the production of heavy oils by partially dissolving the oil, or by helping to separate oil blobs from the rock in mixed-wet systems.

Study of the flow of foam in porous media may be divided into three broad areas.

1. Foam properties. This includes studies of the fluid properties of foam, the most important of which is foam viscosity and how it varies with shear rate.
2. Foam flow mechanisms. This concerns research into the means of propagation of foam in porous media. Snap-off events and bulk propagation of the gas and liquid fractions of foam are studied.
3. Foam interactions with oil. This concerns the way foams react with oil. The ways in which foam increases the mobility of oil and the mechanisms by which oils destroy foam are of particular interest.

Research within the three broad research areas has been undertaken at the field level in field pilot projects, the macroscopic level in laboratory core floods, and at the microscopic level in micromodel studies.

This research was focused on the third broad area of foam research (foam interactions with oil) and was carried out at the microscopic level. Background work designed to verify experimental procedure was completed in homogeneous micromodels. Presently, the construction of an exact, two-dimensional replica of Berea sandstone is underway. Upon completion of the replica micromodel, the effects of foam injection procedure upon foam stability in an oil-filled micromodel will be studied.

3.4.2 LITERATURE REVIEW

The study of foam with application to petroleum engineering began with the pioneering work of Bond and Holbrook (1958). Their work concerned the mobility effects of injected foam, and the benefits of foam injection as a method of enhancing oil reservoir performance. Over the next thirty years, much research and several field experiments studied the flow of foam in porous media on both a qualitative and quantitative level.

Many papers have been written on the fluid properties of foam. The results of these papers are rarely in agreement on the nature of foam and are often contradictory. A chronological review of foam research was prepared by Marsden (1986). Marsden outlined the major advances in the understanding of foam flow and pointed out shortcomings and contradictions in existing work. A brief summary of foam fluid properties is:

1. Foam is a fluid of high apparent viscosity.
2. Foam viscosity is a function of the surfactant concentration.
3. Foam viscosity is a function of flow rate.
4. The flow history of foam affects its viscosity.

Foam flow mechanisms have been studied in numerous papers. Most of this work, however, has focused on a qualitative description of foam rather than a quantitative one. Most recently, the research of Owete and Brigham (1984), and Manlowe and Radke (1988) have extended the understanding of foam flow mechanisms beyond the description of observed phenomena. Owete and Brigham studied the flow of foam in the following areas:

1. The propagation of foam and its components, and
2. The mobility of gas in the presence of foam. Owete carried out his work in micromodels with homogeneous and heterogeneous flow paths, and although most of his conclusions are qualitative, some quantitative results were obtained.

Owete's results for a homogeneous micromodel have been verified as a part of the background work in this research. The quantitative aspects of Owete's work will be extended to include the effects of the foam injection procedure on oil displacement. Future research will be carried out in two-dimensional replicas of Berea sandstone.

Research on the effects of oil on foam has been carried out by Manlowe and Radke (1988) and by Sanchez and Hazlett (1989). The work of Manlowe and Radke was most applicable to this study. Manlowe and Radke studied the foam breaking tendency of oil on foam and described the stability of a pseudo-emulsion film as the determinant of foam stability in the presence of oil. The pseudo-emulsion film will be studied under different foam injection methods.

Research involving flow of foam through micromodels is new. In addition to the micromodel research mentioned above, several studies of the usefulness of micromodels as research too have been carried out. Sarathi (1986) points out the advantages in studying pore level events afforded by micromodels, but warns against extrapolating pore level events to a large scale without additional information. He also describes several disadvantages inherent in commonly used micromodels, most of which will be avoided by the construction process outlined in this report. Sarathi lists the following as important problems with micromodel research:

1) Difficulty in obtaining a continuous specific etch depth.
2) Introduction of microscopic heterogeneity into the model in the etch procedure.
3) Difficulty in replicating reservoir Peclet number due to enlargement of the pores.
4) Loss of three-dimensional continuity.
5) Loss of detail in heterogeneity, pore geometry, connectivity, and surface roughness due to the anealling process used in most micromodel construction processes.

Except for the loss of three dimensional continuity, all of the disadvantages listed were eliminated in the micromodels described in this report.

Huh et. al. (1989) point out the importance of heterogeneity on foam generation in porous media, further supporting the need for accurate replication of a porous medium in a micromodel study.

3.4.3 EQUIPMENT

An experimental apparatus has been constructed that will allow the flow of foam through a micromodel to be simultaneously observed, videotaped, and photographed, and will allow for monitoring of the pressure drop across the micromodel. The micromodels used are two-dimensional representations of porous media made by etching a flow path into a silicon wafer and then bonding the wafer to a flat piece of glass (Fig. 3.4.1), thus creating a flow path. Two homogeneous micromodels were used in the initial phases of the foam flow research. The homogeneous micromodels were used to verify that the experimental apparatus worked as designed and to replicate Owete's results to determine that the experimental procedure was correct. Both homogeneous micromodels were etched to a depth of 30 microns. One micromodel represented cubic packing of spheres of radius 100 microns, while the other micromodel

represented rhombohedral packing of spheres of radius 30 microns. A heterogeneous model, which is an exact two-dimensional replica of Berea sandstone, is being constructed. A detailed description of the construction of the Berea replica micromodel follows.

A thin section of clean Berea sandstone was prepared with the pore spaces filled with blue-dyed epoxy. A color photograph of the thin section was taken at 40 times magnification. The result was a photograph in which pore spaces appear blue and the sand grains appear black to grey. Professional slide film was used to get a true color image. The film was then sent to a photography lab where, after the development with the use of color filters, the blue was transformed to white. After this transformation, the pore spaces were white while the sand grains were black and grey. Finally, a lithograph of the photograph was made. In the lithograph, the pore spaces appear white and the sand grains are black -- there are no grey scales. The lithograph image must be transferred to a computer.

The lithograph of the thin section was put into pict format by using a Macintosh digital scanner. The image was analyzed by using a digital analysis package called Ultimage^{TM}. At various points in the image, pore spaces that should have been continuous were blocked off. This is an artifact of the loss of one dimension in transferring the three-dimensional flow path to two-dimensions. By use of the digital analysis package, a small number of pixels were removed to allow for a continuous flow path through the micromodel. When pixels were removed, the nature of the flow path was always maintained, so after manipulation of the digital image, a computer image of a continuous Berea flow path was obtained (Fig. 3.4.2).

The most difficult problem in obtaining a Berea micromodel is the next step -- moving the computerized image of the sandstone (pict format) to MEBES (Sze, 1988) format which is the format used at the Stanford Center for Integrated Systems to transfer complicated images to silicon wafers. First, an ascii bit map of the image is generated with black pixels given a value of 1 and white pixels given a value of 0. The bit map is then restructured into columnar form with each pixel given an address and size based on its location in the image. Finally, using modified transferring software available at Stanford CIS, the image is transferred to MEBES format. Once the image is put into MEBES format, the final steps are trivial.

A permanent chrome-on-glass mask of the Berea pore space is constructed by the electron beam imaging group at Stanford. Once the mask is complete, the silicon wafer model construction is carried out as in more conventional models (the process will be described in detail). Presently, an attempt to get an accurate description of the Berea image in MEBES format, is a complicated problem.

When the image mask has been completed, the following steps are used to generate the etched silicon flow path:

1. Oxidize one side of a silicon wafer (5 cm. diameter).
2. Coat one side of the oxidized wafer with a photoresist material.
3. Position the sample mask on the photoresist side of the wafer.
4. Expose the sample mask to ultra-violet light. The structure of the photoresist is destroyed by contact with ultra-violet light. Since the sample mask is a negative of the sample, the photoresist is destroyed where pores exist.
5. Etch the wafer with hydrofluoric acid to the desired depth.

Only the parts of the wafer not coated with photoresist will be etched. After etching, the pores and flow channels of the Berea sample will be etched, while the grains will be intact. After etching, the wafer is anodically bonded to a flat glass plate. The process of anodic bonding is uncomplicated and is easy to carry out. The silicon wafer, in contact with the glass plate, is sandwiched between two electrodes (the negative electrode contacting the glass plate) and the entire system is placed on a hot plate (Fig. 3.4.3). The system is heated to 400° C and a potential drop of 600 V is applied across the electrodes. Bonding between the wafer and the glass plate is immediate and is irreversible. The glass plate must be absolutely flat so the small flow channels become distinct and separate flow channels.

Figure 3.4.4 is a schematic of the flow visualization apparatus. A syringe pump will be used to either independently or simultaneously inject a surfactant solution and air which may be mixed in a foam generation cell and observed through a view port. While the foam is passing through the view port, it will be photographed and/or described at regular intervals so a record of foam texture may be kept throughout the run. Next, the foam will pass through the micromodel described in detail above. While in the micromodel, video and still cameras will record the movement of the foam. After leaving the micromodel, the foam will pass through another view port.

The foam will again be observed and compared to the inlet foam to determine whether any structural changes have taken place in the foam during the displacement process. The pressure drop across the micromodel will be monitored with the use of a pressure transducer, and the pressure data will be recorded on a chart recorder.

3.4.4 RESULTS AND PLANNED WORK

Only the preliminary work using homogeneous micromodels has been completed. Air was injected into a surfactant-saturated micromodel at a flow rate of 2.5x10-4 cc/s and the general flow characteristics observed were found to be identical to those observed by Owete. The flow rate used was on the order of 100 ft/s which is much higher than normal reservoir rates of 1 ft/s. Attempts were made to reduce the flow rate to 1 ft/s, but no precise procedure was found to do this.

As soon as the Berea replica micromodel is constructed, the following work is planned.

1. Foam flow properties in the micromodel will be compared with results obtained by Owete and others to determine whether foam behaves the same in models of the same pore size and configuration of real reservoir rock as it does in the larger pore size micromodels commonly used. Flow rates equivalent to about 100 ft/s will be used in these runs.
2. The oil displacement efficiency of foam will be investigated under two different injection methods. First, the micromodel at residual oil saturation will be injected with 0.5 pore volumes of surfactant solution. Nitrogen will be injected and the foam/oil interactions at the fluid interface will be observed. The micromodel at residual oil saturation will be injected with foam produced in the foam generation cell. The foam/oil interactions will be observed, and results from the two different injection methods will be compared. Macroscopic experiments at Stanford have indicated that the former injection method is significantly more efficient, and a microscopic study of the phenomena may yield useful information.

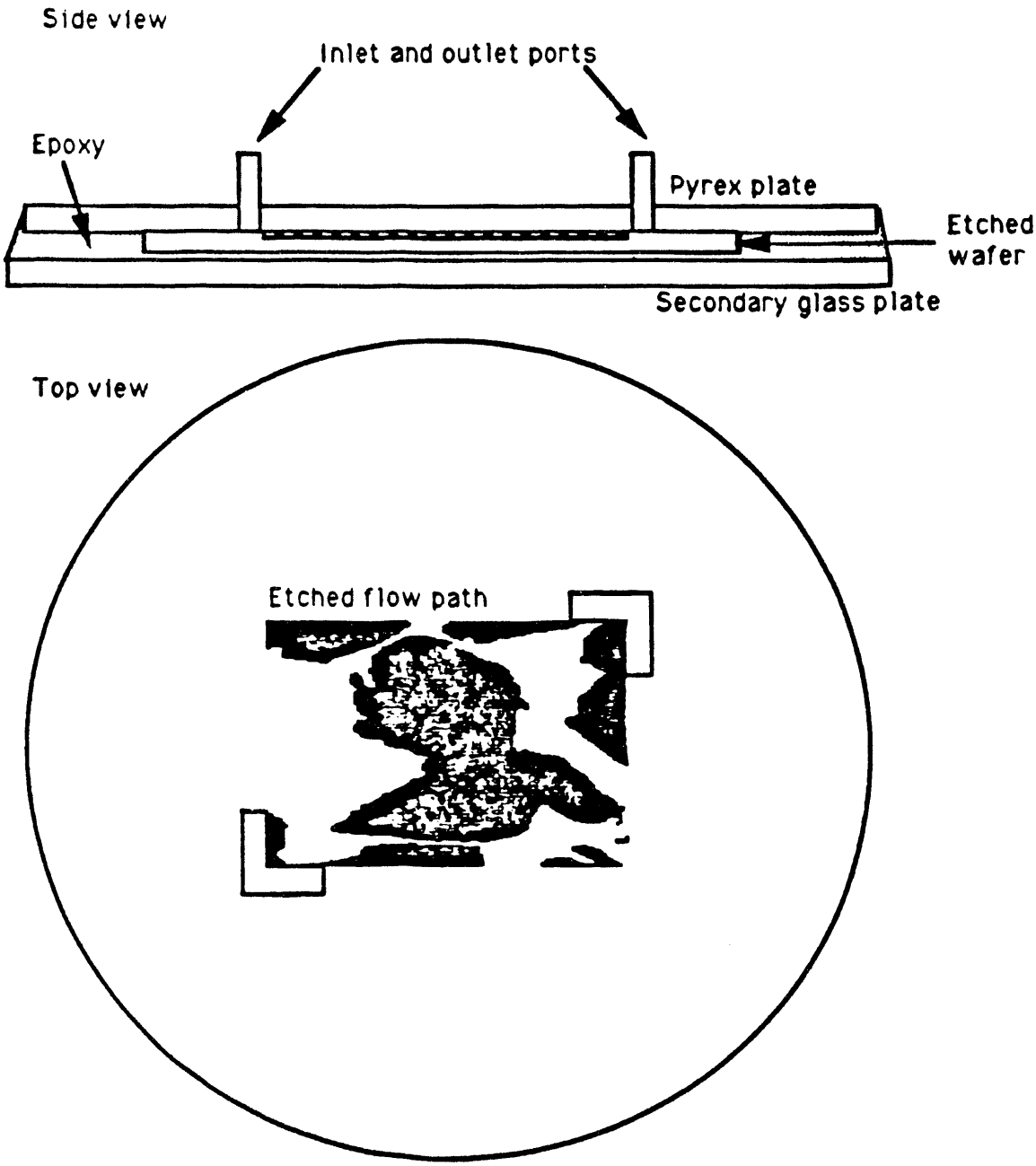

Figure 3.4.1 Schematic of micromodels.

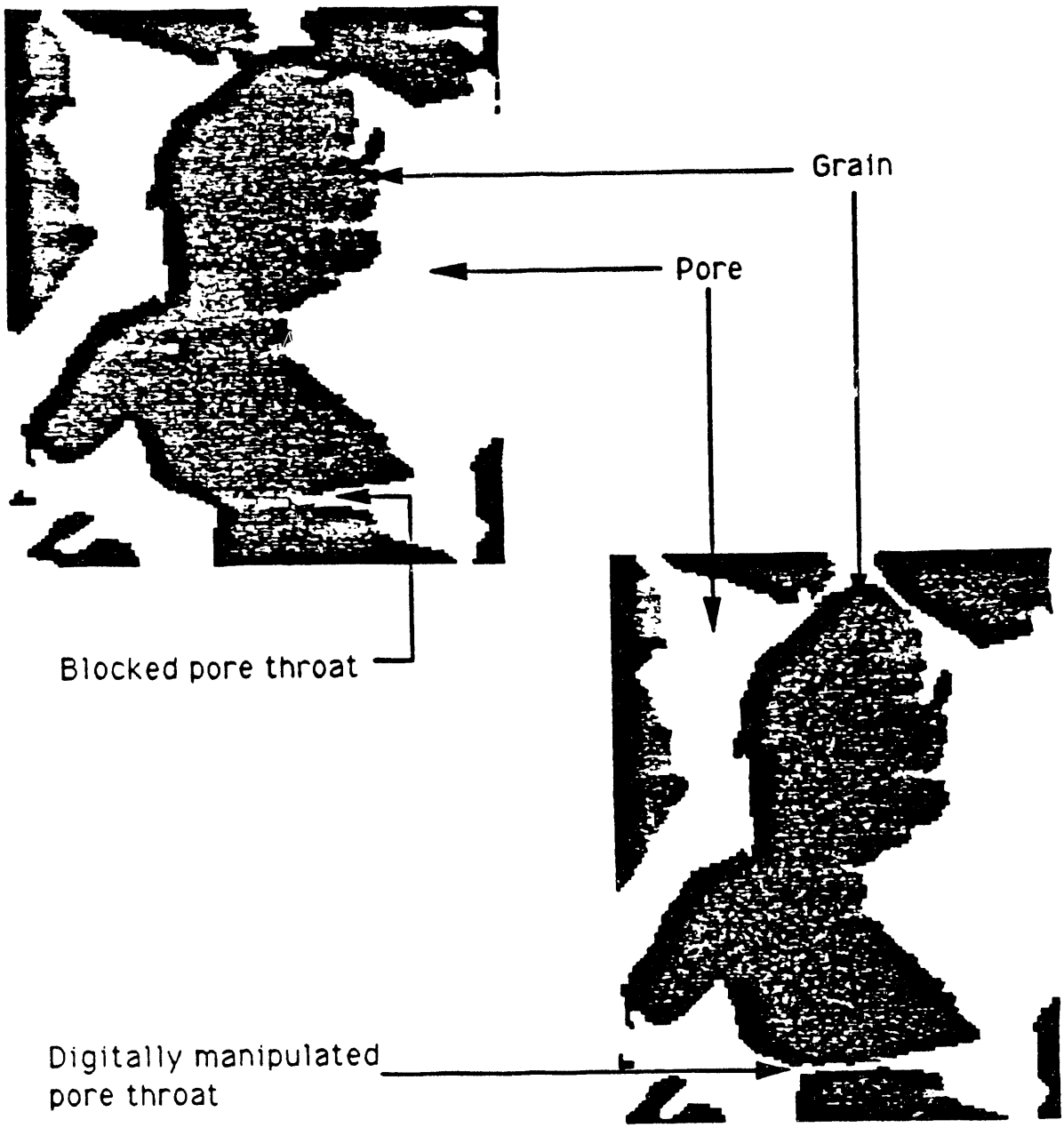

Figure 3.4.2 Image of flow path.

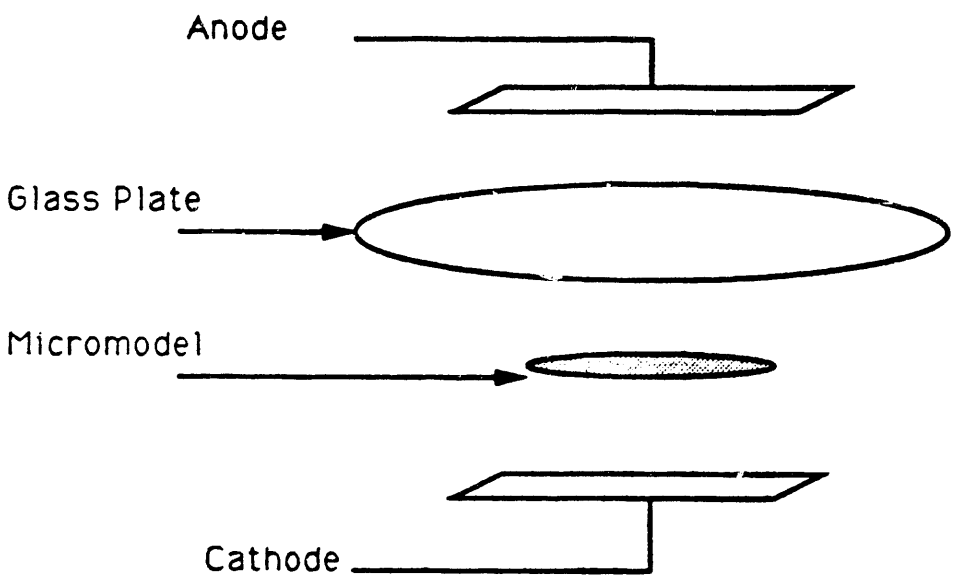

Figure 3.4.3 Anodic bonding schematic.

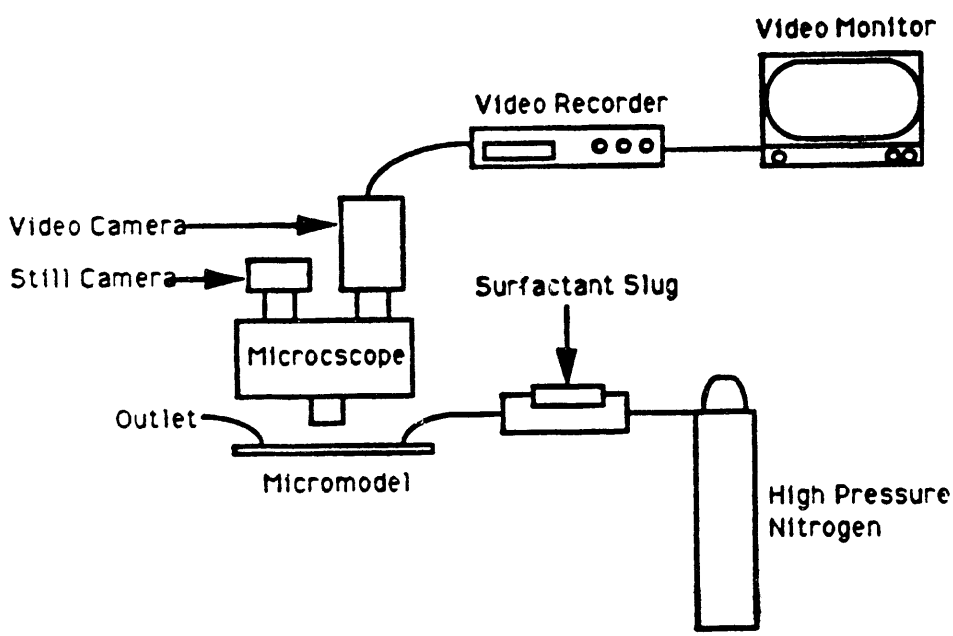

Figure 3.4.4 Experimental schematic.

3.5 TRANSIENT FOAM FLOW IN POROUS MEDIA WITH CAT SCANNER (D. Liu)

This work was published as a technical report for DOE by D. Liu, W. E. Brigham and L. Castanier. For further details, see the reference listed in the footnote.

3.5.1 ABSTRACT

Transient behavior is likely to dominate most of the duration of a foam injection field project. Due to the lack of data, little is presently known about transient foam flow behavior. Foam flow does not follow established models such as the Buckley-Leverett theory, and no general predictive model has been derived. Therefore, both experimental data and a foam flow theory are needed.

In this work, foam was injected at a constant mass rate into one-dimensional sandpacks of 1-in diameter and 24-in or 48-in length that had initially been saturated with distilled water. The system was placed in a CAT Scanner. Data, obtained at room temperature and low pressure at various times, include both the pressure and saturation distributions.

Pressure profiles showed that the pressure gradient was much greater behind the foam front than ahead of it. The pressure gradients kept changing as the foam advance in the sandpack. This behavior differs from Buckley-Leverett theory. The CT scan results demonstrated gas channeling near the front, but eventually the foam blocked all channels and swept the entire cross section after many pore volumes of injection.

Three series of experiments were run: (1) surfactant adsorption measurements, (2) gas displacements of surfactant-laden solutions and (3) foam displacements. The first two series of experiments were made to provide the necessary parameters required to match the foam displacements. To this end, it was necessary to smooth the saturation history data, using a Langmuir-type formula.

A theory was proposed based on the principles of the fractional flow curve construction method. This foam theory treats the foam as composed of infinitesimal slugs of gas of varying viscosities. The foam front has the lowest viscosity and foam at the injection end has the highest.

Liu, D., Brigham, W. E., and Castanier, L. M.: "Transient Foam Flow in Porous Media with Cat Scanner", SUPRI TR 82, DOE Contract No. DE-FG19-87BC14126, October, 1991.

3.6 STUDY OF MATRIX/FRACTURE TRANSFER DURING STEAM INJECTION
(M. D. Sumnu)

3.6.1 INTRODUCTION

There are a lot of petroleum reservoirs throughout the world where discontinuities, such as fractures or joints in the porous matrix, are the main paths for the transmission of fluids. In fact, fractured reservoirs produce 25-30% of the world supply of oil. Usually, the matrix has a low permeability, and fractures occupy only a small portion of the total volume of the reservoir having permeabilities greater than 1 or 2 orders of magnitude larger than the matrix. The matrix stores most of the fluid and fractures are important for the flow path, the performance of a naturally fractured reservoir is strongly related to the rate of fluid exchange between the matrix and fractures. This exchange can be modeled by a matrix-fracture transfer function.

Physical forces that affect the transfer of fluids between fractures and matrix blocks are capillary, gravity and viscous forces. Due to the difficulty in modeling the physical processes taking place in the matrix-fracture transfer, and the lack of experimental data, the matrix-fracture transfer function in flow through fractured reservoirs is not fully understood.

On the other hand, only one third of the original oil in place can be recovered by primary recovery mechanisms. Even this estimate is optimistic for many cases. Thus, enhanced oil recovery (EOR) techniques are intended to recover the remaining oil in place. Steam injection for the production of viscous crudes is by far the most widely used and successful EOR technique today. An advantage of steam injection over other enhanced oil recovery methods is that steam can be applied to a wide variety of reservoirs.

Results of field and laboratory studies indicate that steam injection into fractured reservoirs has great economic potential. Even though injected water moves rapidly through fractures, the heat front moves more uniformly. Oil recovery from heated matrix blocks can be higher than from unheated blocks with recoveries over 60% of the original oil in place. A number of mechanisms operate during steam injection into naturally-fractured reservoirs that are largely independent of oil gravity. This makes steam injection into naturally fractured reservoirs equally attractive for light and heavy oils.

3.6.2 LITERATURE REVIEW

A key publication concerning fractured systems was presented by Barrenblatt and Zheltor (1960). This approach assumes that the fissured porous media can be represented by two overlapping continua referred to as the fracture and the matrix. The fracture continuum consists of the interconnected network of fractures and/or solution vugs which constitute the primary channels for fluid flow. On the other hand, the matrix continuum consists of the intergranular pore space of the rock which comprises the majority of storage space in the rock. The transfer of fluids between these two systems is by pseudosteady state flow between the matrix blocks and the fracture system. The matrix-fracture transfer function is expressed as Darcy's law, but a geometrical factor that describes the characteristic length and flow area between the matrix blocks and fracture system is added.

Early double-porosity models include the ones by Kazemi et al. (1976) and Saidi (1975). The latter modeled a fractured reservoir by dividing it into sectors where the fracture was assumed to have infinite transmissivity. Kazemi et al. (1976), discretized the fracture continuum into grid blocks and modeled fluid flow by a set of fracture mass balance equations. The matrix was assumed to act as source or sink to the fracture, and the flow between the two continua was represented by a single matrix-fracture transfer function.

Understanding the flow mechanisms in matrix-fracture systems during oil recovery is crucial in both experimental and theoretical work. Kleppe and Morse (1974) developed a two-dimensional numerical model to simulate the flow of oil and water in the matrix blocks and the fracture. The validity of the model was checked against data from a laboratory experiment. In their experiments, a circular Berea sandstone core was placed in a plexiglass tube leaving an annular space between the core and the tube. The annulus simulated a fracture surrounding the core. They found that three mechanisms contributed to the exchange of fluids between matrix blocks and fractures. They were:

- dynamic pressure gradients
- capillary pressures
- gravitational forces.

Saidi (1979) studied the drainage performance of a stack of blocks and found that interactions between the blocks were by reinfiltration of oil from fractures into the matrix blocks. They developed a mathematical model which incorporated the interaction effects.

Fung (1990) studied the mechanisms involved in gas/oil gravity drainage in terms of the block-to-block processes. The method involves the calculation of pseudo capillary potentials which, in an average sense, yields the correct flow behavior. Accuracy of the technique was verified by comparing computed results to results from fine-grid simulations.

At the present time, physical processes in fractured systems during steam injection are not fully understood because there is not much work done in this area. There are a few related works cited in literature, though not directly related.

Sahuquet and Ferrier (1982} described a field test in Lacq Superieur field, France, a fractured reservoir. Significant results from steam injection were:

- an increase in oil production,
- oil production coming from those wells completed in the fractured zones of the reservoir,
- heat transfer from injected steam to the reservoir matrix.

The results could not indicate the exact mechanism of oil recovery, but oil swelling and viscosity reduction were believed to be the most probable mechanisms.

Dreher and Kenyon (1986) studied the steam injection process into fractured carbonates both experimentally and with a fully-implicit simulator. They flooded fractured carbonate discs with hot water and steam. Their experimental results indicated that:

- Significant oil can be recovered from matrix elements when hot water or steam is injected into fractures, and heat conduction into the matrix plays a major role in matrix heating with a resulting increase in the rate of oil release from the matrix.
- At steam temperatures, carbonates decompose to produce a significant amount of CO_2, which enhances the recovery rate.
- Oil recovery increases as injection temperature increases.
- Oil recovery reached 30% of OOIP at 200°F, even though pressure differentials were small.

Results from simulations also verified the experimental results. They were:

- Oil recovery increased with increasing steam injection rates.
- There is an optimum steam injection rate for a specified reservoir volume and matrix grid block size.
- Rate of heat conduction from fracture to matrix is a controlling factor.

van Wunnik and Wit (1990} studied the improvement of gas/oil gravity drainage analytically by steam injection in a densely-fissured dome-shaped reservoir. The results were:

- Mixing of steam and hydrocarbon gas occurred.
- Temperature distributed uniformly in the cap rock and reservoir.
- Oil production was due to the thermal expansion of the oil and gravity drainage.

The models developed were applied to the Qarn Alam reservoir of Oman.

Reis (1990) summarized the oil recovery mechanisms during steam injection into a fractured reservoir. He found that the main mechanisms are thermal expansion of oil and matrix volume, chemical reactions within the matrix, drop in pressure, and flashing of the water in the matrix blocks.

3.6.3 OBJECTIVES OF THIS STUDY

Almost all reservoirs have natural fractures due to the stress introduced during geological times. These fractures often create a dominant fracture flow mechanism because of their very high fracture permeabilities compared to the matrix. Furthermore, reservoirs can also be fractured artificially to improve productivity.

On the other hand, some reservoirs contain heavy oil that must be produced by thermal recovery methods. Laboratory studies indicate that steam injection can recover 50% more oil from fractured reservoirs than waterflooding. However, matrix-fracture transfer mechanisms during steam injection are still not clearly known.

The objectives of this research are:

- to understand the transport mechanisms in matrix-fracture systems during steam injection,
- to incorporate these mechanisms in a simulator to understand the matrix/fracture transfer.

The first part of the research will concern fine grid simulations with a commercial simulator to understand the mechanisms before designing the experimental equipment. The purpose will be to understand experimental design parameters such as dimensions, porosity, permeability and etc. The second part concerns steam injection experiments in a fractured lab model to obtain saturation, pressure and temperature data. The results of the experiments will help to understand the transfer mechanisms. Finally, the experimental results will be compared with the results of a double-porosity simulator.

3.6.4 FINE GRID SIMULATIONS

Before beginning the numerical experiments, a number of trial runs were made with the CMG STARS 4.0 thermal simulator. Due to very small grid blocks near a fracture, the run time was very long at the beginning for fine-grid simulations. To decrease the run time, convergence tolerances were changed.

The model used in fine-grid simulations consisted of a matrix block surrounded by fractures. The dimensions of the block were 30x1x10 cm. Because the model was symmetric, only half was modelled. The grid system used changed from coarse to fine as the fracture was approached. The dimensions of the grid blocks in x and z directions are shown in Table 3.6.1 and a schematic view of the quarter of the grid system is given in Figure 3.6.1.

In the simulations, the fracture and matrix have been considered as two separate regions. The process and reservoir data for the base case are given in Table 3.6.2.

3.6.5 FUTURE PLAN

Numerical experiments

First, a number of sensitivity studies will be done and results will be compared with the base case. Porosity, permeability, initial oil saturation, operating conditions, such as injection rate, production pressure and steam quality, will be changed and oil production response to these changes will be observed.

The results of fine grid simulations will help to understand the physical processes taking place during steam injection such as heat and fluid flow.

Experimental Work

A new experimental apparatus will be designed based on the results of the numerical experiments. The model will be two dimensional. The annulus between the core sample and the plexiglass tube will form the fracture. Steam injection runs will be performed on the new model. During the experiments, the saturation distributions will be measured by CT. After completion of the experiments, the experimental results will be used in a thermal simulator. The results will aid understanding the matrix/fracture transfer mechanisms in fractured systems during steam injection.

Table 3.6.1 Dimensions of the grid blocks used in fine grid simulations.

Nx(Number of grid blocks in x-direction)	10
Dx (cm)	0.01 0.09 0.28 0.84 0.99 1.5 2 2.2 2.3 4.79
Nz(Number of grid blocks in z-direction)	12
Dz (cm)	0.01 0.07 0.08 0.32 0.64 8.88 8.88 0.64 0.32 0.08 0.07 0.01
Fracture thickness (cm)	0.01

Table 3.6.2 Process and reservoir data for the base case.

Matrix porosity, %	30
Matrix permeability, md	290
Fracture permeability, md	844000
Initial reservoir pressure, psia	60
Initial reservoir temperature, K	297
Initial oil saturation	0.8
Initial water saturation	0.2
Steam injection rate (Water eq.), m^3/day	0.00021
Production pressure, psia	50

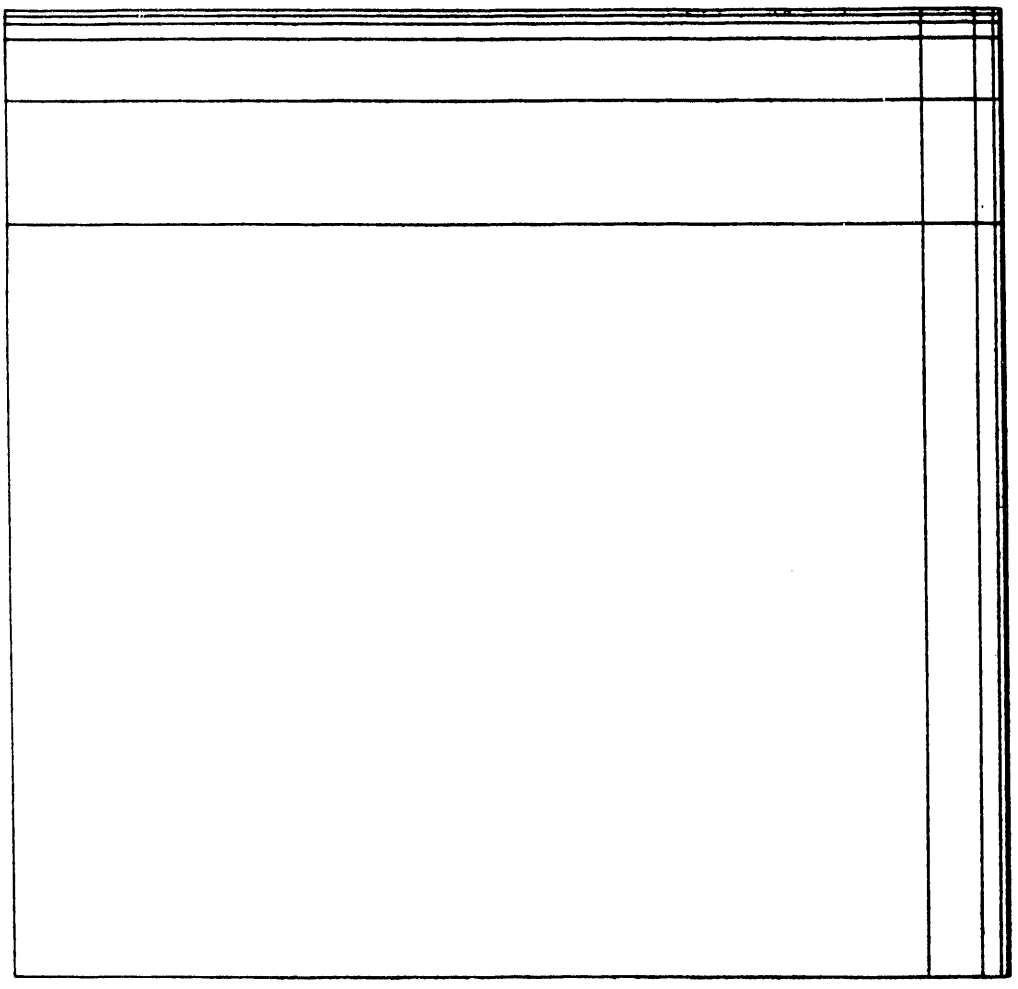

Figure 3.6.1 Schematic view of a quarter of the grid system.

4.1 TRANSIENT BEHAVIOR OF GRAVITY DRAINAGE WELLS
(J. Aa. Aasen)

4.1.1 INTRODUCTION

Significant deposits of heavy oil exist around the world, and as the availability of lighter crudes decreases and the price increases, the production of these fields will become economical. Some of these reservoirs produce by gravity drainage, and productivity evaluation, reservoir geometry, and future performance of these units will be sought. It is important to study well test analysis of gravity drainage systems.

The subject problem is a vertical well producing a slightly compressible single phase fluid at a constant pumping rate. The producing formation is assumed horizontal and of constant height, and the wellbore is exposed to the entire thickness of the payzone. The lower boundary is considered to be an impermeable layer of rock, and the upper boundary is a liquid table which is initially static. It is further assumed that the gas overlying the liquid has zero gauge pressure.

In the customary view of gravity drainage systems, liquid production is attributed to the sum of compressibility effects and the drainage yield as the liquid table is lowered.

The compressibility mechanism dominates behavior in conventional confined reservoirs. As the well is put on production and the wellbore pressure decreases, the combined effects of fluid expansion and porosity reduction give rise to the fluid transport into the wellbore. It can be argued that because of the low pressures usually associated with gravity drainage systems, elastic effects are not likely to be important. On the other hand, rock compressibility may be large because gravity drainage reservoirs are shallow, often unconsolidated, and the fluid may also be compressible because of gas bubbles and dissolved gas present due to the unconfined nature of the system.

For gravity drainage systems, the magnitude of the drainage yield is generally much greater than production due to compressibility effects. As the liquid table in the reservoir drops as a function of time and radius, the porous medium is drained and the ultimate yield of this process will be the product of porosity and the difference between initial and residual liquid saturations. Whether one views this process as the lowering of an imaginary surface free of liquid above and fully saturated below (mathematically convenient), or the lowering of a zone with a saturation gradient (physically more correct), there is a certain time delay inherent in this production mechanism.

The bulk of the research conducted on the transient behavior of gravity drainage systems has been reported in the groundwater literature, and the conventional view among hydrologists appears to be the dual mechanism described above. As a result of this research there are currently several analytical models available for matching pressure transient gravity drainage data. These models are limited because they are based on the same physical view of the problem.

4.1.2 AVAILABLE MODELS

The earliest theory for describing the mechanism of gravity drainage was developed more than a century ago by Dupuit (1863) and Forchheimer (1886), and this approach has become known as the Dupuit-Forchheimer theory of gravity flow systems. The governing partial differential equation may be derived by assuming vertical equipotential lines, thereby neglecting vertical flow effects, and applying the continuity equation to the fluid across the variable fluid head. The fluid is assumed incompressible, and the resulting differential equation contains the pressure or fluid head raised to the second power.

An important paper was published by Wyckoff, Botset and Muskat (1932). The experimental results of gravity drainage experiments were discussed, and interesting theoretical descriptions of the gravity drainage problem were offered as well. These investigators presented a deep understanding of the physical nature of unconfined flow.

In the classical text by Muskat (1937), a chapter is devoted to gravity flow systems, and several of the topics covered there apply directly to the current study of transient behavior of gravity drainage systems.

The Dupuit-Forchheimer theory was scrutinized by Muskat (1937), and several fundamental flaws of this model were identified. The main objection to this theory is the neglected downward vertical flow via the wellbore. As the velocity vector is not horizontal, flow potential theory indicates that the fluid height in the sand will be greater than that observed if the pressure is measured at the base of the sand, and the consequence of this is the seepage face which occurs between the sand and the wellbore.

Methods for analyzing pressure transient data from reservoirs producing under the action of gravity are scarce in the petroleum engineering literature, and the vast majority of the work on this topic has been reported by groundwater researchers. The earliest of these transient models was introduced by Boulton (1954a). By making significant simplifying assumptions, this investigator was able to derive a simple equation for the drawdown as a function of radius and time. In the same year, Boulton (1954b) improved on this simplified approach by introducing the concept of delayed yield. The amount of liquid produced from a gravity drainage well was viewed as the sum of an instantaneous release due to compressibility and a delayed yield due to gravity drainage. An exponential relationship between time and gravity yield was assumed. The mathematical solution to this model was given by Boulton (1963), and the term 'delay index' was introduced as the parameter describing the degree of time lag in the exponential formulation. The use of the exponential relationship between time and gravity yield was purely operational, and the physical meaning of the delay index was not apparent. In fact, this model is based on radial flow only, and the effects of vertical permeability and vertical flow gradients are lumped together in this empirical parameter.

Two years later, Prickett (1965) presented a type curve matching procedure based on this work by Boulton, and a large number of unconfined water wells were analyzed and successfully described in terms of the coefficient of transmissivity, elastic storage, gravity yield and delay index. The author also offered a graphical correlation between the delay index and the grain size of reservoir sands.

The nonphysical nature of Boulton's delay index was a topic for further research, and a few years later two independent papers recast the boundary value problem in a more physically satisfying manner. Neuman (1972) and Streltsova (1972) appeared to have a similar view of the gravity drainage problem, and their solutions differed mainly in the degree of mathematical simplifications. Neuman was able to obtain a linearized solution to the three-dimensional problem using a perturbation technique, and his approach is mathematically more rigorous than the two-dimensional approach used by Streltsova.

The mathematical models described so far neglect the effects of unsaturated flow during gravity drainage, and no considerations was given to the possible effects of delayed gas entry. The influence of the unsaturated zone above the free surface was investigated in detail by Kroszynski and Dagan (1975). In qualitative terms, the drawdown of the liquid table was more rapid at early times than that computed using saturated flow models. This agrees with expectations from a physical point of view. Quantitatively, this effect is negligible and the assumption of negligible capillary effects used in analytical models is justified.

The phenomenon of delayed gas entry was discussed by Bouwer and Rice (1978). All of the delayed yield models discussed previously assume that the initial response of the reservoir is due to compressibility effects, and Bouwer and Rice questioned the importance of fluid expansion and porosity reduction as a primary production mechanism at early times. It was argued that low mobility gas occupying the space above the liquid table may not be able to fill

the void left behind as the liquid level is lowered, and this effect may be an explanation of the high values of compressibility that often are obtained using the delayed yield models.

Neuman (1979) presented a paper devoted solely to the phenomenon of delayed yield, and several relevant aspects of this concept were discussed. The work of Bouwer and Rice was given a great deal of attention, and the author concluded that the proposed gas entry effects may play a role in the delayed yield process. However, Neuman seemed to doubt that gas entry effects are as important as proposed by Bouwer and Rice, and he still advocated the importance of elastic storage. The physical meaning of Boulton's (1954b, 1963) delay index and its relation to the models by Neuman (1972) and Streltsova (1972) was a source of controversy among groundwater researchers during the late 1970's, and Neuman (1979) discussed this question and other related details thoroughly.

During the 1980's, little research on gravity drainage was published in the groundwater literature, and it appears that hydrologists were satisfied with existing models and the notion of compressible flow. The latest contribution to the understanding of gravity drainage systems was given by Ramey, et al. (1989), and this is the only publication found in the petroleum engineering literature. Because of the low pressures usually associated with gravity drainage reservoirs, these authors concluded the elastic properties of the rock and liquid had no effect at early times, and viewed the delayed yield as a vertical flow phenomenon. The analysis of a drawdown test indicated a long period of apparently increasing storage, and this may be explained by the contribution of the zone above the Dupuit free surface. The behavior of a buildup test was also analyzed in this study, and it was concluded that the drawdown and buildup mechanisms were different. The semilog straight line was established much faster during buildup than drawdown, and this observation is in contradiction to the delayed yield models which are fully reversible. The explanation was that vertical gravity drainage during early production could not be reversed during buildup (shut in).

4.1.3 STATEMENT OF THE PROBLEM

In the available transient gravity flow models, compressibility effects are believed to be the main production mechanism at early times, and these models also imply that drawdown and buildup tests are governed by the same mechanisms. Since gravity drainage is associated with low reservoir pressure, the assumed role of elastic storage is questioned. In addition, recent field data have indicated that drawdown and buildup behavior are quite different. The reason for this observation is that the effect of gravity drainage is different from production to shut in.

4.1.4 PROGRESS REPORT FOR 1991

The mathematical derivations leading to the existing transient models have been investigated. Major simplifying assumptions regarding the physical nature of the gravity drainage process are necessary to obtain analytical solutions. The inner boundary condition and the moving upper boundary condition are impossible to state analytically. Available models do not represent the gravity drainage process very well.

The most common simplification made to linearize the problem is to assume the liquid table drawdown to be small compared to the reservoir thickness, and this assumption may often cause unacceptable errors when calculating the pressure behavior at the wellbore. Another assumption inherent in the Dupuit-Forchheimer model is that of radial flow only, and this formulation is poor at early times when vertical flow gradients are significant.

During the course of this study, it appeared that numerical experimentation with a finite difference model would be helpful. Francisco Couri of Petrobras has prepared a computer program for simulating transient gravity drainage flow, and the first version of this simulator was completed in the early part of December. The program is being developed in Brazil, and there

have been problems related to the lack of compiler compatibility. When the simulator is run at Stanford, it fails to reproduce the output obtained by Couri on his computer system in Brazil. Currently, the program is being debugged, and the minor inaccuracies in the source code causing these problems are expected to be corrected soon. We expect Couri to visit Stanford in the first quarter of 1992.

4.1.5 PLANNED WORK FOR 1992

The pressure drawdown behavior of a gravity drainage well is believed to be governed by a different mechanism than that for pressure buildup, and the coming work will be divided into two parts. The drawdown case will be considered first. The task is to produce dimensionless groups of variables that will enable the generation of type curves. The plan is to consider the isotropic case first, and then later extend the type curves to include anisotropy by adding another dimensionless parameter.

The early time behavior may be correlated in terms of an apparent wellbore storage effect, and this parameter is expected to change as a function of time in a manner similar to that often observed during drawdown testing of gas wells (increasing wellbore storage as pressure decreases). Once the drawdown behavior has been correlated in terms of dimensionless parameters, the buildup case will be considered.

In spite of the expected differences between the producing and shut-in reservoir flow mechanisms, the understanding acquired about the drawdown gravity drainage process will be helpful in understanding the buildup case. The result of this study will permit better evaluation of well tests for low pressure oil reservoirs considered targets for EOR.

4.2 MULTIVARIATE OPTIMIZATION OF PRODUCTION SYSTEMS
(N. Ravindran)

4.2.1 INTRODUCTION

When an oil or gas field is being considered for development, considerable resources are devoted to designing well completions and production facilities. Engineers involved in these designs select the best combination of the design variables, such as tubing or flowline diameters and separator size (function of operating pressure), that maximizes an objective. The next common objective is the present value of the project. Currently, the choice of the best values for the design variables is based on nodal analysis of the production system. Nodal analysis finds the operating point (stabilized flow rate) for a specified value of a design variable. Optimizing the production system is carried out by a trial and error process. The procedure is limited to varying a single variable while other variables are held constant.

There are numerical algorithms, commonly known as nonlinear optimization algorithms, that find the global minima of a function. By using these numerical algorithms with mathematical models which describe the behavior of the reservoir, tubing, surface facilities and their interactions, it is possible to obtain a solution which is the optimal value for the decision variables without the use of a trial and error procedure.

Nonlinear optimization algorithms use the objective function to find the optimum solution. The objective function may take the form of a present value of the oil and gas produced, a function of ultimate recovery or capital investment per barrel of oil recovered, or something similar. With the production process modeled and the objective function chosen, the nonlinear optimization algorithms can be applied to find the optimum values for the design variables selected.

4.2.2 NONLINEAR OPTIMIZATION ALGORITHMS

There are two basic types of nonlinear algorithms:

1. Newton and modified Newton techniques. In these cases, the objective function is approximated by a quadratic function. By iterating on the quadratic approximations, the extreme values of the objective function are found.
2. The Polytype technique, where for n decision variables, an $n+1$ dimension polytope is constructed. By flipping this polytope in multidimensional space, the polytope is moved towards the optimum values of the objective function.

4.2.3 APPLICATION

Carroll and Horne (1991) used nonlinear optimization algorithms to study a single well problem where the decision variables were the tubing diameter and separator pressure. Their objective function was the present value of the hydrocarbon income stream. Figure 4.2.1 illustrates the decision space for this problem and the path taken by the polytope algorithm to arrive at the optimum point in the decision space.

The variables used for optimizing may be time dependent. For example, the separator pressure may be altered annually, or the tubing diameter may be changed during a workover. The nonlinear optimization algorithms can also be applied to wells on artificial lift. A well on gas lift could be optimized to operate at the point which uses the least gas to produce the maximum oil. A cyclic steam injection (huff and puff) project could be optimized to maximize the oil-steam ratio.

4.2.4 PURPOSE OF THE RESEARCH

Several specific objectives were selected for this stage of the research. The are as follows.

1. To use nonlinear optimization algorithms to find optimum values for the design variables which may change with time, and
2. To consider optimization of an artificial lift installation using nonlinear optimization on the decision variables.

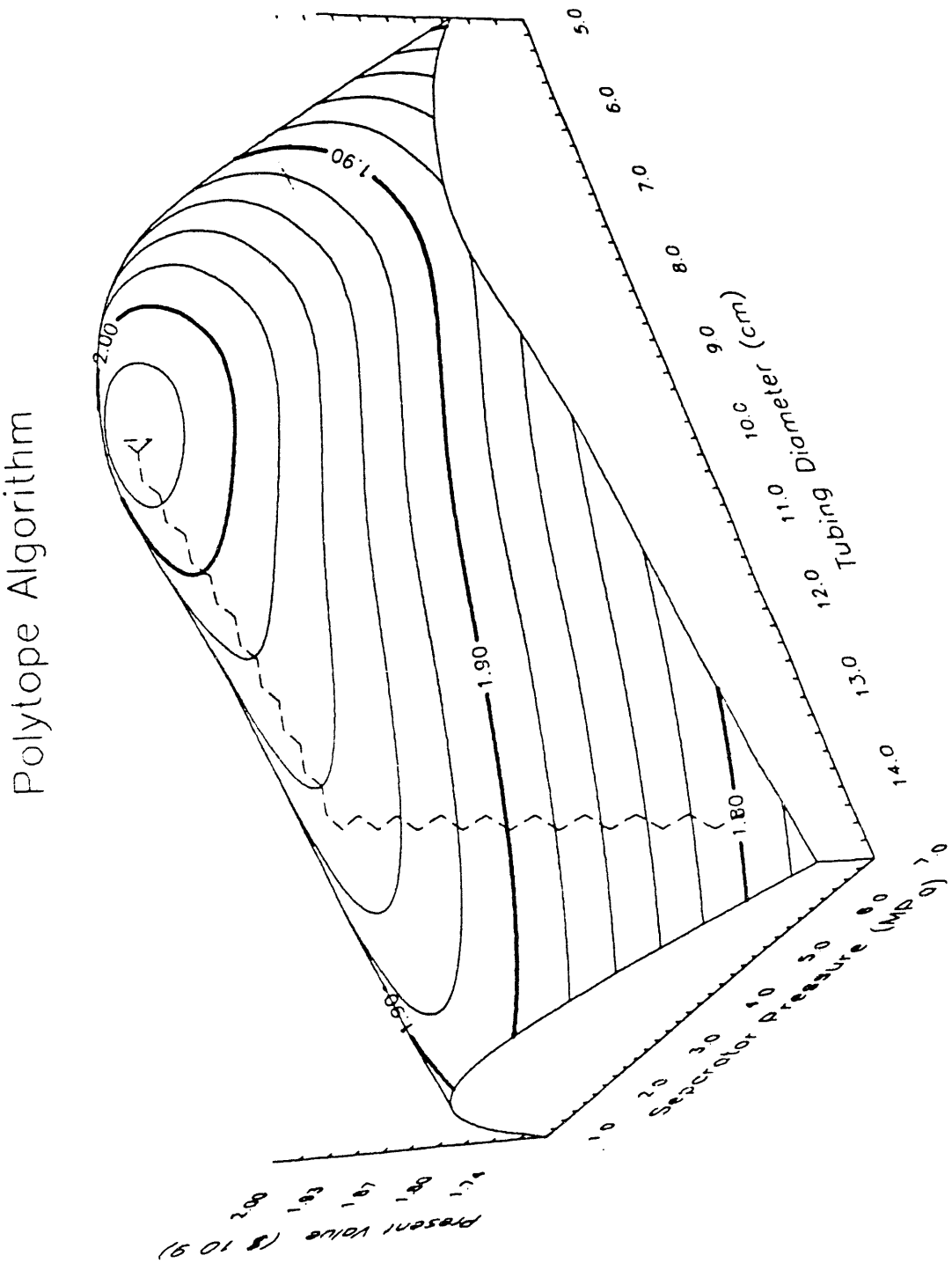

Figure 4.2.1 Convergence path of polytope Heuristic, 3-D.

5.1 ULTRASONIC FLOWMETER
(D. Dannert)

5.1.1 ABSTRACT

The objective of this project is the construction of an accurate downhole flowmeter. The one tool in modern well testing needing improvement is the downhole flowmeter. Currently, testing of an ultrasonic flowmeter is being done in this laboratory. If successful, this device will be installed into a sonde for downhole testing.

5.1.2 THEORY

Sound waves traveling in the same direction as a flowing fluid travel faster than through a stationary fluid and slower when traveling against the flowing fluid. It is possible to take advantage of this by constructing a flow cell with a set of ultrasonic transducers, (sonic transmitter/receivers), one upstream and one downstream (Figure 5.1.1).

The upstream transducer transmits a sound pulse which travels with the fluid flow and is received at the downstream transducer where the travel time is recorded. A travel time against the flow is also measured from the downstream transducer to the upstream transducer. The two travel times are recorded by a computer which calculates the flow rate.

5.1.3 CALCULATIONS

The travel time with the flow is:

$$td=L/(c+Vf) \tag{5.1.1}$$

The travel time against the flow is:

$$tu=L/(c-Vf) \tag{5.1.2}$$

Solving for Vf from Eq. 5.1.1 and Eq. 5.1.2:

$$Vf=L/td-c \tag{5.1.3}$$

$$Vf=-L/tu+c \tag{5.1.4}$$

Adding Eqs. 5.1.3 and Eq. 5.1.4 and dividing by 2:

$$Vf=(L/2)(1/td-1/tu) \tag{5.1.5}$$

The flow rate is related to the fluid velocity by the relationship:

$$Q=A*Vf \qquad (5.1.6)$$

Q - flow rate
Vf - fluid velocity
c - speed of sound in the fluid
L - Wave path length
td - Measured time with flow
tu - Measured time against flow
A - Cross-sectional area of pipe

5.1.4 EXPERIMENT

A flow loop was built in which the flow rate is held constant by using a constant pressure head. The flow cell has been installed into this flow loop. In this way, the data from the flow meter should match the known flow rate.

5.1.5 RESULTS

Data runs are beginning now that the flow loop is complete. The data compares fairly well with the known flow rate for single phase flow of water.

5.1.6 FURTHER RESEARCH

Tests will be run to determine the upper and lower flow rate limits, and the accuracy with different fluids (different flow rates, different sound velocities). The second step will be to test the ultrasonic flowmeter in two-phase flow, using water and air. When the performance of the flowmeter has been documented, installation of the flow cell into a downhole sonde will be done. An attempt is being made to obtain an old spinner tool for this purpose. The last step will be to test the sonde in a large flow loop.

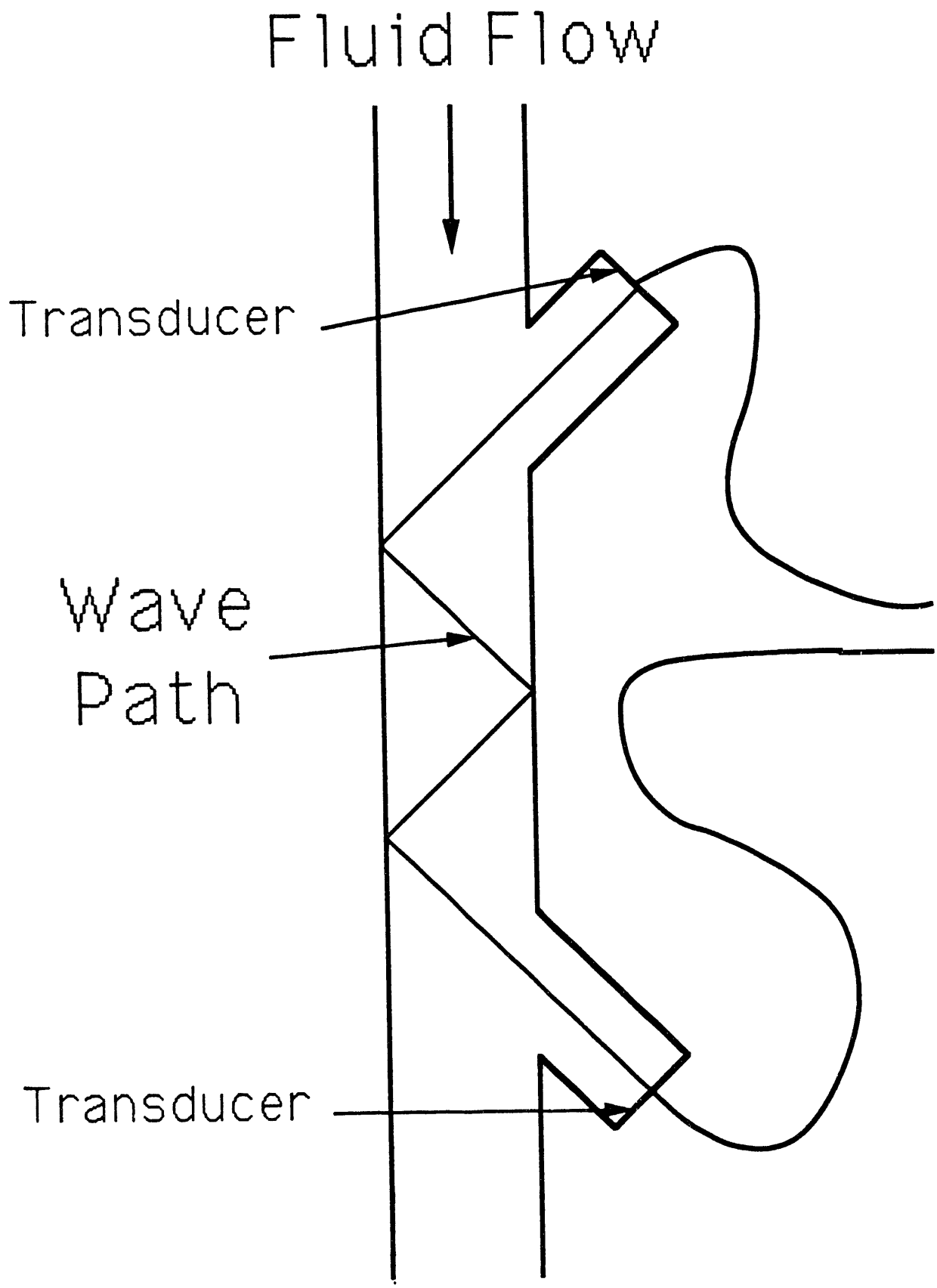

Figure 5.1.1 Experimental equipment of flow meter.

REFERENCES

1. Abramowitz, M. and Stegun, I.A.: "Handbook of Mathematicam Functions", Dover Publications Inc., New York City (1972), p.231.
2. Alexander, J.D., Martin, W.L., and Dew, J.N.: "Factors Affecting Fuel Availability and Composition During In-situ Combustion" JPT 14 1154-1162 (1962).
3. Al-Khafaji, A., Wang F., Castanier, L.M., and Brigham W.E.: "Steam Surfactant Systems at Reservoir Conditions", SPE 10777 March 1982, paper presented at the 1982 California Regional Meeting, San Francisco, California. (Also TR-38)
4. Amyx, J.W. and Bass, D.M.: "Properties of Reservoir Rocks", in Petroleum Production Handbook, Vol. II, ch. 23, published by SPE (1962).
5. Aziz, K., Ramey, H.J., and Brigham, W.E.: "SUPRI Heavy Oil Research Program", 14th Annual Report, Oct. 1, 1990 - Sept. 30, 1990, Dept. of Petroleum Eng., Stanford University, California.
6. Baena C.J., Castanier L.M., and Brigham W.E.: "Effect of Metallic Additives on In-situ Combustion of Huntington Beach Crude Oil" SUPRI TR 78 DOE report contract DE-FG19-87BC14126 June 1990.
7. Barrenblatt, G.I., Zheltov, Y.P., and Kochina, I.N.: "Basic Concept of the Single Phase Flow Through Fractured Porous Media", *Prikladnaia Matematika Mehanika* (1960) 852-64.
8. Bond, D.C. and Holbrook, O.C.: "Gas Drive Oil Recovery Process", U.S. Patent 2,866,507 (1958).
9. Boulton, N.S.: "The drawdown of the water-table under non-steady conditions near a pumped well in an unconfined formation," *Proc. Inst. Civil Eng.* (1954a) **3**, Part 3, 564-579.
10. Boulton, N.S.: "Unsteady radial flow to a pumped well allowing for delayed yield from storage," *Int. Ass. Sci. Hydrol. Rome* (1954b) Tome 2, 472-477.
11. Boulton, N.S.: "Analysis of data from non-equilibrium pumping tests allowing for delayed yield from storage," *Proc. Inst. Civil Eng.* (1963) **26**, 469-482.
12. Bouwer, H. and Rice, R.C.: "Delayed aquifer yield as a phenomenon of delayed air entry," *Water Resour. Res.* (1978) **14** (6), 1068-1074.
13. Burger, J.G. and Sahuquet, B.C.: "Chemical Aspects of In-situ Combustion" Soc. of Pet. Eng J. (October 1972) 410-420.
14. Burger, J., Sourieau, P., and Combarnous, M.: "Thermal Methods of Oil Recovery", published by Institut Francais du Petrole Publications (1985).
15. Butt, J.B.: "Catalyst Deactivation", Adv. Chem. Ser., Vol. 109, p. 259-496 (1972).
16. Carroll III, J.A. and Horne, R.N.: "Multivariate Optimization of Production Systems", SPE 22847, presented at the annual meetingof the SPE, Dallas, Texas, 1991.
17. Castanier L.M. and Brigham W.E.: "Steam With Additives: Field Projects of the Eighties," *J. of Pet. Sci. and Eng.*, 2 193-206 (1989).
18. Chatzis, I., Kantzas, A., and Dullien, F.A.L.: "On the Investigation of Gravity Assisted Inert Gas Injection Using Micromodels, Long Berea Cores and Computer Assisted Tomography," SPE 18204, presented at the 63rd Annual Technical Conference and Exhibition of the SPE, Houston, TX (October 2-5, 1988).
19. De los Rios C.F.: "The Effect of Metallic Additives on the Kinetics of Oil Oxidation Reactions in In-situ Combustion", Engineer's Degree Dissertation, Stanford University (1987).

20. Demiral B.M.R. and Okandan E.: "Steam Foam Injection in a 3-D Laboratory Model," Proceedings 4th European Symposium on Enhanced Oil Recovery, 523-533, October 27-29, 1987, Hamburg, Germany.

21. Demiral, M.R.B., Pettit, A.P., Castanier, M.L., and Brigham, W.E.: "A Three-Dimensional Laboratory Steam Injection Model Allowing Insitu Saturation Measurements," DOE Fossil Energy Report SUPRI TR 83 DOE/BC/14126-29 (to be published), 1992.

22. Dew, J.N. and Martin, W.L.: "Air Requirement for Forward Combustion", Pet. Eng. J. (December 1964) 82 and (January 1965) 82-85.

23. Dreher, K.D. and Kenyon, D.E.: "Heat Flow During Steam Injection into a Fractured Carbonate Reservoir", paper SPE 14902 presented at the 1986 SPE/DOE Fifth Symposium on Enhanced Oil Recovery, Tulsa, OK, April.

24. Drici, O. and Vossoughi, S.: "Study of the Surface Area Effect on Crude Oil Combustion by Thermal Analysis Techniques", JPT (April 1985) (37) 731-735.

25. Dupuit, J.: E´tudes theoriques et pratiques sur le mouvement des eaux, Journel des Ponts et Chaussees, Paris, France, 1863.

26. Fassihi, M.R.: "Analysis of Fuel Oxidation in In-situ Combustion Oil Recovery", Ph. D. Dissertation, Stanford University (May 1981).

27. Ettinger, R.A. and Radke, C.J.: "The Influence of Texture on Steady Foam Flow in Berea Sandstone", Presented at 64th annual Conference of SPE, San Antonio, TX, Oct. 8-11, 1989.

28. Forchheimer, Ph.: *Zeits. Arch. Ing. Ver.*, Hannover (1886).

29. Franshan, P.B. and Jaroslaw, J.: "Displacement of Heavy Oil Visualized by CAT Scan," Petroleum Society of CIM Paper No: 86-37-80, presented at the 1986 CIM Annual Technical Meeting, Calgary (June 8-11).

30. Fung, L.S.K.: "Simulation of Block-to-Block Processes in Naturally Fractured Reservoirs", paper SPE 20019 presented at the 1990 California Regional Meeting, Ventura, CA, April.

31. Gopalakrishnan P., Bories S.A., and Combarnous M.: "An Enhanced Oil Recovery Method: Injection of Steam With Surfactant Solutions," SPE 7109, (Feb. 1978).

32. Hamida, F.: "Characterization of Surfactants as Steamflood Additives", MS report Stanford University, June 1990.

33. Hamida F., Demiral B.M.R., Castanier L.M., and Brigham W.E.: "Characterization of Surfactants as Steamflood additives," DOE Fossil Energy Report SUPRI TR 79 DOE/BC/14126-27 (September 1990).

34. "Handbook of Chemistry and Physics", published by The Chemical Rubber Company, 45th edition (1964).

35. Haunsfield, G.N.: "A Method of and Apparatus for Examination of a Body by Radiation Such as X- or Gamma- Radiation," British Patent No. 1,283,915, London (1972).

36. Hougen, O.A., Watson, K.M., and Ragatz, R.A.: "Chemical Process Principles", Part I, published by John Wiley & Sons Inc., 2nd edition, 1954.

37. Hornbrook, J.W., Castanier, L.M., and Pettit, P.A.: "Observation of Foam/Oil Interactions in a New, High-Resolution Micromodel". SPE 22631, EOR/General Petroleum Engineering, SPE Annual Technical Conference and Exhibition, Dallas, Texas, October 6-9, 1991.

38. Hove, A., Ringen, J.K., and Read, P.A.: "Visualization of Laboratory Corefloods With the Aid of Computerized Tomography of X-Ray," *SPE* Reservoir Engineering, (May 1987) 148-154.

39. Huh, D.G., Cochrane, T.D., and Kovarik, F.S.: "The Effect of Microscopic Heterogeneity on CO_2-Foam Mobility: Part 1- Mechanistic Study", JPT, August, 1989, pp. 872-879.

40. Hutchison, D.A.: "Steam Foam Studies In The Presence of Residual Oil", MS report Stanford University, September 1991.

41. Jensen, J.A. and Friedmann, F.: "Physical and Chemical Effects of an Oil Phase on the Propagation of Foam in Porous Media", SPE 16375 April 1987.

42. Kazemi, H., Merril, L., Porterfield, K., and Leman, P.: "Numerical Simulation of Water-Oil Flow in Naturally Fractured Reservoirs", *SPEJ* (December 1976) 317-326.

43. Khatip Z.I., Hirasaki G.J., and Falls A.H.: "Effects of Capillary Pressure on Coalescence and Phase Mobilities in Foams Flowing Through Porous Media," *SPE Reservoir Engineering*, (August 1988).

44. Kleppe, J. and Morse, R.A.: "Oil Production from Fractured Reservoirs by Water Displacement", paper SPE 5084 presented at the 1974 Annual Fall Meeting, Houston, TX, October.

45. Kroszynski, U.I. and Dagan, G.: "Well pumping in unconfined aquifers: The influence of the unsaturated zone," *Water Resour. Res.* (1975) **11**(3), 479-490.

46. Lim, K.T.: "Steam Distillation Effect and Oil Quality Change During Steam Injection", M. S. report, Stanford University (June 1991).

47. Maneffa, M.G.: "A Laboratory Study of Surfactants as Foam Diverting Agents", MS Report Stanford University, June 1987.

48. Manlowe, D.J. and Radke, C.J.: "A Pore-Level Investigation of Foam/Oil Interactions in Porous Media", SPE 18069, Presented at 1988 SPE Annual Technical Conference and Exhibition, Houston, TX, Oct. 2-5,1988.

49. Marsden, S.S.: "FOAMS IN POROUS MEDIA", SUPRI TR-49, DOE Contract No. DE-AC03-81SF11564, May, 1986.

50. Massoth, F.E.: "Oxidation of Coked Silica-alumina Catalyst", American Chemical Society, Div. Petroleum Chem., Vol. 11, No. 1, p. 75-89 (1966).

51. Muskat, M.: *The Flow of Homogeneous Fluids Through Porous Media,* Chapter 6, McGraw-Hill Book Co., New York (1937).

52. Neuman, S.P.: "Theory of flow in unconfined aquifers considering delayed response of the water table," *Water Resour. Res.* (1972) **8**(4), 1031-1045.

53. Neuman, S.P.: "Perspective on 'delayed yield'," *Water Resour. Res.* (1979) **15**(4), 899-908.

54. Owete, O.S. and Brigham, W.E.: "Flow of Foam Through Porous Media", SUPRI TR-37, DOE Document No. DOE/SF/115646, July, 1984.

55. Prickett, T.A.: "Type-curve solution to aquifer tests under water-table conditions," *Ground Water* (1965) 3(3), 5-14.

56. Racz D.: "Development and Application of a Thermocatalytic In-situ Combustion Process in Hungary" Proceedings 1985 European Meeting on Improved Oil Recovery Rome, Italy April 16-18.

57. Ramey, H.J., Jr., Lichtenberger, G. and Davitt, H.J.: "Well test analysis for gravity drainage systems," paper NMT 890017 presented at the Centennial Symposium at New Mexico Tech, Socorro, NM, October 16-19, 1989.

58. Raza S.H. and Marsden, S.S.: "Foam in Porous Media: Characteristics and Potential Applications," *SPEJ*, 328 (Dec 1970).

59. Reis, J.C.: "Oil Recovery Mechanisms in Fractured Reservoirs During Steam Injection", paper SPE 20204 presented at the 1990 SPE/DOE Seventh Symposium on Enhanced Oil Recovery, Tulsa, OK, April.

60. Sahuquet, B. C. and Ferrier, J. J.: "Steam-Drive Pilot in a Fractured Carbonate Reservoir: Lacq Superieur Field", *JPT* (April 1982) 873-880.

61. Saidi, A.M.: "Mathematical Simulation Model Describing Iranian Fractured Reservoirs and its Application to Haft Kel Field", presented at the 1975 Ninth World Petroleum Congress, Japan.

62. Saidi, A.M.: "Mathematical Simulation of Fractured Reservoir Performance Based on Physical Model Experiments", presented at the 1979 Tenth World Petroleum Congress, Bucharest.

63. Sanchez, J.M. and Hazlett, R.D.: "Foam Flow Through an Oil-Wet Porous Medium: A Laboratory Study", SPE 19687, Presented at 64th annual Conference of SPE, San Antonio,TX, Oct. 8-11, 1989.

64. Sarathi, P.: "Using Micromodels to Study Steam Displacement Processes in Porous Media", NIPER-180 (DE87001201), October, 1986.

65. Shahani, G.H. and Hansel, J.G.: "Oxygen Fireflooding: Combustion Tube Tests with Light, Medium and Heavy Crude Oils", paper SPE/DOE 12726 presented at the 1984 SPE/DOE Enhanced Oil Recovery Symposium, Tulsa (April 1984) (2) 453-464.

66. Shallcross, D.C.: "Modifying In-situ Combustion Performance by the Use of Water-soluble Additives", paper SPE 19485 presented at the Asia-Pacific Conference, Sydney, Australia (Sept. 13-15, 1989).

67. Shallcross, D.C. and Wood, D.G.: "The Accurate Measurements of Heat Flux Using Thin Film Heat Flux Sensors with Application to Petroleum Engineering," DOE Fossil Energy Report SUPRI TR 74 DOE/BC/14126-20 (July 1990).

68. Shallcross D.C, Castanier L.M., and Brigham W.E.: "Characterization of Steam Foam Surfactants Through One Dimensional Sandpack Experiments," DOE Fossil Energy Report SUPRI TR 73 DOE/BC/14126-19 (May 1990).

69. Shallcross D.C., DeLos Rios C.F., Castanier L.M., and Brigham W.E.: "Modifying In-situ Combustion Performance by the Use of water-soluble Additives" SPE Reservoir Engineering J. (August 1991) 287-293.

70. Streltsova, T.D.: "Unsteady radial flow in an unconfined aquifer," *Water Resour. Res.* (1972) **8**(4), 1059-1066.

71. Sze, S.M.: VLSI Technology, Second Ed., McGraw Hill, 1988.

72. van Wunnik, J.N.M. and Wit, K.: "Improvement of Gravity Drainage by steam injection into a fissured reservoir: an analytical evaluation", paper SPE 20251 presented at the 1990 SPE/DOE Seventh Symposium on Enhanced Oil Recovery, Tulsa, OK, April.

73. Vinegar, H.J. and Wellington, S.L.: "Tomographic Imaging of Three-Phase Flow Experiments," *Rev. Sci. Instrum.* Vol. 58 No.1 (January 1987) 97-107.

74. Vossoughi, S., Bartlett, G.W., and Willhite, G.P.: "Prediction of In-situ Combustion Process Variables by Use of TGA/DSC Techniques and the Effect of Sand Grain Specific Surface Area on the process", SPEJ (Oct. 1985) (25) 656-664.

75. Wang, F.P., Castanier L.M., and Brigham W.E.: "A Study of Heat Transfer During Steam Injection and Effect of Surfactants on Steam Mobility Reduction," DOE Fossil Energy Report SUPRI TR 55 DOE/BC/14126-2 (October 1986).

76. Wang, S.Y., Ayral, S., and Gryte, C.C.: "Computer Assisted Tomography for the Observation of Oil Displacement in Porous Media," *SPEJ*, (February 1984) 53-55.

77. Wellington, S.L. and Vinegar, H.J.: "X-Ray Computerized Tomography," *JPT*, (August 1987), 885-898.

78. Withjack, E.M.: "Computed Tomography Studies of 3-D Miscible Displacement Behavior in a Laboratory Five-Spot Model," SPE 18096, presented at the 63rd Annual Technical Conference and Exhibition of the SPE, Houston, TX (October 2-5, 1988).

79. Withjack, E.M.: "Computed Tomography for Rock-Property Determination and Fluid Flow Visualization," *SPE Formation Evaluation*, (December 1988) 696-704.

80. Wyckoff, R.D., Botset, H.G., and Muskat, M.: "Flow of liquids through porous media under the action of gravity," Physics (1932) **3**, 90-113.

APPENDIX A

A.1 Oxygen Consumed and H/C Ratio

The reaction for high-temperature combustion (HTO) is:

$$CH_x + (1 - \frac{m}{2} + \frac{x}{4})\, O_2 \rightarrow (1-m)\, CO_2 + mCO + \frac{x}{2} H_2O \qquad \text{(A-1)}$$

where:

$$m = CO/(CO_2 + CO) \qquad \text{(A-2)}$$

$$x = 4m\,[(O_{2c} - CO_2)/CO - 0.5] \qquad \text{(A-3)}$$

x is the atomic hydrogen-carbon ratio in the fueld and O_{2c}, CO and CO_2 in Eqs. A-2 and A-3 are the mol percent of oxygen consumed, produced carbon monoxide and carbon dioxide, respectively.

$$O_{2c} \approx O_{2i} - O_{2o} \qquad \text{(A-4)}$$

Assuming nitrogen and argon do not oxidize, an accurate determination of O_{2c} and x can be obtained from:

$$O_{2c} = 0.2682\, N_2 - O_{2o} \qquad \text{(A-5)}$$

$$x = \frac{4\,[0.2682\, N_2 - (\, O_{2o} + CO_2 + 0.5\, CO)\,]}{(\, CO_2 + CO\,)} \qquad \text{(A-6)}$$

where N_2 is the mol percent of nitrogen in the produced gas.

A.2 High Temperature Oxidation

If q_o (liter/min) is the effluent gas rate, and because 1 mol gas occupies 22.4138 liters at standard conditions:

Mass of fuel (CH_x) consumed $g/s = \frac{dmf}{dt} =$

$$= \frac{q_o\,(CO + CO_2)\,(12.011 + x)}{60 \times 22.4138} \qquad \text{(A-7)}$$

where the atomic weight of carbon is 12.011.

If r_s is the average radius of a sand grain (assumed spherical), and the sand pack has length, L, cross-sectional area, A, and porosity, ϕ:

$$\text{No. of sand grains in the cell} = \frac{3\,AL\,(1-\phi)}{4\pi\,r_s^3} \tag{A-8}$$

Based on sieve analysis (Table 2.1.2), r_s is 0.0375 cm for 20-30 mesh Ottawa sand.

Assuming the fuel density for crude oil to be equal to that of its residuum at the equivalent normal boiling point of 335 deg. C, the API versus residuum correlation (Lim, 1991) was used to estimate the fuel density. For a kinetics run using carbon, the fuel density is that for carbon, 2 g/cc (Handbook of Chemisty and Physics, 1964).

Spherical Fuel Geometry Model

Let r be the radius of the fuel surface at time, t (Figure 2.1.6) and ρ_f the fuel density:

$$\text{Total mass of fuel at time, } t = (r^3 - r_s^3)\,AL\,(1-\phi)\rho_f/r_s^3 \tag{A-9}$$

Differentiating Eq. A-9 with respect to time t and equating the result with Eq. A-7 yields:

$$\frac{d}{dt}\left[\frac{(r^3-r_s^3)}{r_s^3}\,AL\,(1-\phi)\rho_f\right] = -\frac{q_o(CO+CO_2)(12.011+x)}{60\times 22.4138} \tag{A-10}$$

Integrating Eq. A-10 from t to the end of fuel oxidation, t_e (where $r = r_s$) gives:

$$r = r_s\,(1+\gamma)^{1/3} \tag{A-11}$$

where:

$$\gamma = \frac{\int_t^{t_e} q_o\,(CO+CO_2)(12.011+x)\,dt}{60\times 22.4138AL(1-\phi)\rho_f} \tag{A-12}$$

If q_i is the air injection rate, the molar weight of oxygen is 31.9988, and m_f is the mass of fuel at time t, from Eq. 2.1.2:

$$\frac{31.9988\,q_i\,O_{2c}}{60\times 22.4138} = -\alpha\,\frac{dm_f}{dt} \tag{A-13}$$

The reaction rate for a particular surface area (as given, e.g., by Eq. 2.1.23 in Burger, et al., 1985) is:

$$\frac{dmf}{dt} = -k_o^*\,P_{o_2}^m\,\exp(-E_o/RT)\times surface\ area \tag{A-14}$$

$$\text{Fuel surface area} = 3AL\,(1-\phi)\,(1+\gamma)^{2/3} \tag{A-15}$$

Substituting Eq. A-15 in Eq. A-14 and equating the result with Eq. A-13 yields:

$$\frac{q_i\, r_s\, O_{2c}}{2(1+\gamma)^{2/3}} = \beta_o \exp\left(-E_o/RT\right) \tag{A-16}$$

where

$$\beta_o = 63.0413\ \alpha\ k_o^*\ P_{o_2}^m\ AL(1-\phi) \tag{A-17}$$

A graph of the natural logarithm of the left hand side of Eq. A-16 versus 1/T for the carbon or crude kinetics data at HTO, however, did not yield the expected straight line fit (Fig. 2.1.2). This model was thus rejected, and a model which would consider the fuel surface area better was developed.

Varying Fuel Geometry Model

Fuel in the toroid ($t \geq t_c$)

For $t \geq t_c$, the fuel is assumed to be in the form of a toroid (Figs. 2.1.5 and 2.1.7) where h_f is the fuel height.

Fuel volume per grain contact (i.e., half of the toroid volume) =

$$\pi\left[\frac{r_s h_f^2}{4} - \frac{h_f^3}{8}\right] \tag{A-18}$$

Assuming the porosity of the sand mixture to be intermediate between that of a cubic packing (ϕ = 0.476) and that of a rhombohedral packing (ϕ = 0.2596) (Amyx and Bass, 1962), an average porosity of 0.37 was used for both 20-30 and 100 mesh Ottawa sands. The number of contacts per grain is taken to be six (6). Therefore:

Total fuel volume in the sand mixture =

fuel volume per grain contact × no. of contacts per grain
× no. of grains =

$$\frac{q}{8}\frac{h_f^2}{r_s^2}\,AL\,(1-\phi) \tag{A-19}$$

Differentiating Eq. A-19 and equating the result with Eq. A-7 gives:

$$\frac{d}{dt}\left[\frac{q}{8}\frac{h_f^2}{r_s^2}\,AL\,(1-\phi)\rho_f\right] = \frac{-\,q_o\,(CO + CO_2)\,(12.011 + x)}{60 \times 22.4138} \tag{A-20}$$

Integrating Eq. A-20 from $t = t$ ($h_f = h_f$) to $t = t_e$ ($h_f = 0$) yields:

$$h_f = \frac{r_s}{3} (8\gamma)^{1/2} \tag{A-21}$$

where γ is defined by Eq. A-12.

Total fuel surface area in sand mixture =

fuel surface area per grain contact × no. of contacts per grain × no. of grains ≈

$$\frac{4.1195\ AL\ (1-\phi)\ \gamma^{3/4}}{r_s} \tag{A-22}$$

Substituting Eq. A-22 in Eq. A-14 and integrating yields:

$$\frac{q_i\ r_s\ O_{2c}}{2.7464\ \gamma^{3/4}} = \beta_o\ \exp(-E_o/RT) \tag{A-23}$$

where β_o is defined by Eq. A-17.

Fuel in Non-toroidal Part ($t < t_c$)

For $t < t_c$, the surface area, S, consists of the surface area of the toroid, A' (given by Eq. A-24), and that of the fuel directly deposited on the sand grain surface. The following exponential relationship was assumed:

$$S = A' \exp\left[a\left(\frac{1}{T} - \frac{1}{T_c} \right) \right] \tag{A-24}$$

where a is a proportionality constant. Substituting Eq. A-24 in Eq. A-14 yields:

$$\frac{q_i\ r_s\ O_{2c}}{\gamma^{3/4}} = \beta \exp\ (-E/RT) \tag{A-25}$$

where:

$$\beta = 173.1338\ AL\ (1-\phi)\ \alpha\ k_o^*\ P_{O_2}^m\ \exp(-a/T_c) \tag{A-26}$$

$$E = aR - E_o \tag{A-27}$$

From Eq. A-25, we conclude that for $t < t_c$, a second straight line with slope, $-E/R$, and an intercept of ln β should exist for a graph of the natural logarithm of the left hand side of Eq. A-25 versus 1/T. This is shown in Fig. 2.1.4d. A reasonable straight line is evident.

Calculation of Oxygen Consumption

Calculation of oxygen consumption requires determination of fuel height, h_f, as a function of temperature.

Differentiating Eq. A-20:

$$\frac{9h_f}{4r_s^2}\, AL\, (1-\phi)\rho_f\, \frac{dh_f}{dt} = -\frac{q_o\,(CO + CO_2)\,(12.011 + x)}{60 \times 22.4138} \tag{A-28}$$

From Eq. A-1:

$$q_o(CO + CO_2) = \frac{q_i\, O_{2c}}{(1-\frac{m}{2} + \frac{x}{2})} \tag{A-29}$$

From Eqs. A-21 and A-23:

$$O_{2c} = \frac{3h_f^{3/2}}{q_i\, r_s}\, \beta \exp(-E/RT) \tag{A-30}$$

Substituting Eq. A-29 and A-30 in Eq. A-28 and integrating yields:

$$h_f = \left[h_{f_o}^{1/2} - \frac{\kappa}{2} \int_{t_o}^{t} \exp(-E/RT)dt \right]^2 \tag{A-31}$$

where:

$$\kappa = \frac{9.9145 \times 10^{-4}\, \beta\, (12.011 + x)}{\sqrt{r_s}\, (1-\frac{m}{2} + \frac{x}{2})\, AL\, (1-\phi)\rho_f} \tag{A-32}$$

$$h_{f_o} = \frac{\kappa}{2} \int_{t_o}^{t_e} \exp(-E/RT)dt \tag{A-33}$$

The integrals in Eqs. A-31 and A-33 can be evaluated using exponential integrals of the first kind.

Having obtained h_f, the oxygen consumption curve for fuel oxidation can be computed using Eq. A-30.

*U.S.GPO:1992-661-026/60024

A.3 Low Temperature Oxidation

Based on the simplifying assumptions described in Section 2.1.5.(2), the fuel concentration during LTO increases with increasing temperature. Thus, the argument in the exponential term in Eq. 2.1.1 is positive. That is:

$$\frac{q_i\, O_{2c}}{AL} = A_r\, P_{o_2}^m\, C_f^n \exp\,(E_f/RT) \tag{A-34}$$

Similarly, the right hand side of Eq. 2.1.2 is positive. That is:

$$\frac{q_i\, O_{2c}}{AL} = \alpha\, \frac{dC_f}{dt} \tag{A-35}$$

Integrating Eq. A-35 from $t = 0$ to $t = t$ where $C_f = 0$ at $t = 0$, and substituting the resulting equation in Eq. A-34 yields:

$$\frac{O_{2c}}{\left[\int_o^t O_{2c}\, dt\right]^n} = \beta_f \exp\,(E_f/RT) \tag{A-36}$$

where

$$\beta_f = \left[\frac{q_i}{AL}\right]^{n-1} \frac{A_r\, P_{o_2}^m}{\alpha^n} \tag{A-37}$$

A graph of the natural logarithm of the left hand side of Eq. A-36 should yield a straight line with a slope of E_f/R and an intercept of ln β_f for the correct exponent, n, which is obtained by trial- and-error. Eq. A-36 can be integrated to yield:

$$O_{2c}(t_2) = \beta_f \exp(E_f/RT_2)\left\{\left[\frac{O_{2c}\,(t_1)}{\beta_f \exp(E_f/RT)}\right]^{\frac{1-n}{n}} + (1-n)\,\beta_f \int_{t_1}^{t_2} \exp(E_f/RT)dt\right\}^{\frac{n}{1-n}} \tag{A-38}$$

The integrand in Eq. A-38 can be approximated by a series expansion and the integral evaluated to derive the oxygen consumption curve for LTO.

END

DATE FILMED

7/6/92